



HAL
open science

Mechanism and size effects of helicity-dependent all-optical magnetization switching in ferromagnetic thin films

Yassine Quessab

► **To cite this version:**

Yassine Quessab. Mechanism and size effects of helicity-dependent all-optical magnetization switching in ferromagnetic thin films. Materials Science [cond-mat.mtrl-sci]. Université de Lorraine, 2018. English. NNT: 2018LORR0116 . tel-01887131

HAL Id: tel-01887131

<https://theses.hal.science/tel-01887131>

Submitted on 3 Oct 2018

HAL is a multi-disciplinary open access archive for the deposit and dissemination of scientific research documents, whether they are published or not. The documents may come from teaching and research institutions in France or abroad, or from public or private research centers.

L'archive ouverte pluridisciplinaire **HAL**, est destinée au dépôt et à la diffusion de documents scientifiques de niveau recherche, publiés ou non, émanant des établissements d'enseignement et de recherche français ou étrangers, des laboratoires publics ou privés.



AVERTISSEMENT

Ce document est le fruit d'un long travail approuvé par le jury de soutenance et mis à disposition de l'ensemble de la communauté universitaire élargie.

Il est soumis à la propriété intellectuelle de l'auteur. Ceci implique une obligation de citation et de référencement lors de l'utilisation de ce document.

D'autre part, toute contrefaçon, plagiat, reproduction illicite encourt une poursuite pénale.

Contact : ddoc-theses-contact@univ-lorraine.fr

LIENS

Code de la Propriété Intellectuelle. articles L 122. 4

Code de la Propriété Intellectuelle. articles L 335.2- L 335.10

http://www.cfcopies.com/V2/leg/leg_droi.php

<http://www.culture.gouv.fr/culture/infos-pratiques/droits/protection.htm>



UNIVERSITÉ
DE LORRAINE



UNIVERSITÉ DE LORRAINE

THESIS

FOR THE OBTENTION OF THE DEGREE OF

DOCTOR OF PHILOSOPHY

IN *Physics*

Mechanism and size effects of helicity-dependent all-optical magnetization switching in ferromagnetic thin films

Author:

Yassine QUESSAB

Thèse publiquement soutenue à Nancy le 24 Septembre 2018 devant le jury suivant :

Mme Christine BOEGLIN	Directrice de recherche, Institut de Physique et Chimie des Matériaux de Strasbourg	Rapportrice
Mme Stefania PIZZINI	Directrice de recherche, Institut Néel	Rapportrice
M. Jeffrey BOKOR	Professeur, University of California, Berkeley	Examineur
M. Andrew D. KENT	Professeur, New York University	Examineur
M. Eric E. FULLERTON	Professeur, University of California, San Diego	Examineur
M. Stéphane MANGIN	Professeur, Université de Lorraine	Directeur de thèse

Institut Jean-Lamour
UMR 7198 - Université de Lorraine
Département de Physique de la Matière et des Matériaux
Nanomagnetism and Spintronics team



Institut Jean Lamour

“If your determination is fixed, I do not counsel you to despair. Few things are impossible to diligence and skill.”(chapter 12)

“Great works are performed not by strength, but perseverance.” (chapter 13).

Samuel Johnson, *The History of Rasselas, Prince of Abissinia* (1759)

UNIVERSITÉ DE LORRAINE

Abstract

Institut Jean-Lamour

Doctor of Philosophy

Mechanism and size effects of helicity-dependent all-optical magnetization switching in ferromagnetic thin films

by Yassine QUESSAB

Over the past decade, the demand for an even higher capacity to store data has been gradually increasing. To achieve ultrafast and ultrahigh density magnetic data storage, low-power methods to manipulate the magnetization without applying an external magnetic field has attracted growing attention. The possibility to deterministically reverse the magnetization with only circularly polarized light was evidenced in multiple ferri- and ferro-magnetic materials. This phenomenon was called helicity-dependent all-optical switching (HD-AOS). In ferromagnets, it was demonstrated that HD-AOS was a cumulative and multishot process with a helicity-independent demagnetization followed by a helicity-dependent magnetization recovery. Yet, the microscopic mechanism of this helicity-dependent remagnetization remained highly debated.

In this thesis, we investigated the magnetization reversal mechanism of all-optical switching in ferromagnetic materials. To explore a potential switching process through domain nucleation and domain wall (DW) propagation, we studied the response of a DW upon femto- or pico-second laser irradiation in Co/Pt thin films that exhibit HD-AOS. We reported helicity-dependent all-optical domain wall motion. We demonstrated that it results from the balance of three contributions: the temperature gradient due to the laser heating, the helicity effect and the pinning effects. By measuring the magnetic circular dichroism, a purely thermal mechanism of the laser-induced DW motion appears to be excluded.

Furthermore, we examined the size effects in AOS in Co/Pt films patterned into microdots with a diameter between 10 and 3 μm . This allowed us to explore the role of the dipolar field in the switching mechanism. We discovered that a larger number of laser pulses was required to reverse the magnetization of a microdot compared to the continuous film. This indicated that the dipolar field actually eases the magnetization reversal in the full film. Thus, AOS is less energy-efficient in patterned films, hence making Pt/Co/Pt multilayers not an ideal candidate for integrating AOS in spintronic devices.

Keywords: All-optical switching, spintronics, femtosecond laser pulses, magnetization reversal

Mécanisme et effets de tailles du retournement tout-optique dans les couches minces ferromagnétiques

Pour des applications technologiques d'enregistrement magnétique de l'information à haute densité et vitesse d'écriture et de lecture ultra-rapide, les chercheurs se sont penchés vers des méthodes de manipulation de l'aimantation sans application de champ magnétique externe. Il a été découvert qu'il était possible de renverser de manière déterministe l'aimantation de plusieurs matériaux ferri- et ferromagnétiques à l'aide uniquement d'impulsions laser ultracourtes polarisées circulairement. Ce retournement tout-optique s'est avéré être un processus cumulatif nécessitant plusieurs impulsions ultracourtes dans les matériaux ferromagnétiques. Notamment dans les multicouches (Co/Pt), le retournement tout-optique se fait en deux étapes : une désaimantation indépendamment de l'hélicité suivie d'une ré-aimantation dans une direction ou l'autre selon l'hélicité. Pour autant, le mécanisme à l'origine du rétablissement de l'ordre magnétique n'a pas été étudié jusqu'à présent.

Dans cette thèse, nous avons étudié le mécanisme de renversement de l'aimantation dans les couches ferromagnétiques résultant de l'excitation par impulsions laser ultracourtes polarisées circulairement. Pour cela, nous étions intéressés par la réponse d'une paroi de domaine dans les couches minces de Pt/Co/Pt à la suite d'une excitation laser et en fonction de la polarisation de la lumière. Nous avons démontré la possibilité d'induire un déplacement tout-optique et déterministe d'une paroi de domaine. Nous montrons que la propagation de la paroi résulte de la compétition entre trois contributions : le gradient de température dû aux effets de chauffage par le laser, l'effet de l'hélicité de la lumière et les effets de piépages de la paroi. Par ailleurs, par mesures expérimentales du dichroïsme circulaire, nous excluons un mécanisme purement thermique du déplacement de paroi. Ainsi nous confirmons que le retournement tout-optique des couches ferromagnétiques se fait par une nucléation suivie d'une ré-aimantation par propagation déterministe des parois de domaines selon l'hélicité.

De plus, nous avons exploré la possibilité d'utiliser le retournement tout-optique dans des dispositifs spintroniques pour l'enregistrement de l'information à haute densité. Pour se faire, il est nécessaire d'étudier les effets de tailles du retournement lorsque le matériau est structuré en îlots à l'échelle du micro- ou nano-mètre. Nous avons montré qu'un plus grand nombre d'impulsions laser est nécessaire afin de renverser l'aimantation de micro-disques comparé à la couche continue ferromagnétique. Il en résulte que le champ dipolaire aide le renversement de l'aimantation dans les couches continues rendant ainsi le retournement tout-optique énergétiquement plus favorable.

Mots-clés: Retournement tout-optique, spintronique, impulsions laser femtosecondes, renversement de l'aimantation

Acknowledgements

Ce rapport de thèse met un point final à une aventure exceptionnelle aux mille et une péripéties. Je tiens à remercier sincèrement Pr Jeff Bokor de UC Berkeley, Pr Andrew Kent de New York University, Pr Eric Fullerton de UC San Diego, Mme Stefania Pizzini de l'Institut Néel et Mme Christine Boeglin de l'IPCMS d'avoir accepté d'être membre du jury de thèse ainsi que pour leurs remarques et discussions très enrichissantes.

Par ailleurs, je voudrais remercier tous les membres de l'équipe 101 - nanomagnétisme et spintronics qui ont fait de ces 3 années une très bonne expérience, je les remercie pour leur disponibilité, l'aide qui m'a été apportée et les bons moments passés ensemble en pause café. Je tiens tout particulièrement à remercier Pr Stéphane Mangin, mon directeur de thèse, pour la confiance qui m'a accordé alors que je n'étais que son élève en école d'ingénieur ainsi que son enthousiasme indéfectible. Il a cru en mes capacités afin de mener à bien des travaux de recherche. Je tiens à mentionner à nouveau Pr Eric Fullerton du CMRR (UCSD) qui a accepté de me recevoir au sein de son laboratoire au cours de nombreuses missions de recherche. Non seulement j'y ai beaucoup appris d'un point de vue scientifique, mais j'ai pu également me familiariser avec le monde de la recherche aux États-Unis. Il s'en va sans dire que c'est grâce à ses deux missions à San Diego que j'ai pu fortement amélioré mon niveau d'anglais.

Cette thèse ne serait pas grand chose si je n'avais pas reçu de l'aide de la part des membres de l'équipe 101. Mes remerciements vont tout particulièrement à Grégory Malinowski pour les discussions des résultats, suggestions d'orientation des travaux ainsi que pour son expertise expérimentale. Je remercie Michel Hehn pour les échantillons d'excellente qualité qu'il a pu me faire de temps à autre. Ensuite, je voudrais exprimer aussi toute ma gratitude à Mohammed-Salah El Hadri, ancien doctorant de l'équipe 101, qui fut un réel un mentor dans cette aventure, qui a su me familiariser avec les expériences et problématiques de "all-optical switching". Bien qu'il ait commencé un postdoc à San Diego sur un sujet radicalement différent, il a toujours été disponible pour répondre à mes nombreuses questions dans le domaine. Rajesekhar Medapalli, postdoc au CMRR, m'a également beaucoup aidé à mes débuts dans la thématique de "all-optical switching". Merci pour ses conseils à Jon Gorchon, qui certes, est une recrue CNRS récente de l'équipe, mais j'ai apprécié le peu de temps que nous avons passé à travailler ensemble. Mes remerciements vont par ailleurs à Marwan Deb qui n'a cessé d'être disponible pour apporter une aide et une meilleure compréhension expérimentale bien qu'il eût été très occupé. Je tiens également à remercier Yong Xu pour l'aide apportée sur la PVD. Enfin, une petite mention spéciale pour mon co-bureau Pierre Vallobra qui m'a énormément aidé pour la fabrication de mes échantillons, je le remercie pour les bonnes rigolades et discussions scientifiques que nous avons eues, je lui souhaite bonne chance pour sa future soutenance de thèse qui arrivera très prochainement.

Je tiens à remercier Isabelle Fournelle pour sa gentillesse et sa patience, pour cause elle a vu un certain nombre d'ordre de missions de ma part ! Merci à Aurore Calmes Emonot pour son sourire indéfectible et son organisation des conférences. Je remercie Daniel Lacour et Georgy Kichin pour les nombreuses discussions photographie que nous avons eues et leur aide expérimentale notamment Daniel sur la MFM. Merci à Hélène Fischer pour m'avoir fait découvrir la médiation scientifique, ce fut un plaisir que de participer à cette action, bonne continuation

! J'aimerais remercier ensuite Laurent Badie pour sa joie et son sourire, son extrême disponibilité en salle blanche pour régler les soucis, sans mentionner les petites rigolades au quotidien ! Dans cette aventure extraordinaire chaque membre de l'équipe, bien qu'il travaille sur des thématiques différentes, a contribué d'une manière ou d'une autre de fait je voudrais remercier : Sébastien Petit-Watelot, François Montaigne, Carlos Rojas-Sanchez, Karine Dusmenil et Thomas Hauet.

Enfin, je tiens à remercier les doctorants de l'équipe : Maryam Massouras, Koseila Ait-Oukaci, Thai Pham, Thibaud Fache, Alexandre Dekens, Anton Kyianytsia, Charles Guillemard, Philippe Scheid et Gauthier Masset pour les bons moments passés ensemble, je leur souhaite pleins de réussite pour leur thèse. Je voudrais remercier Vincent Polewczyk, ancien doctorant de l'équipe, pour ses encouragements et son aide étant donné que nous passions presque au même moment notre soutenance, et avec qui je discutais souvent voyage, une passion commune que nous avons. De la même manière, je remercie Elmer Nahuel Montebianco avec qui j'ai nagé quelques fois à la piscine et grâce à qui j'ai beaucoup appris sur le Pérou. Je tiens à mentionner Sheena Patel, qui était en visite à l'Institut Jean-Lamour et qui avait fait le chemin inverse du mien depuis San Diego, merci Sheena pour les bons moments passés ensemble et de t'être occupé de mon chat alors que j'étais en conférence ! Un grand merci à : Filip Scheiler, Ayoub Bourjilat, Sébastien Geiskopf, Kathleen Toussaint et Sarah Xing pour leur encouragements et les moments sympas que nous avons partagé au labo les midis.

Cette thèse qui a duré trois ans a été une réelle aventure mémorable où j'ai rencontré des gens d'une grande intelligence, qui n'ont cessé de m'impressionner, et pourtant qui ont toujours su être disponibles et étaient les premiers à plaisanter. Cette aventure scientifique et humaine restera à jamais graver dans ma mémoire, merci à tous et merci pour votre enthousiasme. Quelle équipe ! Quelle ambiance !

Enfin, et pas des moindres, je voudrais remercier mes parents et ma famille qui ont cru en moi et m'ont encouragé et rassuré dans mes moments de doute et face aux difficultés.

I dedicate this thesis manuscript to

My parents

My sister

Late my grand-father and my family

Contents

Abstract	iii
Acknowledgements	v
General Introduction	1
I State-of-the-art of all-optical switching in ferromagnetic materials	5
1 Introduction: the advent of ultrafast laser-induced magnetization dynamics . . .	6
1.1 Ultrafast spin dynamics in Ni induced by femtosecond laser pulses	6
1.2 Theory of magnetization dynamics	7
1.3 Phenomenological and microscopic model of ultrafast laser-induced spin dynamics	8
2 Ultrafast magnetization switching	10
2.1 Ultrashort current pulses	10
2.2 Ultrashort laser pulses for all-optical switching in ferrimagnets	12
2.3 Femtosecond hot-Electron pulses	18
3 All-optical switching in ferromagnetic materials	19
3.1 Experimental observation of all-optical switching in ferromagnets	19
3.2 A cumulative and multi-shot process	22
3.3 Can a single-pulse switching be achieved in ferromagnets?	24
3.4 Influence of dipolar field and magnetic domain size	27
4 Mechanism and modeling of all-optical switching in ferromagnets	28
4.1 Inverse Faraday effect	28
4.2 Magnetic circular dichroism	31
5 Goals and outline of the thesis	33
II Experimental methods and samples	39
1 Thin film deposition and magnetic properties	39
1.1 DC magnetron sputtering	39
1.2 Magnetic characterization	40
2 Generation of ultrashort laser pulses	43
2.1 Femtosecond laser oscillator	43
2.2 Femtosecond laser amplification	44
2.3 Measurement of temporal and spatial laser profile	46
3 Magneto-optical microscopy technique	48
3.1 Magneto-optical Faraday and Kerr effects	49
3.2 Experimental magneto-optical microscope for all-optical switching	52
III Helicity-dependent all-optical domain wall motion in ferromagnets	57
1 Introduction	57
2 Magnetic interactions and domains	57
2.1 Magnetic interactions and energies	58
2.2 Magnetic domains and domain wall	62

2.3	Domain wall motion	64
3	Domain wall manipulation	66
3.1	Magnetic field-driven DW motion	66
3.2	Electric field-driven DW motion	69
3.3	Current-induced DW motion	69
3.4	Thermal gradient-driven DW motion	71
4	Helicity-dependent all-optical domain wall motion	72
4.1	Outline of the experiment	72
4.2	Observation of domain wall motion induced by circularly-polarized laser pulses	74
4.3	Laser position and fluence dependence of domain wall motion	77
4.4	Effect of the linear polarization and degree of ellipticity on the domain wall	80
5	Mechanism and models of the helicity effect in laser-induced domain wall motion	83
5.1	General mechanism	83
5.2	Inverse-Faraday effect	84
5.3	Magnetic circular dichroism: calculation of the thermal effective field	87
5.4	Measurement of the magnetic circular dichroism	90
5.5	Thermal spin transfer torque via spin-Seebeck effect	94
6	Summary and perspectives	95
IV	Size effects of all-optical switching in patterned ferromagnetic thin films	101
1	Introduction	101
2	Principle of the experiments and sample characterization	101
2.1	Outline of the experiments	102
2.2	Magnetic characterization of the samples	104
3	Sweeping beam experiments on (Co/Pt) microdots	106
3.1	Static imaging of the microdots arrays	106
3.2	Electrical characterization of (Co/Pt) microdots on top of a Hall cross	109
3.3	Summary	112
4	Static beam experiments on (Co/Pt) microdots: influence of the number of laser pulses	112
4.1	Static imaging of the microdots arrays	112
4.2	Electrical characterization of a single (Co/Pt) microdot on top of a Hall cross	114
4.3	Summary and discussion	115
5	Summary and perspectives	116
V	Conclusions and future challenges in all-optical switching	119

General Introduction

In the era of high-density data storage, magnetization manipulation without applying an external magnetic field has become much attractive for potential technological applications in the information industry. Promising candidates are spintronic devices for their low-power consumption, which rely for instance on spin-transfer torque (STT) or spin-orbit torque (SOT). However, the reversal time of the magnetization using ultrashort current pulses via STT or SOT is on the order of sub-nanoseconds. Another example of magnetization switching with no applied magnetic field is based on ultrashort laser pulses typically of femto- or pico-second duration. Indeed, in 2007, it was discovered that the magnetization of a ferrimagnetic GdFeCo alloy could be deterministically reversed upon excitation of fs circularly-polarized laser pulses. This phenomenon was called all-optical switching (AOS). Several studies have shown that the magnetization reversal in GdFeCo takes place on a picosecond timescale. As it could lead to ultrafast data storage by dramatically increasing the writing speed, all-optical switching has become a research topic of great interest. The first results on GdFeCo revealed that all-optical switching was helicity-dependent. Yet, later, it was demonstrated that a single linearly-polarized laser pulse could also induce magnetization reversal in the same material. This helicity-independent magnetization switching was explained by a purely thermal mechanism and the distinct dynamics of the Gd and FeCo sublattices upon laser irradiation. More recently, hot electrons generated by femtosecond laser pulses and picosecond electrical pulses were used to induce magnetization reversal in GdFeCo. These latest experimental results pave a new path for ultrafast magnetization manipulation.

In fact, the underlying physics of all-optical switching is not completely understood yet, and is still under debate. Various mechanisms were suggested to explain all-optical switching. Thermal mechanisms rely on heating effects close or over the Curie temperature, but also magnetic circular dichroism. However, the discovery of ultrafast switching with a single linearly polarized laser pulse in a transparent ferrimagnetic dielectrics rather supports the evidence of a non-thermal mechanism.

Furthermore, in 2014, it was found that ferromagnetic materials could also exhibit helicity-dependent all-optical switching, which questioned the singularity of the mechanism proposed for ferrimagnets. The recent results on ultrafast laser-induced magnetization switching gave evidence that two classes of materials should be clearly distinguished. First, GdFeCo alloys for which toggle switching is observed. Second, for ferromagnetic systems such as Co/Pt multilayers or FePt, and ferrimagnetic Co/Tb multilayers or alloys, it was proved that all-optical switching is a cumulative helicity-dependent process and requires multiple laser pulses. Moreover, there are growing evidence that in ferromagnetic Co/Pt thin films the size of magnetic domains and the mobility of domain walls play an important role. In this thesis, the mechanism of the laser-induced magnetization switching in Co/Pt multilayers was investigated in light of these latest results. We aimed to resolve the possibility of a switching process via laser-induced magnetic domain wall propagation. We also explored the influence of the dipolar field by studying the size effects of AOS in patterned Co/Pt films. This allowed us to examine the feasibility of using AOS for technological applications when scaling down the material dimensions.

This thesis manuscript is divided into four chapters. First, a state-of-the-art of all-optical switching with an emphasis on the results in ferromagnetic materials will be presented. In the second chapter, the experimental methods used to fabricate and characterize the studied samples and to carry out the all-optical switching experiments are detailed. In the third chapter, we investigate and demonstrate helicity-dependent all-optical domain wall motion in Co/Pt thin films and how it can explain the helicity-dependent magnetization recovery process in all-optical switching. It is proved that a purely thermal mechanism may be excluded. Finally in the fourth chapter, the size effects of AOS in (Co/Pt) microdots are studied. We give evidence that all-optical switching is less energy-efficient in micro-patterned (Co/Pt) films. It is suggested that the dipolar field eases the laser-induced magnetization reversal in the continuous film.

Introduction Générale

A l'ère du stockage à haute densité des données informatiques, la manipulation de l'aimantation sans appliquer de champ magnétique externe a attiré beaucoup d'attention pour de potentielles applications technologiques dans l'industrie de l'information. Parmi les candidats prometteurs pour ces technologies, on compte les dispositifs spintroniques du fait de leur faible consommation énergétique, et qui utilisent le "spin-transfer torque" (STT) ou bien le "spin-orbit torque" (SOT). Cependant, le temps de renversement de l'aimantation en utilisant des impulsions de courant via STT ou SOT est de l'ordre de la dixième de nanosecondes. Et un autre exemple de renversement de l'aimantation sans avoir recours à de champ magnétique externe est basé sur des impulsions lasers ultracourtes, typiquement, avec une durée de l'ordre de la femto- ou pico-seconde. En effet, en 2007, il a été découvert que l'aimantation d'un alliage ferrimagnétique de GdFeCo pouvait être renversé de manière déterministe à l'aide d'impulsions laser fs polarisées circulairement. Ce phénomène est ce que l'on appelle le "retournement tout-optique". Plusieurs études réalisées sur les alliages de GdFeCo ont démontré que le renversement de l'aimantation se faisait à l'échelle de la picoseconde. Étant donné que cela pourrait amener à un stockage de l'information ultra-rapide en augmentant drastiquement la vitesse d'écriture des données, le retournement tout-optique a présenté un très un grand intérêt comme la communauté scientifique. Les premiers résultats sur les couches minces de GdFeCo ont révélé que le retournement dépendait de l'hélicité. Pour autant, plus tard, il a été prouvé qu'une simple impulsion laser fs polarisée linéairement pouvait suffire pour renverser l'aimantation dans le même type de matériau mais pour une composition d'alliage différente. Ce retournement indépendant de l'hélicité a été expliqué par un mécanisme purement thermique et résultant de la différence de la dynamique d'aimantation des deux sous-réseaux, à savoir les réseaux de Gd et de FeCo, après excitation laser.

Néanmoins, la physique à l'origine de ce retournement tout-optique n'est pour l'heure pas complètement comprise et fait toujours débat. Plusieurs mécanismes ont été proposés dans la littérature pour expliquer ce renversement ultra-rapide. Les mécanismes dits thermiques reposent sur des effets de chauffage proche ou au-dessus de la température de Curie mais également sur le dichroïsme circulaire magnétique. D'autre part, la découverte du renversement ultra-rapide avec une impulsion laser polarisée linéairement dans un diélectrique ferrimagnétique transparent tend à pointer vers un mécanisme athermique.

De plus, en 2014, il a été démontré que dans les matériaux ferromagnétiques pouvaient également être observé le retournement tout-optique de l'aimantation dépendant de l'hélicité, ce qui a de fait remis en question la singularité des mécanismes de renversement proposés jusqu'à présent dans les ferri-aimants. Les résultats récents dans la manipulation ultra-rapide de l'aimantation à l'aide d'impulsions lasers ont mis en évidence que deux classes de matériaux devaient être considérées. Tout d'abord, les alliages de GdFeCo pour lesquelles le renversement en une seule impulsion peut être obtenu. Et par ailleurs, les systèmes ferromagnétiques tels que les multicouches de Co/Pt ou les films granulaires de FePt, ainsi que les multicouches ou alliages ferrimagnétiques de CoTb montrent quant à eux un renversement tout-optique dépendant de l'hélicité et qui est cumulatif, c'est-à-dire qui nécessite un certain nombre

d'impulsions laser. Mais encore, des études ont mis en avant l'importance de la taille des domaines magnétiques et la mobilité des parois de domaines dans les systèmes de multicouches Co/Pt afin d'observer ce renversement tout-optique cumulatif et dépendant de l'hélicité. Dans cette thèse, nous avons exploré le mécanisme de renversement de l'aimantation induit par impulsions laser dans les multicouches de Co/Pt à la lumière de ces résultats récents. Notre but était d'élucider le rôle des parois de domaines dans le mécanisme de renversement tout-optique de l'aimantation et de résoudre la possibilité d'un retournement par propagation de parois. Nous avons également étudié l'influence du champ dipolaire en examinant les effets de taille du retournement tout-optique dans des couches de Co/Pt structurées en micro-motifs. Ceci nous a permis par ailleurs de vérifier de la faisabilité de l'intégration du retournement tout-optique dans des dispositifs de stockage de l'information lorsque la taille des matériaux est réduite pour parvenir à un stockage à très haute densité.

Ce manuscrit de thèse est divisé en quatre chapitres. En premier un état de l'art du retournement tout-optique est présenté avec une attention toute particulière aux systèmes ferromagnétiques. Dans le deuxième chapitre, nous détaillons les méthodes expérimentales mises en place pour la fabrication et la caractérisation des échantillons étudiés ainsi que pour réaliser les expériences de retournement tout-optique par laser à impulsions ultra-courtes. Dans un troisième chapitre, nous étudions et démontrons la propagation de parois de domaines tout-optique et dépendant de l'hélicité dans les couches minces de Co/Pt et comment cela peut expliquer le renversement tout-optique et dépendant de l'hélicité observé dans ces systèmes. Nous fournissons des preuves expérimentales indiquant qu'un mécanisme purement thermique est très peu probable. Enfin dans un dernier chapitre, l'étude des effets de taille dans les couches de Co/Pt micro-structurées révèle que le renversement est énergétiquement moins favorable dans les micro-motifs en comparaison au film continu. Ce résultat suggère que le champ dipolaire facilite le renversement induit par laser dans les couches minces continues.

Chapter I

State-of-the-art of all-optical switching in ferromagnetic materials

At the age of Big Data and the Internet, not only more data are produced (e.g. new scientific discoveries, the internet) but also organisations and companies collect more and more data. This has set the need for high-density data storage capacities. However, for this purpose it is known that the superparamagnetic limit must be overcome. This limitation is also referred to as the magnetic recording trilemma, that means by decreasing the grain and bit size, a higher magneto-crystalline is needed in order to satisfy the thermal stability requirement. Though the material coercivity is substantially increased, and as a result the head field fails to write the magnetic bit. Heat-assisted magnetic recording [1, 2] and bit-patterned media [3, 4] were developed in that sense to solve this issue. Another way is to manipulate the magnetization without applying a magnetic field, which has continually attracted researchers' attention over the past two decades. Indeed, it could have a major impact on technological applications, such as low-power electronics, memory and data storage devices. Emerging mechanisms include the control of the magnetic properties of materials through electric fields [5], and also magnetization switching via spin-transfer torque [6, 7], and spin-orbit torque [8]. Yet, the discovery of magnetization reversal using ultrashort laser pulses with no external magnetic field has been a real paradigm shift in magnetization manipulation. It was first discovered in 2007 by Stanciu *et al.* in GdFeCo alloys, for which the magnetization was fully and deterministically switched in 10 ps [9]. This phenomenon called "all-optical switching" (AOS) gained much interest as it opened a new path for ultrafast magnetic recording. In the pioneering work of Lambert *et al.* it was demonstrated that AOS was not specific to GdFeCo alloys and ferrimagnets but could also be observed in ferromagnetic materials [10]. Later El Hadri *et al.* gave evidence that materials exhibiting all-optical switching should be classified in two distinct categories with different mechanisms [11]. Nevertheless, there is no clear understanding of the underlying physics involved in AOS. Therefore, in this chapter I we aim at giving a global overview of the recent experimental results and theories in all-optical switching with an emphasis on ferromagnetic materials, for in this thesis we will try to explain the reversal mechanism in this class of materials. In section 1, we report the historical results of ultrafast laser-induced demagnetization in Ni along with theoretical considerations to understand magnetization dynamics. In section 2, we present novel stimuli used to induce ultrafast magnetization switching, and the discovery of all-optical switching in GdFeCo and other ferrimagnetic materials. Section 3 is dedicated to the observation of helicity-dependent all-optical switching in ferromagnets and how it differs from AOS seen in GdFeCo. Finally, in section 4 we discuss potential mechanisms and modeling to explain all-optical switching in ferromagnetic materials.

1 Introduction: the advent of ultrafast laser-induced magnetization dynamics

1.1 Ultrafast spin dynamics in Ni induced by femtosecond laser pulses

In order to study electronic relaxation processes that take place over an ultrashort timescale and govern for instance transport properties in metallic materials, ultrafast optical spectroscopy is the best-suited technique. However, magnetic metals were not studied until late 1980s when researchers started to investigate the response of the spin system upon ultrashort laser excitation. Time-resolved magneto-optical measurements were used to quantify the laser-induced change in magnetization. The widely-used pump-probe method consists in sending a laser beam to excite the material, the pump, and a second delayed laser pulse, the probe, to detect the magneto-optical signal. By varying the pump-probe delay time, the entire ultrafast magnetization dynamics is reconstructed. The first attempts were carried in Ni [12] and Fe [13], yet unsuccessful as they showed no demagnetization until the melting point of the material was reached. Indeed, the laser pulse duration, in the range of tens of ps to ns, did not allow a proper temporal resolution, for at this timescale the system is already at equilibrium [14]. Though, Beaurepaire *et al.* were the first to report ultrafast demagnetization in Ni films triggered by a 60 fs laser pulse [15]. It was found that the magnetic order was almost completely lost within 1 ps followed by a relaxation and a magnetization recovery after 15 ps (see Fig. I.1). By measuring the differential transmittance, they were able to deduce the electron and spin temperature, and the latter suggested a demagnetization time $\tau_M \sim 500$ fs. The thermalization of the system was described and explained with a phenomenological model, the three temperature model that we will discuss in section 1.3. A similar magnetic response was observed in various ferromagnetic transition metals such as Fe [16], NiFe [17] and CoPt_{x3} [18, 19], with a demagnetization time of approximately 300 - 500 fs [20]. Thus, the results of Beaurepaire *et al.* were generalized and opened the way for the much attractive and interesting ultrafast laser-induced magnetization manipulation. It even led to the discovery of THz emission triggered by ultrashort laser pulses which later became a new field of research in ultrafast magnetism [21, 22].

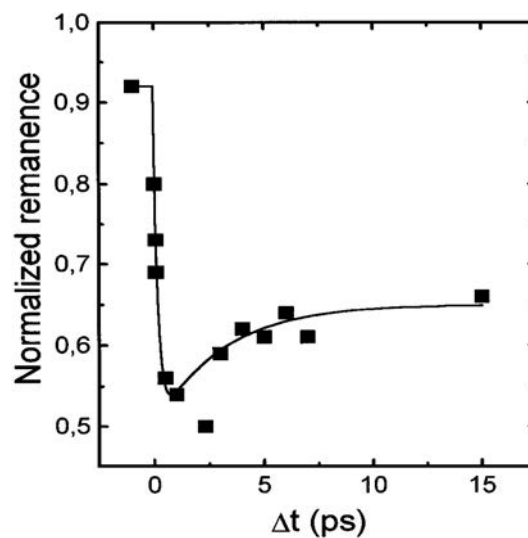


FIGURE I.1: Normalized transient remanent longitudinal magneto-optical Kerr effect signal of a Ni(20 nm)/MgF₂(100 nm) film for 7 mJ cm⁻² pump fluence. Figure extracted from [15].

1.2 Theory of magnetization dynamics

Landau-Lifshitz-Gilbert equation

To understand the spin dynamics in the above-mentioned ultrafast laser-induced magnetization experiments, first we present the theory of magnetization dynamics. Under the macrospin approximation, it is assumed that in a ferromagnetic material the magnetization is uniform in the solid, and that it can be represented by a single "macrospin". As a result, the magnetic moment of the material m is defined as $m = VM$, where V is the total volume and M is the material magnetization. Using this assumption, the motion of the magnetic moment under the action of an effective field H_{eff} is described by the Landau-Lifshitz-Gilbert equation 1.1 [23, 24] (LLG):

$$\frac{\partial \vec{m}}{\partial t} = \gamma \mu_0 \vec{m} \times \vec{H}_{\text{eff}} + \frac{\alpha}{|\vec{m}|} \vec{m} \times \frac{\partial \vec{m}}{\partial t} \quad (1.1)$$

where γ is the gyromagnetic ratio, μ_0 the vacuum permeability and α the Gilbert damping constant. The first term corresponds to the precession of the magnetic moment around the effective magnetic field H_{eff} that is defined as the sum of the applied external magnetic field, the demagnetizing field, the anisotropy field and all other interactions. Second is the damping term, which characterizes the motion of the precessing magnetic moment towards equilibrium, i.e. this is a dissipative term that allows the magnetic moment to be eventually aligned with the effective field. To reverse the magnetization, the damping characteristic time in the antiparallel configuration is on the order of nanoseconds, a faster damping (100 ps) is obtained when an orthogonal field is applied [14] (and ref. therein). However, the LLG equation cannot be used to describe the magnetization dynamics in the case of laser excitation as it does not take into account thermal effects. A way to consider thermal fluctuations is to use the Langevin dynamics based on an approach developed by Brown [25]. In the LLG equation, for each atom i , a stochastic term H_{therm}^i is added to the effective field [26]:

$$H_{\text{therm}}^i = \Gamma(t) \sqrt{\frac{2\alpha k_B T}{\gamma m_S \Delta t}} \quad (1.2)$$

where $\Gamma(t)$ is a Gaussian distribution with the white-noise characteristics, k_B the Boltzmann constant, T the system temperature, m_S the atomic magnetic moment and Δt the integration time for each atom i . Even though, thermal fluctuations at the spin level can be this way introduced in the equation, the LLG-Langevin model is not suitable for high temperatures that induces the laser excitation (see section 1.3), since it does not include the high-frequency spin waves, which results in an overestimation of the Curie temperature (T_C) [27, 28]. Furthermore, as the temperature gets closer to T_C , the longitudinal amplitude of the moment is decreased, which the LLG equation ignores by considering the magnetization of fixed length. Therefore, this model is not satisfactory for ultrafast laser-induced magnetization dynamics.

Landau-Lifshitz-Bloch equation

A more accurate approach to solve this issue is based on the Landau-Lifshitz-Bloch equation which combines the Landau-Lifshitz equation at low temperatures and the Bloch equation at high temperatures. In the case of the atomistic spin dynamics, a magnetic atom i is described by a spin vector \vec{s}_i that verifies the Landau-Lifshitz equation with the stochastic field introduced

in the previous section. The resolution of this equation relies on the fact that the heat bath (phonons and electrons) responds faster than the spin system. As a result the average spin-polarization of the material $\vec{m} = \langle \vec{s}_i \rangle$ is defined as (Eq. 1.3):

$$\frac{d\vec{m}}{dt} = \gamma[\vec{m} \times \vec{H}_{eff}] - \gamma\lambda_{\parallel} \frac{(\vec{m} \cdot \vec{H}_{eff})\vec{m}}{m^2} + \gamma\lambda_{\perp} \frac{[\vec{m} \times [\vec{m} \times \vec{H}_{eff}]]}{m^2} \quad (1.3)$$

where λ_{\parallel} and λ_{\perp} corresponds, respectively, to the longitudinal and transverse damping parameters:

$$\begin{aligned} \lambda_{\parallel} &= \lambda \frac{2T}{3T_C} \\ \lambda_{\perp} &= \lambda \left(1 - \frac{T}{3T_C}\right) \end{aligned} \quad (1.4)$$

with T_C the mean-field Curie temperature. Consequently, it is clear that the LLB equation (Eq. 1.3) takes into account the change of amplitude of the magnetic moment as a function of temperature. Also, the LLB equation offers a better alternative than the atomistic spin dynamics with a faster computational time for macroscopic systems. Finally, the micromagnetic simulations based on the LLB equation successfully reproduced the laser-induced magnetization dynamics and are in good agreement with the experimental results [28].

1.3 Phenomenological and microscopic model of ultrafast laser-induced spin dynamics

Phenomenological three-temperature model

Yet, it remains a challenge to fully understand such a fast change of the magnetization (~ 1 ps) as reported by Beaurepaire *et al.* [15]. The authors proposed a phenomenological model, called "three-temperature model", that presents a thermodynamic description of the exchange of energy in the system and the evolution of the temperature. They assume that the system can be divided into three thermalized reservoirs, namely the electron, the lattice and the spin baths. As depicted in Fig. 1.2, these three baths are coupled through interactions of different nature, i.e. electron-phonon, electron-spin and spin-phonon interactions. Moreover, each bath has its own temperature. It is important to note that it is supposed that equilibrium is reached in each sub-system. The latter point can be questioned if considering the short timescale of the demagnetization. Still, the three-temperature model allows to determine the temporal evolution of the system through three coupled differential equations (Eq. 1.5):

$$\begin{aligned} C_e \frac{dT_e}{dt} &= -G_{el}(T_e - T_l) - G_{es}(T_e - T_s) + P(t) \\ C_s \frac{dT_s}{dt} &= -G_{es}(T_s - T_e) - G_{sl}(T_s - T_l) \\ C_l \frac{dT_l}{dt} &= -G_{el}(T_l - T_e) - G_{sl}(T_l - T_s) \end{aligned} \quad (1.5)$$

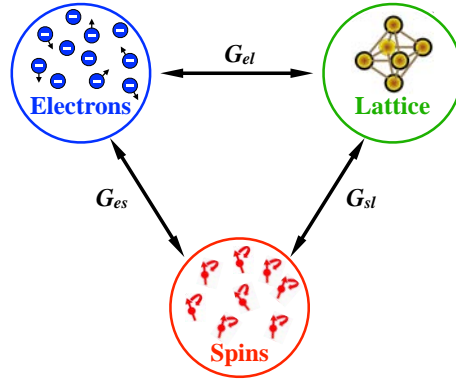


FIGURE I.2: Schematic representation of the three-temperature model and the reservoirs (electrons, spins and lattice) that interact between each other. These interactions of different nature (electron-lattice, electron-spin, spin-lattice) are characterized by a coupling constant G . Figure adapted from [14].

where G_{el} , G_{es} and G_{sl} are the electron - lattice, electron - spin and spin - lattice coupling constants. These parameters are phenomenologically obtained. C_i and T_i are the specific heat capacity and effective temperature of the corresponding i bath. $P(t)$ designates the laser source term, it applies only to the electronic reservoirs as at optical frequencies only the electrons are able to respond. Therefore, it is assumed that the laser-induced heating occurs only in the electron bath.

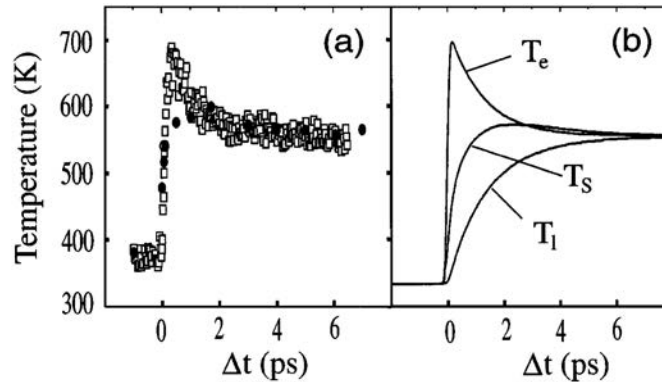


FIGURE I.3: (a) Experimental spin temperature T_s (dots) and electron temperature T_e (squares) deduced from time-resolved magneto-optical Kerr effect measurements, (b) temporal evolution of electron, spin and lattice temperatures calculated from Eq. 1.5. Figure extracted from [15]

The results of the numerical simulations are consistent with the experimental data as shown in Fig. I.3 [15]. Following the optical stimulus, the laser energy is almost instantaneously absorbed by the electronic reservoir which induces a high peak and rapid increase of the electron temperature T_e within the first 500 fs due to electron-electron interactions [29]. Then, after 1 ps it experiences a decay and transfers its energy into the lattice by electron-phonon interactions, which results in the rise of the lattice temperature T_l . The fast thermalization of the electrons leads to a much slower increase of the spin temperature T_s that reaches its maximum around 2 ps. The temporal evolution of T_s is assumed to represent the spin dynamics observed in the ultrafast laser-induced demagnetization. The relaxation of the electrons is faster than for the spins as G_{el} is greater than G_{sl} . As a consequence, the spin bath remains hot and the spin temperature becomes higher than the electron temperature after ~ 2 ps. Finally, T_s decreases which

corresponds to the remagnetization seen in Fig. I.1. Although such a simple phenomenological model successfully reproduced experimental electron and spin dynamics following laser excitation, several limitations can be pointed out. First of all, the distinction between the electronic and spin system with two different effective temperature is not straightforward, as they are both intrinsic characteristics of the same object, the electrons. Secondly, the three-temperature model completely ignores conservation of angular momentum which is at the origin of magnetization dynamics.

Conservation and transfer of angular momentum

Indeed, during demagnetization, transfer of angular momentum from the electrons to the spins or the lattice must be considered. In a ferromagnet, an excited electron can flip its spin via different mechanisms: (i) a Stoner excitation, (ii) scattering of an inelastic electron-spin wave and (iii) the Elliot-Yafet mechanism that is a single-particle-like spin-flip scattering with phonons or impurities. The predominance of one of these three mechanisms will depend on the energy of the excitation. Koopmans *et al.* investigated the dissipation of angular momentum into the lattice upon laser irradiation [30, 31]. For this purpose, they developed a microscopic model based on the Elliot-Yafet type of scattering, which defines a probability a_{sf} that the electron spin is flipped upon emission or absorption of a phonon [30]. In fact, XMCD measurements made on Ni thin films suggested that the only possible way for the angular momentum to be dissipated is into the lattice, which is, therefore, consistent with an Elliot-Yafet spin-flip model [32]. This probability a_{sf} is implemented in a simplified Hamiltonian (see methods in [31]) and in the three-temperature model discussed just above. The authors successfully calculated the demagnetization time [30] and also reproduced laser-induced spin dynamics for various ferromagnetic metals [31]. A major feature of these theoretical results is that the conservation of angular momentum was explicitly taken into account. Nevertheless, we will see later that the possibility to fully switch the magnetization with ultrashort laser pulses will raise new questions.

2 Ultrafast magnetization switching

2.1 Ultrashort current pulses

As we already mentioned the search for high-speed memory and data storage devices with low energy consumption has attracted a lot of attention over the past decade. To induce ultrafast magnetization switching, researchers have investigated the use of ultrashort laser pulses (that we will discuss in section 2.2) but also current pulses. The latter is considered as a promising technique as it allows a more scalable approach with the possibility of switching nano-sized-magnetic bits. As illustrated in Fig. I.4, there are two geometries where either an out-of-plane or in-plane current is injected into the magnetic layers.

The first one is based on spin-transfer torque (STT) [35, 36] and is used to induce magnetization reversal in magnetic tunnel junctions (MTJs) [see Fig. I.4(b)]. MTJs consist of two ferromagnetic layers separated by an insulator: a free layer, i.e. with a switchable magnetization, and a fixed layer for which the magnetization is pinned. The injected out-of-plane current is spin-polarized by the fixed layer. Then, the transfer of the spin angular momentum to the free layer creates a spin torque acting on the free layer magnetization, and that can reverse it. This type of device is referred as spin-transfer torque magnetic random access memory (STT-MRAM) [37]. Several research groups have reported ultrafast magnetization switching by spin transfer torque with

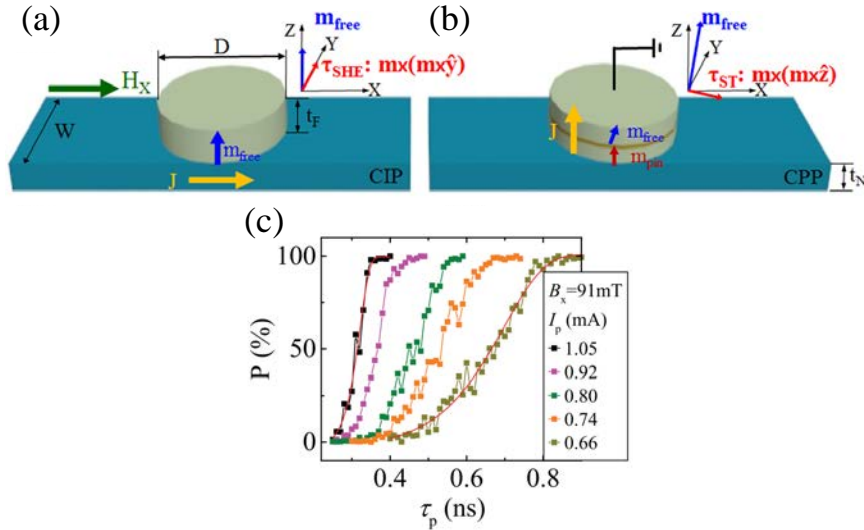


FIGURE I.4: Schematic diagrams of the two geometries used for MRAMs with (a) an in-plane and (b) out-of-plane current [33]. (c) Switching probability of a SOT-MRAM as a function of current pulse duration and current amplitude [34]

current pulses as short as 50 ps, 100 ps or 500 ps [38–40]. However, a downfall of STT-MRAMs is that at rest there is no STT, which results in an incubation delay upon injection of the current pulses. This incubation delay limits the ultrafast reversal and is responsible for a broad distribution of the switching time [41, 42]. Nevertheless, it was found that going from a collinearly magnetized configuration of the fixed and free layer to an orthogonal spin transfer with a perpendicular polarizer allowed the suppression of the incubation delay [40]. Typical energy to induce ultrafast magnetization switching via STT is in the sub-pJ range [40, 42], which satisfies the requirement of lower-power electronic devices. Moreover, a faster switching was achieved when decreasing the temperature [38].

In the second geometry as shown in Fig. I.4(a), an in-plane current is injected in a ferromagnet/heavy metal stack (FM/HM), and the magnetization is reversed via spin-orbit torque (SOT). The spin-orbit coupling results either from a bulk spin Hall effect in the metal layer, typically Pt or Ta, or Rashba interaction at the interface FM/HM [43–45]. From this coupling, a torque is created and is exerted on the magnetization of the FM. Yet, a bias external in-plane magnetic field is needed to achieve deterministic switching. Garello *et al.* reported ultrafast magnetization switching via SOT using current pulses as low as 180 ps in Pt/Co/ AlO_x [34] [see Fig. I.4(c)]. Furthermore, the threshold current to induce reliable switching allows to compare a SOT- or STT-based mechanism. It turns out that STT is more efficient for materials with a large spin polarization and a low damping constant, whereas SOT is more favorable in the case of a large spin Hall angle [34]. Although interesting features of SOT- or STT-MRAMs include scalability and low-energy consumption, especially for MTJs with perpendicular magnetic anisotropy, few limitations can be discussed. First, high current densities are required to achieve magnetization switching in the order of 10^{10} - 10^{12} A m⁻², which can create durability issues and limit the number of writing cycles. Second, the switching speed is only *relatively* "ultrafast". For comparison, recently Yang *et al.* demonstrated magnetization reversal in ~ 10 ps in a GdFeCo thin film using a single sub-10-ps current pulse simply relying on a heating effect [46]. Finally, in most cases an external magnetic field is needed which may hinder the implementation of small-scale devices. In contrast, deterministic magnetization switching with fs laser pulses without applying an external field has been demonstrated, and may be an alternative for ultrafast magnetic recording.

2.2 Ultrashort laser pulses for all-optical switching in ferrimagnets

The surprising results of ultrafast laser-induced demagnetization in Ni by Beaurepaire *et al.* triggered much interest in the field of ultrafast magneto-optics. Yet, the potential technological application was just conceptual since a complete reversal of the magnetization, i.e. the ability to write magnetic bits, was not achieved. Nevertheless, the discovery of full magnetization reversal induced by femtosecond laser pulses in a GdFeCo alloy opened a new path for ultrafast magnetization recording [9]. This phenomenon was called "all-optical switching" (AOS). In this section, we will present the first experimental results and the different types of AOS in GdFeCo. Then, we will discuss the mechanisms that were proposed to explain AOS in GdFeCo thin films. Lastly, AOS was demonstrated to be a more general mechanism and that could be achieved in various ferrimagnetic materials.

All-optical switching in GdFeCo alloy films

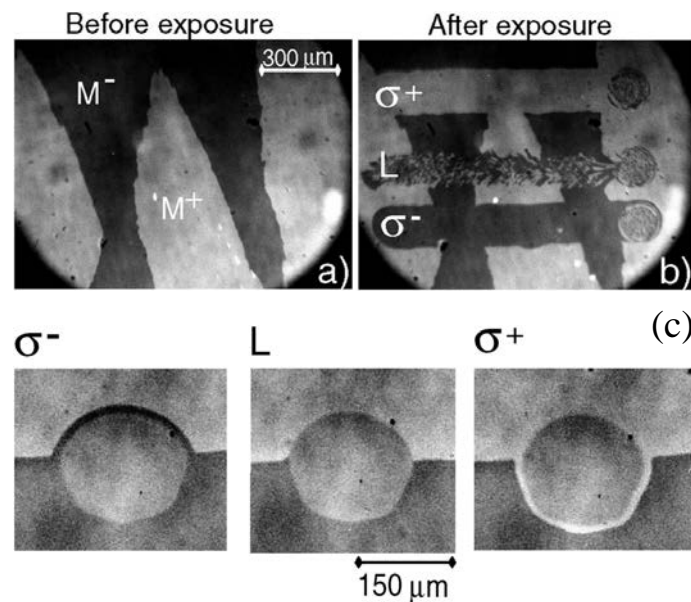


FIGURE I.5: (a) Initially the sample shows magnetic domains of opposite direction (M^+ bright contrast, M^- dark contrast). (b) Slowly sweeping the laser beam at $\sim 30 \mu\text{m s}^{-1}$ with linearly-polarized (L) pulses leaves a demagnetized area, while right- and left- circular polarizations reverse the magnetization down (M^-) and up (M^+) respectively. (c) A linearly- and circularly-polarized laser beam is focused onto a domain wall boundary and kept static. Independently of the laser polarization, the central part of the beam shows random distribution of up- and down- magnetic domains due to excessive heating. For circular polarization, magnetization switching takes place in the perimeter of the excited area where the temperature is just below the Curie temperature. Figure adapted from [9].

In 2007, Stanciu *et al.* demonstrated for the first time deterministic switching with circularly-polarized fs laser pulses in a 20 nm-thick $\text{Gd}_{22}\text{Fe}_{74.6}\text{Co}_{3.4}$ [9]. This amorphous ferrimagnetic alloy exhibits a strong perpendicular magnetic anisotropy, which makes it an ideal candidate for magnetic recording. The principle of the experiment consists in exciting the material with 40-fs laser pulses of a wavelength of 800 nm and a repetition rate of 1 kHz. As depicted in Fig. I.5, the sample initially shows magnetic domains of "up" (M^+) and "down" (M^-) direction, then the laser beam is swept over the sample surface at normal incidence with different light polarizations (linear L, right-circular σ^+ and left-circular polarization σ^-). It is found that σ^+ -polarized

pulses (resp. σ^-) reverses the M^- domain (resp. M^+ domain), and it leaves the M^+ domain (resp. M^-) unchanged as seen in Fig. I.5(b). In contrast, linearly-polarized light creates only a demagnetized area. It is clear that the reversal is deterministic and depends on light helicity. This type of behavior is referred to as helicity-dependent all-optical switching (HD-AOS). Moreover, it is proved that magnetization reversal happens only in the outer part of the Gaussian profile of the laser beam as seen in Fig. I.5(c). Indeed, a "switching rim" of opposite magnetization contrast can be observed for left- and right-circular polarizations. In the case of linear polarization, no rim is seen. On the opposite, in the central part of the laser beam, independently of the light polarization, there is an intermediate gray contrast which indicates a demagnetized area. Indeed, this is due to laser heating well above the Curie temperature. However, it is important to note that in this experiment, this is a multipulse laser-induced magnetization switching as the laser beam is slowly swept over the sample surface. To clearly exhibit the helicity dependency, the sweeping speed was increased in such a way a single circularly-polarized laser pulse hit the sample, which was proved to be sufficient to deterministically reverse the magnetization (see Fig. 4.a in [9]). Single 100-fs-laser pulse helicity-dependent switching was unambiguously demonstrated in another GdFeCo alloy [47].

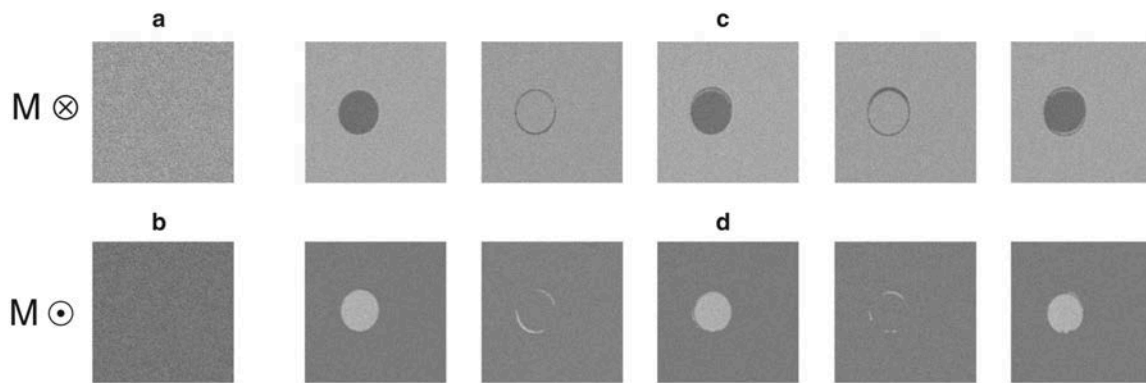


FIGURE I.6: Magneto-optical images of a $\text{Gd}_{24}\text{Fe}_{66.5}\text{Co}_{9.5}$ continuous film obtained after the action of a sequence of N 100 fs laser pulses. (a) and (b) initial magnetic state of the sample with saturation magnetization up and down, respectively. (c) and (d) the film being excited by N laser pulses ($N=1,2,\dots$). Each pulse completely switches the magnetization, independently of the initial saturation direction and light polarization. Figure extracted from [48].

In 2011, Radu *et al.* reported a fascinating result in $\text{Gd}_{25}\text{Fe}_{65.9}\text{Co}_{9.4}$ alloy [49]. It was revealed that magnetization switching could be achieved with a single 60-fs linearly-polarized laser pulse. This intriguing discovery raised many fundamental questions regarding the mechanism, as linearly polarized light carries no angular momentum but brings only heat. Yet, magnetization reversal within 12 ps was observed [49]. It was evidenced by using X-ray magnetic circular dichroism (XMCD) measurements, which allowed them to probe the magnetization dynamics of the two sublattices Gd and FeCo composing the alloy film. This phenomenon can be called helicity-independent all-optical switching (HI-AOS). Later, many other research groups reported similar results of HI-AOS with fs laser pulses in GdFeCo alloys of various compositions [48, 50–52]. In Fig. I.6, a GdFeCo film is irradiated with a sequence of 5 consecutive 100-fs laser pulses [48]. Independently of the initial saturation direction and the light polarization, the first laser pulse switches the magnetization, while the second incoming pulse reverses it back and so forth [Figs. I.6(c) & I.6(d)]. This is a clear signature of HI-AOS, which is also referred to as toggle switching. Notably, a complete magnetization reversal over a uniform area is achieved, i.e. there is no demagnetization in the center part of the beam below a certain power threshold.

Thermal mechanisms of all-optical switching in GdFeCo alloy films

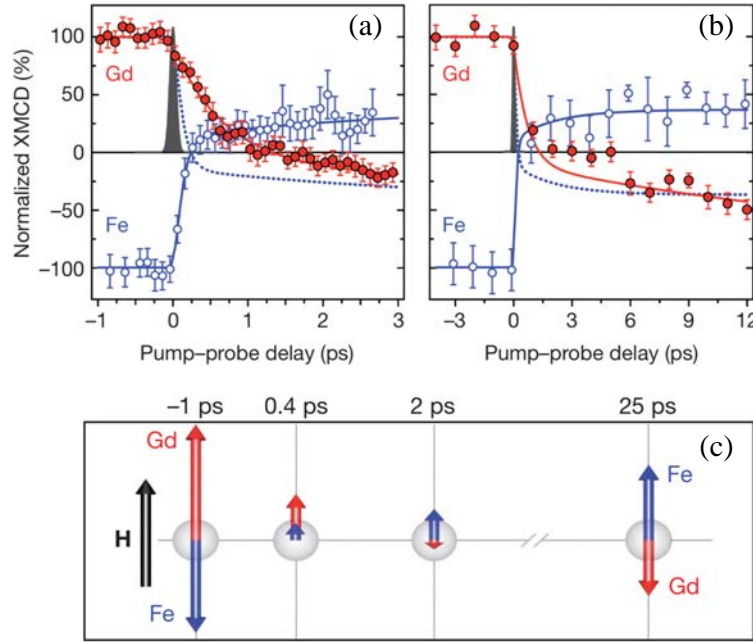


FIGURE I.7: Element-resolved dynamics of the Fe and Gd magnetic moments measured by time-resolved XMCD upon irradiation of linearly-polarized 100-fs laser pulse, (a) within the first 3 ps, which shows the transient ferromagnetic-like state, and (b) on a 12 ps timescale to exhibit reversal of the net magnetization. (c) Illustration of the temporal evolution of the amplitude and direction of the Fe and Gd magnetic moments. Figures extracted from [49].

The intriguing results of HI-AOS were an unequivocal indication that ultrafast laser-induced magnetization in GdFeCo alloy films occurs via a pure thermal mechanism. The latter was suggested by the XMCD measurements performed by Radu *et al.* [49]. GdFeCo alloy is a ferromagnetic material composed of two sublattices, Gd and FeCo, that are antiferromagnetically coupled. The net magnetization results from the non-equivalent sublattices' magnetization. Depending on the concentration and temperature, it is along either sublattice moment. The advantage of XMCD is that it is an element-specific detection technique, which, therefore, allows to independently probe the response of each sublattice upon laser excitation. Due to its small percentage, the Co moment was ignored and the photon energy of X-rays was tuned to the Fe L_3 and Gd M_5 absorption edges. The dynamics of the Fe and Gd magnetic moments following the irradiation of a single linearly-polarized 100-fs- laser pulse is shown in Fig. I.7 [49]. It was discovered that the two sublattices had distinct dynamics. Indeed, the Fe moment is quenched in 300 fs, while the demagnetization of Gd is much slower and takes 1.5 ps as seen in Fig. I.7(a). Thereafter, their respective magnetic moment is rebuilt in the opposite direction after ~ 12 ps [Fig. I.7(b)]. As a consequence of the difference in reversal time, a transient ferromagnetic-like state appears during which the Fe moment is temporarily aligned with the Gd moment as illustrated in Fig. I.7(c). This result was surprising considering the strong antiferromagnetic coupling between the sublattices. To have a better understanding of the underlying physics, the authors carried theoretical simulations based on the atomistic spin model using the LLG equation and Langevin dynamics (that we discussed in section 1.2) [49, 53]. They were able to numerically reproduce the distinct spin dynamics of the two sublattices. Besides, it was found that immediately after the laser excitation, as the temperature is well above T_C , the sublattices behave independently and transfer their angular momentum into the lattice. At longer

timescales, the system temperature decreases and becomes lower than T_C , therefore the thermal effects are negligible against the exchange interaction between Fe and Gd [49, 51]. Thus, heating is the driving mechanism of the ultrafast toggle switching observed in GdFeCo alloys, which is a direct consequence of a transient ferromagnetic state.

However, as we mentioned it is possible to observe HD-AOS in GdFeCo alloys. A different mechanism was proposed by Khorsand *et al.* [54]. It was first demonstrated that helicity-dependent magnetization switching occurs only in a very narrow fluence window (see Fig.1 in [54]). To investigate the microscopic origin of HD-AOS in GdFeCo, they studied magnetic circular dichroism (MCD). They measured refractive indices by ellipsometry, which allowed them to calculate the absorption coefficient as a function of light polarization and wavelength. The spectral dependence of MCD in GdFeCo is depicted in Fig. I.8. It was proved that MCD varies less with respect to the wavelength, but most strikingly the switching window Δ to observe HD-AOS presented a similar behavior unlike for the effective magnetic field arising from the Inverse-Faraday (that we will discuss in section 4.1). Thence it was concluded that all-optical switching depends only on the absorbed photon energy by the material, which confirms the role of the increase in the system temperature above T_C . Consequently, it seems that helicity-independent and helicity-dependent all-optical switching, both, rely on a pure thermal mechanism.

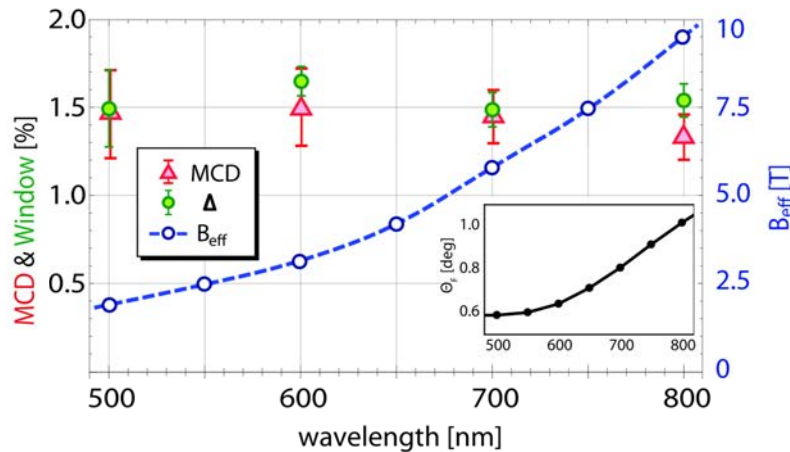


FIGURE I.8: Spectral dependence of the MCD, switching window Δ and the effective inverse-Faraday effect field B_{eff} in 20 nm-thick $\text{Gd}_{26}\text{Fe}_{65}\text{Co}_9$ alloy. The material is illuminated with 60-fs laser pulses. The inset shows the Faraday rotation θ as a function of wavelength [54].

Evidence of all-optical switching in multiple ferrimagnetic materials

The first experimental work in all-optical switching was almost exclusively carried out in amorphous ferrimagnetic alloy films such as GdFeCo [9, 48], TbCo [55, 56] and TbFe [57]. Nevertheless, later multiple ferrimagnetic materials of different structure were shown to exhibit AOS. In this section, we will present a quick overview of the ferrimagnets used for ultrafast laser-induced magnetization reversal.

Mangin *et al.* have engineered a large variety of ferrimagnetic materials ranging from amorphous alloys, multilayers, heterostructures to rare-earth-free synthetic ferrimagnets [58]. In order to observe HD-AOS, the idea was to tune the magnetic properties such as the exchange coupling and the compensation temperature T_M , that is the temperature at which the net magnetization vanishes by compensation of the magnetic moments of the two sublattices. Indeed,

previous work had demonstrated the importance of the non-equivalence of the two sublattices in the laser-induced demagnetization and also the value of T_M compared to T_C and room temperature (T_R) [48, 49, 55]. First, Mangin *et al.* investigated various amorphous rare-earth-transition metal (RE-TM) ferrimagnetic alloys with RE = Gd, Tb, Dy and Ho and TM = Fe, Co or FeCo. Four types of alloy were studied as a function of RE composition x : Gd_xFeCo_{1-x} , Tb_xCo_{1-x} , Dy_xCo_{1-x} and Ho_xFeCo_{1-x} . All samples, except Gd-based alloys, have an out-of-plane magnetization. It was found that, regardless of the RE element, all the studied alloys could exhibit HD-AOS for a RE concentration around $x = 25\%$. The results are summed up in Fig. I.9. Interestingly, most alloys showing HD-AOS have a T_M near or above T_R , which suggests that laser-heating above T_M plays a major role in ultrafast magnetization reversal. The authors also examined the influence of the exchange coupling between the two sublattices by engineering RE-TM multilayers. For a given average composition and repeat number (N), RE-TM multilayers presented a similar behavior than amorphous alloys (see. Fig. I.9). For instance, $[Co(0.5\text{ nm})/Tb(0.4\text{ nm})]_{N=28}$ showed HD-AOS. This proves that magnetic compensation at the atomic level as in alloys is not a condition to observe AOS but can be established over larger length scales as long as perpendicular magnetic anisotropy (PMA) is maintained [58]. Finally, Mangin *et al.* have synthesized RE-free ferrimagnetic heterostructures based on Co/Ir multilayers to mimic the magnetic properties of the ferrimagnets showing HD-AOS. An example of such material is $Ta(4\text{ nm})/Pd(3\text{ nm})/[Co(1\text{ nm})/Ir/Co(0.4\text{ nm})/Ni(0.6\text{ nm})/Pt(0.3\text{ nm})/Co(0.4\text{ nm})/Ir]_{N=5}/Pd(3\text{ nm})$ that exhibits HD-AOS. Therefore, it was demonstrated that the presence of RE element, i.e. a slow demagnetization time and consequently a clear difference in the sublattices dynamics [49], is not a necessary condition to observe HD-AOS. This was also suggested by Alebrand *et al.* [56]. To conclude, this in-depth material-dependence study gave evidence that a broad range of materials can be engineered for HD-AOS, which would allow designing complex structures with tunable properties for technological applications.

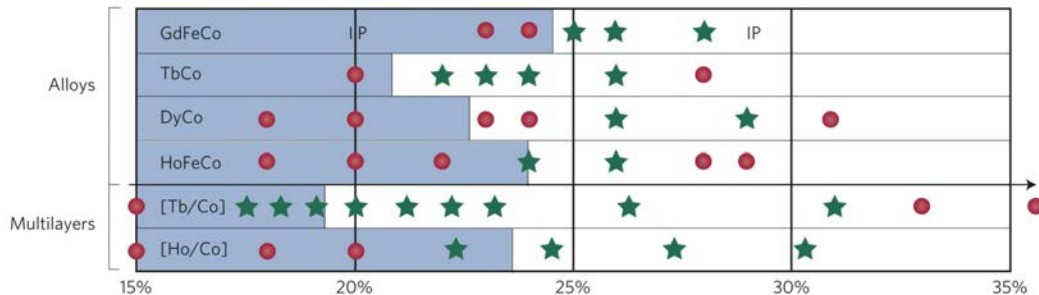


FIGURE I.9: Response to fs optical excitation for RE-TM alloys and two types of RE-TM multilayers as a function of RE concentration. Red dots indicate thermal demagnetization and green stars HD-AOS. The blue shaded area corresponds to the materials with a compensation temperature below room temperature [58].

The motivation of this work by Mangin *et al.* was to find materials with two antiferromagnetic coupled sublattices and a compensation temperature near or above room temperature as a condition for HD-AOS. Yet, we will see in section 3 by studying ferromagnetic materials, that this cannot be a general rule to observe all-optical switching. In addition, AOS was evidenced only by sweeping the laser beam over the sample surface and was helicity-dependent. In the following paragraphs, we discuss other ferrimagnetic materials that exhibit single-laser pulse and helicity-independent magnetization switching.

In 2017, Lalieu *et al.* studied another type of synthetic ferrimagnetic material [59]. Indeed, they demonstrated that deterministic switching could be achieved in Pt/Co/Gd stack using a single linearly-polarized 100-fs laser pulse. This synthetic ferrimagnetic multilayer showed HI-AOS for a Cobalt thickness between 0.8 nm and 1.2 nm. A thicker layer of Cobalt (1.4 nm) led to

thermal demagnetization (see. Fig. 2.d in [59]). Therefore, laser-induced toggle switching is not an exclusive signature of the optical response of GdFeCo alloys. Besides, an interesting feature of this synthetic ferrimagnetic multilayer lies in the fact it has built-in Dzyaloshinskii-Moriya interaction (DMI). Indeed, it was shown that DMI originates from spin-orbit interactions at the Pt/Co interface [60]. In addition to the DMI, considering the large spin Hall angle of Pt, this material provides valuable possibilities for controlling domain wall motion, which combined to AOS could open a new path for developing memory devices.

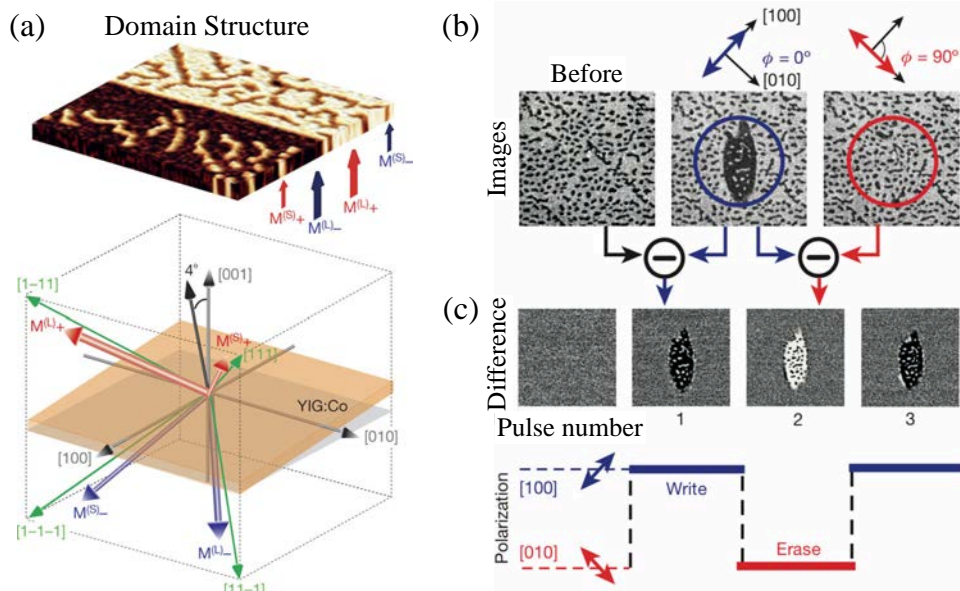


FIGURE I.10: (a) Magnetic states and domain structure of YIG:Co. Orientations of the easy magnetization axes and the pattern of magnetic domains with the magnetization directions close to the $[111]$, $[1-11]$, $[11-1]$ and $[1-1-1]$ axes, measured at zero magnetic field with a magneto-optical polarizing microscope. (b) Magneto-optical imaging after single-pulse excitation. Magnetization reversal was performed with a laser beam with a wavelength of 1,300 nm and a fluence of 150 mJ cm^{-2} . From left to right, domain pattern before the laser excitation and after excitation with two different polarization states. Φ indicates the angle between the pump pulse polarization and the $[100]$ axis. (c) Differential images after each pump pulse and illustration of the magnetic-recording process. Figure adapted from [61].

Up to now, HI-AOS in ferrimagnets was explained by a pure thermal mechanism, the rise of the system temperature above T_C and the distinct dynamics of the two sublattices. Though, the recent discovery of ultrafast laser-induced magnetization switching in a transparent medium hints that it is not the unique mechanism that leads to HI-AOS [61]. In fact, they investigated a cobalt-substituted yttrium iron garnet (YIG:Co), which is an optically transparent ferrimagnetic dielectrics. Because of its unique magnetocrystalline structure, this material has four magnetization states and complex domain pattern at zero field as depicted in Fig. I.10(a). As shown in Figs. I.10(b) & I.10(c), they were able to reverse the magnetization with a single laser pulse polarized along the $[100]$ axis, resulting in a $M^{(L)+}$ magnetic state. In the opposite, a pulse polarized along the $[010]$ axis switches the magnetization in the opposite direction ($M^{(L)-}$). Surprisingly, the domain pattern remained overall unperturbed, only the magnetic contrast of the small and large domains was changed. Furthermore, the magnetization was shown to be completely reversed within 60 ps. Yet, a single write-read event was achieved only in 20 ps (see Fig. 4 in [61]). This result makes YIG:Co an interesting material for ultrafast magnetic recording. Indeed, a minimum fluence of 34 mJ cm^{-2} was required to write a domain for a $7.5 \mu\text{m}$ thick film that absorbs 12 % of photon energy. By scaling down the minimum writing fluence, about 22 aJ would be necessary to write a $(20 \text{ nm})^2 \times 10 \text{ nm}$ bit, which is much lower than for

STT-MRAM (pJ range) for instance. Lastly, this discovery would rather support the idea of a non-thermal and optical effective magnetic field-based mechanism.

2.3 Femtosecond hot-Electron pulses

We saw that ultrafast magnetization reversal could be induced by ultrashort current or laser pulses in a broad variety of materials. Here, we report the possibility of using hot-electron pulses generated by ultrafast optical excitation to reverse the magnetization of GdFeCo alloy films [52, 62]. First demonstrated by Wilson *et al.*, it was found that illumination of a Pt/Au/GdFeCo stack through the bottom Pt layer could lead to deterministic single-pulse magnetization switching of the GdFeCo layer [62]. For Au layers thicker than 30 nm, no significant photon energy was absorbed by the GdFeCo films. As a consequence, the observed magnetization reversal was safely attributed to electronic heat currents generated in the Pt layer by femtosecond laser irradiation. The authors developed a thermal model based on a multilayer variation of the so-called two-temperature model [62] (and ref. therein). In each metallic layer, electrons and phonons are described by two-coupled heat-diffusion equations, while for the GdFeCo layer a third equation is added that corresponds to the spin bath. According to their numerical simulations, the temperature of the Au electrons exceeds 1000 K. Considering the high diffusivity of the Au electrons, the heat diffusion into the GdFeCo layer is extremely fast leading to TW m⁻² picosecond heat currents. Nevertheless, the dynamics and the magnetization reversal timescale were not exactly assessed.

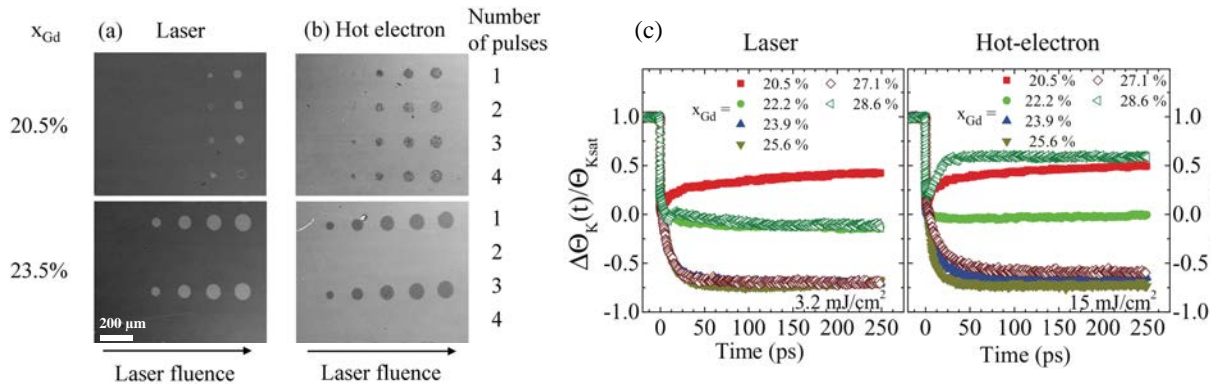


FIGURE I.11: (a) and (b) Magneto-optical Kerr images obtained in Gd_xCo_{1-x}FeCo films after N = 1, 2, 3 or 4 direct laser pulses (a) or hot-electron pulses (b) as a function of composition (x_{Gd}) and fluence. Laser fluence ranged from 0.75 to 3.5 mJ cm⁻² in (a) and from 4 to 12.25 mJ cm⁻² in (b). (c) Comparison between the magnetization dynamics induced by either laser or hot-electron pulses as a function of GdFeCo composition. Figure adapted from [52].

For this purpose, Xu *et al.* carried out a comparative study of the magnetization dynamics upon direct laser excitation or hot-electron pulses as a function of the composition of the GdFeCo alloy layer [52]. The investigated material was a Glass/Ta/Pt/Cu/Gd_xFeCo_{1-x}/Ta film with 23% < x < 28%. For a 80 nm-thick Cu layer, when pumping from the back, i.e. from the Pt layer, less than 0.1% of photon energy is transmitted to the GdFeCo layer. Thus, in this configuration any contribution of the optical stimulus is removed. In the opposite, the effect of a direct laser pulse can be observed when pumping from the front GdFeCo/Ta side. As seen in Fig. I.11, both for Gd-rich and FeCo-rich films, direct laser irradiation [Fig. I.11(a)] and hot electrons [Fig. I.11(b)] led to single fs-pulse HI-AOS [52]. Only samples with composition (x = 20.5%) far from the compensation point showed a multidomain state after single-pulse excitation. Notably, the fluence required to observe magnetization switching with hot-electron pulses was

about four times greater than with a direct laser pulse. Besides, the authors also performed time-resolved magneto-optical kerr (TR-MOKE) measurements to investigate the magnetization dynamics. As seen in Fig. I.11(c), full magnetization switching was observed for samples with a composition close to the compensation point, which corresponds to materials with low M_S and large magnetic domains (see ref in [52]). In both configurations, the magnetization reversal occurred within 5 ps. No significant difference in the magnetization dynamics between direct laser excitation and electronic heat currents was seen. The latter was attributed by the authors to the ballistic nature of the electron transport. To conclude, these studies gave evidence that magnetization switching induced by hot electrons could efficiently be implemented in complex spintronics devices. Yet, a question remains about the clear advantage of electronic heat currents over direct optical excitation.

3 All-optical switching in ferromagnetic materials

Following the discovery of helicity-dependent magnetization switching by Stanciu *et al.* in GdFeCo alloy films [9], much progress have been made in the field of all-optical switching. The results of Radu *et al.* gave some insight into the underlying physical process, and more importantly highlighted the importance of having two antiferromagnetically-coupled sublattices with distinct dynamics upon fs laser pulse excitation [49]. It is under this consideration that many research groups engineered ferrimagnetic materials with the aforementioned properties in order to observe AOS [48, 58]. Yet, the experimental results of Lambert *et al.* questioned the specificity of AOS to ferrimagnets [10]. In fact, they revealed that ferromagnetic materials can also exhibit AOS, which makes it a more general phenomenon. In the next two sections, we will discuss AOS in ferromagnets and see how it raises new fundamental questions regarding the mechanism and microscopic origin of AOS.

3.1 Experimental observation of all-optical switching in ferromagnets

Ferromagnetic films and multilayers

In 2014, Lambert *et al.* made the breakthrough discovery that AOS could also be observed in ferromagnetic materials [10]. They studied a wide range of ferromagnets such as [Co/Pt], [Co/Pd], [Co_{1-x}Ni_x/Pt] and [Co/Ni] multilayers as a function of the number of repeats (N) and the layer thickness. All these materials exhibit an out-of-plane magnetization with a strong perpendicular magnetic anisotropy (PMA), which make them good candidates for high-density magnetic recording. They performed two different types of experiments where the femtosecond laser beam is either swept at a low speed or kept static. Furthermore, the optical response is classified as thermal demagnetization (TD) or helicity-dependent all-optical switching (HD-AOS). Fig. I.12 shows the results for [Co(0.4 nm)/Pt(0.7 nm)]_N multilayers with N = 8, 5 or 3. For N = 8 repeats, independently of the laser polarization, only TD was observed which corresponds to a multidomain state in the scanned region. Still, a rim of opposite magnetization contrast compared to the background can be seen at the edge of the scanned area. This is due to the stabilization by the dipolar field from the surrounding film. As the number of repeats was decreased to N = 5, TD was still found. Notably, the domain size is much larger than for N = 8, this is attributed to the decrease of the thin film thickness. On the contrary, for N = 3, a complete HD-AOS was observed. TD was obtained only with linear polarization. This result was confirmed by keeping the laser static as shown in Fig. I.11(d). In the case of an uniformly magnetized film, for low power a full reversed domain was written with σ^+ pulses, while σ^-

induced no change. While increasing the laser power, a demagnetized area appeared in the center, indicating a laser heating above T_C . Nevertheless, a switching rim can be observed only with σ^+ polarization. The latter demonstrated the deterministic nature of the laser-induced magnetization switching. Lambert *et al.* confirmed these results with other ferromagnetic multilayers, e.g. [Co/Pd], [Co_{1-x}Ni_x/Pt] and [Co/Ni]. For optimized layer thickness and number of repeats, these materials also exhibited full magnetization switching [10]. This was a clear indication that HD-AOS is rather a general phenomenon and not restricted to ferrimagnets. Overall, full switching was achieved for the thinnest samples and with low number of repeats, which suggests that the demagnetizing field plays an important role.

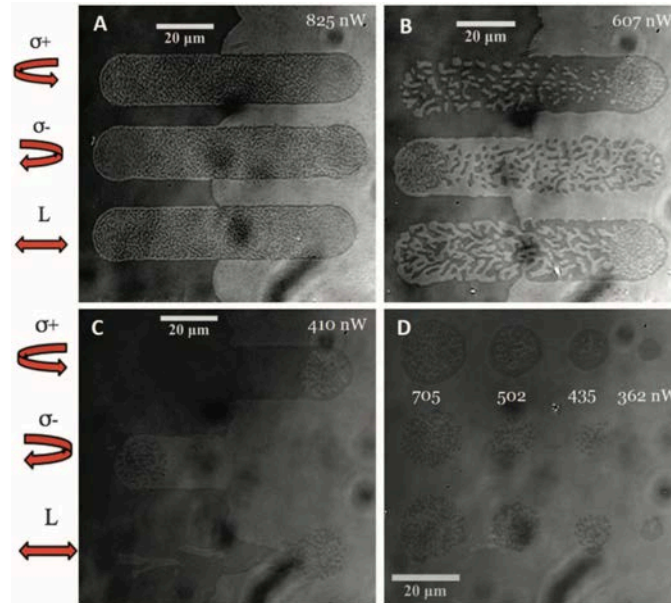


FIGURE I.12: Magneto-optical response of [Co(0.4 nm)/Pt(0.7 nm)]_N multilayer samples to various laser polarizations. (a) N = 8 repeats, (b) N = 5, (c) and (d) N = 3. The sample was prepared to initially show two domains of opposite magnetization direction. The laser beam was swept over the domains with either circular (σ^+ and σ^-) or linear polarization (L). (d) the laser beam is kept static on an uniformly magnetized sample for different laser powers. Figure extracted from [10].

This major result was confirmed and quantified via electrical measurement of the anomalous Hall effect by El Hadri *et al.* [11]. They studied a Pt/Co/Pt film that shows HD-AOS and was patterned into a Hall bar. The principle of the experiment consists in measuring the anomalous Hall voltage while sweeping or keeping the laser beam at a fixed position and for different light polarizations. Precise quantification of the laser-induced change in magnetization comes from the anomalous Hall effect (AHE) [63]. As depicted in Fig. I.13, when sweeping a σ^+ -polarized beam for a sample initially saturated up, the Hall voltage drops as the beam gets closer to the center of the Hall cross. Indeed, magnetization reversal is first initiated by the switching rim present in the outer part of the laser beam (region II). For a centred laser beam, the Hall voltage vanishes corresponding to full demagnetization as the inner part of the beam is composed of multi-domains due to overheating (region III). Finally, the rear part of the rim switches the up-domains and a complete magnetization reversal is obtained (region IV). Furthermore, the authors investigated the influence of the sweeping speed. They found out that increasing the sweeping speed led to a drop of the switching probability. As the sweeping speeds controls the distance between two consecutive laser pulses, this was the first indication that HD-AOS in Co/Pt multilayers is a cumulative process (see. section 3.2). Moreover, the evidence of

laser-induced magnetization reversal via transport measurement supports the feasibility of integrating AOS into opto-spintronic devices.

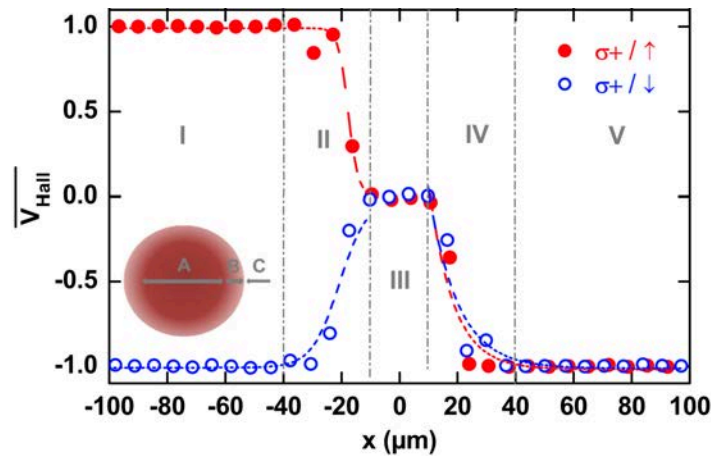


FIGURE I.13: Normalized Hall voltage V_{Hall} as a function of the position of the beam x and for right-circular polarization (σ^+). The values 1 and -1 of the V_{Hall} are the saturation of magnetization values. The laser beam is swept over the whole x axis of Hall cross from position $100 \mu\text{m}$ to $100 \mu\text{m}$, with a sweeping speed of $40 \mu\text{m s}^{-1}$ and a power of 0.95 mW . Inset shows a schematic representation of the laser beam. Figure adapted from [11].

FePt granular media

Besides, optical response of FePt granular media upon femtosecond laser pulse excitation attracted growing attention. Indeed, this ferromagnetic material due to its high anisotropy, large coercivity and granular structure is an ideal material for ultra-high density heat-assisted magnetic recording (HAMR) [1, 2, 64]. AOS was first examined in FePt-based granular media by Lambert *et al.* [10]. They studied two media, namely FePtAgC and FePtC granular films, in which the FePt grains are separated by C grain boundaries. The average grain size was $\sim 9.7 \text{ nm}$ and $\sim 7.7 \text{ nm}$ for FePtAgC and FePtC media, respectively, and with a coercivity of 7 T and 3.5 T , respectively. They performed similar experiments than the ones we reported for ferromagnetic multilayers. The laser beam was either swept over the sample surface or kept static for various light polarizations. However, in this case, the FePt film was initially in a demagnetized state with grains randomly oriented with spin up or down. In Fig. I.14, the demagnetized background appears grey since the grain size is well below the Faraday microscope resolution. When sweeping the fs laser, a net magnetization was achieved which depended upon the light helicity. Indeed, as seen in Fig. I.14(a), exposition to σ^+ - and σ^- - polarized pulses led to opposite magnetic contrast. This was a clear sign that even in granular media the magnetization can be controlled by the light polarization. Though, the magnetization reversal is incomplete unlike e.g. for Co/Pt multilayers. The authors mentioned an induced change of magnetization of $\sim 10 \%$ to $\sim 20 \%$ of saturation [10]. This behavior of FePt media was attributed to the fact that HD-AOS was affecting only a subset of the grains or that due to laser heating near T_C the grains were thermally activated, which, therefore, limited the maximum amount of magnetization reversal. Similarly than for [Co/Pt] multilayers [Fig. I.12(d)], HD-AOS could also be observed with a fixed laser as seen in Fig. I.14(b). In addition, when increasing the laser power, the switching rim appeared at the edge of the beam.

Takahashi *et al.* also investigated FePt-C granular media [65]. They precisely quantified the laser-induced change in magnetization using the same electrical characterization than reported

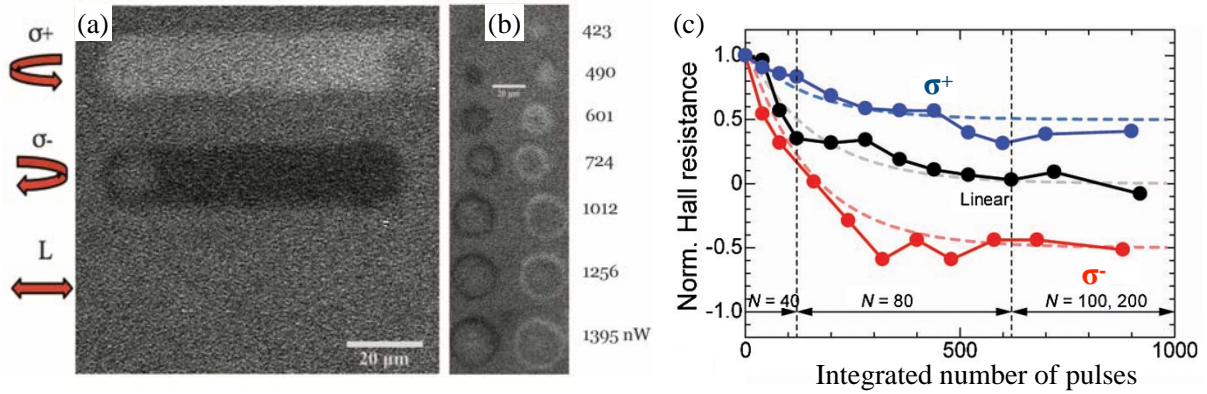


FIGURE I.14: (a) and (b) Magneto-optical response in zero applied magnetic field of a 15-nm FePtAgC granular film sample starting with an initially demagnetized sample. (a) line scans for circular (σ^+ and σ^-) and linear (L) polarization. (b) Images of magnetic domains written by keeping the laser spot at a fixed position and as a function of laser power (left column σ^+ -pulses, right column σ^- -pulses). Figure extracted from [10]. (c) Normalized Hall resistance after applying circularly and linearly polarized light as a function of the integrated number of pulses and light polarization. The sample is initially saturated 'up'. The dotted lines show the fit obtained using the switching model described in [65]. Figure adapted from [65].

by El Hadri *et al.* [11]. A FePt-C film was patterned into a 20- μm -wide Hall cross. For a laser beam kept static in the Hall cross region, the film was exposed to several trains of pulses. The results are shown in Fig. I.14(c), the sample was initially saturated in the 'up' direction. After each train of pulses, the Hall resistance was measured. Further, the number of pulses was gradually increased while maintaining the same laser fluence of 101.9 mJ cm^{-2} . For σ^- polarization, the Hall resistance decreased and reached a minimum of -0.5. This indicates that σ^- polarization reversed about 3/4 of the FePt grains. In the opposite, for σ^+ polarization, the Hall resistance remained at positive values ~ 0.5 , which means that only 1/4 of the grains switched. Finally, linear polarization led to a vanishing Hall resistance corresponding to a full demagnetization state. Therefore, clearly this demonstrates that in granular media the light helicity governs the final magnetization direction after fs laser exposure. Besides, the authors investigated the influence of the microstructure in AOS by comparing the results between FePt-C granular media and a 10-nm-thick FePt continuous film. They found that independently of the light polarization, only thermal demagnetization was observed in FePt continuous films, which is consistent with the results of Lambert *et al.* in thick ferromagnetic multilayers. Indeed, in granular media the dipolar energy is smaller than of the continuous film. Furthermore, HD-AOS in FePt media was explained by a stochastic process [65, 66]. Finally, a full deterministic magnetization switching was accomplished with the combination of circularly-polarized light and a modest external out-of-plane magnetic field of $\sim 0.2 \text{ T} - 0.7 \text{ T}$ [10, 65]. The latter demonstrates that indeed HD-AOS can help magnetic recording via a HAMR-like process by reducing the value of the external field.

3.2 A cumulative and multi-shot process

The discovery of AOS in ferromagnetic materials questioned the uniqueness of the reversal mechanism proposed in ferrimagnetic materials that we previously discussed. In fact, it is not required to have two antiferromagnetically coupled sublattices to observe AOS, for ferromagnets do not present such structure. Thus, at this point the microscopic mechanism of AOS was still under debate.

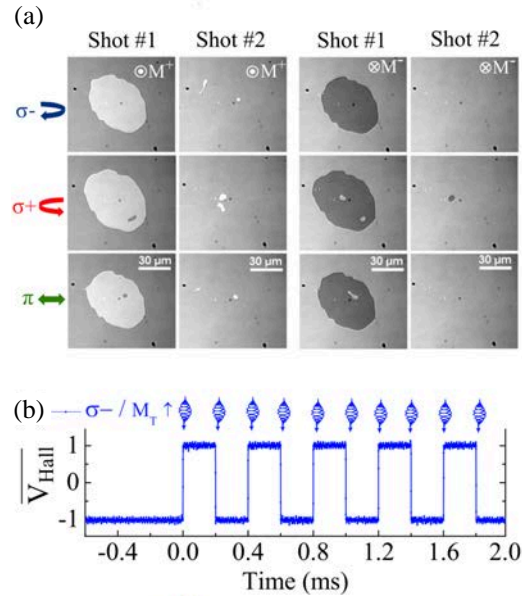


FIGURE I.15: (a) Magneto-optical Faraday images of a $\text{Gd}_{28}\text{Fe}_{48}\text{Co}_{24}$ continuous film, with an initial magnetization saturation 'up' (M^+) and 'down' (M^-) illuminated with two consecutive pulses with three different polarizations: right- (σ^+), left- (σ^-) circular polarization and linear polarization (π). (b) Electrical measurement of magnetization reversal of the patterned $\text{Gd}_{28}\text{Fe}_{48}\text{Co}_{24}$ Hall cross under the action of ten consecutive pulses. The material was initially saturated up. The Hall voltage is normalized to the values of saturation. Figure extracted from [11].

Nevertheless, El Hadri *et al.* tried to elucidate this question in their recent work [50]. They gave evidence that two types of AOS could be distinguished. In their study, they combined two approaches. First, they used magneto-optical Faraday imaging after one or several pulses. Second, they performed time-dependent electrical measurements via AHE to quantify the laser-induced change in magnetization with a $1 \mu\text{s}$ resolution. They investigated two kinds of ferromagnets, namely a GdFeCo alloy and a TbCo alloy, but also a ferromagnetic Pt/Co/Pt film. As previously reported [48, 49], they verified that the studied $\text{Gd}_{28}\text{Fe}_{48}\text{Co}_{24}$ alloy exhibited single-pulse HI-AOS. As shown in Fig. I.15(a), independently of the initial saturation direction and light polarization, a uniform magnetization reversal is achieved with one pulse, and the written domain is completely erased with a consecutive fs-laser pulse. The transport measurements revealed a similar result with reproducible writing/erasing cycles as seen in Fig. I.15(b). However, in $\text{Pt}(4.5 \text{ nm})/\text{Co}(0.6 \text{ nm})/\text{Pt}(4.5 \text{ nm})$, single-laser pulse exposure led only to thermal demagnetization [see. Fig. I.16(a)]. Notably, the fluence used in the experiment allowed full magnetization reversal when sweeping the laser. This implies that the switching rim does not emerge after two consecutive laser pulses. But most importantly, it hints that AOS in ferromagnetic films requires multiple pulses. To reveal the latter, they carried time-dependent electrical measurements in a $5\text{-}\mu\text{m}$ -wide $\text{Pt}(4.5 \text{ nm})/\text{Co}(0.6 \text{ nm})/\text{Pt}(4.5 \text{ nm})$ Hall cross under the action of 600 35-fs laser pulses. As depicted in Fig. I.16(b), the results shows a two-regime-process taking place at different timescales. First, a helicity-independent drop of the Hall voltage within the first 1 ms. Then, a helicity-dependent reversal of the Hall voltage within several tens of ms, which corresponds to about 150 pulses. Therefore, they provided a clear demonstration that AOS in ferromagnetic materials is a cumulative and multipulse process with two distinct regimes: a helicity-independent demagnetization corresponding to a multi-domain formation, followed by a helicity-dependent remagnetization [50]. The authors assumed that the helicity-dependent magnetization recovery resulted from a helicity-dependent domain wall

motion due to thermal spin currents via spin-Seebeck effect and the magnetic circular dichroism (MCD). Further evidence for this potential scenario was brought by Medapalli *et al.* who also studied multishot switching in Co/Pt multilayers [67]. On the other hand, Gorchon *et al.* proposed a thermal mechanism based on MCD and the temperature difference between magnetization up- and down- domain in Co/Pt, which may experience stochastic switching [68]. We will discuss this mechanism more into details in section 4.2. Lastly, the cumulative nature of HD-AOS was also proved in FePt granular media [65]. As seen in Fig. I.14(c), nearly 1000 σ^- -pulses were required to reach the maximum switching in FePt.

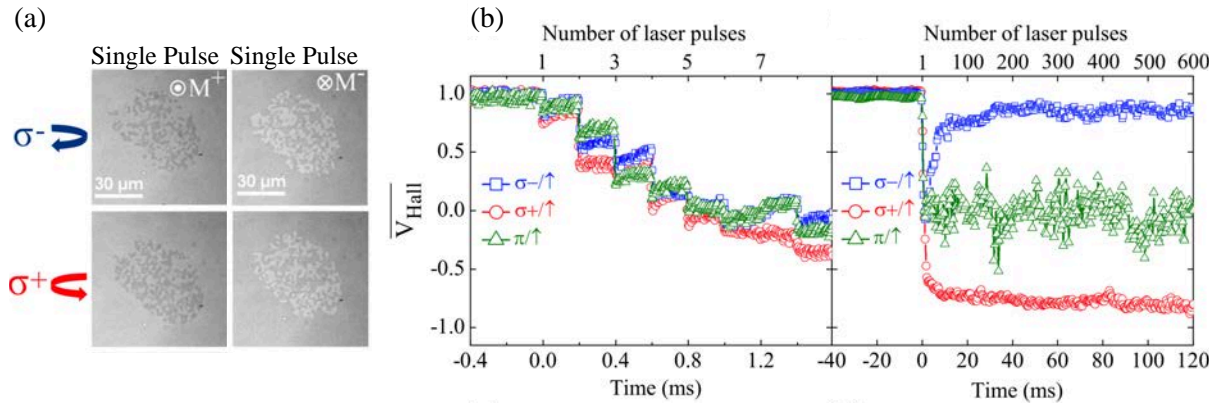


FIGURE I.16: (a) Magneto-optical imaging of Pt(4.5 nm)/Co(0.6 nm)/Pt(4.5 nm) after single-laser pulse excitation. Only thermal demagnetization is observed for both circular polarizations (σ^+ and σ^-) and saturation magnetization directions (M^+ and M^-). (b) Normalized Hall voltage measurement in patterned Pt/Co/Pt Hall cross as a function of light polarization and number of laser pulses. Figure adapted from [11].

Previous studies demonstrated that HD-AOS could be observed in ferrimagnetic TbCo alloys [55, 58]. Yet, in these research works, AOS was obtained only by sweeping the laser. Later, it became apparent that the optical response to fs-laser irradiation of TbCo alloys differed from the one observed in GdFeCo films but was actually similar than in ferromagnetic Co/Pt films [11]. This was already hinted by Alebrand *et al.* who gave evidence that the laser-induced magnetization dynamics of the Co and Tb sublattices took place within a similar timescale [56]. This result tended to put in perspective the need of a transient ferromagnetic-like state as proposed for GdFeCo alloy films [49]. Indeed, El Hadri *et al.* proved that AOS in TbCo was a cumulative multishot process as seen in Pt/Co/Pt films [11]. To conclude, we can now say that materials exhibiting AOS can be arranged in two distinct classes. The first includes materials showing single-pulse helicity-independent all-optical switching such as GdFeCo, Pt/Co/Gd and YIG:Co. The second consists of materials for which all-optical switching is cumulative and helicity-dependent (e.g. Co/Pt, Co/Ni, FePt, TbCo, TbFe etc.). Hence, the mechanism and microscopic origin of AOS remain an open question.

3.3 Can a single-pulse switching be achieved in ferromagnets?

The cumulative nature of AOS in ferromagnets is much intriguing. Nevertheless, it will tend to cast doubt upon the use of such materials for light-induced ultrafast magnetic recording. Indeed, it means that it requires several laser pulses, which thus limits the speed of magnetization reversal. The latter was shown to be in the ms timescale [50, 65]. In comparison, in GdFeCo ferrimagnetic films multiple studies reported magnetization reversal within few picoseconds [49, 52, 53]. However, ferromagnetic materials for their large PMA are of greater interest for technological applications, e.g. for memory devices. Therefore, a legitimate question would be:

can we accomplish deterministic single-pulse switching, hence ultrafast reversal, in ferromagnetic systems as demonstrated in GdFeCo? Is there any optimized laser excitation conditions and material structure to observe toggle switching in ferromagnets?

The first approach consisted in studying the magnetization dynamics of ferromagnetic materials via TR-MOKE measurements. As observed in Ni films [15], single 60-fs-laser pulse led only to demagnetization in Co/Pt trilayers within 1 ps [69]. Although this materials was proved to reveal HD-AOS [10, 67], magnetization reversal could not be achieved after a single 60-fs-laser pulse even for increased laser fluences (see. Fig. 2. in [69]). Another study involved the use of unpolarized hot electrons [70] in a similar manner as described in section 2.3. The authors investigated a Co/Pt multilayer on top of a thick Cu layer to impede any absorption of photon energy by the ferromagnetic material. This system showed hot-electron-induced ultrafast demagnetization in a sub-picosecond timescale. An identical behavior was observed for direct 35-fs-laser pulse excitation.

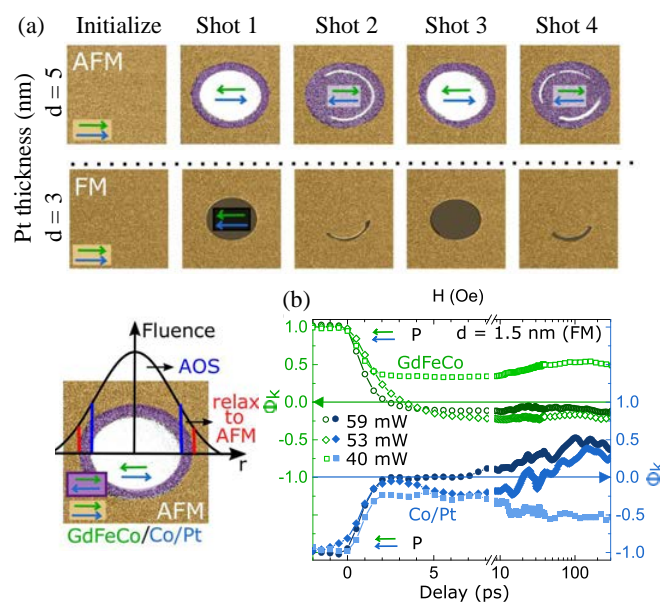


FIGURE I.17: (a) Digitally re-colored MOKE images of single-shot AOS in GdFeCo/Co/Pt(d)/Co/Pt stack series for a spacer thickness $d = 3$ or 5 nm. Green and blue arrows represent GdFeCo and Co/Pt magnetizations, respectively. Below, laser intensity profile and resulting domain configuration on film $d = 5$ nm after the first laser shot. (b) Time-resolved depth-sensitive magneto-optical measurements of laser induced dynamics for various fluences and a spacer thickness of $d = 1.5$ nm. Figure adapted from [71].

Remarkably, Gorchon *et al.* employed a much different approach [71]. Indeed, their idea was to take advantage of the toggle switching of GdFeCo films. Thus, they grew an exchange-coupled layer of Co/Pt on top of GdFeCo. The goal was to profit from the exchange coupling between the two layers in order to extend the helicity-independent single-shot switching of GdFeCo to the Co/Pt layer. They engineered several GdFeCo/Co/Pt(d_{spacer})/Co/Pt stacks for different Pt spacer thicknesses (d_{spacer}). This resulted in either an antiferromagnetic (AFM) or ferromagnetic (FM) exchange coupling. They, further, investigated the optical response of the stacks to single 70-fs-laser pulse with linear polarization. The samples were first exposed to a positive external magnetic field so that the GdFeCo and Co/Pt magnetic moments were parallel. After turning off the field, the materials were illuminated with consecutive laser pulses. Fig. I.17(a) shows the magneto-optical images after each laser pulse. Two behaviors can be distinguished according to the nature of the exchange coupling. For samples with a Pt spacer thickness d

= 4 or 5 nm, i.e. with AFM coupling, two regions of opposite magnetic contrast can be observed. In the central area, the laser fluence is high enough to reverse the GdFeCo magnetization. Nonetheless, the Co/Pt magnetization direction remains unchanged to relax the structure into a more stable AFM configuration. Conversely, in the surrounding area, the fluence is below the switching threshold. Therefore, the GdFeCo moment is not reversed. Still, the hot Co/Pt layer switches to relax into the stable AFM state. Notably, the magnetic moments in the surrounding and center areas are antiparallel. When the sample is illuminated with a second laser shot, the outer rim remains stable while the magnetization in the center switches to the opposite AFM configuration leading to an uniformly magnetized area. For samples exhibiting FM coupling, complete reversal of the central area only occurred. Consecutive pulses switch the magnetization in the other direction. Consequently, toggle switching was clearly demonstrated in, both, AFM and FM-coupled GdFeCo/Co/Pt/Co/Pt stacks. Moreover, the authors performed time-resolved depth-sensitive magneto-optical measurements of the magnetization dynamics as illustrated in Fig. I.17(b). They found that the Co/Pt magnetization was switched within ~ 7 ps, and a faster reversal of GdFeCo in ~ 3 ps. Besides, they concluded that the exchange interaction was responsible for the reversal of the Co/Pt magnetization considering the two-step process observed in the Co/Pt magnetization dynamics [71]. This was the first evidence of toggle switching in an exchange-coupled ferromagnetic layer. However, it is important to note that overall the GdFeCo/Co/Pt/Co/Pt stack presents a ferrimagnetic order.

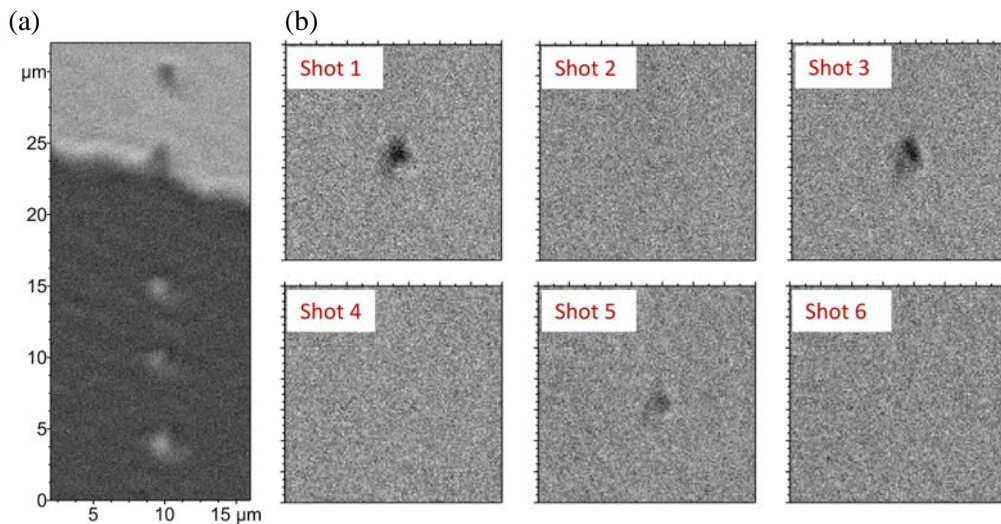


FIGURE I.18: Magneto-optical images of single-fs-laser pulse switching with linear polarization (a) across magnetic domains of opposite saturation direction and (b) for consecutive laser pulses. Figure adapted from [72].

More recently, a surprising result came from Vomir *et al.* who demonstrated single-shot AOS in a Pt/Co/Pt film [72]. They were able to reverse the Co/Pt magnetization with a single linearly-polarized pulse while it was said that in this type of material AOS was helicity-dependent and cumulative [50, 67]. For this purpose, they used a highly focused laser beam spot of a $0.8 \mu\text{m}$ -size. In contrast, in previous studies where HD-AOS was reported in Co/Pt multilayers, a spot size of about $45 - 60 \mu\text{m}$ was used [10, 50, 67]. Fig. I.18(a) shows that linearly-polarized laser pulses switches the magnetization for both saturation state. In Fig. I.18(b) are displayed the magneto-optical images after the excitation of 6 consecutive pulses. It is shown that each pulse reverses the magnetization, and thus a clear proof of toggle switching was provided [72]. They also studied the laser-induced dynamics upon single-laser pulse irradiation. They found that the magnetization crossed the 0 point of the magneto-optical signal in less than a few μs (see. Fig. 3(c) in [72]). However, full magnetization reversal was not observed in the 1 ms timescale.

Finally, the authors explained their results by the fact that the laser spot size was of the order of the intrinsic domain size of the Pt/Co/Pt film, making the latter a key element to observe toggle switching in ferromagnetic materials. Nevertheless, the mechanism of such reversal remains unclear. Vomir *et al.* assumed a nucleation/propagation process, as suggested also by El Hadri *et al.* and Medapalli *et al.* but in the case of multishot HD-AOS [50, 67]. Therefore, questions can be raised about the origin of the helicity-independent switching observed by Vomir *et al.* [72].

3.4 Influence of dipolar field and magnetic domain size

The latest results of AOS in ferromagnets highlighted the importance of the nucleation process prior to the magnetization reversal [50, 67, 72]. An emphasis on the potential role of the dipolar field was already speculated by Lambert *et al.* in 2014 [10]. Indeed, they demonstrated that by reducing the number of repeats in ferromagnetic layers they could observe HD-AOS. This was explained by the fact that the dipolar energy gain for domain formation is strongly suppressed in the ultrathin-film limit. Thus, in high number of repeats, the demagnetizing field is larger and only thermal demagnetization is observed. Similar conclusion was also drawn for FePt granular media [10, 65]. The incomplete magnetization reversal in FePt was justified by the thermal activation of the magnetic grains. After the laser excitation, during sample cooling, partial demagnetization can be experienced in an assembly of grain due to the thermal switching of individual grains. This process is accentuated by the dipolar fields from the neighboring grains [10]. In addition, only thermal demagnetization was observed in FePt continuous film in contrast with the granular media, which can be understood in terms of the large dipolar energy stored in the continuous film [65].

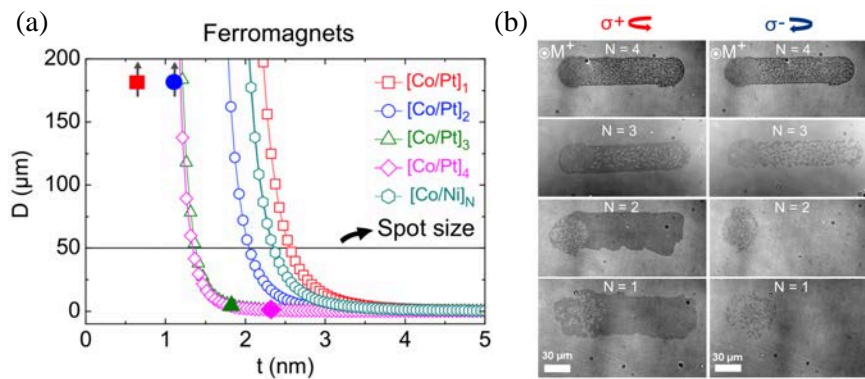


FIGURE I.19: (a) Estimation of the magnetic domain size D as a function of the magnetic thickness t at room temperature for the studied ferromagnetic materials. The filled symbols indicate the studied samples. (b) Optical response of $[\text{Co/Pt}]_N$ multilayers to fs laser pulse excitation. Only ferromagnetic multilayers with $N = 1$ or 2 shows HD-AOS, and for these materials the domain size is larger than the spot size. Figure extracted from [73].

El Hadri *et al.* gave further evidence of the decisive role of the demagnetizing energy gain and by extension the size of stable domains [73]. They investigated the thickness dependence of HD-AOS in ferromagnetic multilayers such as Co/Ni and Co/Pt, but also ferrimagnetic TbCo alloys for different compositions. For Tb-dominated alloys, a wide range of Tb concentrations was found to lead to HD-AOS. However, for Co-dominated alloys, the signature of HD-AOS gradually appeared as the material thickness was reduced below 6.5 nm. For $[\text{Co/Pt}]_N$ and $[\text{Co/Ni}]_N$ multilayers similar results were obtained than in the study of Lambert *et al.* [10]. By scaling down the number of repeats N , hence lowering the magnetic thickness, HD-AOS could

be achieved. To elucidate the role of the dipolar field, the authors estimated in these material the domain size using the model proposed by Kooy *et al.* [74]. Indeed, the stable magnetic domain size is determined by the competition between the exchange, anisotropy and dipolar energy, which depend on the magnetic thickness. They discovered that all the ferromagnetic materials exhibiting HD-AOS had a domain size at room temperature (RT) larger than the laser spot size (as seen in Fig. I.19). Thus, this allowed them to establish the following criterion: to observe a persistent helicity-dependent magnetization switching, the magnetic domain size must be larger than the laser spot size during the cooling process. This criterion was also verified for ferrimagnetic TbCo alloys. Moreover, they argued that the laser-induced increase of temperature in the system would result in a drop of the saturation magnetization, hence a larger domain size than at RT. Therefore, the criterion is even fulfilled when considering the domain size at higher temperatures. Although this domain size criterion seems to be quite simple, it found an echo in the study of Vomir *et al.* [72]. In fact, toggle switching in Co/Pt was achieved specifically for a laser beam spot size of the the order of the intrinsic domain size.

4 Mechanism and modeling of all-optical switching in ferromagnets

The nature of AOS is many-fold, it can be helicity-dependent or helicity-independent, multi-pulse or single-pulse. Thus, it is clear that it has a complex underlying physical origin. While HI-AOS in GdFeCo alloy films was explained by a pure thermal mechanism [48, 49, 54], the discovery of AOS in ferromagnetic materials evidenced that the microscopic mechanism cannot be unique. Two main possible origins of the symmetry breaking in AOS were studied: (i) a non-thermal mechanism based on the inverse Faraday effect (IFE) and angular momentum transfer, (ii) a pure thermal mechanism that is only a consequence of laser-induced heating effects.

4.1 Inverse Faraday effect

One of the many manifestations of the interaction of light with a magnetic material is the magneto-optical Faraday effect [75]. The transmission of light through a magnetic medium is accompanied with a rotation of the polarization plane of the electromagnetic wave. Reciprocally, it is said that circularly-polarized light may induce a magnetic polarization. This phenomenon was called "inverse Faraday effect" (IFE). It was first observed in the mid-1960s in a non-absorbing magnetic dielectrics [76]. A Phenomenological relation was established and experimentally verified [76]:

$$\vec{M} = \frac{\chi}{16\pi} [\vec{E}(\omega) \times \vec{E}^*(\omega)] \quad (4.1)$$

where \vec{M} is the static induced-magnetization, $\vec{E}(\omega)$ and $\vec{E}^*(\omega)$ are the electric field of light and its complex conjugate, χ is the magneto-optical susceptibility and ω the electromagnetic wave frequency. It results from Eq. 4.1 that circularly-polarized light should induce a magnetization along the light wave vector. In other words, the IFE can be seen as an effective magnetic field \vec{H}_{eff} acting on the material magnetization, and for which its direction depends upon light helicity. Should we mention a first quantum mechanical approach to explain this effect by Pershan *et al.* in 1966 who defined an "effective" Hamiltonian H_{eff} in non-dissipative magnetic media to translate the magneto-optical interaction [77]. In a more recent work, a quantum theory of the IFE supported by *ab initio* calculation was developed [78].

The first attempt to explain ultrafast laser-induced magnetization control with the IFE was proposed by Kimel *et al.* in 2005 in a ferrimagnetic material [79]. They demonstrated that circularly-polarized fs-laser pulses could non-thermally excite and coherently control the spin dynamics via the IFE. Besides, the effect of 500-mJ cm⁻²- 200-fs-laser pulses was found to be equivalent to an effective magnetic field of about 5 T and of a duration similar than the optical excitation. Another approach consisted in describing HD-AOS in GdFeCo films with a two-step process [47]. Firstly, the magnetic system is brought to a highly nonequilibrium state due to ultrafast laser heating. And secondly, owing to the IFE circularly-polarized laser pulses induce an effective magnetic field of up to 20 T and thus can reverse the magnetization [47]. To support this mechanism and understand the observed helicity-dependent magnetization reversal, Vahaplar *et al.* performed numerical simulations [47]. The spin dynamics was calculated using the two-temperature model and the LLB equation under a multimacrospin approximation in which a phenomenological expression of the IFE was incorporated. Their modeling appeared to be in good agreement with the experimental results.

The demonstration of HD-AOS in ferromagnets triggered an increased interest in ultrafast magneto-optical effects [10]. Legitimately, we can therefore ask whether the helicity-dependence of AOS observed in ferromagnetic materials can also be interpreted with the inverse Faraday effect. Answers to this question have been provided by Cornelissen *et al.* who developed a microscopic model for AOS in ferromagnetic Co/Pt multilayers [80]. Their theoretical work follows a model introduced by Koopmans *et al.* who explicitly took into account dissipation of angular momentum in the three-temperature model (3TM) [30, 31] (see. section 1.3). Conservation and transfer of angular momentum was successfully explained by an Elliot-Yafet type of electron scattering [30], which allowed them to derive the microscopic version of the 3TM (M3TM). They used a simplified Hamiltonian to describe the electron, phonon and spin systems and their respective interactions. Several hypotheses were made for this purpose. It was assumed: (i) a Fermi sea of spinless electrons with a constant density of states described by Bloch functions, (ii) phonons according to Einstein or Debye model and (iii) a separate spin reservoir that verifies the mean-field Weiss model. The M3TM results in the following magnetization dynamics equation Eq. 4.2 (see. supplementary materials in [31]):

$$\frac{dm}{dt} = Rm \frac{T_p}{T_C} \left(1 - m \coth \left(\frac{mT_C}{T_e} \right) \right) \quad (4.2)$$

where m is the magnetization relative to saturation, T_C the Curie temperature, T_e and T_p the electron, phonon temperature, respectively. R is a prefactor in the demagnetization rate and is equal to:

$$R = \frac{8a_{sf}T_C^2g_{ep}}{k_B T_D^2 D_s} \quad (4.3)$$

with a_{sf} the Elliot-Yafet-driven spin-flip probability, g_{ep} the electron-phonon coupling, T_D the Debye temperature, D_s the atomic magnetic moment divided by the Bohr magneton and k_B the Boltzmann constant. For Co/Pt systems, $R = 9.4 \text{ ps}^{-1}$. In 2010, the numerical solutions of the M3TM (Eq. 4.2) were consistent with the ultrafast laser-induced demagnetization reported in ferromagnetic metals (e.g. Ni, Co, Fe) [20, 31]. Further, to illustrate the impact of the IFE, an effective magnetic field accordingly to Kimel *et al.* [79] was implemented in Eq. 4.2 leading to:

$$\frac{dm}{dt} = R (m + b_{eff}) \frac{T_p}{T_C} \left(1 - m \coth \left(\frac{T_C}{T_e} [m + b_{eff}] \right) \right) \quad (4.4)$$

where b_{eff} is the IFE-based effective magnetic field. Fig. I.20(a) shows the results of the simulations of the magnetization dynamics upon fs-laser irradiation in Co/Pt and as a function of light polarization. For linear polarization L (no IFE), only an ultrafast quenching of the magnetization takes place then the magnetization slowly relaxes back as experimentally observed in Co and Co/Pt₃ films [31, 69]. Similar behavior is obtained for σ^+ -polarized laser pulses (positive IFE) for a ferromagnetic system initially in a magnetization-up state. On the other hand, for σ^- -pulses (negative IFE), an ultrafast demagnetization is followed by a magnetization reversal in a picosecond timescale. Hence, the IFE seems to be a potential driving mechanism to explain HD-AOS. By adding the effect of dipolar fields into their model, they were even able to reproduce the magnetization profile after single-laser pulse exposure in [Co(0.4 nm)/Pt(0.7 nm)]₃ (see. Fig. I.20(b)) comparable to the multipulse static irradiation in Lambert *et al.* [10]. Finally, Cornelissen *et al.* also discussed the amplitude and lifetime of the IFE-induced effective field [80]. They demonstrated that in Co/Pt multilayers due to the strong spin-orbit coupling a minimal lifetime of the IFE in the order of 0.1 ps is required to achieve AOS for a field strength ranging from ~ 10 T to 24 T. Although this is the first successful attempt to model HD-AOS in ferromagnets, several questions can be raised. First of all, H_{eff} was evidenced in non-absorbing magnetic media, and to date no clear experimental proof of the existence of IFE in dissipative ferri- and -ferro- magnetic materials such as GdFeCo alloys, Co/Pt and Fe/Pt has been brought out. Moreover, the element-specificity of such field is not well defined yet, which often explains the wide range of the estimation of the amplitude. Besides, it remains unclear why the IFE would last longer than the optical excitation itself. Lastly, no helicity-dependent single-pulse magnetization switching has been reported in Co/Pt multilayers until now. Nonetheless, the observation of ultrafast non-thermal magnetization reversal in YIG:Co, which is an optical transparent ferrimagnetic dielectrics, proves that IFE- and athermal- mechanisms cannot be ruled out [61].

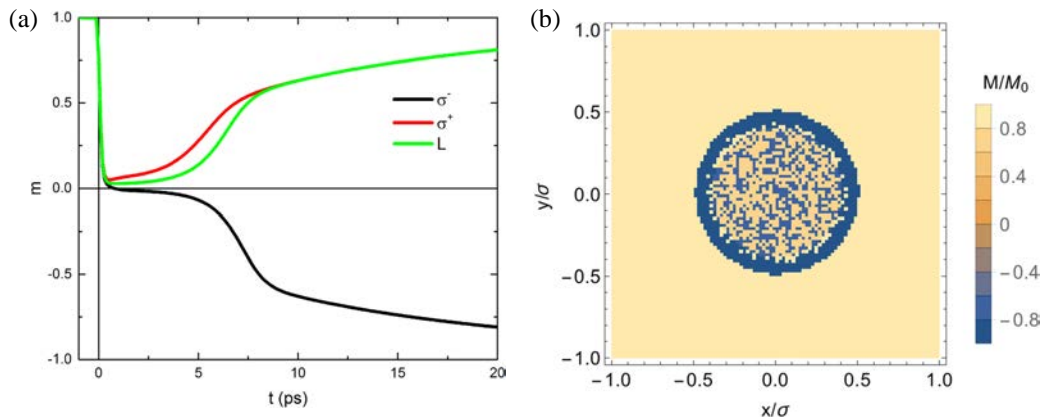


FIGURE I.20: (a) Magnetization dynamics calculated with the M3TM described in the text as a function of light polarization. The circularly-polarized laser pulses (σ^+ and σ^-) are assumed to induced a 10 T field with a 0.4 ps lifetime. (b) Single-pulse magnetization profile obtained from M3TM simulations on a [Co(0.4 nm)/Pt(0.7 nm)]₃ multilayer. The switching rim can clearly be seen in the outer part of the laser beam. Figure extracted from [80].

4.2 Magnetic circular dichroism

The helicity-dependence in AOS has also been explained and modelled by pure thermal mechanisms. In section 2.2, we have already mentioned the work of Khorsand *et al.* who investigated AOS in GdFeCo films [54]. It was shown that HD-AOS could occur only in a narrow window Δ of laser fluences. They investigated the role of magnetic circular dichroism (MCD) in the microscopic origin of AOS. They found that Δ and the relative absorption of right- and left-circular polarizations presented a weak similar spectral dependence, unlike for the IFE effective magnetic field which highly depends on the laser wavelength. Therefore, they were able to conclude that HD-AOS in GdFeCo films originated from MCD.

More recently, in 2016, Gorchon *et al.* developed a multi-pulse stochastic all-thermal model of HD-AOS in ferromagnets, taking the example of FePt-C granular media [68]. It is a purely heat-driven mechanism based on MCD. The interaction of the laser excitation and the magnetic medium is described as follows: upon irradiation, a laser pulse heats the magnetic system close to T_C , due to a drop of magnetic anisotropy the stability of the magnetic state is significantly decreased. Taking into account the MCD, for a circularly-polarized laser beam, domains with opposite magnetization directions will absorb different amounts of light, leading to hotter T_{hot} and colder T_{cold} regions. This difference of temperature will result also in a difference of magnetic stability. If T_{hot} is close to T_C , and the MCD large enough, then hot regions will experience stochastic switching, while the cooler regions will remain stable. This process is repeated many times for all the consecutive laser pulses, which will statistically give rise to helicity-dependent magnetization reversal. To validate this mechanism, the magnetic system was subdivided into an array of two types of cells (grains or macrospins). By neglecting the exchange and the dipolar energies, only two magnetic states are possible for the cells corresponding to a magnetization 'up' or 'down'. Using the Arrhenius-Néel law, the hopping time τ for the magnetization for going from 'up' to 'down' is defined as:

$$\tau(T) = \tau_0 \exp\left(\frac{E(T)}{k_B T}\right) \quad (4.5)$$

where τ_0 is a characteristic time of about 0.1 ns, k_B is the Boltzmann constant, T is the grain/macrospin temperature, and E represents the energy barrier. Considering a laser-induced temperature increase $\Delta(T)$ above room temperature T_0 during a duration of t_{hot} , the magnetic cell has a probability P to switch from a 'up' to 'down' state, and $1-P$ to remain in its initial state:

$$P = \frac{1}{2} \left[1 - \exp\left(-\frac{t_{hot}}{\tau(T_0 + \Delta T)}\right) \right] \quad (4.6)$$

The expression of the probability for magnetization switching from 'down' to 'up' is assumed to be the same as above. The authors implemented the MCD (%) in their model and Eq. 4.6 by defining the temperature of the *hot* and *cold* cells as:

$$\begin{aligned} T_{hot} &= T_0 + \left(1 + \frac{MCD}{2}\right) \Delta T \\ T_{cold} &= T_0 + \left(1 - \frac{MCD}{2}\right) \Delta T \end{aligned} \quad (4.7)$$

assuming that for σ^+ polarization (resp. σ^-) the magnetization 'down' (resp. 'up') is more absorbed. Therefore, hot and cold grains will have different switching probabilities. Gorchon *et al.* derived a cumulative probability for the magnetization to end in one of either states in order to take into account the multi-pulse nature of AOS in ferromagnets (see. supplementary materials in [68]). It is found that for high number of pulses, and for significant temperature difference, deterministic switching will take place. A numerical solution to the cumulative probability was calculated for FePt-C granular media with 7-nm-thick- and 5-nm-wide- grains and a MCD of 5.8 %. The results of the simulations are shown in Fig. I.21(a). They demonstrated that from a certain temperature difference ΔT , i.e. for an adequate laser power and value of MCD, there is a finite number of laser shots that leads to magnetization reversal. It is also proved that single-pulse exposure can only induce thermal demagnetization. In addition, the authors investigated the dependence on the value of MCD. They concluded that a MCD as small as 0.5 % for a narrow range of laser power can give rise to magnetization switching. The latter confirms that such all-thermal mechanism can be generalized to a broader variety of magnetic materials, including Co/Pt and ferrimagnetic Co/Tb alloys. Besides, they simulated the spatial magnetization profile for a static laser beam or after sweeping the laser (see. Fig. I.21(b)). Their results are consistent with the experimental observations of Lambert *et al.* in FePt-C [10]. Thus, unambiguously HD-AOS in ferromagnets can also be described by a purely thermal mechanism based on MCD, which even includes the cumulative and multi-shot process observed in Co/Pt multilayers and Fe/Pt [50, 65, 67]. Notably, Takahashi *et al.* gave clear evidence of the multi-pulse switching occurring in FePt granular media [65]. Moreover, at the same time than Gorchon *et al.* [68], they developed a statistical model, which defines a switching probability for the magnetic grains depending on the light helicity [65]. Both models are similar and in good agreement with the experimental results. Lastly, Tsema *et al.* demonstrated that ultrafast magnetization dynamics in Co/Pt multilayers upon 60 fs-laser pulse irradiation exhibited a small helicity-dependence, which highlights the influence of MCD [69]. However, it is important to note that possibly the MCD and IFE could be present at the same time. In this sense, a model that includes both effects was established in the case of FePt [66].

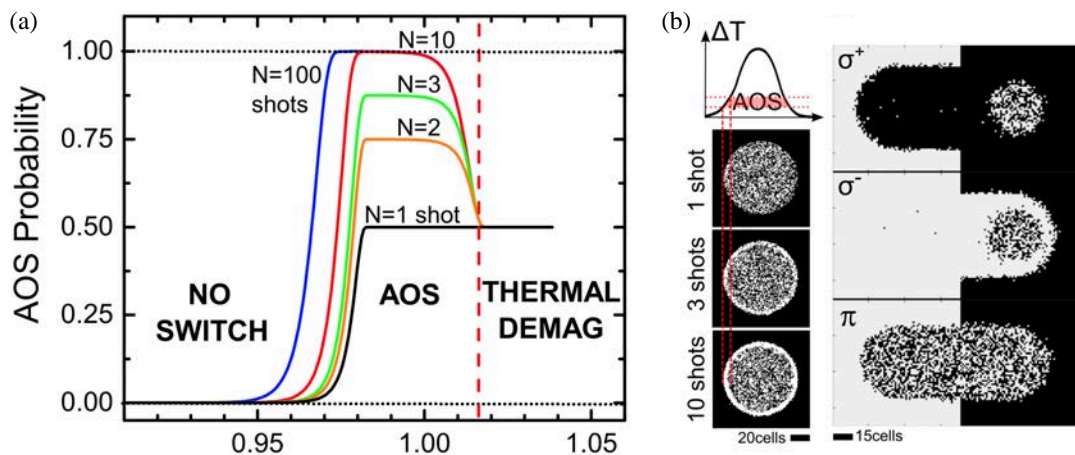


FIGURE I.21: (a) AOS probability as a function of the laser-induced temperature increase ΔT for different number of shots. For a hot temperature close to T_C , i.e. for a MCD and laser power large enough, AOS probability increases with the number of laser pulses. At higher temperatures, the material is thermally demagnetized. (b) Spatially-resolved simulations of the magnetization state after assuming a Gaussian temperature profile induced by the laser. Left column: simulations for consecutive laser shots with left circular polarization (σ^-) for an initial saturation down state (dark contrast). The switching rim appears when increasing the number of laser shots. Right column: simulations when sweeping the laser across two magnetic domains of opposite saturation direction and with left-circular (σ^-), right-circular (σ^+) and linear (π) polarization. Figure adapted from [68].

5 Goals and outline of the thesis

In ferrimagnetic GdFeCo alloy films, toggle switching is almost unanimously considered to result from a purely thermal mechanism. On the other hand, we saw that for ferromagnetic materials the underlying physics of AOS remains an open question. Therefore, our aim in this thesis is to tackle this issue, and more specifically investigate the process that allows helicity-dependence magnetization reversal after ultrafast demagnetization in multi-shot AOS in ferromagnets. Furthermore, we will study the possible integration of AOS in patterned media for high-density magnetic recording. This will allow us to examine the role of dipolar energy in micro-structured materials. In chapter II, experimental methods we used to fabricate the metallic layers and carry out AOS experiments will be first introduced. Thereafter, in chapter III, the growing evidence of the influence of demagnetizing fields, hence magnetic domain size, and also the suggestion of a nucleation/propagation process taking place in HD-AOS led us to study laser-induced manipulation of domain wall in ferromagnetic multilayers. We demonstrate helicity-dependent all-optical domain wall motion in Co/Pt multilayers. Thus, we confirm the feasibility of helicity-dependent magnetization recovery through helicity-dependent domain wall motion. Finally, in chapter IV, we explore the size effects of AOS by scaling down the material dimensions. We fabricate patterned ferromagnetic materials, which enables us to reduce the influence of dipolar fields compared to a full film. We prove that HD-AOS can be reproduced in μm -sized Co/Pt disks. Moreover, the cumulative nature of AOS is accentuated in micro-structures, which tends to indicate that actually the presence of dipolar fields may ease laser-induced magnetization switching.

References

1. Kryder, M. H. *et al.* Heat Assisted Magnetic Recording. *Proceedings of the IEEE* **96**, 1810–1835. ISSN: 0018-9219 (2008).
2. Stipe, B. C. *et al.* Magnetic recording at 1.5 Pb m⁻² using an integrated plasmonic antenna. *Nature Photonics* **4**, 484–488 (2010).
3. Richter, H. J. *et al.* Recording potential of bit-patterned media. *Applied Physics Letters* **88**, 222512 (2006).
4. Albrecht, T. R. *et al.* Bit Patterned Media at 1 Tdot/in² and Beyond. *IEEE Transactions on Magnetics* **49**, 773–778. ISSN: 0018-9464 (2013).
5. Ohno, H. *et al.* Electric-field control of ferromagnetism. *Nature* **408**, 944–946 (Dec. 2000).
6. Katine, J. A., Albert, F. J., Buhrman, R. A., Myers, E. B. & Ralph, D. C. Current-Driven Magnetization Reversal and Spin-Wave Excitations in Co /Cu /Co Pillars. *Phys. Rev. Lett.* **84**, 3149–3152 (14 2000).
7. Diao, Z. *et al.* Spin-transfer torque switching in magnetic tunnel junctions and spin-transfer torque random access memory. *Journal of Physics: Condensed Matter* **19**, 165209 (2007).
8. Akyol, M. *et al.* Current-induced spin-orbit torque switching of perpendicularly magnetized Hf|CoFeB|MgO and Hf|CoFeB|TaOx structures. *Applied Physics Letters* **106**, 162409 (2015).
9. Stanciu, C. D. *et al.* All-Optical Magnetic Recording with Circularly Polarized Light. *Physical Review Letters* **99**, 047601 (July 2007).
10. Lambert, C.-H. *et al.* All-optical control of ferromagnetic thin films and nanostructures. *Science* **345**, 1337 (Sept. 2014).
11. El Hadri, M. S. *et al.* Electrical characterization of all-optical helicity-dependent switching in ferromagnetic Hall crosses. *Applied Physics Letters* **108**, 092405 (2016).
12. Agranat, M. B., Ashitkov, S. I., Granovskii, A. B. & Rukman, G. I. Interaction of picosecond laser pulses with the electron, spin, and phonon subsystems of nickel. *Journal of Experimental and Theoretical Physics* **59**, 804 (1984).
13. Vaterlaus, A., Milani, F. & Meier, F. Spin polarization of thermoemitted electrons from cesiated Ni and Fe. *Physical Review Letters* **65**, 3041–3043 (Dec. 1990).
14. Kirilyuk, A., Kimel, A. V. & Rasing, T. Ultrafast optical manipulation of magnetic order. *Reviews of Modern Physics* **82**, 2731–2784 (Sept. 2010).
15. Beaurepaire, E., Merle, J. C., Daunois, A. & Bigot, J. Y. Ultrafast Spin Dynamics in Ferromagnetic Nickel. *Physical Review Letters* **76**, 4250–4253 (May 1996).
16. Kampfrath, T. *et al.* Ultrafast magneto-optical response of iron thin films. *Physical Review B* **65**, 104429 (Feb. 2002).
17. Melnikov, A. V., Gdde, J. & Matthias, E. Demagnetization following optical excitation in nickel and permalloy films. *Applied Physics B* **74**, 735–740 (2002).
18. Beaurepaire, E. *et al.* Spin dynamics in CoPt₃ alloy films: A magnetic phase transition in the femtosecond time scale. *Physical Review B* **58**, 12134–12137 (Nov. 1998).
19. Guidoni, L., Beaurepaire, E. & Bigot, J.-Y. Magneto-optics in the Ultrafast Regime: Thermalization of Spin Populations in Ferromagnetic Films. *Physical Review Letters* **89**, 017401 (June 2002).
20. Koopmans, B. *Handbook of Magnetism and Advanced Magnetic Materials Vol 3*. 1589–1613 (Wiley, 2007).
21. Beaurepaire, E. *et al.* Coherent terahertz emission from ferromagnetic films excited by femtosecond laser pulses. *Applied Physics Letters* **84**, 3465–3467 (2004).
22. Huisman, T. J. *et al.* Femtosecond control of electric currents in metallic ferromagnetic heterostructures. *Nature Nanotechnology* **11**, 455–458 (Feb. 2016).

23. Landau, L. & Lifschitz, E. On the theory of the dispersion of magnetic permeability in ferromagnetic bodies. *Phys. Z. Sowjet* **153**, 101–114 (1935).
24. Gilbert, T. L. A phenomenological theory of damping in ferromagnetic materials. *IEEE Transactions on Magnetics* **40**, 3443–3449 (2004).
25. Brown, W. Thermal fluctuation of fine ferromagnetic particles. *IEEE Transactions on Magnetics* **15**, 1196–1208 (1979).
26. Evans, R. F. L. *et al.* Atomistic spin model simulations of magnetic nanomaterials. *Journal of Physics: Condensed Matter* **26**, 103202 (2014).
27. Grinstein, G. & Koch, R. H. Coarse Graining in Micromagnetics. *Physical Review Letters* **90**, 207201 (May 2003).
28. Atxitia, U. *et al.* Micromagnetic modeling of laser-induced magnetization dynamics using the Landau-Lifshitz-Bloch equation. *Applied Physics Letters* **91**, 232507 (2007).
29. Sun, C. K., Vallée, F., Acioli, L. H., Ippen, E. P. & Fujimoto, J. G. Femtosecond-tunable measurement of electron thermalization in gold. *Physical Review B* **50**, 15337–15348 (Nov. 1994).
30. Koopmans, B., Ruigrok, J. J. M., Longa, F. D. & de Jonge, W. J. M. Unifying Ultrafast Magnetization Dynamics. *Physical Review Letters* **95**, 267207 (Dec. 2005).
31. Koopmans, B. *et al.* Explaining the paradoxical diversity of ultrafast laser-induced demagnetization. *Nature Materials* **9**, 259–265 (Dec. 2010).
32. Stamm, C. *et al.* Femtosecond modification of electron localization and transfer of angular momentum in nickel. *Nature Materials* **6**, 740–743 (Aug. 2007).
33. Lee, K.-S., Lee, S.-W., Min, B.-C. & Lee, K.-J. Threshold current for switching of a perpendicular magnetic layer induced by spin Hall effect. *Applied Physics Letters* **102**, 112410 (2013).
34. Garello, K. *et al.* Ultrafast magnetization switching by spin-orbit torques. *Applied Physics Letters* **105**, 212402 (2014).
35. Slonczewski, J. C. Current-driven excitation of magnetic multilayers. *Journal of Magnetism and Magnetic Materials* **159** (1996).
36. Berger, L. Emission of spin waves by a magnetic multilayer traversed by a current. *Physical Review B* **54**, 9353–9358 (Oct. 1996).
37. Katine, J. A. & Fullerton, E. E. Device implications of spin-transfer torques. *Journal of Magnetism and Magnetic Materials* **320**, 1217–1226 (2008).
38. Tulapurkar, A. A. *et al.* Subnanosecond magnetization reversal in magnetic nanopillars by spin angular momentum transfer. *Applied Physics Letters* **85**, 5358–5360 (2004).
39. Lee, O. J., Ralph, D. C. & Buhrman, R. A. Spin-torque-driven ballistic precessional switching with 50 ps impulses. *Applied Physics Letters* **99**, 102507 (2011).
40. Liu, H. *et al.* Ultrafast switching in magnetic tunnel junction based orthogonal spin transfer devices. *Applied Physics Letters* **97**, 242510 (2010).
41. Devolder, T., Chappert, C., Katine, J. A., Carey, M. J. & Ito, K. Distribution of the magnetization reversal duration in subnanosecond spin-transfer switching. *Physical Review B* **75**, 064402– (Feb. 2007).
42. Bedau, D. *et al.* Ultrafast spin-transfer switching in spin valve nanopillars with perpendicular anisotropy. *Applied Physics Letters* **96**, 022514 (2010).
43. Miron, I. *et al.* Current-driven spin torque induced by the Rashba effect in a ferromagnetic metal layer. *Nature Materials* **9**, 230–234 (Jan. 2010).
44. Miron, I. M. *et al.* Perpendicular switching of a single ferromagnetic layer induced by in-plane current injection. *Nature* **476**, 189–193 (July 2011).
45. Liu, L. *et al.* Spin-Torque Switching with the Giant Spin Hall Effect of Tantalum. *Science* **336**, 555 (May 2012).
46. Yang, Y. *et al.* Ultrafast magnetization reversal by picosecond electrical pulses. *Science Advances* **3** (Nov. 2017).

47. Vahaplar, K. *et al.* All-optical magnetization reversal by circularly polarized laser pulses: Experiment and multiscale modeling. *Physical Review B* **85**, 104402 (Mar. 2012).
48. Ostler, T. A. *et al.* Ultrafast heating as a sufficient stimulus for magnetization reversal in a ferrimagnet. *Nature Communications* **3**, 666 EP – (Feb. 2012).
49. Radu, I. *et al.* Transient ferromagnetic-like state mediating ultrafast reversal of antiferromagnetically coupled spins. *Nature* **472**, 205–208 (Mar. 2011).
50. El Hadri, M. S. *et al.* Two types of all-optical magnetization switching mechanisms using femtosecond laser pulses. *Physical Review B* **94**, 064412 (Aug. 2016).
51. Gorchon, J. *et al.* Role of electron and phonon temperatures in the helicity-independent all-optical switching of GdFeCo. *Physical Review B* **94**, 184406 (Nov. 2016).
52. Yong, X. *et al.* Ultrafast Magnetization Manipulation Using Single Femtosecond Light and Hot-Electron Pulses. *Advanced Materials* **29**, 1703474 (2017).
53. Kirilyuk, A., Kimel, A. V. & Rasing, T. Laser-induced magnetization dynamics and reversal in ferrimagnetic alloys. *Reports on Progress in Physics* **76**, 026501 (2013).
54. Khorsand, A. R. *et al.* Role of Magnetic Circular Dichroism in All-Optical Magnetic Recording. *Physical Review Letters* **108**, 127205 (Mar. 2012).
55. Alebrand, S. *et al.* Light-induced magnetization reversal of high-anisotropy TbCo alloy films. *Applied Physics Letters* **101**, 162408 (2012).
56. Alebrand, S. *et al.* Subpicosecond magnetization dynamics in TbCo alloys. *Physical Review B* **89**, 144404 (Apr. 2014).
57. Alexander, H. *et al.* Thermally Assisted All-Optical Helicity Dependent Magnetic Switching in Amorphous Fe_{100-x}Tbx Alloy Films. *Advanced Materials* **25**, 3122–3128 (2013).
58. Mangin, S. *et al.* Engineered materials for all-optical helicity-dependent magnetic switching. *Nature Materials* **13**, 286–292 (Feb. 2014).
59. Lalieu, M. L. M., Peeters, M. J. G., Haenen, S. R. R., Lavrijsen, R. & Koopmans, B. Deterministic all-optical switching of synthetic ferrimagnets using single femtosecond laser pulses. *Physical Review B* **96**, 220411 (Dec. 2017).
60. Yang, H., Thiaville, A., Rohart, S., Fert, A. & Chshiev, M. Anatomy of Dzyaloshinskii-Moriya Interaction at Co/Pt Interfaces. *Physical Review Letters* **115**, 267210 (Dec. 2015).
61. Stupakiewicz, A., Szerenos, K., Afanasiev, D., Kirilyuk, A. & Kimel, A. V. Ultrafast non-thermal photo-magnetic recording in a transparent medium. *Nature* **542**, 71–74 (Jan. 2017).
62. Wilson, R. B. *et al.* Ultrafast magnetic switching of GdFeCo with electronic heat currents. *Physical Review B* **95**, 180409 (May 2017).
63. Luttinger, J. M. Theory of the Hall Effect in Ferromagnetic Substances. *Physical Review* **112**, 739–751 (Nov. 1958).
64. Zhang, L. *et al.* L10-ordered FePtAg–C granular thin film for thermally assisted magnetic recording media (invited). *Journal of Applied Physics* **109**, 07B703 (2011).
65. Takahashi, Y. K. *et al.* Accumulative Magnetic Switching of Ultrahigh-Density Recording Media by Circularly Polarized Light. *Physical Review Applied* **6**, 054004 (Nov. 2016).
66. John, R. *et al.* Magnetisation switching of FePt nanoparticle recording medium by femtosecond laser pulses. *Scientific Reports* **7**, 4114 (2017).
67. Medapalli, R. *et al.* Multiscale dynamics of helicity-dependent all-optical magnetization reversal in ferromagnetic Co/Pt multilayers. *Physical Review B* **96**, 224421 (Dec. 2017).
68. Gorchon, J., Yang, Y. & Bokor, J. Model for multishot all-thermal all-optical switching in ferromagnets. *Physical Review B* **94**, 020409 (July 2016).
69. Tsema, Y. *et al.* Helicity and field dependent magnetization dynamics of ferromagnetic Co/Pt multilayers. *Applied Physics Letters* **109**, 072405 (2016).
70. Bergeard, N. *et al.* Hot-Electron-Induced Ultrafast Demagnetization in (Co/Pt) Multilayers. *Physical Review Letters* **117**, 147203 (Sept. 2016).
71. Gorchon, J. *et al.* Single shot ultrafast all optical magnetization switching of ferromagnetic Co/Pt multilayers. *Applied Physics Letters* **111**, 042401 (2017).

72. Vomir, M., Albrecht, M. & Bigot, J. Y. Single shot all optical switching of intrinsic micron size magnetic domains of a Pt/Co/Pt ferromagnetic stack. *Applied Physics Letters* **111**, 242404 (2017).
73. El Hadri, M. S. *et al.* Domain size criterion for the observation of all-optical helicity-dependent switching in magnetic thin films. *Physical Review B* **94**, 064419 (Aug. 2016).
74. Kooy, C. & Enz, U. Experimental and theoretical study of the domain configuration in thin layers of BaFe₁₂O₁₉. *Philips Res. Repts* **15**, 7–29 (1960).
75. Faraday, M. On the magnetization of light and the illumination of magnetic lines of force. *Phil. Trans. R. Soc. Lond.* 104–123 (1846).
76. Van der Ziel, J. P., Pershan, P. S. & Malmstrom, L. D. Optically-Induced Magnetization Resulting from the Inverse Faraday Effect. *Physical Review Letters* **15**, 190–193 (Aug. 1965).
77. Pershan, P. S., van der Ziel, J. P. & Malmstrom, L. D. Theoretical Discussion of the Inverse Faraday Effect, Raman Scattering, and Related Phenomena. *Physical Review* **143**, 574–583 (Mar. 1966).
78. Battiato, M., Barbalinardo, G. & Oppeneer, P. M. Quantum theory of the inverse Faraday effect. *Physical Review B* **89**, 014413 (Jan. 2014).
79. Kimel, A. V. *et al.* Ultrafast non-thermal control of magnetization by instantaneous photo-magnetic pulses. *Nature* **435**, 655–657 (May 2005).
80. Cornelissen, T. D., Córdoba, R. & Koopmans, B. Microscopic model for all optical switching in ferromagnets. *Applied Physics Letters* **108**, 142405 (2016).

Chapter II

Experimental methods and samples

All-optical switching requires not only an ultrashort laser excitation but also a magnetic medium with a thickness typically ranging from few atomic layers to few nanometers. In this chapter II, we will first describe the ultrathin film deposition method I used to grow our samples. Secondly, we introduce the femtosecond laser system used at l'Institut Jean-Lamour (Nancy) to perform the all-optical switching experiments. Moreover, a temporal and spatial characterization of the output laser pulse is provided. Finally, we will give an overview of the quasi-static imaging setup which aims at probing the laser-induced change in magnetization. This microscopy technique relies on magneto-optical effects that we will explain.

1 Thin film deposition and magnetic properties

1.1 DC magnetron sputtering

Examples of ultrathin film deposition techniques include chemical vapor deposition, atomic layer deposition, molecular beam epitaxy, pulsed laser deposition and so forth. In this thesis, to elaborate our samples I used DC Magnetron sputtering, which is a physical vapor deposition technique. The sputtering process involves the ejection of atoms from a pure element material, the target, that are, thereafter, condensing onto a substrate. It is built upon the formation of a plasma made of inert gas ions such as Ar^+ . Hence, a high vacuum is needed. A rarefied Ar gas is introduced in a vacuum chamber. Then, to create the plasma a high voltage is applied between the target and the substrate that serves as the ground. The Ar^+ ions are accelerated in the glow tube and bombard the target material at the cathode. By energy and momentum transfer, target atoms are ejected in the form of neutral particles that can be atoms, cluster of atoms or molecules. These neutral particles isotropically travel in the vacuum space in straight lines. Those reaching the substrate starts condensing and binding to each other, thus progressively forming atomic layers. The bombardment of the incident ion can engender the emission of electrons, which will entertain the electrical discharge. Indeed, the released electrons collide subsequently with Ar atoms that are ionized, participating therefore at maintaining the plasma. Besides, a DC voltage is used to bombard a conductive target, for a semiconductor or an insulator a RF power is required.

However, two main issues with standard DC sputtering may be pointed out. Indeed, the deposition velocity (nm s^{-1}) is very low compared to other techniques. This is mainly due to a low ionization rate in the vacuum chamber. Additionally, the highly thermalized sputtered atoms lead to the growth of a porous film. A solution is to use a magnetron discharge by adding a magnetic field in the vicinity of the target, which increases the plasma density. As shown in Fig. II.1, two magnets of opposite polarity are placed underneath the target. The resulting

magnetic field is parallel to the target surface and orthogonal to the electric field applied to ionize Ar atoms. Furthermore, the magnetic field lines trap the secondary electrons released during the bombardment. Considering the Lorentz force acting on these electrons, emerging from the magnetic field B and the electric field E , the magnetron drift velocity E/B is perpendicular to both fields. It results a helicoidal flow of the electrons around the magnetic field lines. Therefore, electrons travel over longer distances, which increases the probability of ionizing collisions with Ar atoms. Thus, it emerges a local enhancement of the plasma density and stability near the target surface. Consequently, the deposition rate is substantially increased and the quality of the film improved. In this thesis, all the samples were grown by DC Magnetron sputtering with an Orion system from AJA International. It provides a film uniformity better than $\pm 2\%$ for a 4" wafer. As we used a 1" \times 0.8" glass substrate placed in the center of the substrate holder, we expect an even better uniformity of the film coating. Ar is used as for the sputter gas with a 50 SCCM flow. The main chamber pressure is usually around 5×10^{-8} Torr. All the depositions were performed at room temperature, although it was proved that sputtering at higher temperatures increases the film quality. Our system can work up to 850°C. Initially, to create the plasma, we set the Ar pressure at 60 mTorr, while during the deposition we used a pressure of 3 mTorr. In addition, to ensure good film uniformity, we employed a rotating stage at 40 rpm. The deposition rates, priorly calibrated, were about $\sim 0.5 \text{ \AA s}^{-1}$ depending on the target and input power.

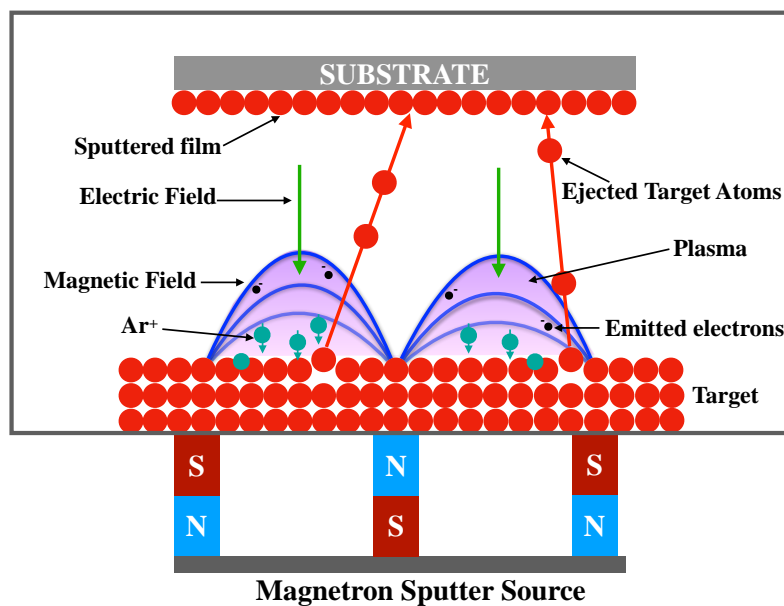


FIGURE II.1: Schematic representation of DC Magnetron sputtering process.

1.2 Magnetic characterization

Magnetometry

In order to characterize the magnetic properties of the deposited samples, I utilized two different techniques, based on, respectively, a vibrating sample magnetometer (VSM) and magneto-optical Kerr effect (MOKE) microscope. Here, we will describe only the VSM as further in section 3, we will discuss more into details magneto-optical effects. Vibrating sample magnetometry was first developed by Foner in 1959 [1]. The measurement is accomplished by oscillating the sample within an uniform magnetic field, which hence induces a voltage that is

detected by a pickup (sensing) coil. A magnetic field of up to 3 T is generated using conventional electromagnets, or up to 16 T with superconducting magnets.

In this thesis, we operated a VSM head mounted on a physical property measurement system (PPMS) from Quantum Design, Inc. PPMS allows magnetometry measurements over a wide range of temperature from 1.9 K to 400 K. Relying on a compact gradiometer pickup coil configuration in the VSM, relatively large oscillation amplitudes of 1 - 3 mm (peak value) at a frequency of 40 Hz can be measured. In addition, the sensing coils are able to resolve magnetization changes of $\sim 10^{-6}$ emu. Therefore, this technique is not suitable for weakly magnetized sample. For this purpose, our lab is equipped with a SQUID-VSM that is based on a superconducting quantum interference device. These sensors have a much higher magnetization sensitivity of theoretically 10^{-12} and practically of 10^{-8} emu. However, the ferromagnetic Co/Pt multilayers we studied in this thesis have a magnetic moment $m \geq 10^{-6}$ emu. Thus, the PPMS-VSM provided a sufficient resolution. Finally, the VSM head is designed to measure a maximum magnetic moment of 40 emu per peak oscillation amplitude. It is important to mention that VSM gives an open loop measurement as the sample magnetization and field source do not establish a closed flux line loop. In fact, due to the demagnetizing field, the magnetic field experienced by the sample differs from the applied field. Consequently, a correcting factor must be implemented in the processed data in order to obtain the intrinsic magnetic properties. Moreover, one should take into account the diamagnetism induced by the substrate, especially at high applied fields. Fig. II.2 shows an example of a hysteresis MH loop for two Co/Pt samples. The diamagnetic contribution from the substrate has been subtracted for the plotted data.

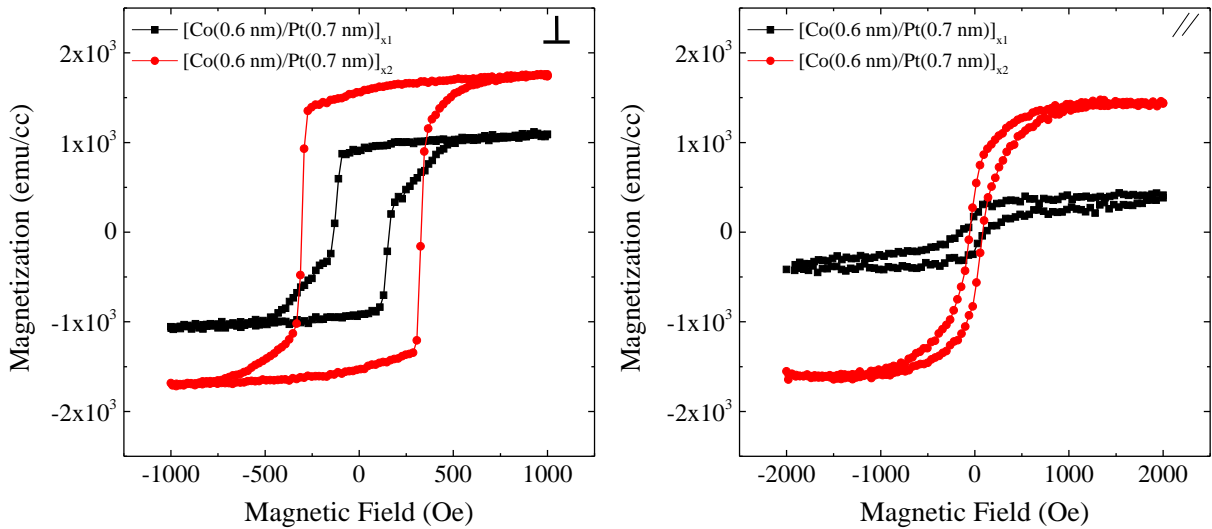


FIGURE II.2: Out-of-plane (left) and in-plane (right) $M(H)$ loops for Ta(5 nm)/Pt(4.5 nm)/[Co(0.6 nm)/Pt(0.7 nm)]_N/Pt(3.8 nm) with $N = 1$ or 2. (Co/Pt) bilayer system presents a stronger PMA than (Co/Pt) single layer. Hysteresis loops obtained by PPMS-VSM measurement. In both configurations, out-of-plane and in-plane, the substrate diamagnetic contribution has been subtracted to the plotted data.

Magnetic properties of the samples

Our research study focused on ferromagnetic materials, and more specifically Co/Pt multilayers. Not only much progress has been made over the past few years in the understanding of the mechanisms of HD-AOS in Co/Pt [2–5], but also these materials exhibit interesting features for perpendicular high density magnetic recording [6]. Indeed, it was discovered that ultrathin

multi-stack of Co/Pt had strong perpendicular magnetic anisotropy (PMA) for a Co thickness typically $\lesssim 1$ nm [7] (see. Fig. II.3). This large PMA was attributed to interfacial anisotropy, crystallographic orientation of buffer layers and magnetoelastic strain [8–10]. It was found also that interfacial hybridation between the magnetic and non-magnetic metal played an important role in establishing PMA [11–13]. In addition, magnetic polarization of the Pt layer by the Co was evidenced [14], which contributes to the large Kerr rotation observed in Co/Pt multilayers (MLs). To ensure strong PMA in Co/Pt MLs, one or more buffer layers are needed in order to create the (111) crystallographic texture [15, 16]. Pt and Ta are the most common layers used for that purpose (see refs. therein [17]). A Co/Pt ML grown on a Ta oxide exhibited a larger PMA than on Pt [17]. Furthermore, the influence of the nature of the buffer layer and the Pt interlayer thickness on the magnetic properties of (Co/Pt) MLs was studied [7]. It revealed that the effective anisotropy increased with the Pt thickness, simultaneously with a decrease of the roughness. The saturation magnetization of these structures was significantly enhanced in the case of intermixed Pt/Co interfaces. As a result, the standard ferromagnetic stack we grew is the following: Ta(5 nm)/Pt(4.5 nm)/[(Co(0.6 nm)/Pt(0.7 nm)]_N/Pt(3.8 nm) sputtered on a 0.5 mm-thick glass substrate with N (Co/Pt) repetitions. The Ta(5 nm)/Pt(4.5 nm) layer ensures therefore the crystallographic texture (111) and thus the PMA, while the Pt capping prevents the sample from oxidation. Occasionally, the thickness of the different layers were modified. As shown in Fig. II.2, when increasing the number of repeats N, the PMA is accentuated, although a small in-plane component can be observed.

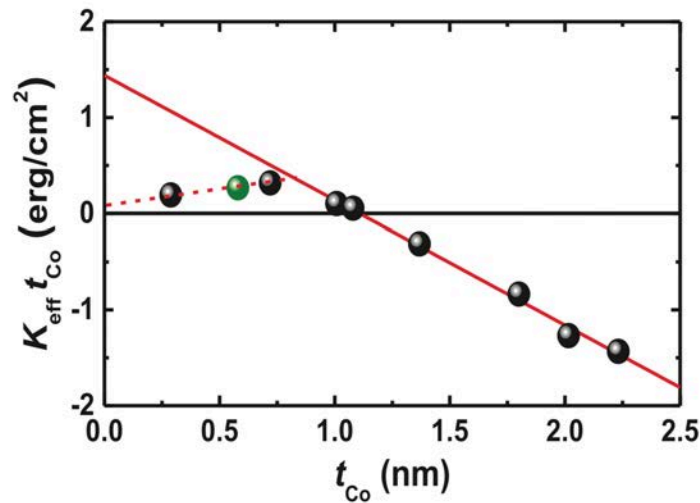


FIGURE II.3: (a) Room temperature effective anisotropy multiplied by the Co thickness as a function of Co thickness t_{Co} in Ta(5)/Pt(5)/[Co(t_{Co})/Pt(1.8)]₄/Pt(5). The dashed and solid lines correspond to linear fit for below and above $t_{Co} = 0.75$ nm, respectively. Figure adapted from [7].

Besides, HD-AOS in ferromagnetic (Co/Pt) MLs involves the use of ultrashort circularly polarized laser pulses, thus bringing not only heat but also angular momentum to the system. Many studies have mentioned the importance of reaching a high out-of-equilibrium state upon laser irradiation in order to induce magnetization reversal in ferrimagnetic GdFeCo and TbCo alloys [18–20] and in ferromagnetic FePt and CoPt [3, 21], therefore highlighting the influence of laser heating. As a result, it is essential to take into account the temperature dependence of magnetic properties of our samples. These studies suggested that a laser heating close to the Curie temperature T_C eases AOS. Fig. II.4 shows the evolution of magnetization versus temperature as a function of Co thickness (a) and Pt buffer thickness (b) for Pt/Co/Pt sputtered on Ta, a similar system than the one we studied in this thesis [22]. Decreasing the Co thickness

causes a dramatic drop of T_C . It even falls below room temperature for a Co thickness ≤ 0.44 nm. For our studied structures Pt(4.5)/Co(0.6)/Pt(4.5), T_C is often extrapolated to be about ~ 650 K, compared to the value of bulk Co $T_C = 1400$ K (as found in handbooks). This can be attributed to the intermixing of Co and Pt. Indeed, reducing the Pt buffer thickness, therefore increasing the intermixing, leads also to a decline of T_C . Hence, the temperature dependence of saturation magnetization has to be adequately monitored when engineering ferromagnetic materials for HD-AOS, as T_C is tunable in (Co/Pt) MLs.

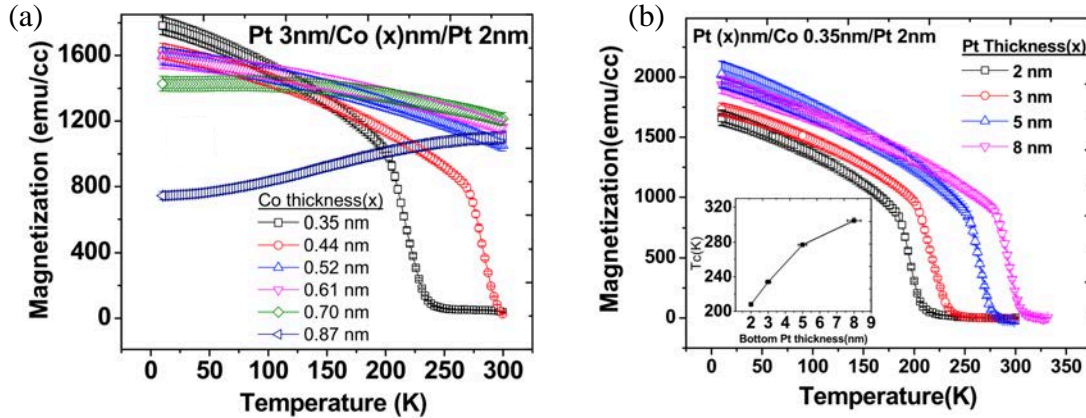


FIGURE II.4: Temperature dependence of saturation magnetization as a function of (a) Co thickness and (b) Pt buffer thickness. Figure adapted from [22].

2 Generation of ultrashort laser pulses

A key element in all-optical switching is to use ultrashort laser pulses of duration in the femtosecond range (up to few picoseconds) and of high-energy (\sim mJ). If the laser pulse duration is too long, the system remains at equilibrium. Indeed, in the first attempts of laser-induced magnetization manipulation in Ni and Fe, a laser pulse duration in the range of tens of ps to ns was used, and no magnetization change was observed [23, 24]. Conversely, Beaurepaire *et al.* were able to induce ultrafast demagnetization in Ni films with 60 fs laser pulses [25]. In this section 2, we will present the femtosecond laser system with which we performed the all-optical switching experiments and how ultrashort laser pulses are generated. A femtosecond laser source is composed of an oscillator that produces ultrashort pulse trains, and of an amplifier to increase the laser pulse energy. At l'Institut Jean-Lamour, we use a femtosecond Ti:sapphire laser commercialized by Coherent Inc.

2.1 Femtosecond laser oscillator

It was in 1986 that the first Ti:sapphire laser was built by Moulton [26]. Ti:sapphire oscillators are the most-widely used ultrafast lasers, for it has the widest tuning range from 680 nm to 1130 nm. It can generate laser pulses shorter than 5 fs. A Sapphire crystal doped with Titanium ions (Ti^{+3}) absorbs over a broad range of wavelength from 400 to 600 nm. That is why it is typically pumped by Nd:YAG lasers. As the absorption and emission bands overlap with the short wavelength end of the emission spectrum, it can therefore operate only at wavelength longer than 660 nm. Ultrashort laser pulses are the result of the so-called Kerr-lens mode-locking (KLM). First, a Gaussian seed beam, which is a continuous wave radiation, propagates through the Ti:sapphire, which is a nonlinear optical medium. Moreover, for such material it is known

that the refractive index varies with intensity. Considering the Gaussian distribution of the beam intensity, the refractive index changes along the laser beam diameter. Thus, the central part of the beam with higher intensity experiences a larger refractive index than at the edge. This leads to the self-focusing phenomenon of the beam, also called Kerr lens effect. In its usual regime, the laser oscillates over all the resonance frequencies of the cavity, which constitute the longitudinal modes of the laser. Due to the Kerr lens effect, the modes are forced to have an equal phase (i.e. mode-locking). Hence, all the electromagnetic waves will constructively add leading to a very intense short pulse. Finally, an aperture smaller than the seed beam diameter will allow only the shortest and most intense pulses go through. As a result, the Ti:sapphire laser is mode-locked and in a pulsed mode.

2.2 Femtosecond laser amplification

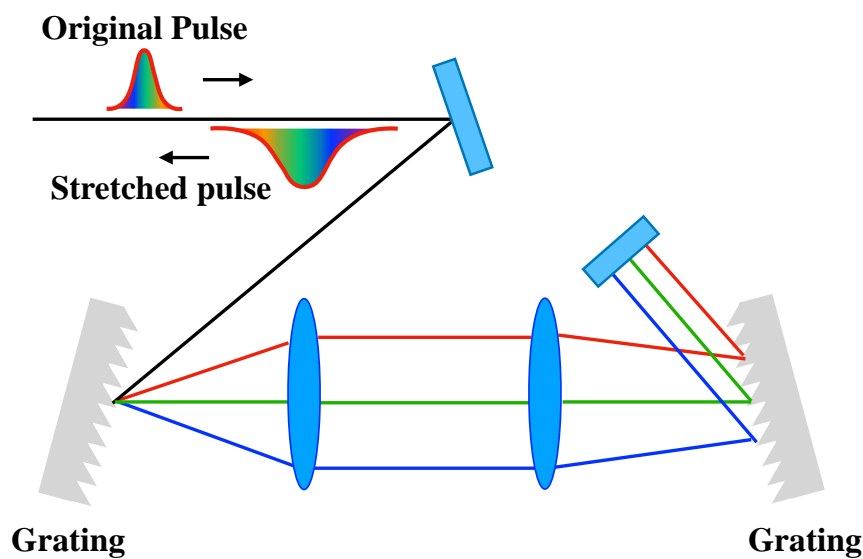


FIGURE II.5: Illustration of the stretching process of the input pulse (~ 10 fs) with a pair of gratings.

In order to generate laser pulses with a high peak power, amplification of the oscillator beam is required. In femtosecond laser sources, the chirped pulse amplification (CPA) method is often used, which was introduced by Strickland *et al.* [27]. The amplification process is achieved in a gain medium, which is, here, another Ti:sapphire crystal. Initially, the amplifier is pumped with the femtosecond oscillator beam, which serves as a seed beam. To avoid the damage of the gain medium by the high intensities of the seed pulses, it is necessary to reduce their peak power. In CPA, this is performed by stretching out the laser pulse via diffraction gratings. These gratings expand the spectrum of the incident laser beam in a such way that the low-frequency components travel a shorter path than the high frequencies as depicted in Fig. II.5. As a result, a negative dispersion is introduced and the pulse duration is increased by a factor of 10^3 to 10^5 . Thence, the stretched pulse can be safely amplified by at least 6 orders of magnitude via a regenerative amplifier. In the regenerative amplification technique illustrated in Fig. II.6, the stretched pulse to amplify is trapped in a laser cavity. The pulse is maintained in the resonator until all the energy stored in the Ti:sapphire is extracted. The latter is made possible by the use of Pockels cell and a broad-band thin film polarizer. By applying a voltage on the Pockels cell, which consists of a birefringent crystal, the light polarization can be changed. At first, the Pockels cell behaves as a quarter-wave plate. When the laser pulse is sent into the cavity, the voltage is turned on and the Pockels cell acts as a half-wave plate. Consequently, the

pulse is kept inside the resonator. Once it reaches saturation, a second voltage is applied to the Pockels cell and the amplified laser pulse is released.

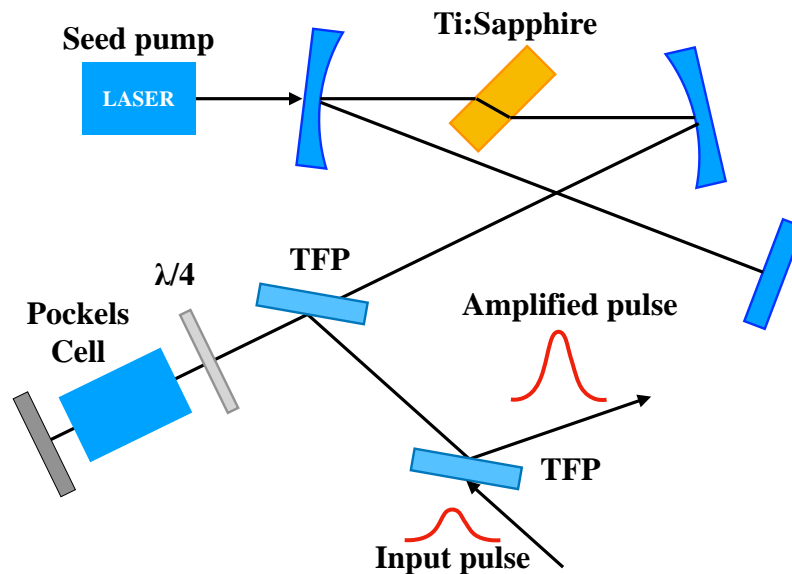


FIGURE II.6: Schematic representation of the regenerative amplification. TFP: thin film polarizer. $\lambda/4$ quarter-wave plate.

The final step is the recompression of the laser pulse to a much shorter duration through the reversal process of the aforementioned stretcher. The pulse compressor is composed of a pair of gratings that induces a positive dispersion as shown in Fig. II.7. Therefore, the high-frequency component travels a shorter path as opposed to the stretcher. The width of the restored short pulse is tuned by the distance of the gratings in the compressor. Thusly, an ultrashort laser pulse of high energy is achieved.

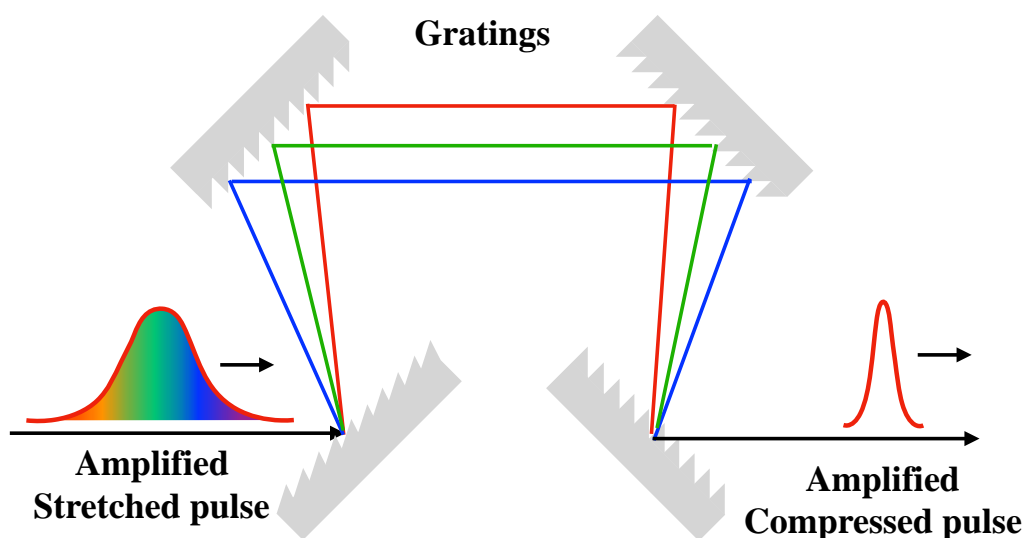


FIGURE II.7: Illustration of the compression process with two pairs of gratings. The output pulse is amplified (8W, 5 kHz) and with a restored short width ~ 35 fs.

At l'Institut Jean-Lamour, the femtosecond laser system consists of a Vitera Ti:sapphire oscillator developed by Coherent Inc., which relies on a conventional KLM. It is pumped by a Verdi-G laser, which is a semiconductor laser. The oscillator provides laser pulses of a duration shorter

than 10 fs and a repetition rate of 80 MHz for a central wavelength of 800 nm. The maximum output power is greater than 500 mW. The CPA method is performed in a Legend Elite ultrafast Ti:sapphire amplifier that delivers laser pulses of up to 8 W, 5 kHz and with a pulse width of ~ 40 fs. Additionally, a pulse picker combined with a pair of gratings allows us to select a finite number of laser pulses and also to tune the pulse duration up to few picoseconds. Moreover, the pulse width is measured with an autocorrelator (PulseCheck by A.P.E Berlin) that covers a wide range of durations from 10 fs to 400 ps. Finally, the wavelength of the laser beam can be changed using the TOPAS-prime from Coherent Inc. This optical parametric amplifier (OPA) enables varying the wavelength from 190 nm to 1200 nm. Nonetheless, the OPA requires ultrashort incoming laser pulses of ~ 35 fs. Therefore, the tuning of the wavelength cannot be simultaneously performed with the tuning of the pulse width. In this thesis, we rather took the pulse duration as a parameter and fixed the wavelength at 800 nm.

2.3 Measurement of temporal and spatial laser profile

As we mentioned, we used an autocorrelator developed by A.P.E Berlin in order to precisely measure the temporal profile of the laser beam and deduce the pulse width. Here, we will explain the principle of autocorrelation. To measure an event in time, it must be probed by an even shorter one. However, this cannot be possible for ultrashort laser pulses. For a pulse width greater than 20 ps, it can be directly measured using high speed photo-detectors. To solve this issue, the laser pulse is used to measure itself. This is the autocorrelation method. The pulse is split in two and a delay τ is introduced between the two beams. The two pulses are further focused into a nonlinear optical crystal, often a second-harmonic generation (SHG) crystal as depicted in Fig. II.8(a). In the intensity autocorrelation, the two beams are non-collinearly overlapped on the crystal. The SHG medium will produce an electric field $E^{(2)}$ with twice the frequency 2ω of the input pulse. The induced polarization by the crystal is therefore a convolution of the two interfering electric fields:

$$E^{(2)}(t) \propto E(t) \cdot E(t - \tau) \quad (2.1)$$

The autocorrelated intensity I_{AC} is proportional to the product of the intensities of the two incoming pulses, and is averaged over time since the photo-detector cannot resolve the beam in time:

$$I_{AC}(\tau) \propto \int_{-\infty}^{+\infty} I(t) \cdot I(t - \tau) dt \quad (2.2)$$

where $I(t) = |A(t)|^2$ with $A(t)$ being the complex envelope of the input pulse. After deconvolution of the intensity autocorrelation function, the full-width half-maximum (FWHM) of the autocorrelated signal τ_{AC} can be related to the laser pulse width τ_p . For a Gaussian input pulse, $\frac{\tau_p}{\tau_{AC}} = 0.7071$. However, few limitations of the intensity autocorrelation method can be pointed out. First, the autocorrelated width is highly dependent on the shape of the pulse, if it is e.g. a Sech^2 , Gaussian or Lorentz pulse. Moreover, this technique tends to wash out the structure of complex intensities, and for instance satellite pulses will not appear in the autocorrelated signal. Finally, the intensity autocorrelation does not provide full information about the electric field of the pulse, for in the time-domain the pulse phase is lost. This corresponds to the 1D phase-retrieval problem that cannot be mathematically solved.

In order to characterize a pulse width and simultaneously obtain some information about the pulse phase, an interferometric autocorrelation method can be implemented [28]. Unlike for

the intensity autocorrelation, the two pulses are sent collinearly into the SHG crystal as shown in Fig. II.8(b). A filter is added in order to detect only the second harmonic component. This autocorrelation method is based on the Michelson interferometer and the total electric field $E(t + \tau)$ can be written as follows:

$$\begin{aligned} E(t, \tau) &= E(t + \tau) + E(t) \\ &= A(t + \tau)e^{j\omega_c(t+\tau)}e^{j\Phi_{CE}} + A(t)e^{j\omega_c t}e^{j\Phi_{CE}} \end{aligned} \quad (2.3)$$

where ω_c is the carrier frequency and Φ_{CE} the carrier-envelope phase. Additionally, the second harmonic signal is proportional to the square of the total electric field. Thus, the interferometric autocorrelation intensity $I_{iAC}(\tau)$ is defined as:

$$I_{iAC}(\tau) \propto \int_{-\infty}^{+\infty} |(A(t + \tau)e^{j\omega_c(t+\tau)} + A(t)e^{j\omega_c t})^2|^2 dt \quad (2.4)$$

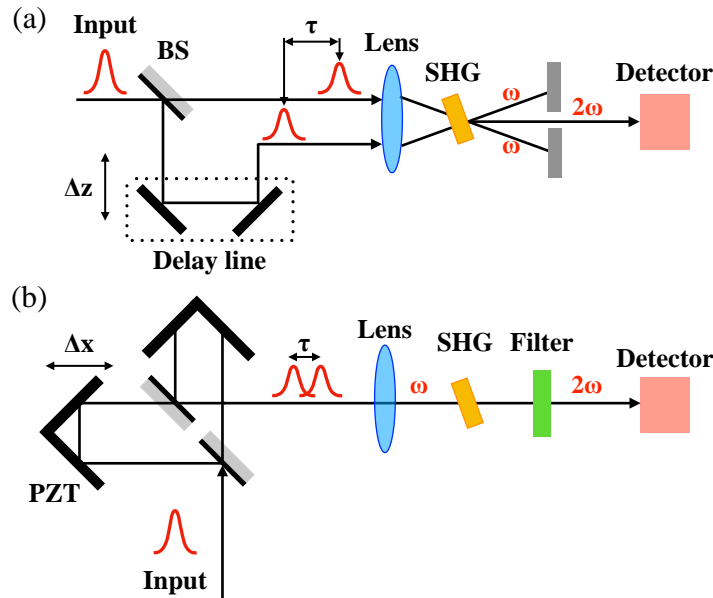


FIGURE II.8: Schematic representations of (a) intensity and (b) interferometric autocorrelation methods. (a) A beam-splitter (BS) divides the input laser pulse into two pulses. A delay stage introduces a variable (Δz) delay τ between the two beams that non-collinearly focused onto a second-harmonic generation (SHG) crystal. The first harmonic is blocked by a screen, and only the second harmonic reaches the detector. (b) The delay stage uses a piezoelectric translator (PZT) in order to delay a pulse with respect the other and collinearly focus them onto the SHG crystal. A filter is added to cut the first harmonic.

Then, $I_{iAC}(\tau)$ can be decomposed into a sum of four intensities: the background signal, the intensity autocorrelation, the interferogram of the input field (coherence term oscillating at ω_c) and the interferogram of the second harmonic (coherence term oscillating at $2\omega_c$). It is important to note that the latter is true only if the two laser beam paths are strictly identical. To compensate potential dispersion and phase shifting when the pulses go through optics, the delay line must be accordingly adjusted. At zero time delay $\tau = 0$, the four intensities are the same. This gives a system of 3 conditions that I_{iAC} must meet:

$$\begin{aligned}
I_{iAC}(\tau)|_{max} &= I_{iAC}(0) = 8 \\
\lim_{\tau \rightarrow \pm\infty} I_{iAC} &= 1 \\
I_{iAC}|_{min} &\rightarrow 0
\end{aligned}
\tag{2.5}$$

From these equations, the fringes at ω_c and $2\omega_c$ can be solved. This gives access to the coherence time that provides information about the pulse phase. Nevertheless, the phase still cannot be totally resolved. Moreover, if Eq. 2.5 is verified, then proper alignment in the autocorrelator is achieved. In this thesis, we emphasize the fact that if the laser pulse duration was changed, the pulse width was measured accordingly to the methods we just described. However, one must be aware of the limits and ambiguities of such technique. Yet, it yields a descent estimation of the pulse width. Fig. II.9(a) shows the standard temporal laser profile we used for the all-optical switching experiments. The gratings in the pulse-picker are arranged so that the shortest laser pulse width is approximately $\sim 35 - 40$ fs. Unless specified otherwise, the laser duration was set to this value. To estimate the spatial profile of the laser beam, we used density filters and a CCD camera. Optics were set in such a way that the FWHM of the laser beam was about $50 - 60 \mu\text{m}$ as depicted in Fig. II.9(b). Notably, this is not the most accurate technique to obtain the spatial profile of the laser beam. Still, it provides a fast and efficient way to control the size of the laser spot when changing the focusing. We mention that e.g. knife-edge laser beam profiling gives a high spatial resolution [29]

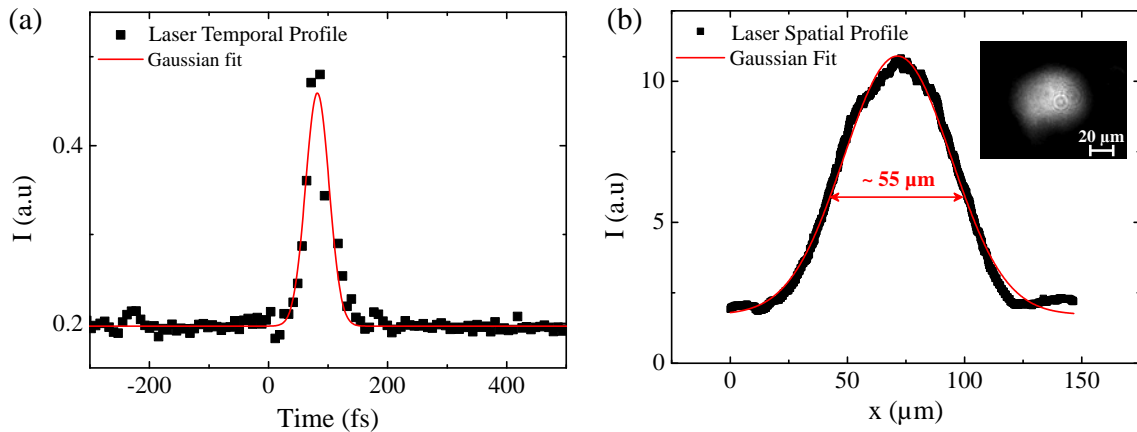


FIGURE II.9: Examples for temporal (a) and spatial (b) profiles of the laser beam we used in the HD-AOS experiments. (a) The iAC technique yields a FWHM of about 47 fs, taking into account the deconvolution factor, the laser pulse width is ~ 33 fs. (b) The laser beam spatial profile is plotted and fitted with a Gaussian distribution of FWHM $\sim 55 \mu\text{m}$. The inset shows the image recorded with a CCD camera.

3 Magneto-optical microscopy technique

There are several methods to characterize and measure the magnetic properties of a material. Examples include, as we previously reported, VSM and SQUID, but also magnetic force microscopy [30] or nuclear magnetic resonance spectroscopy [31, 32] among many others. However, to probe the effect of all-optical switching, a non-destructive method must be implemented (i.e. that conserves the magnetic moment). The latter can be obtained via magneto-optical (MO) techniques. In this section, we will give brief theoretical considerations of MO

effects, and more specifically of the Faraday effect and its corollary the Kerr effect. Then, we will introduce the MO microscopy technique used to probe all-optical switching.

3.1 Magneto-optical Faraday and Kerr effects

Introduction

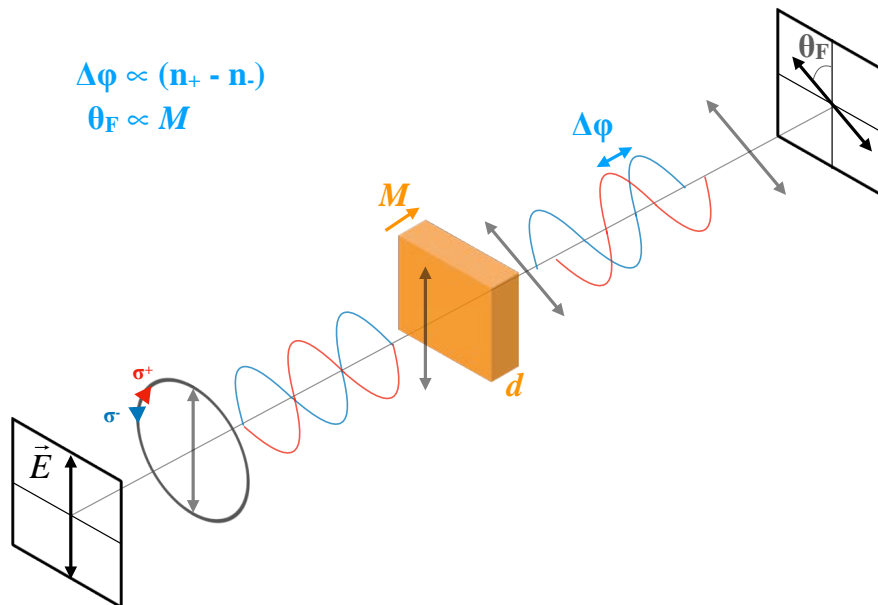


FIGURE II.10: Schematic illustration of the Faraday rotation when linearly polarized (LP) light \vec{E} is transmitted through a magnetic material with an out-of-plane magnetization M parallel to the direction of propagation of the electric field. Linear polarization can be decomposed as a sum of two circularly polarized (CP) waves (σ^+ and σ^-). Projections of both waves in the light wave vector plane is depicted (blue and red curves). The magnetic material due to MCB induces a phase difference $\Delta\phi$ between the CP waves.

Interactions between light and magnetism can lead to a change of the frequency or the polarization state of light. The first MO effect was observed by Faraday in 1845 [33]. It was found that the electric field of linearly polarized light is rotated upon transmission of a non-dissipative material exposed to a magnetic field parallel to the propagation direction of light. This phenomenon was called Faraday effect. The Faraday rotation is illustrated in Fig. II.10 and is demonstrated to be proportional to the magnetic field. About 30 years later, the same phenomenon was observed when light is reflected on the surface of a magnetized sample: this is the magneto-optical Kerr effect (MOKE) [34]. Ever since, many other MO effects had been reported, e.g. the Zeeman, Voigt and Cotton-Mouton effects [35]. Remarkably, MO effects result from the magnetic ordering of a material that can be either induced by an external magnetic field or intrinsic such as ferromagnetism. The Faraday and Kerr effects were first evidenced in experiments using light in the visible spectrum. More recently, these effects were also observed in the X-Ray regime along with X-Ray magnetic circular dichroism (XMCD) and X-Ray magnetic linear dichroism (XMLD) spectroscopy. This had tremendously broadened the scope of MO effects. Not only does it provide a new way to characterize saturation magnetization, the coercivity, the Curie temperature, but also element-specific probing of magnetization dynamics and element-specific imaging of domain patterns in complex magnetic media relying on the tunability of X-Rays.

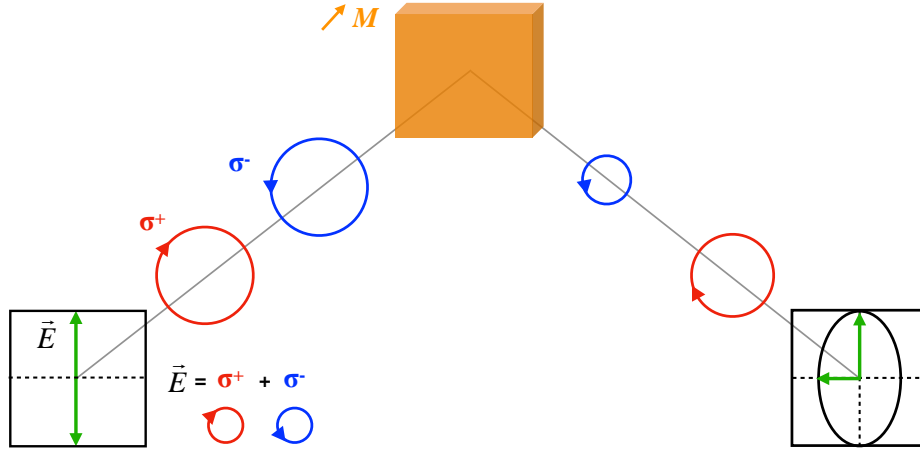


FIGURE II.11: Illustration of the principle of magnetic circular dichroism (MCD). LP light is decomposed as a sum of left- and right- circular polarizations. The two CP waves experience different absorption upon transmission or reflection on a magnetic material. Thus, they have different amplitudes after interaction with the magnetic medium leading to an elliptical wave. MCB and MCD effects can be combined resulting in an elliptical field with the major axis rotated with respect to the initial polarization axis of \vec{E} .

Theory of Faraday and Kerr effects

Faraday and Kerr effects share the same microscopic origin, which lies in magnetic circular birefringence (MCB). Indeed, linearly polarized light can be seen as a combination of left- (σ^-) and right- (σ^+) circular polarizations. These two modes experience different refractive indices upon reflection or transmission of a magnetic material. From this, a phase difference appears between the two corresponding electric fields leading to the rotation θ of the polarization vector of linearly polarized light (see. Fig. II.10). In addition, magnetic circular dichroism (MCD), that is the difference in light absorption between left- and right- circular polarizations, must be also considered. Therefore, the two vectorial components of linear polarization after transmission or reflection have different amplitudes. Hence, the incident linearly polarized light becomes elliptical as depicted in Fig. II.11. Notably, MCB and MCD may co-exist at the same time. As a result, information about the magnetic properties can also be extracted from the ellipticity ϵ .

The macroscopic description of MO effect is based on the complex dielectric tensor $\tilde{\epsilon}$ derived from Maxwell equations. Assuming an anisotropic medium with a magnetization along the z-axis, parallel to the light propagation direction, $\tilde{\epsilon}$ satisfies Onsager symmetry relation, i.e. $\epsilon_{ij}(M) = \epsilon_{ji}(-M)$, and can be defined as:

$$\tilde{\epsilon} = \epsilon_0 \begin{pmatrix} \epsilon_{xx} & \epsilon_{xy} & 0 \\ -\epsilon_{xy} & \epsilon_{xx} & 0 \\ 0 & 0 & \epsilon_{zz} \end{pmatrix} \quad (3.1)$$

Since the linearly polarized light propagates along the z-axis, $\vec{E} = \begin{pmatrix} E_x \\ E_y \\ 0 \end{pmatrix}$, a transformation of coordinates can be operated which brings the tensor in 2 dimensions. Moreover, some specific polarizations of the light are not altered by the magnetization. These modes correspond to the eigenvectors of $\tilde{\epsilon}$ and are obtained from:

$$\vec{D} = \epsilon_0 \begin{pmatrix} \epsilon_{xx} & \epsilon_{xy} & 0 \\ -\epsilon_{xy} & \epsilon_{xx} & 0 \\ 0 & 0 & \epsilon_{zz} \end{pmatrix} \begin{pmatrix} E_x \\ E_y \\ 0 \end{pmatrix} = \tilde{n}^2 \vec{E} \quad (3.2)$$

where \vec{D} is the displacement vector, $\tilde{n}^2(\omega) = \tilde{\epsilon}(\omega)$ and ϵ_0 the vacuum permeability. It is found that the eigenvectors are circularly polarized (CP) waves with the following eigenvalues, \tilde{n}_+ and \tilde{n}_- , being the complex refractive indices of σ^+ and σ^- , respectively:

$$\tilde{n}_{\pm} = \sqrt{\epsilon_0(\epsilon_{xx} \pm i\epsilon_{xy})} \quad (3.3)$$

It is clear now that the polarization of CP light remains unchanged by the magnetization, but the refractive index experienced by the medium depends upon the chirality of light. Thence, the difference in velocity of σ^+ and σ^- electric fields leads to a phase difference giving rise to the Faraday and Kerr effects that can be expressed according to Eq. 3.3. Thus, it yields the complex Faraday rotation $\Phi_F = \theta_F + i\epsilon_F$, with θ_F the Faraday rotation angle and ϵ_F the Faraday ellipticity [36]:

$$\begin{aligned} \Phi_F &= \frac{\omega d}{2c} (\tilde{n}_+ - \tilde{n}_-) \\ \Phi_F &\simeq \frac{\epsilon_{xy}}{\sqrt{\epsilon_{xx}(\epsilon_{xy} - 1)}} \end{aligned} \quad (3.4)$$

where ω and c are the light frequency and celerity, d the material thickness, and assuming that $|\epsilon_{xx}| \gg |\epsilon_{xy}|$. Similarly, the complex Kerr rotation can be written as $\Phi_K = \theta_K + i\epsilon_K$, with θ_K and ϵ_K the Kerr rotation angle and ellipticity, respectively [36]:

$$\Phi_K \simeq \frac{\sqrt{\tilde{n}_+} - \sqrt{\tilde{n}_-}}{\sqrt{\tilde{n}_+ \tilde{n}_-} - 1} \quad (3.5)$$

From the linear dependence of the complex Faraday rotation angle Φ_F on the complex refractive index in Eq. 3.4, it appears that the real and imaginary parts of Φ_F are connected via Kramers-Kronig relations [37]. However, this is not the case with the Kerr angle. Importantly, this theoretical framework is verified for a cubic magnetic medium with the magnetization pointing along one of the cubic axes or along the [111] direction. Yet, it is still true for hexagonal and tetragonal systems if the magnetization lies along the c-axis.

Moreover, it is apparent now that the asymmetry in the real part of the complex Faraday angle in Eq. 3.4 gives rise to the Faraday rotation θ_F . Therefore, MCB is related to the real part of the off-diagonal term of the dielectric tensor. Conversely, the asymmetry in the imaginary part of the Faraday angle yields the ellipticity ϵ . Thus, the imaginary part of the off-diagonal term of $\tilde{\epsilon}$ is responsible for the MCD. As a result, it becomes straightforward that MO effects are a direct consequence of the presence of non-diagonal terms in $\tilde{\epsilon}$ (Eq. 3.1). Finally, the linear dependence of θ_F on the out-of-plane magnetization has been demonstrated (see ref. therein [38]) with the factor of proportionality corresponding to the wavelength-dependent magneto-optical susceptibility. In the case of a magnetization induced by an external field B , it is simply expressed with the Verdet constant V : $\theta_F = VBd$. Nevertheless, such a clear dependence on M_z is not possible for θ_K as seen in Eq. 3.5. Lastly, it was proved that spin-orbit coupling was responsible for MOKE in ferromagnetic materials [39]. Interestingly, a connection can then be

made between MOKE and the magneto-crystalline anisotropy as they share the same origin [40].

Magneto-optical effects are thus a powerful tool to probe the magnetization of a material, even for ultrafast magnetization dynamics. Indeed, the pioneering discoveries of ultrafast demagnetization and magnetization switching in Ni and GdFeCo, respectively, by ultrashort laser pulses relied on time-resolved MOKE measurements [25, 41]. Yet, unlike for the VSM or SQUID, in most cases it cannot lead to precise quantification of M . Since in all-optical switching we are interested only in the change in magnetization induced by the laser irradiation, this is not an issue for our experiments. Furthermore, the relative orientation of M with respect to the normal of the light's plane of incidence strongly influences the magneto-optical contrast. 3 configurations are distinguished. The polar configuration corresponds to an out-of-plane magnetization lying in the light's plane. The theoretical discussion we conducted was for the polar Faraday and Kerr effects. The two others are longitudinal and transverse configurations for which the magnetization is in-plane. Due to the symmetry of ferromagnetic systems, the polar configuration leads to the largest MO contrast. Hence, in this thesis, we used this geometry to probe the magnetization in all-optical switching experiments and measure the hysteresis loops with a commercial MOKE microscope.

3.2 Experimental magneto-optical microscope for all-optical switching

Most experiments presented in this research project were performed with a quasi-static magneto-optical imaging setup depicted in Fig. II.12. It is composed of three main parts: the laser beam pump, a probe and a microscope objective combined with a CCD camera. The laser beam output from the system we describe in section 2 has a 5 kHz repetition rate and a central wavelength of 800 nm. It goes through several optics, namely a Glan-Taylor polarizer, a half-wave plate, a quarter-wave plate and a convex lens before reaching the sample surface. The laser pulse is linearly polarized after the Glan-Taylor polarizer. The quarter-wave plate ($\lambda/4$) introduces a phase delay of $\pm \pi/2$, which allows us to obtain left- or -right- circular polarization. On the other hand, the half-wave plate ($\lambda/2$) induces a phase difference of π which enables us to change the laser power. The convex lens focuses the laser beam onto the sample surface to a spot size of $\sim 50 \mu\text{m}$. Note that one can displace the lens in order to modify the beam spot size, which in addition to the half-wave plate allows tuning of the laser fluence over a large range of values. Additionally, the laser pulse duration can be changed by stretching or compressing the pair of gratings in the pulse picker. The laser frequency and how many laser pulses are sent to excite the material can also be chosen with the pulse picker.

The optical response to fs-laser pulse irradiation of ferromagnetic materials is probed with a magneto-optical imaging microscope which combines a source of light (the probe) and a pair of polarizer-analyzer. The probe light is emitted from a 680-nm monochromatic high intensity LED and is linearly polarized. The polarizer and analyser are crossed in a such way that in absence of sample, a full extinction can be observed which allows us to obtain a maximum magneto-optical contrast by even the smallest Faraday or Kerr rotation. The contrast is improved by using Glan-Taylor polarizers with high extinction coefficients and by setting initially the probe polarization direction perpendicular to the magnetization. It is important to note that in our setup we chose a Kerr configuration (reflection mode). Indeed the laser pump comes from one side of the magnetic medium and the probe from the other side. This allowed us to avoid the use of beam-splitters (BS) which alter the polarization state of incoming laser pulses. In fact, beam-splitters have different reflection and transmission coefficients for s- and p- polarizations. Therefore, a circular polarization becomes elliptical after transmission through a beam-splitter. Notably, in the reflection configuration, we were able to obtain

circular polarization with 92 - 95 % of helicity. However, since the Kerr rotation angle is often much smaller than the Faraday rotation angle (e.g. for Co $\theta_F = 1.88 \times 10^5$ deg, θ_K 0.85 deg), this microscope setup is not suitable for materials with low MO contrast.

Lastly, the magnetic domains are imaged with a regular charge-coupled device (CCD) camera that provides an image of 2448×2048 pixels. The CCD camera is accompanied with a $\times 20$ -magnification microscope objective for which the pixel size is $\sim 0.10 \mu\text{m}$. Proper alignment is performed in order to overlap the pump and probe on the sample surface, which enables us to directly image the change of magnetization induced by the fs-laser. An IR filter is added before the camera to block the laser beam and let only the reflected probe light go through.

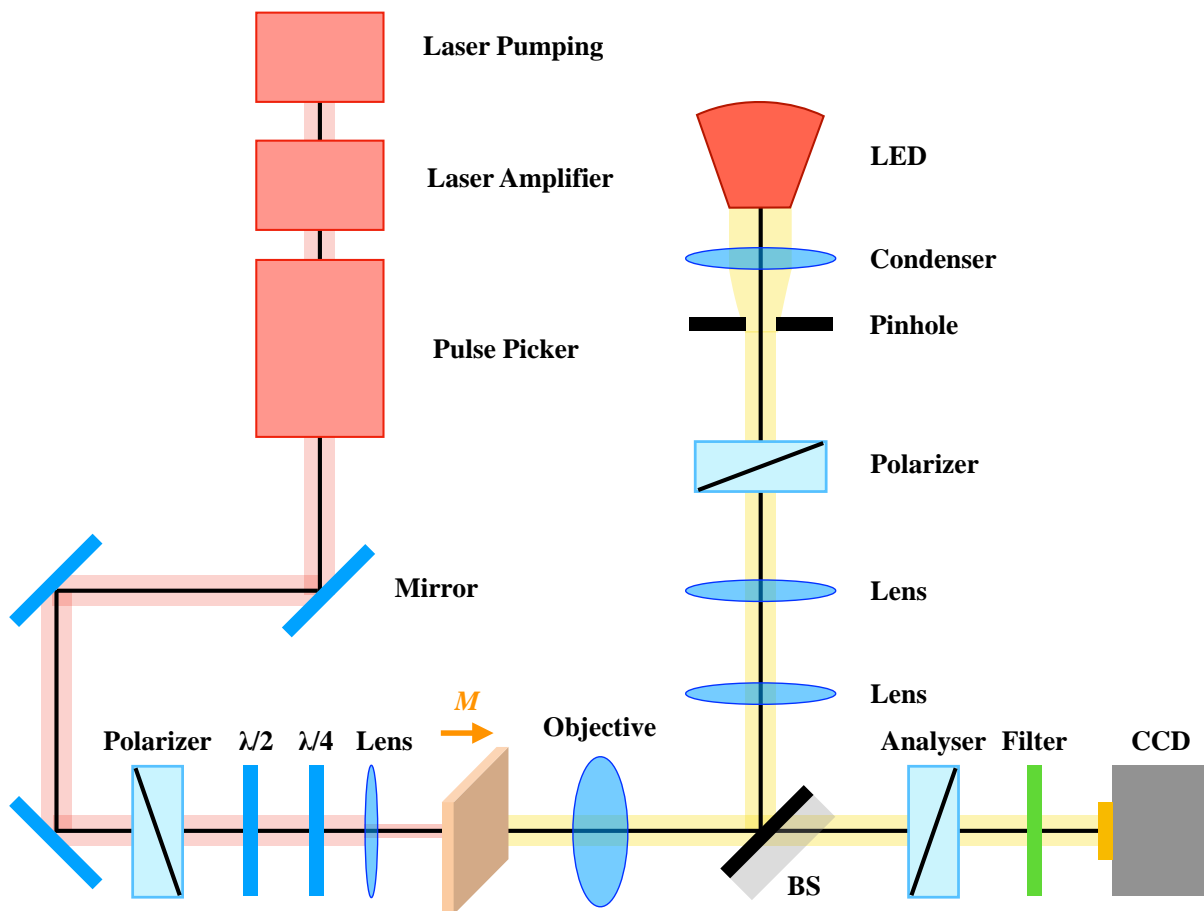


FIGURE II.12: Magneto-optical imaging setup in Kerr configuration to observe fs-laser-induced magnetization in ferromagnetic materials as described in the text. A condenser focuses the LED light onto a pinhole. Then a set of lenses are used to perform Kohler illumination in order to have uniform lighting on the magnetic medium after going through the objective. The beam-splitter in this setup intervenes after interaction between the laser pulse and the sample and has therefore no influence on the laser polarization.

References

1. Foner, S. Versatile and sensitive vibrating-sample magnetometer. *Rev. Sci. Instrum.* **30**, 548–557 (1959).
2. El Hadri, M. S. *et al.* Two types of all-optical magnetization switching mechanisms using femtosecond laser pulses. *Physical Review B* **94**, 064412 (Aug. 2016).
3. Gorchon, J., Yang, Y. & Bokor, J. Model for multishot all-thermal all-optical switching in ferromagnets. *Physical Review B* **94**, 020409 (July 2016).
4. Medapalli, R. *et al.* Multiscale dynamics of helicity-dependent all-optical magnetization reversal in ferromagnetic Co/Pt multilayers. *Physical Review B* **96**, 224421 (Dec. 2017).
5. Cornelissen, T. D., Córdoba, R. & Koopmans, B. Microscopic model for all optical switching in ferromagnets. *Applied Physics Letters* **108**, 142405 (2016).
6. Kawada, Y., Ueno, Y. & Shibata, K. Co-Pt multilayers perpendicular magnetic recording media with thin Pt layer and high perpendicular anisotropy. *IEEE Transactions on Magnetics* **38**, 2045–2047 (2002).
7. Bersweiler, M., Dumesnil, K., Lacour, D & Hehn, M. Impact of buffer layer and Pt thickness on the interface structure and magnetic properties in (Co/Pt) multilayers. *Journal of Physics: Condensed Matter* **28**, 336005 (2016).
8. Johnson, M. T., Bloemen, P. J. H., den Broeder, F. J. A. & de Vries, J. J. Magnetic anisotropy in metallic multilayers. *Reports on Progress in Physics* **59**, 1409 (1996).
9. Zhang, B., Krishnan, K. M., Lee, C. H. & Farrow, R. F. C. Magnetic anisotropy and lattice strain in Co/Pt multilayers. *Journal of Applied Physics* **73**, 6198–6200 (1993).
10. Kim, J. & Shin, S. Interface roughness effects on the surface anisotropy in Co/Pt multilayer films. *Journal of Applied Physics* **80**, 3121–3123 (1996).
11. Engel, B. N., Wiedmann, M. H., Van Leeuwen, R. A. & Falco, C. M. Anomalous magnetic anisotropy in ultrathin transition metals. *Physical Review B* **48**, 9894–9897 (Oct. 1993).
12. Bruno, P. *et al.* Hysteresis properties of ultrathin ferromagnetic films. *Journal of Applied Physics* **68**, 5759–5766 (1990).
13. Nakajima, N. *et al.* Perpendicular Magnetic Anisotropy Caused by Interfacial Hybridization via Enhanced Orbital Moment in [Co/Pt] Multilayers: Magnetic Circular X-Ray Dichroism Study. *Physical Review Letters* **81**, 5229–5232 (Dec. 1998).
14. Knepper, J. W. & Yang, F. Y. Oscillatory interlayer coupling in Co/Pt multilayers with perpendicular anisotropy. *Physical Review B* **71**, 224403 (June 2005).
15. Lin, C. J. *et al.* Magnetic and structural properties of Co/Pt multilayers. *Journal of Magnetism and Magnetic Materials* **93**, 194–206 (1991).
16. J., K. *et al.* Influence of buffer layers on the texture and magnetic properties of Co/Pt multilayers with perpendicular anisotropy. *physica status solidi (a)* **204**, 3950–3953 (2007).
17. Emori, S. & Beach, G. S. D. Optimization of out-of-plane magnetized Co/Pt multilayers with resistive buffer layers. *Journal of Applied Physics* **110**, 033919 (2011).
18. Alebrand, S. *et al.* Light-induced magnetization reversal of high-anisotropy TbCo alloy films. *Applied Physics Letters* **101**, 162408 (2012).
19. Mangin, S. *et al.* Engineered materials for all-optical helicity-dependent magnetic switching. *Nature Materials* **13**, 286–292 (Feb. 2014).
20. Ostler, T. A. *et al.* Ultrafast heating as a sufficient stimulus for magnetization reversal in a ferrimagnet. *Nature Communications* **3**, 666 EP – (Feb. 2012).
21. John, R. *et al.* Magnetisation switching of FePt nanoparticle recording medium by femtosecond laser pulses. *Scientific Reports* **7**, 4114 (2017).
22. Parakkat, V. M., Ganesh, K. R. & Anil Kumar, P. S. Tailoring Curie temperature and magnetic anisotropy in ultrathin Pt/Co/Pt films. *AIP Advances* **6**, 056118 (2016).

23. Agranat, M. B., Ashitkov, S. I., Granovskii, A. B. & Rukman, G. I. Interaction of picosecond laser pulses with the electron, spin, and phonon subsystems of nickel. *Journal of Experimental and Theoretical Physics* **59**, 804 (1984).
24. Vaterlaus, A., Milani, F. & Meier, F. Spin polarization of thermoemitted electrons from cesiated Ni and Fe. *Physical Review Letters* **65**, 3041–3043 (Dec. 1990).
25. Beaurepaire, E., Merle, J. C., Daunois, A. & Bigot, J. Y. Ultrafast Spin Dynamics in Ferromagnetic Nickel. *Physical Review Letters* **76**, 4250–4253 (May 1996).
26. Moulton, P. F. Spectroscopic and laser characteristics of Ti:Al₂O₃. *J. Opt. Soc. Am. B* **3**, 125–133 (1986).
27. Strickland, D. & Mourou, G. Compression of amplified chirped optical pulses. *Opt. Commun.* **56**, 219 (1985).
28. Diels, J.-C. M., Fontaine, J. J., McMichael, I. C. & Simoni, F. Control and measurement of ultrashort pulse shapes (in amplitude and phase) with femtosecond accuracy. *Applied Optics* **24**, 1270–1282 (1985).
29. Plass, W., Maestle, R., Wittig, K., Voss, A. & Giesen, A. High-resolution knife-edge laser beam profiling. *Optics Communications* **134**, 21–24 (1997).
30. Hartmann, U. Magnetic Force Microscopy. *Annual Review of Materials Science* **29**, 53–87 (1999).
31. Carr, H. Y. & Purcell, E. M. Effects of Diffusion on Free Precession in Nuclear Magnetic Resonance Experiments. *Physical Review* **94**, 630–638 (May 1954).
32. Bloembergen, N., Purcell, E. M. & Pound, R. V. Relaxation Effects in Nuclear Magnetic Resonance Absorption. *Physical Review* **73**, 679–712 (Apr. 1948).
33. Faraday, M. On the magnetization of light and the illumination of magnetic lines of force. *Phil. Trans. R. Soc. Lond.* 104–123 (1846).
34. Kerr, J. XLIII. On rotation of the plane of polarization by reflection from the pole of a magnet. *The London, Edinburgh, and Dublin Philosophical Magazine and Journal of Science* **3**, 321–343 (May 1877).
35. Freiser, M. A survey of magneto-optic effects. *IEEE Transactions on Magnetics* **4**, 152–161 (1968).
36. Ebert, H. Magneto-optical effects in transition metal systems. *Reports on Progress in Physics* **59**, 1665 (1996).
37. Smith, D. Y. Comments on the dispersion relations for the complex refractive index of circularly and elliptically polarized light*. *Journal of the Optical Society of America* **66**, 454–460 (1976).
38. Haider, T. A review of magneto-optics effects and its application. *International Journal of Electromagnetics and Applications* **7**, 17–24 (2017).
39. The Faraday effect in ferromagnetics. *Proceedings of the Royal Society of London. Series A* **135**, 237 (Feb. 1932).
40. Weller, D., Harp, G. R., Farrow, R. F. C., Cebollada, A. & Sticht, J. Orientation dependence of the polar Kerr effect in fcc and hcp Co. *Physical Review Letters* **72**, 2097–2100 (Mar. 1994).
41. Radu, I. *et al.* Transient ferromagnetic-like state mediating ultrafast reversal of antiferromagnetically coupled spins. *Nature* **472**, 205–208 (Mar. 2011).

Chapter III

Helicity-dependent all-optical domain wall motion in ferromagnets

1 Introduction

The recent results of all-optical switching in ferromagnetic materials unambiguously highlighted the cumulative nature of HD-AOS in (Co/Pt) MLs and FePt granular media [1–3]. The multi-shot switching observed in (Co/Pt) MLs was explained by a nucleation of magnetic domains and domain wall (DW) propagation mechanism [1, 3]. Later, it was found that the magnetic domain size with respect to the laser spot size was a relevant criterion to observe HD-AOS [4]. Single-fs-laser pulse reversal with linear polarization was even reported in (Co/Pt), specifically for a laser spot size of the order of the intrinsic magnetic domain size [5]. Moreover, the authors also suggested a nucleation/propagation switching process. Therefore, there were growing evidence of the importance of magnetic domains and DW mobility upon laser irradiation to achieve all-optical switching. In this third chapter III, we investigated the response of a DW to direct optical excitation in (Co/Pt) MLs that show HD-AOS. We present here a novel way to deterministically manipulate DWs with only ultrashort laser pulses and no applied field in ferromagnetic thin films. The aim of this study was to corroborate a helicity-dependent switching mechanism based on helicity-dependent DW motion. First in section 2, we will briefly introduce magnetic interactions and domains in ferromagnetic systems. Second in section 3, we describe several usual methods to induce DW motion. Then in section 4, we report helicity-dependent all-optical domain wall (HD-AODW) motion in (Co/Pt) structures. We study the influence of several parameters such as the laser fluence, the beam position, the temperature gradient and the degree of light ellipticity. Finally in section 5, we discuss the possible non-thermal and thermal mechanisms that could induce HD-AODW motion. We compute the DW motion under the assumption of the inverse Faraday effect or magnetic circular dichroism that we experimentally measure. Lastly in section 6, we consider the perspectives of our results in the light of the recent advances made in AOS in ferromagnets and how it could explain the reversal mechanism.

2 Magnetic interactions and domains

In order to understand DW mobility and magnetization reversal by DW propagation, it is essential to be aware of the many magnetic interactions and energies resulting in the formation of magnetic domains in ferromagnets. Note that in this theoretical framework, all equations will be presented in *cgs* units.

2.1 Magnetic interactions and energies

Zeeman energy

The potential energy of a magnetic dipole \vec{m} in an external magnetic field \vec{H}_{ext} is defined by the Zeeman energy E_{ext} as:

$$E_{ext} = -\vec{m} \cdot \vec{H}_{ext} \quad (2.1)$$

The Zeeman interaction of a permanent magnet placed in an applied field is found by summing Eq. 2.1 over all the magnetic dipoles in the system:

$$E_{ext} = - \int_V \vec{M} \cdot \vec{H} dV \quad (2.2)$$

Assuming uniform magnetization and applied field, the potential can simply be written as $E_{ext} = -V \vec{M} \cdot \vec{H}_{ext}$, where V is the total system volume. The Zeeman effect is minimized when the magnetization points out in the same direction as the applied field. Thus, this interaction tends to align the magnetization along the direction of the external magnetic field.

Exchange interaction

The Weiss theory states that ferromagnetism is the consequence of a molecular field which aligns all the atomic moments. The origin of this field remained unclear until Heisenberg demonstrated that it results from a quantum mechanical exchange interaction. The exchange force between two neighboring spins arises from Coulomb interaction and the Pauli exclusion principle, which specifies that two electrons can have the same energy only if they have opposite spins. The Heisenberg exchange hamiltonian \mathcal{H}_{ex} for two atoms i and j can be written as:

$$\begin{aligned} \mathcal{H}_{ex} &= -2J_{ij} \vec{S}_i \cdot \vec{S}_j \\ &= -2J_{ex} S_i S_j \cos \Phi_{ij} \end{aligned} \quad (2.3)$$

where \vec{S} is the total spin moment of the corresponding atom and J_{ex} the exchange integral. The angle Φ_{ij} between the two spin moments can be introduced if we consider the spin operators as classical vectors. Consecutively, \mathcal{H}_{ex} can be summed over all the nearest neighbors of atom i and finally over the entire crystal. Assuming that the spins have same amplitude, the exchange energy E_{ex} comes as : $\mathcal{H}_{ex} = E_{ex} = -2J_{ex} S^2 \sum \cos \Phi_{ij}$. This equation can be written in an integral form assuming that the direction of magnetization is a continuous function of position. The exchange energy is hence proportional to the exchange stiffness constant $A_{ex} = \frac{2J_{ex} S^2}{a}$, where a is the crystal lattice constant. Thus, the magnetic order in the specimen can be understood in terms of the sign of J_{ex} . Indeed, for $J_{ex} > 0$, to minimize the exchange energy the spin moments needs to be parallel, which corresponds to ferromagnetism. Conversely, a negative exchange constant J_{ex} leads to an antiparallel arrangement of spins and therefore to an antiferromagnetic order.

The exchange interaction is a short-range interaction affecting only the neighboring atoms. Yet, it leads to a long-range magnetic order. This ordering can be lost due to thermal fluctuations.

Indeed, above a critical temperature, the Curie temperature for ferromagnets and Néel temperature for antiferromagnets, the thermal energy $k_B T$ is greater than the exchange interaction, with k_B the Boltzmann constant. As a result, the magnetic moments are randomly oriented and the specimen becomes paramagnetic.

Dipolar interaction and shape anisotropy

Unlike the exchange interaction, the dipolar interaction is a long-range interaction. A magnetic dipole with a magnetic moment \vec{m} creates a dipolar field \vec{H}_{dip} at a distance \vec{r} from the dipole:

$$\vec{H}_{dip} = \frac{1}{4\pi} \left[\frac{(\vec{m} - \vec{r}) \cdot \vec{r}}{r^5} - \frac{\vec{m}}{r^3} \right] \quad (2.4)$$

This field is sensed in all the surrounding space of the dipole but it quickly decays as $1/r^3$. In the case of a permanently magnetized sample \vec{M} constituted of many small magnetic dipoles, the total dipolar field is given as the sum of all individual dipolar fields. It emerges a field outside of the sample but also sensed inside the system, which points in the opposite direction of \vec{M} . Therefore, the dipolar field tends to lower the material magnetization and is consequently often called *demagnetizing* field \vec{H}_d . The self-energy of the magnetization in its own field, similarly named demagnetizing or magnetostatic energy, is equal to:

$$E_d = -\frac{1}{2} \int_V \vec{H}_d \cdot \vec{M} dV \quad (2.5)$$

The demagnetizing field is always positive. For this reason, to minimize the magnetostatic energy, the magnetic moments tend to align in the direction in which \vec{H}_d is minimum. In most cases, the demagnetizing field depends on the geometry of the specimen, which induces preferential orientation for the magnetization in order to reduce the magnetostatic effect. Indeed, in a non-spherical system, an applied field will not uniformly magnetize the material. This is referred as shape anisotropy. A demagnetizing tensor $[N_d]$ can be introduced and yields \vec{H}_d as:

$$\vec{H}_d = -[N_d] \cdot \vec{M} \quad (2.6)$$

Numerical calculations are often not trivial to find the demagnetizing tensor. However, in a few simple geometries such as an ellipsoid, we can explicitly express the demagnetizing factor and \vec{H}_d is given by:

$$\vec{H}_d = - \begin{pmatrix} N_{xx} & 0 & 0 \\ 0 & N_{yy} & 0 \\ 0 & 0 & N_{zz} \end{pmatrix} \cdot \vec{M} \quad (2.7)$$

with $N_{xx} + N_{yy} + N_{zz} = 4\pi$. Specifically for a sphere, $N_{xx} = N_{yy} = N_{zz} = 4\pi/3$, thus illustrating that the demagnetizing field is the same in all spatial directions.

Let us now consider a prolate spheroid with a semi-major axis c and semi-minor axis $a = b$ that is uniformly magnetized with \vec{M} at an angle θ to c along the z -axis (see. Fig. III.1). E_d can be written as:

$$\begin{aligned}
 E_d &= \frac{1}{2} \left[(M \cos \theta)^2 N_{zz} + (M \sin \theta)^2 N_{xx} \right] \\
 &= \frac{1}{2} M^2 N_{zz} + \frac{1}{2} (N_{xx} - N_{zz}) M^2 \sin^2 \theta
 \end{aligned} \tag{2.8}$$

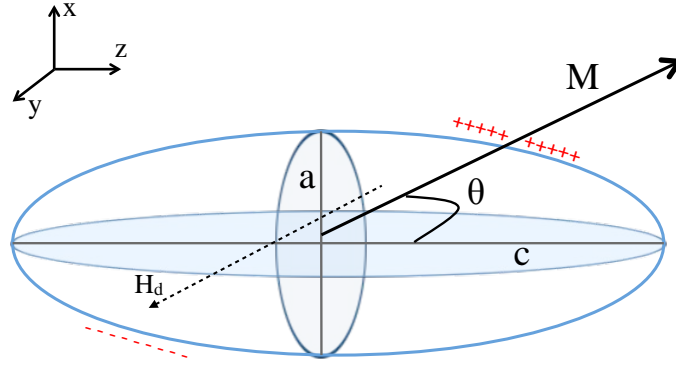


FIGURE III.1: Prolate spheroid with uniform magnetization M at an angle θ with respect to the c -axis. H_d is the demagnetization field opposite to M resulting from the 'magnetic charges' at the surface.

For an ultrathin film (infinite 1D object) with perpendicular magnetization \vec{M} along the z -axis, $N_{xx} = N_{yy} = 0$ and $N_{zz} = 4\pi$, the demagnetizing energy per unit of volume is simply given by: $E_d = 2\pi M^2$. The latter designates the shape anisotropy related to the accumulation of 'magnetic charges' on both sides of the film.

Magneto-crystalline anisotropy

If we consider a spherical shape and only the Heisenberg exchange interaction which is invariant with respect to the choice of coordinate system, it comes that a ferromagnetic specimen is isotropic. Nevertheless, it is experimentally observed that the magnetization tends to lie along certain crystallographic axes: this is known as magneto-crystalline anisotropy (MCA). Therefore, the energy stored in a ferromagnetic crystal depends on the orientation of the magnetization with respect to crystallographic directions. MCA arises from spin-orbit coupling and the interaction between the crystal lattice and the orbital magnetic moments. The existence of crystalline anisotropy is evidenced by the measurement of MH curve of single-crystal systems. For given directions, a smaller applied field is required to magnetize the material: these are called easy axes. Conversely, the directions in which it is difficult to make the magnetization lie are called hard axes.

Let's examine the case of a cubic crystal. As shown in Fig. III.2, it is found for instance for Fe (bcc crystal) that the easy axes are the cube edges [100] and the hard axes the body diagonals [111]. The opposite is observed for Ni that is a fcc crystal. It was demonstrated that the MCA energy E_K can be expressed in terms of a series expansion of the direction cosines α_i of saturation magnetization M_s relative to the crystal axes. It comes that:

$$E_K = K_1 (\alpha_1^2 \alpha_2^2 + \alpha_2^2 \alpha_3^2 + \alpha_1^2 \alpha_3^2) + K_2 (\alpha_1^2 \alpha_2^2 \alpha_3^2) + \dots \tag{2.9}$$

where K_i are anisotropy constants. We can see that K_2 is associated with a sixth-degree term that is often neglected. Thus, the direction of the easy magnetization is determined by the sign

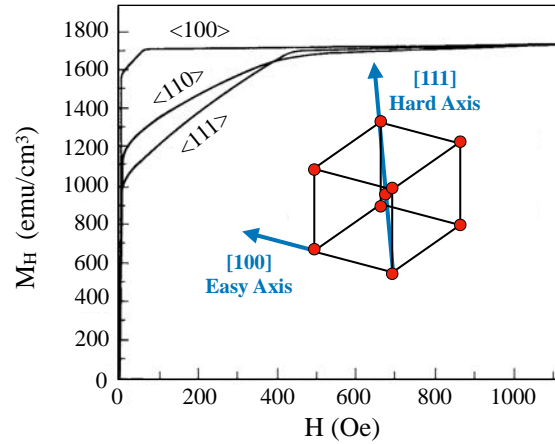


FIGURE III.2: Magnetization curves for a single crystal of Fe (bcc structure). Saturation is reached for lower values of field in the $\langle 100 \rangle$ direction (easy axis) than in the $\langle 111 \rangle$ direction (hard axis).

of K_1 . If K_1 is positive (resp. negative), the MCA energy is minimum when M_s is along $\langle 100 \rangle$ (resp. $\langle 111 \rangle$).

If we consider now, hexagonal crystals such as Co which has a hcp structure at room temperature. The hexagonal c -axis is the easy axis, while all directions in the basal plane are found to be equally hard. Therefore, the crystalline anisotropy energy can be solely described by the angle θ between M_s and the c -axis. Thusly, the anisotropy is defined as uniaxial with:

$$E_K = K_1' \sin^2 \theta + K_2' \sin^4 \theta \quad (2.10)$$

If K_1' and K_2' are both positive, then E_K is minimum for $\theta = 0$. While if they are both negative, the magnetization lies in a easy plane perpendicular to the c -axis. If they are of opposite signs, $K_2' = -K_1'$ defines the boundary between uniaxial and planar anisotropy. Finally, for small rotations of the magnetization away from the easy axis, MCA acts as a magnetic field H_K that tends to align it with the easy axis. To find the anisotropy field, the Zeeman energy brought by the applied field must be balanced by the crystalline anisotropy energy, which leads to $H_K = 2K_1/M_s$ for a $\langle 100 \rangle$ easy axis (Fe) or uniaxial crystal (Co).

Thin films with perpendicular magnetic anisotropy

In this thesis, we employed ultra-thin films with strong perpendicular magnetic anisotropy (PMA) as an important feature to observe AOS. In magnetic thin films, the demagnetizing field is weaker in the direction of a long axis. As a consequence, the shape anisotropy tends to align the magnetization \vec{M} parallel to the plane and is given by: $K_{shape} = -2\pi M_s^2$, with M_s the saturation magnetization. The negative sign indicates that it prefers an in-plane configuration of the magnetization. In order to obtain an out-of-plane magnetization, the shape anisotropy must be overcome. The volume magneto-crystalline anisotropy (K_u) and interface anisotropy (K_s) favor such orientation.

In 1954, Néel revealed the existence of an interface contribution to the magneto-crystalline anisotropy [6]. Indeed, for thin films with a thickness typically of the order of few atomic monolayers, the crystalline symmetry responsible for the quenching of the orbital momentum is broken by the interfaces. Thus, an increase of the orbital momentum may be observed at the

interface leading to a local enhancement of the anisotropy. As a result of this symmetry breaking, the axis perpendicular to the interface may become an easy axis for the magnetization. This is commonly verified for magnetic/non-magnetic metallic multilayers such as (Co/Pd), (Co/Ni) or (Co/Pt) [7–9]. For an ultrathin film, for it is considered as an infinite 1D object, two interfaces (1) and (2) can be distinguished with $K_s^{(1)}$ and $K_s^{(2)}$ their respective interface anisotropy. For a film of a thickness t , the interface anisotropy energy per unit of volume is given by:

$$K_s = \frac{K_s^{(1)} + K_s^{(2)}}{t} \sin^2 \theta \quad (2.11)$$

The relative orientation of the magnetization results from the competition between the total MCA and the shape anisotropy. Therefore, we can define an effective anisotropy K_{eff} per unit of volume as:

$$K_{eff} = K_u + \frac{K_s^{(1)} + K_s^{(2)}}{t} \sin^2 \theta - 2\pi M_s^2 \quad (2.12)$$

PMA occurs when $K_{eff} > 0$, i.e. when the total MCA is greater than the shape anisotropy (as seen in Fig. II.3). This is achieved by scaling down the lateral dimension of the film which causes an increase of the interface contribution due to the high surface to volume ratio. It is under these considerations that the thicknesses of the (Co/Pt) multilayers we studied were adequately chosen in order to show strong PMA and also exhibit AOS.

2.2 Magnetic domains and domain wall

The total free energy of a ferromagnetic system in an applied magnetic field can be written as the sum of all the energies we previously discussed:

$$E_{tot} = E_{ext} + E_{ex} + E_d + E_K + \dots \quad (2.13)$$

In addition to the Zeeman, exchange, dipolar and MCA energies, other interactions could intervene such as the magnetostriction. A stable equilibrium state is achieved by minimizing E_{tot} . On one hand, the exchange interaction favors a parallel arrangement of the magnetic moments, thus an uniform magnetized specimen. On the other hand, the dipolar interaction will tend to induce an antiparallel orientation of the moments in order to reduce the magnetic charges at the surface. As a result, the specimen may break into magnetic regions, called magnetic domains, with opposite magnetization direction and separated by a domain wall (DW). The magnetic domain configuration of a ferromagnetic specimen is a direct consequence of the competition between the exchange and dipolar interaction.

Magnetic domain configurations

Let's consider a single crystal of a ferromagnetic material as represented in Fig. III.3. Suppose no applied field and uniaxial anisotropy along the parallelepiped long edges. Consequently, E_K will be minimum if all the atomic magnetic moments lie parallel to the long edges (see Fig. III.3(a)). Simultaneously, the exchange energy E_{ex} will also be minimum as all the moments are parallel. Yet, such an uniform magnetization introduce important accumulation of magnetic

charges on the top and bottom surface of the crystal, which generates a strong demagnetizing field. To reduce the dipolar energy, the specimen may break into two domains as in Fig. III.3(b). However, this happens at the cost of increasing the exchange and anisotropy energies, although the magnetostatic energy is cut by half. Indeed, in the transition region between the two domains, the atomic moments are not parallel to each other anymore and additionally rotate away from the easy axis. Nevertheless, it can be demonstrated that the total free energy in a 2-domain configuration is less than for the single domain. Subsequently, the division into domains will continue as long as the total energy is reduced. For a cubic crystal with $\langle 100 \rangle$ easy axis, a special arrangement with closure domains can be obtained for which the demagnetizing energy is vanished (Fig. III.3(c)). Moreover, as the exchange force is a short-range interaction, over short distances, i.e. within one domain, the magnetization is expected to be uniform.

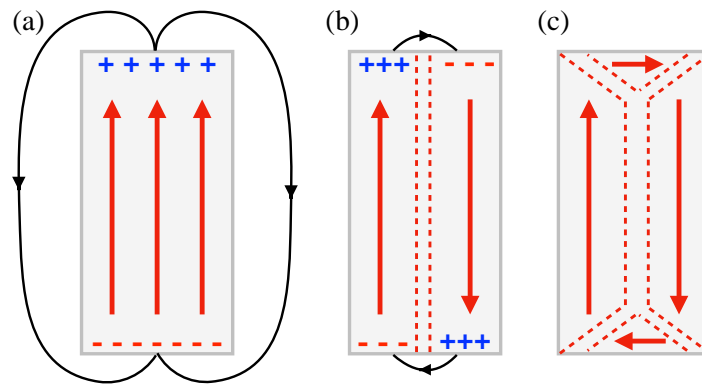


FIGURE III.3: Magnetic domain configurations of a single ferromagnetic crystal with uniform magnetization. (a) Single domain particle. (b) Two-domain configuration. (c) Closure domains for a cubic crystal. Magnetic charges are represented on the surfaces and the demagnetizing field lines.

Domain wall width and energy

If we consider a π rad wall, an abrupt change of the direction of the atomic magnetic moments will be associated with an exchange energy of $E_{ex} = J_{ex} S^2 \pi^2$. Conversely, a gradual change over N atoms with an equal small angle π/N between neighboring atoms will lead to $E_{ex} = J_{ex} S^2 \pi^2 / N$. This way the exchange energy is dramatically reduced. The wider the DW, the lower the exchange energy. However, for a wide wall the crystalline anisotropy energy significantly increases as more atomic spins lie along a hard axis. Therefore, the width of a DW (δ) is governed by the competition between exchange and anisotropy forces. Let's assume a perpendicularly magnetized thin film with $K_u > 0$ and a π rad wall parallel to a (100) plane. A minimum of the DW energy per unit of area σ_s is reached for:

$$\delta = \pi \sqrt{\frac{A_{ex}}{K_u}} \quad (2.14)$$

$$\sigma_s = 4 \sqrt{A_{ex} K_u}$$

Thus, for high anisotropy materials such as Fe/Pt the DW width is of the order of few atoms, while for permalloys it can be as great as 100 nm. Typically, the surface energy of DW is of a few erg cm^{-2} . There are two main types of DWs, namely Bloch and Néel walls as illustrated in Fig. III.4. In a Bloch wall, the magnetization rotates in the plane of the wall, in the opposite in

the plane of the sample for a Néel wall. A Bloch wall creates free poles on the sample's surface, while in a Néel configuration magnetic charges accumulate on the wall. As a result, for materials with a small thickness comparable to the DW width, the energy associated with the free poles arising from a Bloch wall becomes significant and a Néel wall is more favorable. To observe magnetic domains and domain walls, one can use magneto-optical effects, we previously described, in a Kerr or Faraday microscope. Other methods include scanning probe microscope, Lorentz microscopy and magnetic force microscopy. Domain patterns highly depends on the crystallographic structure of a material, and complicated patterns can be observed other than stripe domains for uniaxial crystals. Finally, in particular cases, a specimen may consist of a single domain. Intuitively, if a particle is smaller than the thickness of a DW, it cannot break into two domains. Indeed, a critical diameter can be calculated below which the magnetostatic energy is minimized for a single-domain state.

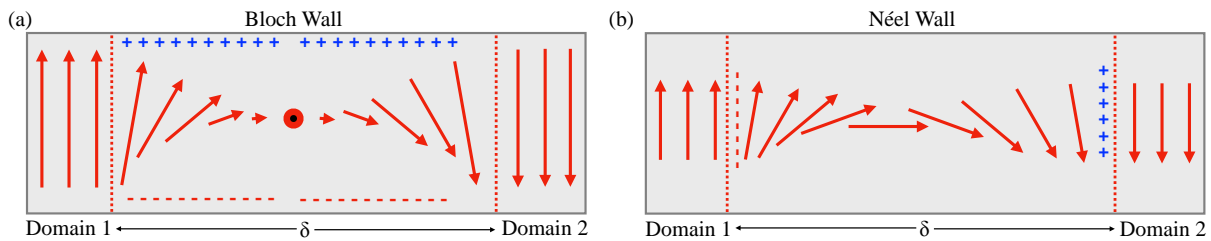


FIGURE III.4: Domain wall with (a) Bloch (out-of-plane rotation) or (b) Néel (in-plane rotation) configuration.

2.3 Domain wall motion

Hysteresis loops as those obtained by VSM measurements (Fig. II.2) show that magnetization reversal occurs via both domain wall motion at low field and magnetization rotation at higher field values. For an uniaxial crystal, e.g. a perpendicularly magnetized thin film, the most conventional way to switch the magnetization is to apply a magnetic field parallel to the easy axis and opposite to the magnetization. If we assume a perfect crystal, for an applied field greater than the anisotropy field, the magnetization in the film will homogeneously reverse. Similarly, a small field will be enough to expand a domain in a perfect specimen. However, the anisotropy in real ferromagnets is not uniformly distributed in the system, which results in an inhomogeneous magnetization reversal. Indeed, the magnetization will start switching in regions with low anisotropy, namely local defects and crystal imperfections. This would lead to domain nucleation. The process of magnetization reversal often involves both domain nucleation and DW propagation.

We will discuss the combination of these two phenomena in the next section 3.1. Here, we focus on the propagation of DWs. Due to the crystal imperfections, the movement of DW is impeded, and this causes a smaller initial permeability and a larger coercive force. A consequence of the presence of imperfections is the variation of the DW energy E with the location x . A schematic example is presented in Fig. III.5. Let us consider a π rad wall. At zero field, the DW lies at an energy minimum (position O). By increasing the magnetic field, the wall reversibly moves to A. At this position if the field is suppressed, the DW returns to its stable position O. However, if the field is high enough to overcome the potential barrier OA, the DW will irreversibly move to E. Hence, position A is a point of maximum restoring force. By reversing the field, the wall moves toward C. If the field is switched off, the wall will move back to the stable position D and not O. On a further increase of the field, the motion is again reversible between E and F, while after F another irreversible jump occurs. This is called a Barkhausen jump. Therefore,

it emerges that DW motion is discontinuous and jerky. If the applied field is not high enough with respect to the barrier, the DW will be pinned in a potential valley that corresponds to a local defect.

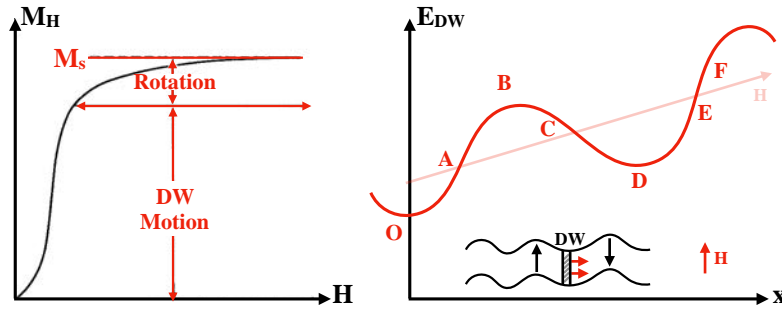


FIGURE III.5: On the left, MH curve that shows DW motion until the 'knee' of the curve as observed in VSM Fig. II.2. On the right, domain wall potential map that exhibits Barkhausen jumps. At the bottom, DW motion under the action of an applied field in an imperfect specimen.

Imperfections that hinder DW motion can be due to inclusions and residual microstress [10]. Examples of inclusions are holes, cracks or particles. An inclusion in a domain is considered as a region with opposite magnetization from the surrounding material or simply as a nonmagnetic region. Let's assume a nonmagnetic spherical inclusion with a radius r . The DW will tend to cling to the inclusion in order to decrease its area, and thence its energy as illustrated in Fig. III.6. When the DW bisects the inclusion, the wall area decreases by πr^2 and thus the wall energy by $\pi r^2 \sigma_s$. However, magnetostatic effects were not taken into account, and Néel demonstrated that free poles on inclusions are a source of much greater energy.

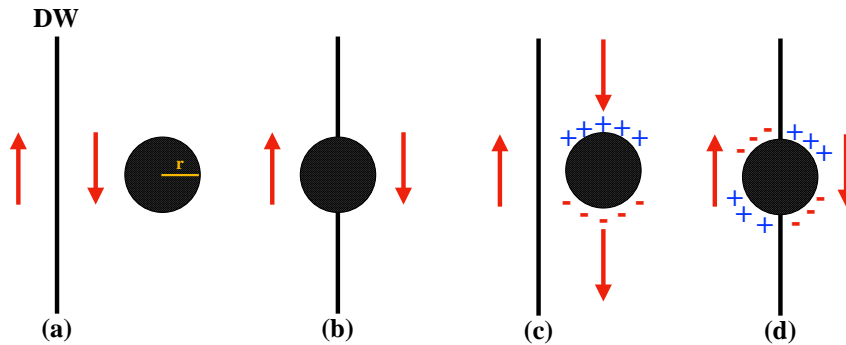


FIGURE III.6: Interaction of a DW with a spherical inclusion. (a,b) The bisection of a DW with the inclusion leads to a reduction of its surface energy by πr . (c,d) the magnetostatic energy is taken into account, and the bisection of the DW induces compensated magnetic poles on the surface of the inclusion.

Indeed, the demagnetizing energy of a spherical inclusion is equal to $(8/9)\pi^2 M_s^2 r^3$, which is larger than the decrease of the surface wall energy. When the DW moves and bisects the inclusion, the magnetic charges over the surface of the inclusion are redistributed, and the magnetostatic energy is reduced by half (Fig. III.6). As a result, this mechanism can explain large coercive forces that pin the DW. Furthermore, the demagnetizing field of inclusions is also responsible for the domain nucleation process. The other kind of hindrance is due to microstress, and more specifically magnetostriction. Yet, magnetostriction will have an effect only on $\pi/2$ walls. For a π wall, microstress will only increase its energy by adding a stress anisotropy, while for a $\pi/2$ wall the direction of magnetization will be altered. Lastly, surface roughness can significantly affect DWs especially in thin films. In order to reduce its total area, DWs will

prefer to stay in valleys where the sample is the thinnest. Finally, the effect of temperature on the DW mobility should also be addressed. Indeed, the DW surface energy will decrease with temperature as it depends on the exchange stiffness and anisotropy constants that are strongly dependent on the temperature. Moreover, the hills of the DW potential will tend to be flattened due to thermal fluctuations increasing the DW mobility and as a result the Barkhausen volume, i.e. the distances the wall jumps over [11]. Another consequence is therefore the reduction of the coercivity. To conclude, the shape of MH curves and hence the magnetization reversal process are intrinsically related to DW motion.

3 Domain wall manipulation

In this section, we will discuss the different methods used to control domain walls. DWs, with their high mobility, are of great interest for low-power spintronic applications, such as racetrack memories [12] and logic devices [13, 14].

3.1 Magnetic field-driven DW motion

DW dynamics under the action of an external magnetic field has been extensively studied in ferromagnetic materials over the past decade [15–18]. High DW velocity of about 500 m s^{-1} for an applied field of 40 Oe was even observed in a 200-nm wide NiFe nanowire with out-of-plane magnetization [16], which is several orders of magnitude larger than in Pt/Co/Pt nano-strips with PMA [15]. In a ferromagnetic system with defects and crystal imperfections, the DW will interact with pinning sites as we previously discussed. DW dynamics induced by a magnetic field will thus exhibit three velocity regimes. At zero temperature, due to the local disorder, the DW is pinned for all coercive forces below the depinning field H_{dep} at which a depinning transition occurs as seen in Fig. III.7. At finite temperatures, there is a non-zero DW velocity even for fields below H_{dep} . This corresponds to the thermally activated creep regime. Indeed, thermal excitation will allow the DW to jump from one pinning site to another. On the other hand, for high applied fields $H_{app} \gg H_{dep}$, disorder becomes negligible and the DW motion is characterized by a dissipative and viscous flow motion. Between, these two extremes regimes, the depinning takes place and is smeared out at finite temperature. In ultrathin films with PMA, DWs can be studied as a 1D object at low fields. However, in the flow regime, there is a change of the wall structure during DW propagation as the magnetization within the wall starts to precess. This is the Walker breakdown. Above the Walker field H_w , the DW enters a precessional regime which depends on the material saturation magnetization and Gilbert damping parameter.

More into details, in the creep and low field regime, the DW velocity v_{DW} follows a thermal activated law:

$$v_{DW} = v_0 \exp \left[- \left(\frac{T_{dep}}{T} \right) \left(\frac{H_{dep}}{H} \right)^\mu \right] \quad (3.1)$$

where T_{dep} is the depinning temperature defined as $E_{dep} = k_B T_{dep}$ with E_{dep} the height of the pinning energy barrier. H_{dep} is the depinning field, μ an universal dynamic constant equal to 1/4 for a 1D object in a 2D weakly disordered system, v_0 an exponential prefactor. Metaxas *et al.* reported among the first DW velocity measurements in the three regimes [17]. They investigated DW motion in ultrathin Pt(4.5 nm)/Co(t_{Co})/Pt(4.5 nm) films with PMA and t_{Co} ranging from 0.5 to 0.8 nm. They recorded DW displacements induced by magnetic field pulses

and by increasing the acquisition duration (from 250 ns to ~ 10 hrs). Fig. III.7(c,d) shows the experimental results for $t_{Co} = 0.5$ nm and 0.8 nm. In order to verify the creep motion velocity regime Eq. 3.1, the authors plotted $\ln(v_{DW})$ vs $H^{-\mu}$ in Fig. III.7(d). A linear behavior was established at low field, thus validating the creep law and the universality of μ . The upper field limit, for which Eq. 3.1 was verified, was set to correspond to the depinning field. The authors reported a depinning field ranging from 230 Oe to 650 Oe and T_{dep}/T from 9 to 35 when increasing the Co thickness. Nevertheless, it is important to note actually Eq. 3.1 should be formally valid only for much smaller fields, and due to the smearing of the depinning transition at finite temperature, the depinning fields provided by the authors are rough overestimations. In addition, DW imaging depicts an uneven wall surface which hints the influence of the local disorder in the creep regime (see inset Fig. III.7(c)).

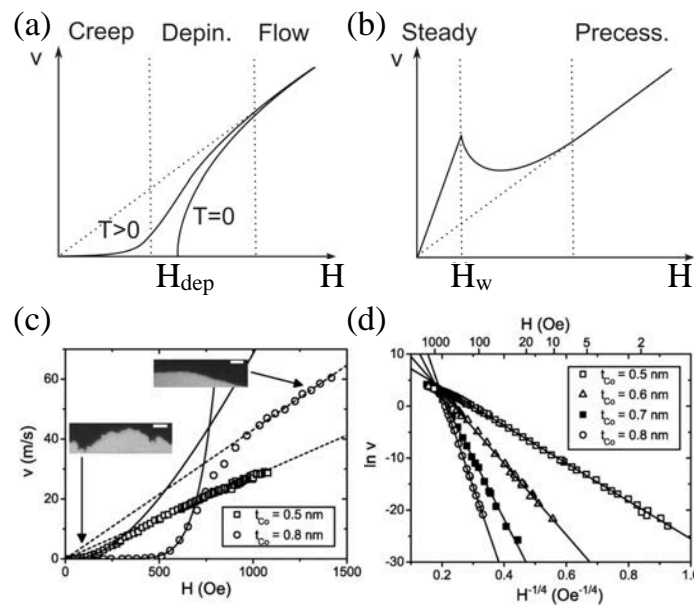


FIGURE III.7: (a) Theoretical DW velocity evolution as a function of applied field in a weakly disordered medium at $T = 0$ and finite temperature. (b) DW flow motion in a specimen free of pinning sites and exhibiting the Walker breakdown at H_w and the transition from a steady to precessional DW motion. (c) DW velocity vs applied field in the Pt/Co/Pt films studied in [17]. The dashed line indicates the linear behavior in the flow regime. (d) $\ln(v)$ vs the scaled applied field to verify the creep motion law. Figures adapted from [17].

Moreover, they successfully observed the DW flow motion for which the velocity exhibits a linear dependence on the applied field (Fig. III.7(c)). The results indicate the existence of a steady flow motion characterized by a DW velocity $v_{DW} = mH$, with m the DW mobility. m was found to vary between 2.8×10^{-2} to 4.3×10^{-2} m s $^{-1}$ Oe $^{-1}$ when increasing the Co thickness. Besides, the DW mobility in the flow regime depends mainly on the materials properties such as the gyromagnetic ratio, the Gilbert damping parameter and the DW width. Indeed, the MOKE images show a smoother DW which is an indication of the reduced relevance of the pinning effect at high field values (see inset Fig. III.7(c)). Furthermore, it becomes straightforward that a temperature variation will affect the DW velocity. Thermal dependence of the DW dynamics in ultrathin Pt(3.5 nm)/Co(0.45 nm)/Pt(4.5 nm) films was studied between 50 K and 300 K [18]. When decreasing the temperature, the shift of the DW velocity towards high-field regions was observed (see. Fig. III.8). This behavior was explained by an increase of both the elastic DW energy and the pinning energy barrier.

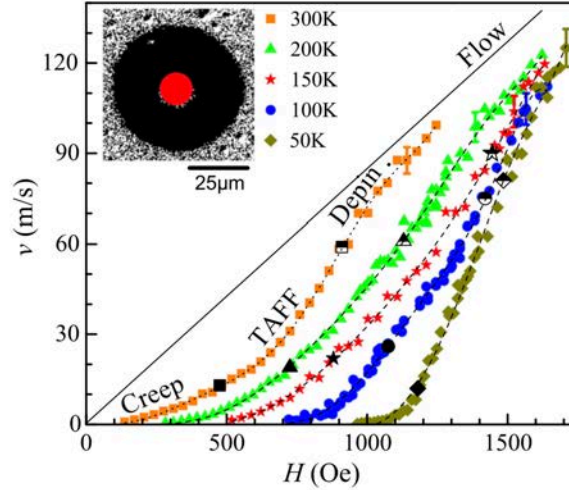


FIGURE III.8: Variation of the DW velocity in Pt/Co/Pt for different temperatures and applied field. A creep regime is observed followed by a thermally-assisted flux flow then the depinning transition. The solid line indicates the linear fit for the flow regime. Figure adapted from [18].

Finally, we discuss DW motion in the case of magnetization reversal and relaxation. We previously mentioned that in ultrathin films with PMA magnetization switching in imperfect specimens could occur via magnetic domain nucleation and/or domain wall propagation. The prevalence of nucleation or propagation strongly depends on the material properties and crystal imperfections. It can be intuitively expected that for a weakly disorder system, it is easier to propagate a DW than nucleating a magnetic domain. Conversely, due to the high demagnetizing field at rough edges and of inclusions, magnetization reversal in a disordered specimen would rather take place through domain nucleation, while the walls will be pinned. The domain nucleation rate R_N can be described as a Néel-Brown thermal process [19, 20]:

$$R_N = R_N^0 \exp\left(-\frac{E_N - 2HM_S V_N}{k_B T}\right) \quad (3.2)$$

with E_N the nucleation energy barrier, M_S the material saturation magnetization, V_N the characteristic volume of domain nucleation at the temperature T . Thus, the thermal activation over the barrier E_N gives a probability proportional to R_N to nucleate. Additionally, the Fatuzzo-Labrune model allows the description of thermally activated magnetization reversal in PMA films in terms of both nucleation and domain wall propagation [20–22]. A dimensionless parameter k is introduced as $k = \frac{v_p}{R_N r}$ for an initial domain of a radius r . The DW velocity is given also by a Néel-Brown-like law:

$$v_p = v_p^0 \exp\left(-\frac{E_p - 2HM_S V_p}{k_B T}\right) \quad (3.3)$$

where E_p is the propagation energy barrier, i.e. the pinning potential barrier, and V_p the propagation volume, i.e. in a jump-like motion this is the Barkhausen volume. The shape of the magnetization relaxation curve, thusly the value of k , gives information about the competition between nucleation and DW propagation. Indeed, for $k \gg 1$, the curve has a S-shape and the magnetization reversal is dominated by DW propagation. On the other hand, for $k \ll 1$, the relaxation curve has a L-shape and reflects a nucleation-dominated reversal process [20].

3.2 Electric field-driven DW motion

An alternative way to control DWs without an applied magnetic field is to use electric fields [23–25]. As we discussed in the previous section, DW motion in the creep regime depends on the disorder and pinning potential barrier. Therefore, the idea was to control the pinning strength, hence the DW mobility, via a voltage-induced change of magnetic anisotropy. The first attempts relied on an electric field-induced shift of DW velocity under the action of a magnetic field in perpendicularly magnetized ultrathin ferromagnets by a charge modulation of the pinning energy barrier [26–28]. Another possibility is to manipulate magnetic anisotropy via a voltage-induced strain in ferromagnetic/ferroelectric coupled heterostructures [23–25]. Indeed, Franke *et al.* reported deterministic DW motion triggered by out-of-plane electric field pulses in ferromagnetic (FM) CoFe grown on top of ferroelectric (FE) BaTiO₃ without any applied magnetic field [25]. Single-crystal BaTiO₃ exhibits alternating in-plane and out-of-plane FE domains, a and c, respectively. The rotation of the polarization at the a-c boundaries coincides with an abrupt change of the BaTiO₃ lattice structure. This results in a strong pinning of the FM domains on top of the FE boundaries due to the sudden rotation of the strain-induced magnetoelastic anisotropy in the top FM layer. The authors utilized electric field pulses to displace the magnetic anisotropy boundaries and the corresponding pinning potential in the elastically coupled ferromagnetic film in order to induce DW motion by local strain transfer. The results are shown in Fig. III.9. A positive bias voltage of 100V ($E = 2 \text{ kV cm}^{-1}$) leads to the shrinkage of c domains by moving the FE boundary. As a consequence of the strong elastic coupling, the FM must follow the displacement of the FE domain boundary [see. Fig. III.9(b)]. A negative field pulse drives the FM wall in the other direction. Large DW displacements of about $\sim \lambda$ were observed.

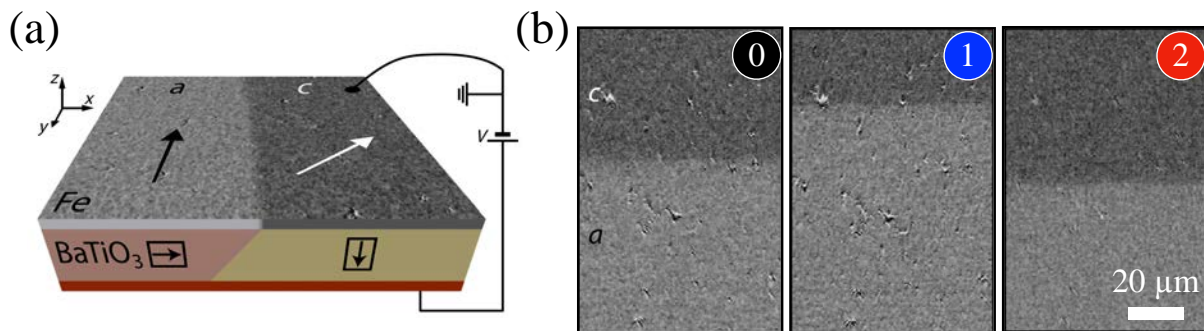


FIGURE III.9: (a) Schematic illustration and Kerr images of the CoFe/BaTiO₃ heterostructure with FE a and c domains. A bias voltage V is applied between the Fe and bottom Au (red) layers. (b) Kerr images showing the electric field-induced FM DW motion. (0) indicates the initial position. (1) [resp. (2)] after the application of positive (resp. negative) electric field pulse. Figure adapted from [25].

3.3 Current-induced DW motion

As we discussed in section 3.1, the conventional way to displace a DW is with magnetic fields. Yet, this approach has several drawbacks. First, two adjacent head-to-head and tail-to-tail DWs will move in opposite direction annihilating then each other. Second, scalability towards nanoscale memory devices is challenging for magnetic-field driven processes. A different approach than the manipulation of pinning strength with electric fields is the use of current to induce DW motion via spin-transfer torque (STT). We already described magnetization reversal by the mean of ultrashort current pulses via STT and spin-orbit torque (SOT) in section I.2.

The transfer of the spin of conduction electrons when moving across a magnetic texture such as a DW was predicted in the 1970s by Berger [29]. When a spin-polarized current is injected in a ferromagnet, the electrons flowing through the DW must align their spins with the local magnetization due to the exchange interaction. Since the exchange interaction conserves the total spin moment, angular momentum transfer from the spins to the local magnetization is expected. In other words, this results in a torque acting on the magnetization leading to a DW displacement in the direction of the applied current. Thus, a deterministic DW motion can be achieved. Two main mechanisms may be considered. The spins may precess around the local magnetization, and thus follow the direction of the magnetic moments. This so-called adiabatic process prevails in materials with low anisotropy and therefore large domain walls ~ 100 nm for instance in permalloys. Second, spin-flip scattering events may occur due to impurities. In this non-adiabatic process, due to the spin-orbit interaction, the spin is not conserved. Most of the first studies were carried out in NiFe permalloy wires with in-plane magnetization [30–32]. However, relatively high threshold current densities were necessary to depin a DW in the order of a couple 1×10^{12} A m $^{-2}$ [31, 33]. Additionally only few research groups reported high DW velocities above 100 m s $^{-1}$ using ultrashort current pulses [34, 35]. Moreover, controllable DW motion could not be reliably observed due to a stochastic behavior arising from thermal effects and local pinning [36].

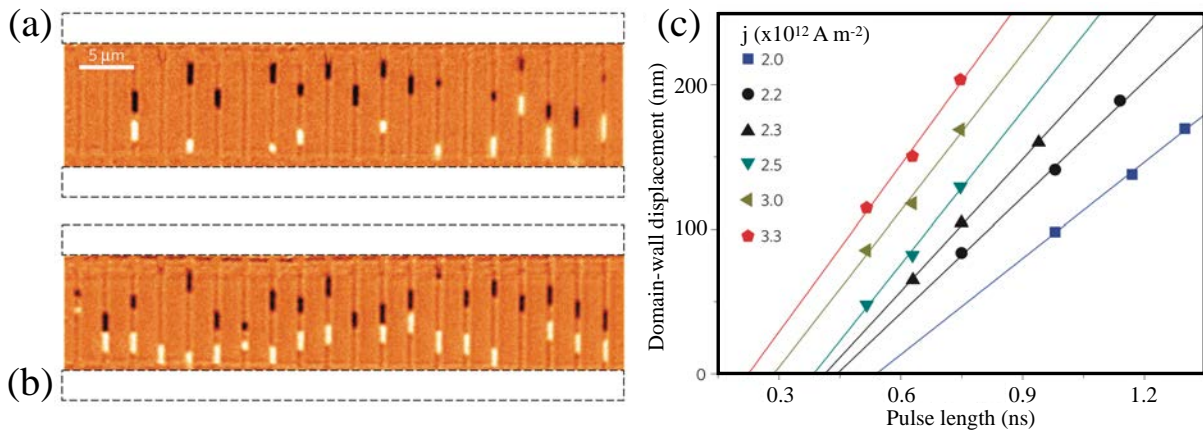


FIGURE III.10: (a) and (b) Differential Kerr micrographs showing DW displacement induced by 20×3.0 ns current pulses of density 1.2×10^{12} A m $^{-2}$ and 15×0.64 ns current pulses of density 2.6×10^{12} A m $^{-2}$, respectively. Black and white regions indicate the domain position before and after the pulse, respectively in 500 nm-wide and $10 \mu\text{m}$ long wires of Pt/Co/AlOx. (c) DW displacement as a function of current density and pulse duration. Figure adapted from [37].

As a consequence, researchers turned towards out-of-plane magnetized thin films with large PMA. For these materials, the non-adiabatic torque is expected to be much larger due to high spin-orbit coupling leading to lower threshold current densities [38]. Simultaneously, the rigidity of the narrow DWs (~ 10 nm) allows high DW velocities, for the Walker breakdown is repelled. Example materials include [Co/Pt] and [Co/Ni] multilayers [38, 39]. A reproducible DW motion induced by SOT was demonstrated in Pt/Co/AlOx wires with PMA and a velocity greater than 100 m s $^{-1}$ for a current density of $1.5 - 1.8 \times 10^{12}$ A m $^{-2}$ [40]. Similarly in a Pt/Co/AlOx wire with structural inversion asymmetry and high spin-torque efficiency, ultrashort current pulses of about 0.64 nanosecond led to a reproducible DW motion with a velocity of up to 400 m s $^{-1}$ as seen in Fig. III.10 [37]. The authors also studied the DW displacement as a function of the current pulse duration as shown in Fig. III.10(c) [37]. For a fixed current density, the DW velocity goes up with the pulse duration. It is predicted that the DW velocities

could reach up to 10 km s^{-1} for materials properly engineered with low damping. A complete review of current-induced DW motion can be found in [41].

3.4 Thermal gradient-driven DW motion

An alternative method to manipulate DWs is built upon thermal gradients. The application of a temperature gradient in a ferromagnetic can lead to spin accumulation or the creation of spin currents: this is called the spin-Seebeck effect (SSE). It was experimentally demonstrated by Uchida *et al.* in 2008 in NiFe films detected via the inverse spin Hall effect. Arising from the SSE, thermal spin transfer torques were theoretically predicted [42, 43] and experimentally proved in spin valves [44]. Naturally, it comes that these thermal STT could interact with magnetic textures the same way as with current pulses. Numerous theoretical studies confirmed this possibility [42, 45–49]. Two main mechanisms can explain thermally-induced DW motion. First, the so-called entropy field is said to drive the DW towards hotter regions due to the maximization of the entropy and hence a minimization of the DW free energy [48, 49]. This process rests on the temperature dependence of the material exchange stiffness and anisotropy. Nonetheless, a spin current can be seen as a current of angular momentum. Magnons carry also angular momentum and can transfer it to the local magnetization to induce DW displacement. Thence, a pure magnonic spin transfer torque may also occur and drag the DW, in some cases, towards hotter parts of a wire [42, 47]. The predominance of an entropic or magnon-based mechanism remains an open question and is still highly debated (see the comparative study in [49]).

In spite of the rich theoretical predictions, only few experiments reported thermal gradient-driven DW motion in ferromagnetic conductors. In 2012, Torrejon *et al.* demonstrated unidirectional DW motion in a NiFe nanowire induced by thermal effects [50]. By injecting ultrashort current pulses of high density $J = 3 \times 10^{12} \text{ A m}^{-2}$, a temperature gradient was introduced in the nanostripe. The authors revealed that the DW always moved towards the hotter region independently of the current polarity as shown in Fig. III.11(a). Moreover, they argue that the thermal effects either add to or reduce the DW displacement due current-induced STT. Another example of thermally-driven DW motion is the control of DW hopping with a laser in CoFeB nanowire that exhibits PMA [51]. As we previously discussed in section 2.3, in an imperfect specimen, driven by thermal fluctuations, a DW hops between two pinning sites (Barkhausen jumps). In zero magnetic field, the authors placed a laser tip in the vicinity of a nearby pinning sites and they were able to observe DW hopping towards the center of the laser spot, which is the hottest point (see. Fig. III.11(b)). This was explained by the temperature dependence of the saturation magnetization and anisotropy that leads to a reduction of the DW energy.

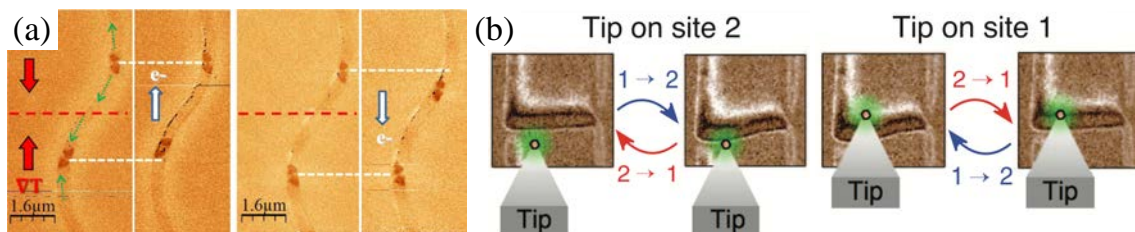


FIGURE III.11: (a) Vortex wall (VW) motion observed by MFM in a NiFe nanostrip induced by thermal effects and current pulses of 2 ns and $3 \times 10^{12} \text{ A m}^{-2}$. The upper (lower) VW is in a tail-to-tail (head-to-head) configuration [50]. (b) Laser control of DW hopping in CoFeB nanowire. The DW jumps towards the center of the laser spot, i.e. the hottest point [51].

4 Helicity-dependent all-optical domain wall motion

As we previously discussed, there were growing evidence of the importance of magnetic domains and DW mobility in the mechanism of HD-AOS, which was assumed to take place through a nucleation/propagation process in ferromagnets [1, 3]. Here, we demonstrate helicity-dependent all-optical domain wall motion in ferromagnetic films that show HD-AOS. This was hinted by Medapalli *et al.* [3]. In addition, we present an investigation of the laser position and power dependence on the induced-DW motion. Moreover, we study the influence of the linear polarization and the degree of light ellipticity, which will allow us to suggest a mechanism for the AODW motion.

4.1 Outline of the experiment

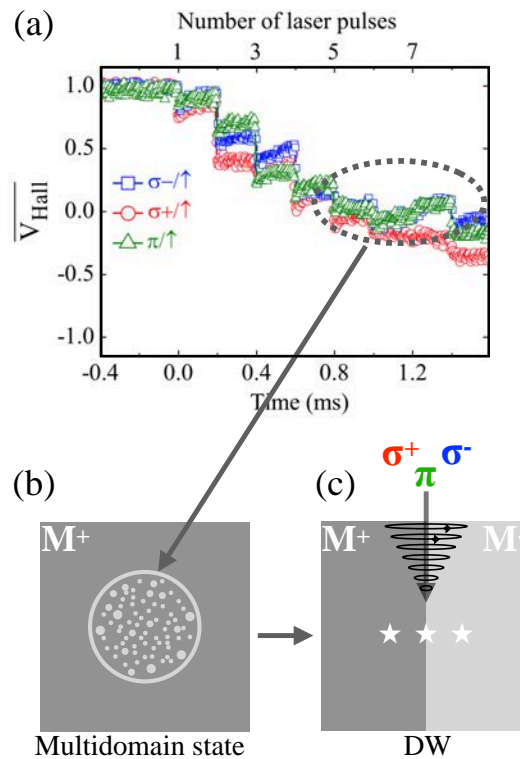


FIGURE III.12: Schematic representation of the principle of the experiment. (a) Helicity-independent demagnetization measured by El Hadri *et al.* in Pt/Co/Pt ultrathin film patterned into a Hall bar [1]. This demagnetization corresponds to a multidomain state as sketched in (b) that we simplify by creating a domain wall in an initially uniformly magnetized Pt/Co/Pt ultrathin film (c). Then, we place the center of the laser beam spot (represented by a star) at different distances with respect to the DW and for three light polarizations.

El Hadri *et al.* proved that HD-AOS in Pt/Co/Pt was a cumulative and multi-shot process via a helicity-independent demagnetization (multi-domain state) followed by a helicity-dependent magnetization switching [1]. Our aim was to study the mechanism of this helicity-dependent magnetization recovery assumed to result from helicity-dependent domain wall motion. Therefore, we were interested in studying the optical response of a DW upon ultrashort circularly or linearly polarized laser pulses. The principle of the experiment is depicted in Fig. III.12. We simplified the case of a multidomain state by nucleating a domain in an uniformly magnetized

ferromagnetic thin film with an out-of-plane magnetic field. Then after turning off the magnetic field, we placed a polarized laser beam at different distances from the DW. Further, we performed magneto-optical Faraday image recording with the same microscope we described in Chapter II. This allowed us to obtain the DW position as a function of time, i.e. against the number of laser pulses. We acquired one frame per second, hence the pulse resolution was governed by the laser repetition rate.

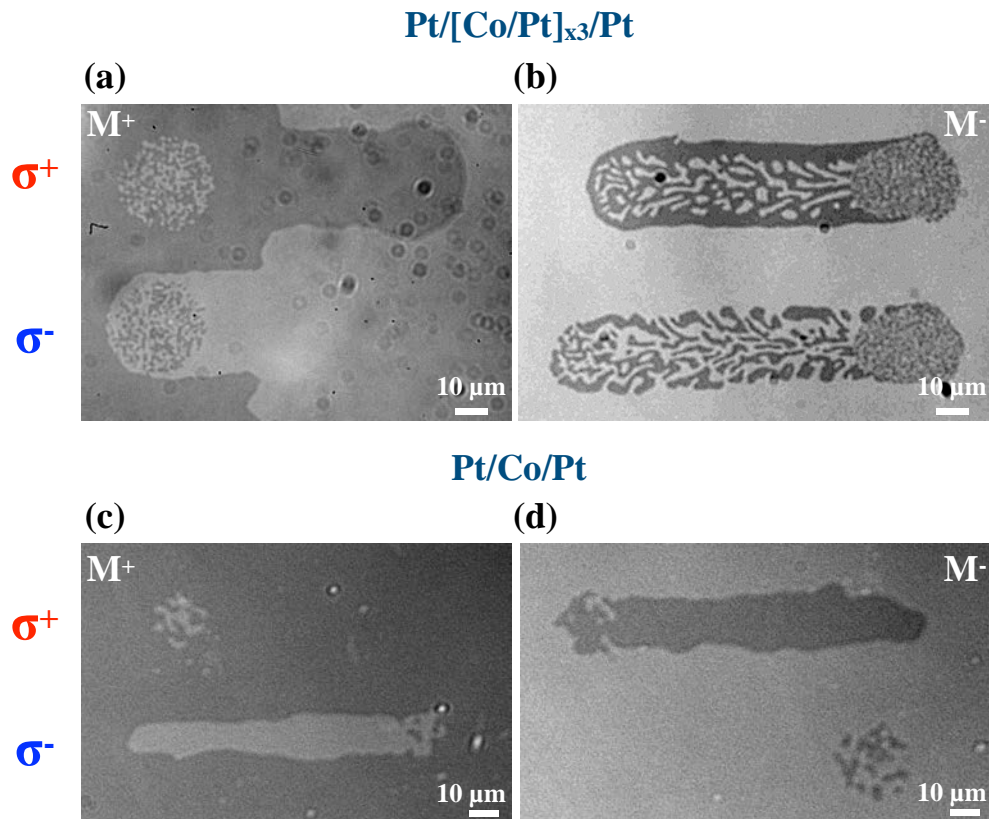


FIGURE III.13: Magneto-optical Faraday images after laser exposure in (a,b) (Co/Pt) trilayer and (c,d) single layer. Right-circularly (σ^+) [resp. left-circularly (σ^-)] laser beam is swept over the sample surface at a speed of $40 \mu\text{m s}^{-1}$. The dark (resp. bright) contrast corresponds to magnetization pointing up M^+ (resp. down M^-). In (a) laser pulses of 2 ps duration are sent to excite the material and HD-AOS is observed. In (b) 40-fs laser-pulse exposure leads only to thermal demagnetization. The (Co/Pt) single layer exhibits HD-AOS with a 40-fs laser beam (c,d). The laser fluence was set just above the fluence threshold of 0.44 mJ cm^{-2} and 14.5 mJ cm^{-2} for the (Co/Pt) trilayer and single layer, respectively.

This study was first initiated in the Center for Memory & Recording Research (CMRR) at the University of California San Diego (USA), where I was a visiting graduate student for a couple months. In the CMRR, we used a Ti:Sapphire laser producing laser pulses of ~ 2 ps duration at a central wavelength of 800 nm and with a full-width half-maximum (FWHM) of $45 \mu\text{m}$ and with a repetition rate of 1 kHz. This system was used to excite a (Co/Pt) trilayer grown by DC magnetron sputtering with the following stack: glass/Ta(5)/Pt(5)/[Co(0.4)/Pt(0.7)]_{x3}/Pt(2) (in parentheses the thicknesses in nanometers). Later, this work was continued in our lab at l'Institut-Jean Lamour (IJL) in Nancy (France). At l'IJL, we studied a Pt/Co/Pt single layer: glass/Ta(5)/Pt(4.5)/Co(0.6)/Pt(4.5) with the 40-fs laser system we described in Chapter II. It is important to note that two different laser systems and laser pulse durations (τ_{pulse}) were used in this study. The (Co/Pt) trilayer and single layer exhibit HD-AOS with 2-ps and 40-fs laser pulses, respectively when sweeping the laser beam as shown in Fig. III.13. Right-circularly

polarized (σ^+) laser pulses reverse the magnetization down (M^-). Conversely, left circular polarization (σ^-) switches the magnetization up (M^+). On the other hand, linear polarization (π) creates a demagnetized area. AOS was extensively studied in these ferromagnetic thin films [1, 3, 52, 53] and the cumulative mechanism of HD-AOS was demonstrated in the same systems we investigated. Notably, the (Co/Pt) trilayer film does not show HD-AOS with 40-fs laser pulses as seen in Fig. III.13. Moreover, the Faraday microscope in the CMRR did not allow us to image Pt/Co/Pt single layer since it has a very weak magneto-optical contrast. Then, we measured in both samples the switching threshold defined as the laser fluence above which a reproducible deterministic magnetization switching is achieved. A fluence threshold of 0.44 and 14.5 mJ cm⁻² were found for (Co/Pt) trilayer and single layer structures, respectively. We mention that the incident laser power P_i is measured in order to calculate the laser fluence F given by $F = \frac{P_i/f}{\pi D^2/4}$.

4.2 Observation of domain wall motion induced by circularly-polarized laser pulses

DW motion in Pt/[Co/Pt]_{x3}/Pt with 2-ps laser pulses

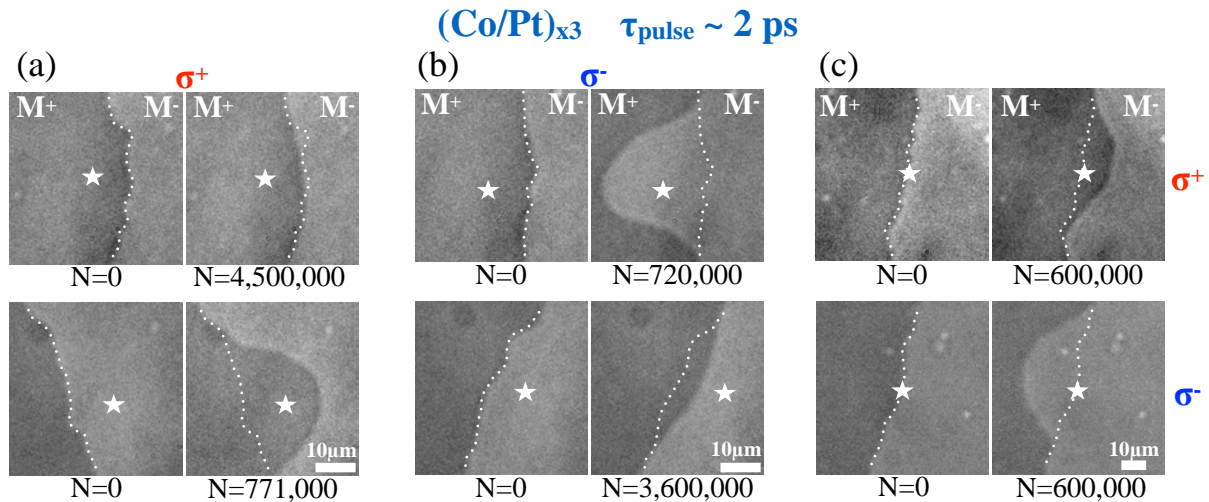


FIGURE III.14: Magneto-optical images of domain wall motion in [Co(0.4 nm)/Pt(0.7 nm)]_{x3} induced by 2-ps 1 kHz laser pulses with right-circular (σ^+) and left-circular (σ^-) polarization with an energy per pulse of 0.4 mJ cm⁻². (a,b) The center of the polarized laser beam spot is placed 10 μm away from the DW either on a M^+ or M^- domain. (c) The laser beam spot is centered on the DW. The white star indicates the location of the beam spot and N the number of laser pulses. The dotted line shows the initial position of the DW prior to laser exposure.

In order to investigate the optical response of a DW upon laser irradiation, we performed the experiments at a fluence lower than the switching threshold so that no reversed magnetic domains are observed. This is a necessary condition since the ferromagnetic films we studied exhibit HD-AOS. Therefore, the changes in the DW pattern can be attributed only to DW propagation and not to domain nucleation. Fig. III.14 shows the results for Pt/[Co/Pt]_{x3}/Pt exposed to 2-ps laser pulses at a fluence of 0.4 mJ cm⁻². In Fig. III.14(a,b), the center of the laser beam spot is placed 10 μm from the DW on either a magnetization-down or -up domain. The white star indicates the center of the beam. Thus, four combinations of light polarization and position of laser beam were studied, namely: (σ^+ , M^+), (σ^+ , M^-), (σ^- , M^+) and (σ^- , M^-). Notably, with a FWHM of $\sim 45 \mu\text{m}$, the laser beam spot overlaps both magnetic domains. Nonetheless, what is relevant is the position of the maximum of laser intensity, i.e. the location of the

hottest region with regard to the DW. When clear DW displacement (DWD) was observed, image recording was stopped after stabilization of the DW. Hence, the images displayed in Fig. III.14 correspond to initial and final DW configuration after N number of laser pulses. Only two combinations, (σ^+, M^-) and (σ^-, M^+) , led to significant DWD. As seen in Fig. III.14(a), when a M^- domain is exposed to σ^+ pulses, the DW moves in such a way that that the M^+ domain expands. On the opposite, a M^+ domain irradiated with σ^- polarization leads to an expansion of the M^- domain. More strikingly, when the laser beam spot is centered on the DW, the displacement direction of the DW is directly given by the helicity of the laser pulses as shown in Fig. III.14(c). Furthermore, for a σ^+ -polarized laser beam placed within a M^+ , no DWD was observed even after a tremendous amount of laser pulses (more than one hour of exposition) as seen in Fig. III.14(a). However, a small displacement can be detected with σ^- polarization when the beam is within a M^- domain in Fig. III.14(b). This can be explained by thermal fluctuations and the fact that laser beam spot was probably closer to the DW.

DW motion in Pt/Co/Pt with 40-fs laser pulses

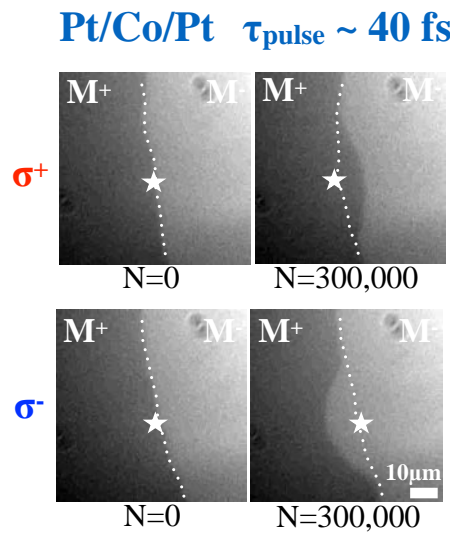


FIGURE III.15: Magneto-optical images of domain wall motion in Pt(4.5 nm)/Co(0.6 nm)/Pt(4.5 nm) induced by 40-fs 5 kHz laser pulses with right-circular (σ^+) and left-circular (σ^-) polarization with an energy per pulse of 12.5 mJ cm^{-2} . The laser beam spot is centered on the DW.

Similar results were obtained in the Pt/Co/Pt single layer exposed to 40-fs laser pulses with a fluence of 12.5 mJ cm^{-2} as depicted in Fig. III.15. However, a laser-induced DW motion could be reported only when the laser beam spot was located in the vicinity of the DW. The same helicity dependence of the DW displacement was observed. Indeed, for a centered σ^+ (resp. σ^-) -polarized laser, an expansion of the M^+ (resp. M^-) domain occurred. Interestingly, to induce DW motion in the Pt/Co/Pt single layer structure a much higher fluence is required than for the (Co/Pt) trilayer. This is actually related to the pulse duration dependence of all-optical switching. It was reported in a microscopic model [54] and experimentally proved [3] that deterministic switching is more efficient for longer laser pulses and takes place over a wider range of fluences. Consequently, AOS with shorter laser pulses is achieved at higher fluences.

Additionally, we found that the laser-induced DW motion in the Pt/Co/Pt single layer could be canceled with a small out-of-plane magnetic field of a couple Oersteds (< 5 Oe) whose direction depends on the light helicity. Comparably, the film has a coercivity of 500 Oe (see Fig. II.2).

For instance, the DW motion induced by σ^- -pulses was annihilated with an out-of-plane field pointing out in the opposite direction of the expanded domain as seen in Fig. III.16. Indeed, in position 1, σ^- pulses lead to a DW displacement and expansion of the M^- domain. On the other hand, in position 2, in addition to the σ^- laser beam the out-of-plane field is added at the same time and no significant displacement is detected. Besides, we verified that the magnetic field with itself alone was not able to induce any DW propagation. Interestingly, applying a field of the same amplitude perpendicular to the sample was also sufficient to cancel HD-AOS when sweeping circularly polarized light. The latter is in agreement with what was reported by Lambert *et al.* [52]. Therefore, this was a clear evidence that the direction of the induced-DW motion is intrinsically related to the reversal direction observed in HD-AOS. In fact, in sweeping measurements, σ^+ (resp. σ^-) polarization switches M^- (resp. M^+). Thus, we demonstrated deterministic DW motion with circular polarization and that depends on light helicity in all-optical switchable Co/Pt multilayers. We call this phenomenon helicity-dependent all-optical domain wall motion.

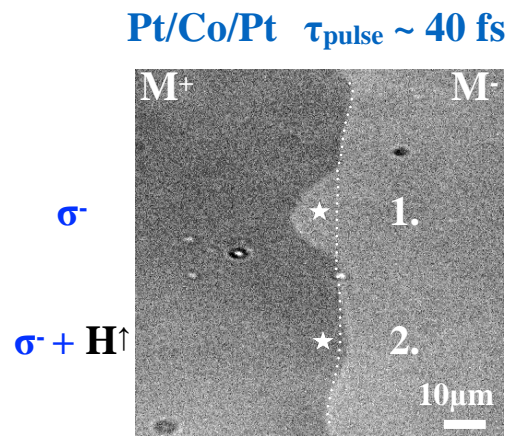


FIGURE III.16: Suppression of the laser-induced DW motion with an out-of-plane field in Pt(4.5 nm)/Co(0.6 nm)/Pt(0.7 nm) exposed to 40-fs laser pulses. In position 1. initially a σ^- beam is placed at $5 \mu\text{m}$ from the DW within a M^+ domain. In position 2. same as previously but a magnetic field of a couple Oe parallel to the M^+ domain is added.

Finally, one could notice that the induced displacements with σ^+ and σ^- polarizations are not equal as seen in Figs. III.14(c) & III.15. This can be explained by the non uniform distribution of pinning sites in the sample and around the created DW. As a result, in one direction the DW may sooner encounter a stronger pinning site. Similarly, a small laser power fluctuation might have the same consequences. At last, we mention that very few laser-induced DW motion experiments were reported in the literature. It was revealed that a single fs laser pulse could change the magnetic domain pattern in an epitaxial Co/Cu/Ni film with linear polarization [55]. However, no deterministic motion could be observed. On the opposite, Janda *et al.* gave evidence of inertial DW motion with ultrashort circularly polarized laser pulses [56]. This helicity-dependent DW motion was reported in a ferromagnetic semiconductor, and no direct connection with helicity-dependent all-optical switching was made.

4.3 Laser position and fluence dependence of domain wall motion

Influence of the laser beam position

Thereafter, we tried to more quantitatively investigate this helicity-dependent domain wall motion as a function of the laser beam spot position and laser power. Though, the study of the DW displacement as a function of time was possible only in Pt/[Co/Pt]_{x3}/Pt with 2-ps laser pulses. Indeed, the DW dynamics in the Pt/Co/Pt single layer with 40-fs and 5 kHz laser pulses was too fast to be resolved by the magneto-optical Faraday image recording technique we implemented. In Fig. III.17, we present the results obtained with 2-ps laser pulses in Pt/[Co/Pt]_{x3}/Pt. σ^+ polarization was used to induce DW motion. As illustrated in Fig. III.17(a), the center of the beam spot was placed either on the DW (position 1) or within a M^+ domain at 5 or 8 μm from the DW (position 2 and 3, respectively). First, one can see that the further the laser beam, the greater the final DW displacement. Indeed, a DWD of $\sim 22 \mu\text{m}$ was obtained for a laser beam - DW distance of 8 μm . Conversely, for a centered beam or at 5 μm from the DW, we report smaller DWD of 10 μm and 18 μm , respectively. Second, these plots reveal that the DW motion can be decomposed into three distinct regimes: (1) the DW slowly starts moving; (2) then it experiences a rapid displacement as the DW gets closer to the center of the laser spot, and finally (3), the speed decreases and the DW reaches a stable position. The first regime is absent when the center of the beam is on the DW, and thus the depinning process immediately takes place. In contrast, the three regimes are distinctly observed when the beam is 5 or 8 μm from the DW.

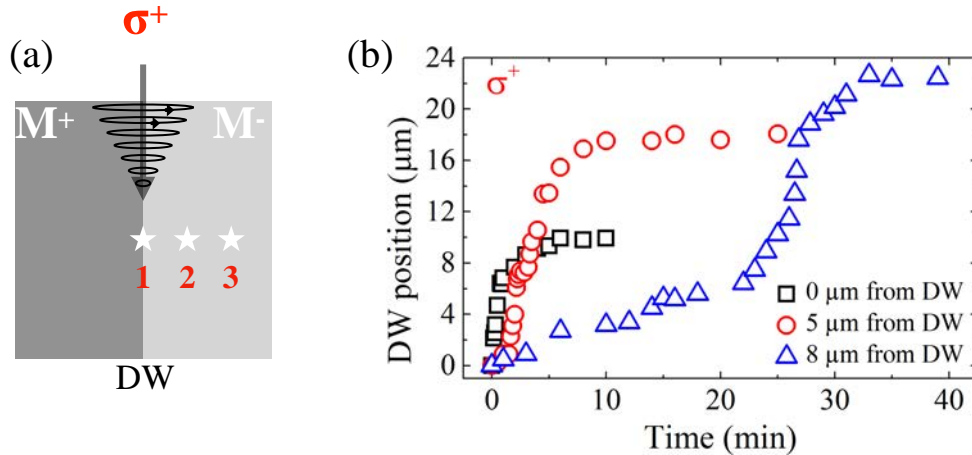


FIGURE III.17: Time evolution of the all-optical domain wall displacement as a function of the laser beam spot position as sketched in (a). The center of the σ^+ polarized beam is either placed at 0 (position 1), 5 (position 2) or 8 μm (position 3) from the DW. (b) DW displacement in [Co(0.4 nm)/Pt(0.7 nm)]_{x3} induced by 2-ps σ^+ -laser pulses and a fluence of 0.4 mJ cm^{-2} .

Furthermore, by taking the derivative of the DWD as a function of time, the DW velocity profiles are obtained for the three different laser beam spot positions as shown in Fig. III.18(a). The velocity profiles distinctly exhibit the three above-discussed regimes. As seen in Fig. III.18(b), the peak in the DW velocity coincides with the DW reaching the center of the laser beam. Then, when the DW moves further from the DW, the velocity dramatically drops. A maximum DW velocity of $\sim 20 \mu\text{m min}^{-1}$ was achieved for relatively low laser fluences of 0.4 mJ cm^{-2} . This corresponds to an average displacement of $\sim 0.3 \text{ nm}$ per 2-ps pulse. Note that we were limited by a resolution of 1000 pulses. A more accurate probing of the DW dynamics could be obtained

by improving the magneto-optical image acquisition with for instance a streak camera that allows a temporal resolution in the picosecond timescale. Moreover, one could notice that the maximum DW velocity in Fig. III.18(a) differs with the laser beam position, although the experiments were performed at the same laser fluence of 0.4 mJ cm^{-2} . This may result once again from pinning effects as the measurements were carried out in different places in the sample. Indeed, the DW motion is in the creep regime, and hence the influence of local defects is not negligible. Consequently, HD-AODW motion is stochastic due to the pinning effects, which makes a precise quantification of the maximum velocity and DW displacement complicated. This stochastic behavior can be seen in Fig. III.19 where are plotted the DW displacements for a centered σ^- polarized beam for four measurements in different locations but with the same laser fluence. It can be seen that the DW displacement ranges from 10 to $14 \mu\text{m}$. However, the modification of the material deposition technique could reduce the defect density and thus partially suppress the stochastic behavior.

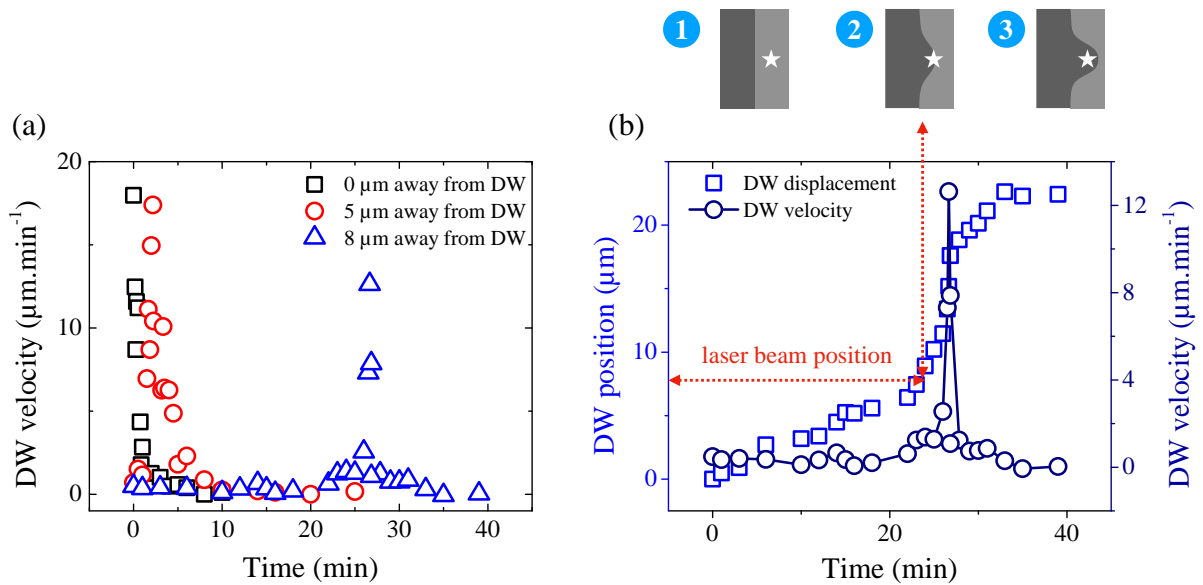


FIGURE III.18: Domain wall velocity profiles as a function of the laser beam position. (a) The DW velocity is obtained by taking the derivative of the DW displacement plotted in Fig. III.17(b). (b) Time evolution of the DW position and velocity for a σ^+ beam placed at $8 \mu\text{m}$ from the DW within a M^- domain. The three DW regimes are distinctly exhibited and can be correlated with the position of the center of the beam spot with respect to the DW as schematically illustrated. The rapid DW depinning coincides with a vanishing laser beam - DW distance.

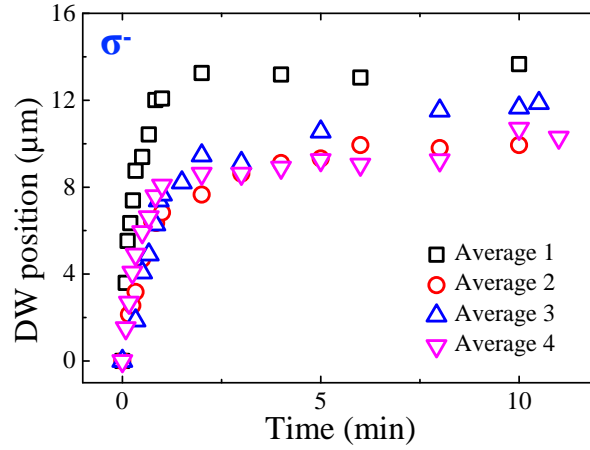


FIGURE III.19: Domain wall displacement induced by a centered σ^- laser beam in $[\text{Co}(0.4 \text{ nm})/\text{Pt}(0.7 \text{ nm})]_{\text{x}3}$ measured as a function of time at the same fluence of 0.4 mJ cm^{-2} in four different locations in the sample.

Influence of the laser beam fluence

Besides, the laser fluence dependence of the DW motion was studied. σ^- polarization was used to induce DW motion, and the beam spot was placed at $5 \mu\text{m}$ from the DW within a M^+ domain. As depicted in Fig. III.20, the higher the fluence, the faster the DW motion and the larger the displacement. Increasing the laser fluence only from 0.34 to 0.37 mJ cm^{-2} leads to a dramatic increase of the maximum DW displacement from 4 to $14 \mu\text{m}$ as seen in Fig. III.20(a). Likewise, the peak velocity goes from 1 to $100 \mu\text{m min}^{-1}$ (see Fig. III.20(b)). Yet, the DW reaches the same final position for $F = 0.36$ and 0.37 mJ cm^{-2} , thus indicating another limiting factor in addition to the laser fluence. The latter can be related to the distribution of pinning energy in the continuous film. Nevertheless, the DW speed for $F = 0.37 \text{ mJ cm}^{-2}$ is twice as large as for $F = 0.36 \text{ mJ cm}^{-2}$ as seen in Fig. III.20(b). A maximum DW displacement of $\sim 2 \text{ nm}$ per 2-ps pulse was achieved for the highest fluence. In addition, the fluence window in which significant DW motion is observed is extremely narrow. For a fluence larger than 0.37 mJ cm^{-2} , nucleation started to take place. In contrast, for a fluence below 0.34 mJ cm^{-2} no DW displacement was measured. These threshold values may vary over the sample surface due to local defects. The fluence dependence of laser-induced DW motion can be understood considering that the DW creep regime is a thermal activated process as discussed in section 3.1. Indeed, by providing more energy to the system (higher than the pinning potential barrier), the DW is likely to jump over several pinning sites. In other words, the Barkhausen jumps increase with the laser fluence. As a result, the depinning is more efficient when the DW is close to the center of the laser beam spot and for higher fluences. Also, for any laser beam-DW distance larger than $10 \mu\text{m}$, no DW motion was observed at any fluence (without nucleating a domain). This indicates the existence of a power threshold and thus a maximum initial distance between the DW and the laser center to achieve DW propagation. This maximum initial distance may be deduced from the abscissa of the power threshold on the laser Gaussian profile. Thence, the study of the DW dynamics allows us to correlate the depinning process to the energy brought by the laser and the beam position, i.e. the spatial energy (temperature) profile that the DW sees.

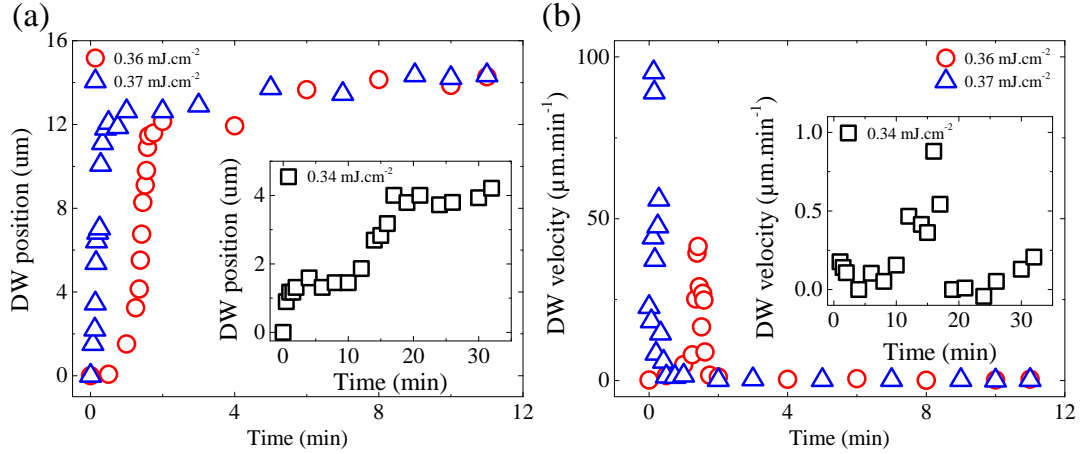


FIGURE III.20: Laser fluence dependence of all-optical DW motion in $[\text{Co}(0.4 \text{ nm})/\text{Pt}(0.7 \text{ nm})]_{\times 3}$ with 2-ps laser pulses. (a) DW displacement induced by a σ^- laser beam placed at $5 \mu\text{m}$ from the DW within a M^+ domain for three different laser fluences, and (b) the corresponding DW velocity profiles.

4.4 Effect of the linear polarization and degree of ellipticity on the domain wall

Effect of linear polarization on the domain wall motion

In order to understand how DW motion is induced by light, it is important to separate the effects due to the temperature, as the laser brings heat to the sample, and also due to the helicity. For this reason, we reproduced the same experiments as described for Fig. III.14 but with linear polarization (π) for which only an increase in the temperature system is associated with the optical excitation. The results are shown in Fig. III.21. In the Pt/Co/Pt single layer structure, a DW was created and then exposed to 40-fs linearly polarized light for three different laser beam positions. In Fig. III.21(a), the laser beam spot is centered on the DW, and no DW motion is observed. Indeed, this can be understood in the sense that the temperature profile with respect to the DW is symmetrical. Consequently, no specific direction for the DW to move in is preferred. However, this symmetry is broken when the laser beam is slightly off-centered ($< 5 \mu\text{m}$) on either a magnetization-up or -down domain as displayed in Fig. III.21(b,c). One can see that the DW moves towards the center of the laser beam independently of the magnetization direction. A fluence of 7 mJ cm^{-2} was required to break the DW symmetry. If the fluence is too low, no significant DW displacement is observed, thus indicating that the energy brought by the laser was not enough to overcome the pinning energy barrier. These findings demonstrate that in absence of helicity the DW tends to move towards the hottest region. This is in agreement with previous studies that reported DW motion in thermal gradients in ferromagnetic systems as we discussed in section. 3.4 [49–51]

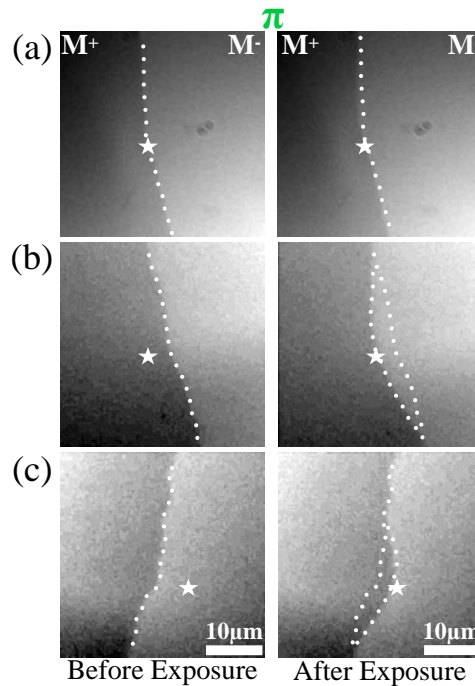


FIGURE III.21: (a)-(c) Magneto-optical images of a DW in a Pt(4.5 nm)/Co(0.6 nm)/Pt(4.5 nm) thin film irradiated with 40-fs linearly polarized (π) laser pulses with a fluence of 7 mJ cm^{-2} . The center of the laser beam spot, represented by a white star, is on the DW (a) and off-centered in (b) and (c).

Effect of the helicity on the domain wall motion

Afterwards, we investigated the laser-induced DW displacement as a function of the degree of light ellipticity ε . For right (resp. left) -circular polarization, $\varepsilon = \pi/4$ (resp. $-\pi/4$), and for linear polarization $\varepsilon = 0$. We measured the farthest stable DW position while gradually changing the angle θ of the quarter-wave plate (QWP), i.e., progressively introducing or reducing helicity in the optical excitation. A DW was created in the same material as before. Initially, the center of the laser beam was placed on the DW and the angle of the QWP was set to 0° . The polarization was changed by a step of 10° , and a magneto-optical image was taken only after stabilization of the DW. The results are presented in Fig. III.22(a), where normalized DW displacement is plotted against the degree of light ellipticity and QWP angle. The DWD is defined as the relative motion of the DW with respect to its initial position. The maximum DWD is reached when the sample is illuminated with circular polarization (σ^+ and σ^-), i.e., for $\varepsilon = \pm \pi/4$. Noticeably, the amplitude of the displacement is almost the same for both helicities; only the direction of the DW motion differs. Yet, there is a small shift of the curve that may be attributed to the nonuniform distribution of pinning sites on either side of the DW.

For linear polarization, $\varepsilon = 0$, the DWD is close to zero, which is consistent with the results in Fig. III.21. In addition, the evolution DW displacement with the polarization can be fitted with a sinusoid. This indicates that as the measurement was conducted in the same location in the sample, the laser-induced DW motion is reproducible and robust with regard to the light polarization that is used. Fig. III.22(a) shows that for a centered laser beam on the DW, linear and circular polarizations have antagonistic effects. Linear polarization brings the DW towards the hottest spot, while circularly polarized light tends to move the DW away from the center of the beam, i.e. towards colder regions. Nonetheless, even circular polarization brings heat to the sample. Therefore, the resulting displacement must be seen as a balance between the effect of helicity and temperature increase. Actually, Fig. III.22(a) highlights the competition between

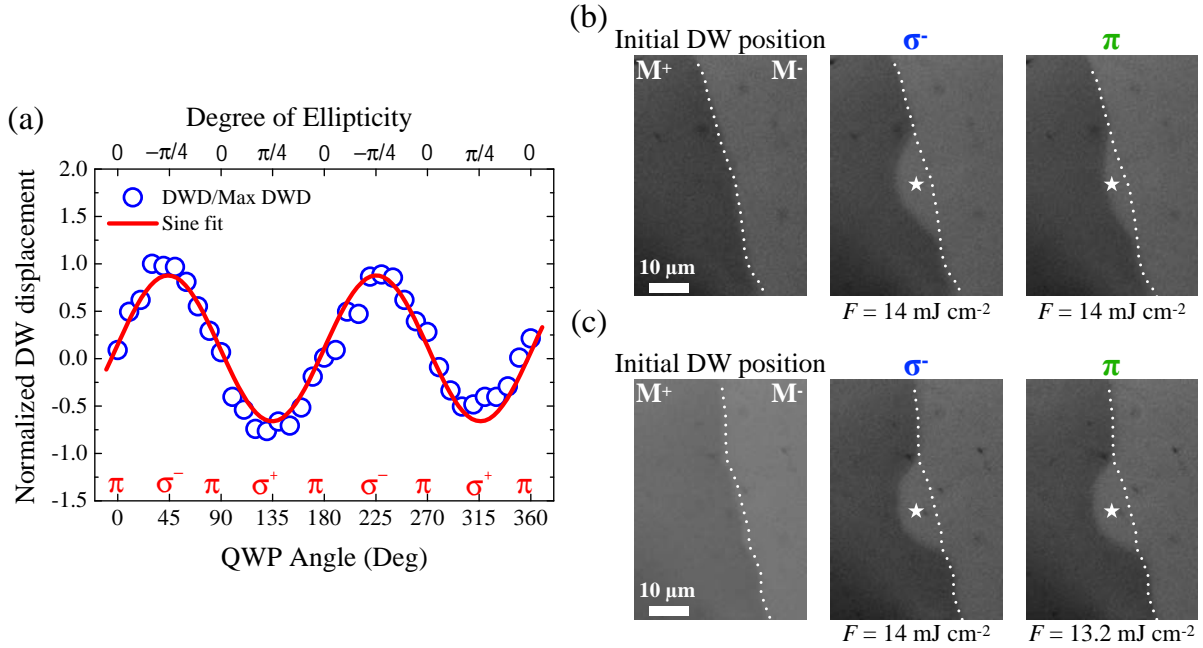


FIGURE III.22: (a) Normalized DW displacement induced by 40-fs laser pulses in Pt(4.5 nm)/Co(0.6 nm)/Pt(4.5 nm) plotted against the angle of the quarter-wave plate and the degree of light ellipticity. The fluence is set to 12.5 mJ cm^{-2} and the laser beam is initially centered on the DW. (b,c) Two-step DW motion sequence. Left-circularly polarized (σ^-) pulses are first sent to excite the Pt/Co/Pt single layer, then followed by linearly polarized (π) pulses. The laser beam is off-centered within a magnetization-up domain.

the two. Any amount of ellipticity ($\varepsilon \neq 0$), in other words angular momentum, introduced in the light induces a displacement that is then balanced by the temperature gradient, which tends to push the DW towards the hottest point. As the degree of ellipticity increases in absolute (ε from 0 to $-\pi/4$), the DW moves farther. By decreasing the light ellipticity (ε from $-\pi/4$ to 0), the temperature gradient gradually overcome the helicity effect, and the DW moves back to its initial position. When changing the sign of the light ellipticity, the DW moves in the opposite direction.

The opposing effects of linear and circular polarization are also revealed in a 2-step DW motion sequence as shown in Fig. III.22(b,c). An off-centered σ^- beam placed within a M^- domain is used to produce a DW displacement. Then linearly polarized laser pulses are sent to excite the material at the exact same position. In Fig. III.22(b), the laser fluence is kept constant throughout the experiment. One can see that linear polarization indeed brings the DW back towards the center of the beam spot, which is here the initial laser beam position with respect to the DW. In Fig. III.22(c), the laser fluence of linear polarization is reduced to 13.2 mJ cm^{-2} , and no reverse DW displacement is observed. Above this laser fluence, linear polarization systematically brings the DW towards the hottest point. The latter is a clear indication of the existence of a temperature difference threshold to induce DW motion. Thus, all the experiments give an unequivocal evidence that helicity-dependent all-optical DW motion triggered by laser excitation results from the balance of three contributions: the DW pinning, the effect of light helicity and the temperature gradient across the DW induced by laser heating. In the light of these findings, we can have a better understanding of the fluence dependence of the all-optical DW motion. To depin a DW, an energy barrier E_{dep} associated with a depinning field H_{dep} has to be overcome. For an off-centered circularly polarized beam, by increasing the fluence, the helicity effect and the temperature gradient across the DW both increase. Simultaneously, resulting from the temperature increase, the pinning barrier (resp. the depinning field) is lowered and

the Barkhausen jump goes up as proved in [11, 18, 19]. The latter is due to the fact that in the creep regime, DW motion is thermally activated. Thence, all of these changes make the depinning process more efficient and the DW more mobile as observed in Fig. III.20.

5 Mechanism and models of the helicity effect in laser-induced domain wall motion

In this section, we will first introduce a global overview of the mechanism taking place in HD-AODW motion. This will be examined with regard to the effect of temperature and helicity that we previously brought out. Then, we will discuss the microscopic origin of the effect of the helicity and its contribution to the laser-induced DW motion via an athermal or purely thermal mechanism.

5.1 General mechanism

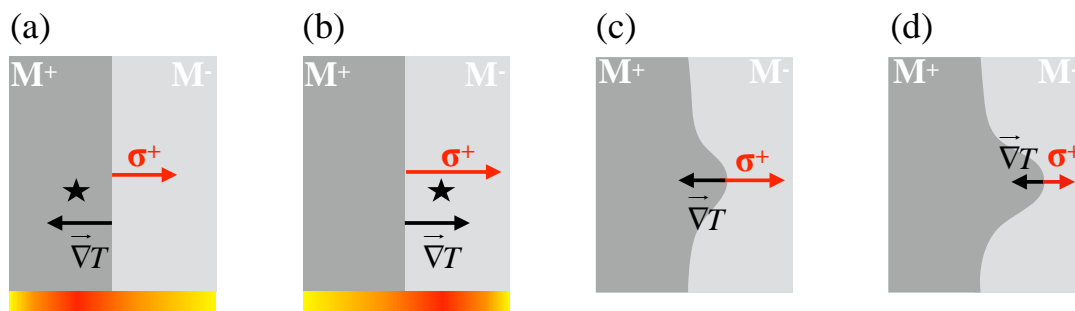


FIGURE III.23: Schematic representation of the mechanism of helicity-dependent all-optical domain wall motion resulting from the balance of the helicity effect, temperature gradient and the pinning for an off-centered σ^+ laser beam.

The influence of the increase of the temperature can be easily elucidated by studying the effect of linear polarization. The temperature gradient drives the DW towards the hottest region. On the other hand, it is more ambiguous for circular polarization, as σ^+ and σ^- polarizations not only carry angular momentum but also bring heat to the system. Yet, a pure helicity effect can be seen for a laser spot centered on the DW. Indeed, in this configuration, we saw that linear polarization, hence pure heating effect, cannot break the symmetry. In such configuration, the observed displacement gives the direction of the helicity effect. Let's take the example of an off-centered σ^+ polarization as seen in Fig. III.14. The mechanism is schematically drawn in Fig. III.23. When the center of the laser spot is on an M^+ domain, the temperature gradient tends to pull the DW towards the hottest area, i.e. to the left, and the helicity in the other direction as shown in Fig. III.23(a). As a result, all the effects cancel each other out, and the pinning barrier cannot be overcome. Thus, no displacement is observed. However, when σ^+ illuminates an M^- domain, the temperature gradient and the helicity add up and are stronger than the pinning. Consequently, they both pull the DW in the same direction leading to a large DW displacement as seen in Fig. III.23(b). Once the DW crosses the center of the beam spot, the temperature gradient changes direction as featured in Fig. III.23(c). Yet, the helicity effect can still overcome the temperature gradient. Therefore, the DW keeps on moving. As the DW gets farther from the center of the beam spot, the temperature gradient gets weaker but still competes with the helicity that is also diminished. In addition, the pinning also opposes to the displacement of

the DW. Hence, DW motion continues until equilibrium of the three contributions is reached as in Fig. III.23(d).

5.2 Inverse-Faraday effect

So far, we have discussed the observable effect of the helicity on the DW and how it competes with the temperature gradient. Though, we have not addressed the microscopic origin of this helicity effect yet. In the first chapter I, we presented several studies that attempted to explain the helicity dependence of AOS in ferromagnets with either the inverse Faraday effect (IFE) [54, 57] or the magnetic circular dichroism [58]. Hence, we will here discuss two possible mechanisms for light-induced DW motion based either on athermal or purely thermal effects of the helicity. First, let's consider the inverse Faraday effect. In the literature, a wide range of estimations for the IFE-induced field can be found from 0.1 to several tens of teslas [54, 59, 60]. In addition, it is often considered that the opto-magnetic field lasts longer than the pulse duration itself. The shortest femtosecond laser pulses are said to generate a field in the subpicosecond timescale [54, 60]. Indeed, for an IFE field of 20 T, a minimum duration of 0.15 ps was calculated in order to reproduce HD-AOS in Co/Pt films [54]. Nevertheless, here we will consider that the laser pulses produce an IFE field of the same duration. Besides, in our experiments we can expect a field value much lower since we used a laser fluence below the switching threshold.

To obtain the laser-induced DW displacement under the IFE assumption, we used the Fatuzzo-Labrune model [21, 22] based on the Néel-Brown like law that we have introduced in section 3.1. This model describes the external energy $E_{\text{ext}} = -\vec{M} \cdot \vec{H}$ that has to be brought when applying a magnetic field \vec{H} to overcome the pinning barrier E_{dep} and to make the DW move within a given volume, the Barkhausen volume V_B . Thus, the DW velocity is expressed as:

$$v_{H,T} = v_0 \exp\left(-\frac{E_{\text{dep}} - 2HM_S V_B}{k_B T}\right) \quad (5.1)$$

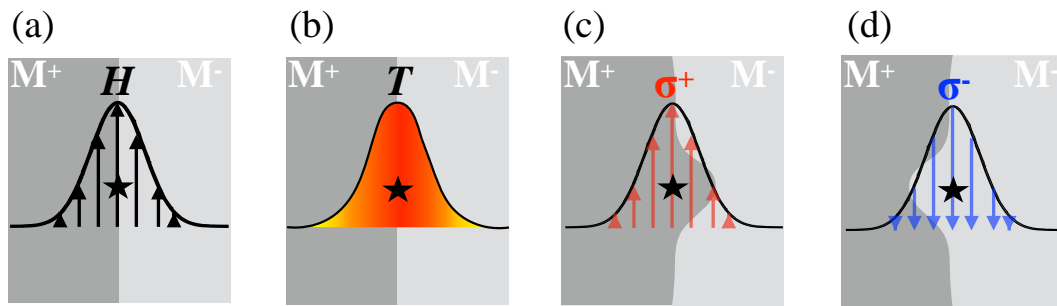


FIGURE III.24: Schematic representation of all-optical domain wall motion assuming an IFE-based mechanism. (a,b) The laser beam spot can be seen as a Gaussian distribution of effective magnetic field and temperature. (c,d) Opposite helicities lead to effective fields of opposite directions.

Indeed, it is clear that in our experiments the DW motion is dominated by pinning effects. Thusly, it is in a thermal activated creep regime characterized by Barkhausen jumps. Moreover, the laser fluence was chosen in a such way that no domain nucleation could be observed, but instead only DW propagation. Consequently, we can calculate the DW velocity as given by Eq. 5.1. In the following, we tried to model the DW motion in Pt/Co/Pt single layer induced by 40-fs circularly polarized laser pulses. Moreover, the laser beam can be represented by a

Gaussian distribution of effective magnetic field and temperature as schematically drawn in Fig. III.24(a,b). Taking into account the helicity-dependence of the direction of the IFE-induced field, σ^+ (resp. σ^-) pulses generate a distribution of positive (resp. negative) magnetic field as shown in Fig. III.24(c) [resp. Fig. III.24(d)] leading to an expansion of the M^+ (resp. M^-) domain. We assumed that the laser pulse would generate a maximum field of $H_0 = 10$ mT, which is five times less than the film coercivity. The circularly polarized laser pulse is also responsible for a temperature increase in the system. Hence, we calculated the laser temperature distribution using the two temperature model (2TM) which will be explained in greater details in the next section. It is important to note that both the induced magnetic field and temperature profiles have a spatial and temporal dependence. Therefore, it comes that:

$$\begin{aligned} H(x,t) &= H_0 \exp \left[-\frac{1}{2} \left(\frac{x}{\sigma_x} \right)^2 \right] \exp \left[-\frac{1}{2} \left(\frac{t}{\tau_L} \right)^2 \right] \\ T(x,t) &= T_e(t) \exp \left[-\frac{1}{2} \left(\frac{x}{\sigma_x} \right)^2 \right] \end{aligned} \quad (5.2)$$

where σ_x is the laser spatial standard deviation defined as $\sigma_x = \frac{FWHM}{2\ln(2)}$ with a FWHM $\simeq 50 \mu\text{m}$, τ_L is the laser pulse width of about 40 fs and $T_e(t)$ is the electron temperature as calculated in the 2TM [61, 62]. While the IFE field vanishes after several tens of 40 fs, the temperature electron slowly decays in the sub-microsecond timescale. The temperature relaxes back to room temperature between each laser pulse, since the repetition rate is fixed at 5 kHz (period of 0.2 ms). Thus, there is no heat accumulation. Furthermore, the DW velocity has a spatial and temporal dependence. The latter is implicitly expressed in Eq. 5.1 via the spatial and temporal dependence of the IFE field and the system temperature. $H(x,t)$ and $T(x,t)$ as calculated in Eq. 5.2 can be implemented in Eq. 5.1 to obtain the DW velocity profile $v_{H,T}(x,t)$ for a single laser pulse. Each combination of magnetic field and temperature $(H,T)[x,t]$ at a distance x from the center of the beam generates a DW displacement $u_{H,T}(x,t)$ at a velocity $v_{H,T}(x,t)$. Notably, the DW dynamics we previously reported were not pulse-resolved as a result we were not able to perform a fitting between our experiments and this model. Thus, we decided to test a set of parameters to verify the validity of an IFE-based model. We assumed a depinning barrier $E_{\text{dep}} = 29 k_B RT$ where k_B is the Boltzmann constant and RT the room temperature. Metaxas *et al.* reported a pinning barrier of about $14 k_B RT$ for a Pt(4.5 nm)/Co(0.6 nm)/Pt(3.5 nm) thin film with a low density of efficient nucleation sites [17]. However, in our samples grown by DC magnetron sputtering pinning effects are expected to be much stronger, that is why a higher value of the pinning barrier was chosen. Additionally, we took $V_B = 9.7 \times 10^{-18} \text{ cm}^3$ which is in the same order of magnitude than the Barkhausen volume for Co ultrathin films with PMA [11], and $v_0 = 2 \times 10^{-1} \text{ m s}^{-1}$ (deduced from the estimated maximum velocity per pulse) for a saturation magnetization M_S of 1400 emu cm^{-3} . The results for a centered σ^+ laser beam are shown in Fig. III.25(a). The spatial dependence of the IFE field is depicted. Fig. III.25(a) also displays the projection of the DW velocity profile of a single 40-fs σ^+ laser pulse for $t = 0$. Interestingly, the DW velocity is contained over a narrower range of position x . Indeed, for $x \gtrsim 10 \mu\text{m}$ the DW velocity is almost vanishing. This is consistent with what we observed. In fact, no DW displacement could be reported for an initial distance between the center of the beam spot and the DW greater than $10 \mu\text{m}$. Moreover, although high velocities can be reached, the DW velocity is characterized by a temporal width of only 28 fs. Hence, the DW velocity is nonzero only around the peak values of the IFE field.

To calculate the DW displacement, we proceeded as follows. First let's assume a σ^+ centered laser beam on the domain wall, i.e., $x = 0$. The DW displacement $u_{H,T}(0,t)$ is defined as:

$$\begin{cases} u_{H,T}(x = 0, 0) = 0 \\ u_{H,T}(x = 0, t + \delta t) = u_{H,T}(x = 0, t) + v_{H,T}[u_{H,T}(x = 0, t), t + \delta t] \times \delta t \end{cases} \quad (5.3)$$

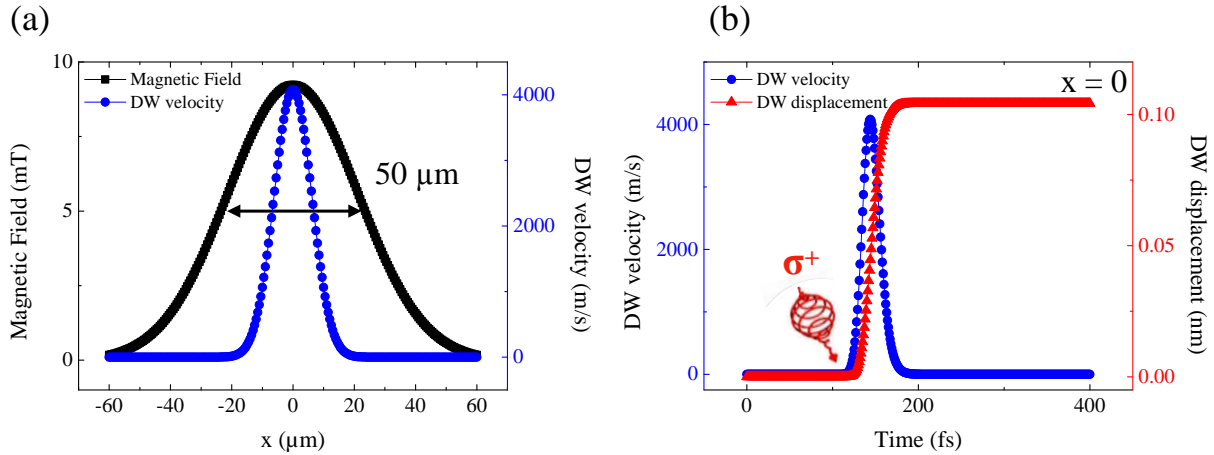


FIGURE III.25: Results of the numerical simulations of all-optical domain wall motion under the assumption of IFE. (a) The spatial dependence of the effective magnetic field and corresponding DW velocity profile are shown. (b) The calculated DW displacement as a function of time is displayed along with the temporal dependence of the velocity.

We took a step of $\delta t = 1$ fs to compute the DW displacement. The result is depicted in Fig. III.25(b). A displacement in the sub-nanometer scale is found in agreement with what we estimated in our experiments (~ 0.3 nm per pulse). To deduce the DW displacement in the same timescale as we reported in section 4.2, one would need to compute Eq. 5.3 for $N_{\text{pulses}} = 300,000$ by reinitializing the initial condition with the final DW displacement reached after the i^{th} pulse. However, this was not possible with our computing capabilities. It is expected that for the first laser pulses, the DW will linearly propagate. Then as it gets further from the center of the beam, its velocity will decrease until it completely stabilizes. Now if we assume a σ beam placed within a M^+ domain then $E_{\text{ext}} = +HM_S$. This leads to a vanishing DW velocity profile calculated as previously. On the other hand, if a σ^+ beam placed within a M^+ then $E_{\text{ext}} = -HM_S$, and a DW displacement similar than in Fig. III.25(b) can be seen. Thence, this a clear indication of the helicity-dependence of laser-induced domain wall motion.

However, a better understanding of the parameters controlling DW motion in our Pt/Co/Pt ultrathin films, such as the pinning barrier, the pinning site density and the Barkhausen volume, would be required to conduct a deeper study of an IFE-based mechanism. Indeed, we tested one set of parameters in Eq 5.1, ideally these should be deduced from a fitting with the experiment. It would certainly yield more realistic values of the DW velocity. In addition, it is known that DWs can experience inertia motion as demonstrated by Janda *et al.* in a ferromagnetic semiconductor irradiated with ultrashort circularly polarized laser pulses [56]. In fact, the DW motion is likely to pursue for a certain time while the laser pulse is off. The DW inertia will have a direct impact on the calculation method of the displacement $u_{H,T}$ as it will determine the value of the step δt . Finally, we have neglected the temperature dependence of the pinning energy, while as the temperature increases upon laser illumination, the pinning barrier is expected to reduce and ease DW motion [18]. Nonetheless, we were able to prove that helicity-dependent all-optical domain wall motion can be reproduced with the inverse Faraday

effect. A single small effective magnetic field pulse of 10 mT with a duration of 40 fs engenders a DW displacement of ~ 0.1 nm. It also provides a DW dynamics similar to what we observed.

5.3 Magnetic circular dichroism: calculation of the thermal effective field

One could argue that the DW motion we reported results only from purely thermal effects, namely, magnetic circular dichroism (MCD) combined with a laser heating close to the Curie temperature. Several studies have explained HD-AOS with a mechanism solely based on MCD effects in GdFeCo [63] or ferromagnetic materials [58, 64] as we already discussed in the first chapter I. MCD indicates a difference in light absorption between left- and right- circular polarization for a given magnetization state. Conversely, left- (resp. right-) circular polarization will absorb different amounts of light if it illuminates a material with a magnetization pointing up or down. As in our experiments the laser beam spot overlaps with two domains of opposite magnetization directions, a difference in absorption of the M^+ and M^- domain would result in a temperature difference and thus a temperature gradient across the DW. As we discussed in section 3.4, a thermal gradient can induce DW motion via thermal spin transfer torques or a thermal field [48–51]. Exposed to a thermal gradient, a DW is driven towards hotter regions in order to minimize its free energy. Torrejon *et al.* performed a thermodynamic modelling of the effect of a thermal gradient across a DW [50]. They found that a temperature gradient would induce an effective magnetic field given by:

$$H_T = \frac{\sigma_s}{2\mu_0 M_s (T_c - T_0)} \frac{dT}{dx} \quad (5.4)$$

where σ_s is the DW surface energy, μ_0 the vacuum permeability, T_c the material Curie temperature, T_0 room temperature and $\frac{dT}{dx}$ the temperature gradient along the (Ox) direction perpendicular to the DW. To depin the DW, the thermal field has to be greater than the depinning field. The latter gives a condition of the minimum temperature difference in order to observe DW motion, which can be related to the value of MCD in the material. Consequently, here we tried to see whether HD-AODW motion in Pt(4.5 nm)/Co(0.6 nm)/Pt(4.5 nm) induced by 40 fs laser pulses could be explained by a thermal field whose direction depends upon light helicity.

To verify the possibility of a MCD-based DW motion mechanism, the first step is to calculate the temperature difference resulting from the MCD. The calculations were based on the two temperature model. The 2TM was used to study ultrafast magnetization dynamics induced by ultrashort laser pulses in FePt and (Co/Pt) multilayers [61, 62]. Unlike for the phenomenological 3TM, which was used to explain ultrafast demagnetization in Ni films [65], in the 2TM only two coupled reservoirs are considered, namely: the electrons (T_e) and the lattice, i.e., the phonons (T_p). The absorption of the laser energy occurs only in the electronic bath. Thence, a system of rate equations can be defined which allows to determine the time evolution of the electron and phonon temperatures:

$$\begin{aligned} C_e \frac{dT_e}{dt} &= -G_{ep}(T_e - T_p) + P(t) - C_e \frac{(T_e - T_0)}{\tau_p} \\ C_p \frac{dT_p}{dt} &= G_{ep}(T_e - T_p) \end{aligned} \quad (5.5)$$

where C_e and C_p are the specific heat of the electrons and the phonons, respectively, G_{ep} is the coupling constant between the two reservoirs. $P(t)$ is the absorbed laser energy. A third term is added to take into account the heat diffusion to the substrate and is characterized by a time constant τ_p . Under the free electron approximation, $C_e = \gamma_e T_e$, while C_p is set constant. Importantly, we assume a thermalization of all the layers composing our sample. Thus, no dependence of the temperature through the thickness of the material is examined here. The parameters ruling the temperature of each bath is usually deduced from a fitting with time-resolved MOKE measurements. Instead, here we will take values found in the literature. A electron specific heat capacity of $800 \text{ J m}^{-3} \text{ K}^{-2}$ was taken, which is in the same order of magnitude than what can be found in the literature [66] (and refs. therein). A phonon capacity of $3 \times 10^6 \text{ J m}^{-3} \text{ K}^{-1}$ was assumed. A electron-phonon coupling constant of $1 \times 10^{18} \text{ W m}^{-3} \text{ K}^{-1}$ was chosen which is similar than for transition metals [61, 67]. The heat diffusion time into the substrate was set to 340 ps as in [61], although it is found that this term has no major impact on the electron temperature dynamics. We assumed that 10% of the laser fluence (12 mJ cm^{-2}) is absorbed by the electrons. Fig. III.26 shows the calculated electron and lattice temperature upon laser irradiation. A laser heating well above T_c , which is $\simeq 650 \text{ K}$ in (Co/Pt) multilayers [66, 68, 69], is observed. However, we note that the peak electron temperature and the broad increase of the lattice temperature highly depend on the values chosen for C_e and C_p . A more accurate estimation of the temperatures would be obtained with the parameters extracted from TR-MOKE measurements. Nonetheless, our aim here is only to discuss the possibility of a DW depinning mechanism via a pure thermal process.

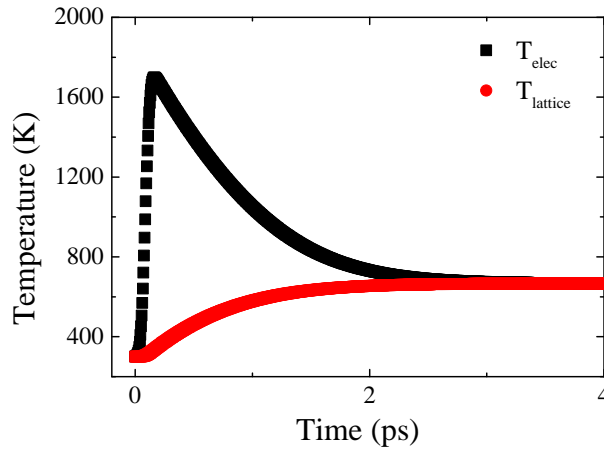


FIGURE III.26: Time evolution of the electron and lattice temperature as resolved from the two temperature model.

Now to take into account the MCD, we introduce two different electron temperatures $T_{e, x < 0}$ and $T_{e, x > 0}$ which correspond to the temperature of an electron in a M^+ or M^- domain, respectively as featured in Fig. III.27. Let's consider a σ^+ laser beam centered on the DW. Due to the MCD, $T_{e, x < 0}$ and $T_{e, x > 0}$ will be different and a temperature gradient across the DW will arise. The absorbed laser power to calculate the two electron temperatures can be expressed as:

$$P(t) = \begin{cases} P_0(1 - MCD) \exp\left[-\frac{1}{2} \left(\frac{t}{\tau_L}\right)^2\right], & \text{if } x > 0 \\ P_0 \exp\left[-\frac{1}{2} \left(\frac{t}{\tau_L}\right)^2\right], & \text{if } x < 0 \end{cases} \quad (5.6)$$

where P_0 is proportional to the absorbed fluence and MCD the difference in absorption ($A^{+/-}$) between left- and right-circular polarization defined as $MCD = 2 \frac{A^+ - A^-}{A^+ + A^-}$ (in %) and $\tau_L = 40$

fs is the laser pulse width. Eq. 5.6 can be implemented in the 2TM in order to calculate the electron temperature in the corresponding magnetic domain. We varied the MCD between 0 and 5%. Fig. III.27(a,b) show the time evolution of the temperature difference ($T_{e, x>0} - T_{e, x<0}$) as a function of the MCD . Within the first hundreds femtosecond following the laser pulse, the temperature difference between the two magnetic domains reaches a high peak between 5 and 45 K depending on the MCD as seen in Fig. III.27(a). As a comparison, based on *ab initio* calculation of the dielectric tensor, John *et al.* found a temperature difference of 40 K due to the MCD in FePt upon femtosecond laser excitation [57]. In the longer timescale after the rapid decay of the electron temperature, the system slowly relaxes back to room temperature, and the temperature difference between the two domains varies between 2 and 18 K at 30 ps [see. Fig. III.27(b)]. The question now is: which timescale is relevant for the temperature difference, hence the thermal gradient, with regards to laser-induced DW motion? The answer will highly depends on the DW inertia following the laser excitation. Though, we saw in the previous section that the DW velocity rapidly vanishes after the triggering of the laser pulse. Therefore, as a result of the ultrashort pulse width, in a first approximation we can consider only the peak value of the temperature difference to deduce the thermal gradient. Thus, it is found that, for a domain wall width $\delta \simeq 10$ nm, the thermal gradient ranges from 0.5 to 4.5 K nm⁻¹. For a $MCD \geq 1\%$, the calculated thermal gradient is ten times greater than the gradient resulting from ns current pulses which was demonstrated to induce DW motion in NiFe nanostrips [50].

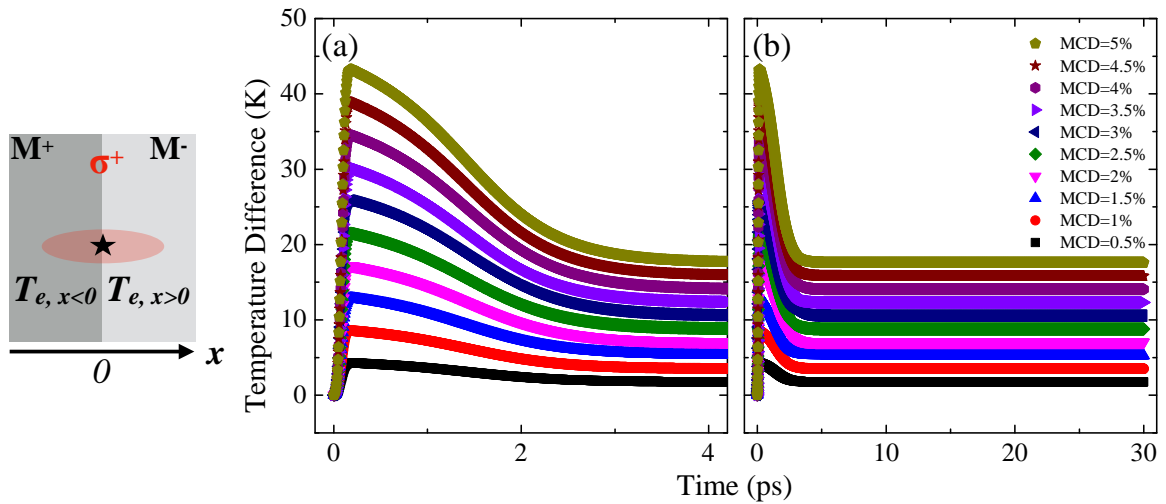


FIGURE III.27: Time evolution of the electron temperature difference between a magnetization -up and -down domain for a σ^+ laser beam centered on the DW over (a) a short or (b) broader timescale.

Now we can estimate the thermal field given by Eq. 5.4 for a DW surface energy of 8 mJ m⁻² as expressed in Eq. 2.14. It comes an effective magnetic field that increases with the MCD from 2.5 mT to 28 mT. If we compare these values with the previous DW motion modelled with the IFE, we can say that a MCD of 1% that generates an effective field of ~ 8 mT is sufficient to induce DW motion. Similarly, a σ^- laser beam centered on the DW will result in a negative temperature difference, and thus in a negative effective field that will pull the DW in the other direction. Thus, at this point it seems that helicity-dependent all-optical domain wall motion can also be explained by pure thermal effects. To have a precise condition on the minimum MCD to observe DW displacement with circularly polarized light, one would need to know the depinning field at the laser temperature. At room temperature, Metaxas *et al.* reported a depinning field of 59 mT in ultrathin Pt/Co/Pt [17]. As the creep regime is thermally activated, a much lower value is expected due to high laser heating. To date, no studies have explored the temperature dependence of the depinning field well above room temperature. Although the

temperature difference we calculated depends upon the set of parameters taken in the 2TM, it appears that MCD may produce an effective field high enough to depin a DW. This is consistent with a previous work in which the authors stated that a MCD of 0.5 % would be sufficient to observe helicity-dependent multishot magnetization switching in ferromagnets [58]. However, in our all thermal model we have implicitly assumed that σ^+ (resp. σ^-) laser pulses absorb more in a M^- (resp. M^+) domain. The sign of the MCD determines the direction of the thermal gradient. Hence, it would be important to measure the sign of the MCD to confirm or not the pure thermal mechanism of AODW motion. Indeed, a negative MCD would indicate a negative effective field for σ^+ pulses, which would lead to an expansion of the M^- domain while we observed the opposite.

5.4 Measurement of the magnetic circular dichroism

Here our aim is to experimentally determine the sign of the MCD. One could find in the literature for (Co/Pt) MLs values of the MCD or Kerr ellipticity as they are related over a wide range of wavelengths [70–73]. However, to be able to conclude on the HD-AODW motion mechanism, one would need to make sure that the definition of left- and right-circular polarization is the same that we used. Another question remains regarding to the true orientation of the magnetization of the (Co/Pt) films in these studies. Hence, our aim was to perform direct measurements of the MCD *in situ*, i.e., in the same experimental setup used for HD-AOS experiments. This would allow us to make a comparison between the sign of the MCD, i.e., which helicity absorbs more for a given magnetic state, with the reversal direction observed in AOS.

For a photon energy of 1.5 eV, the Kerr ellipticity is significantly reduced in (Co/Pt) MLs as shown in [70, 73]. Moreover, these studies were performed on (Co/Pt) films with a high number of repeats ($N = 33 - 66$), while we worked on a single layer Pt(4.5 nm)/Co(0.6 nm)/Pt(4.5 nm) structure. Not only do we expect a small light absorption in our sample, but also a small difference between σ^+ and σ^- polarization considering the thickness of the magnetic medium in our sample. To verify the former, we computed the laser absorption profile in the Ta/Pt/Co/Pt system via a transfer matrix method. The complex refractive indices ($\tilde{n} = n + jk$) of each layer of our sample were extracted from [74] and are summed up in Table III.1:

Layer	n	k	thickness (nm)
Ta	0.99	7.29	5
Pt	0.58	8.08	4.5
Co	0.65	7.59	0.6

TABLE III.1: Complex refractive indices of each layer in Ta/Pt/Co/Pt.

We considered that the structure is illuminated through the glass substrate as in our AOS experiments. The computed absorption profile is depicted in Fig. III.28. Only 9.3 % of light is absorbed in the whole stack. While most of the absorption takes place in the first Ta layer, the magnetic layer absorbs only 0.3 % of the incident light. Thus, Ta(5 nm)/Pt(4.5 nm)/Co(0.6 nm)/Pt(4.5 nm) is not an ideal candidate to measure the MCD as it would require a highly sensitive photodetection method. It is necessary to find a material that not only exhibits HD-AOS but also has a larger absorption and Kerr ellipticity. Hence, we propose to perform such measurements in a ferrimagnetic CoTb alloy: Ta(2 nm)/Co₇₀Tb₃₀(20 nm)/Pt(2 nm). Indeed, El Hadri *et al.* demonstrated that the mechanism of HD-AOS in ferrimagnetic CoTb alloys was the same than in (Co/Pt) films, i.e., a multishot and cumulative process [1]. Therefore, the

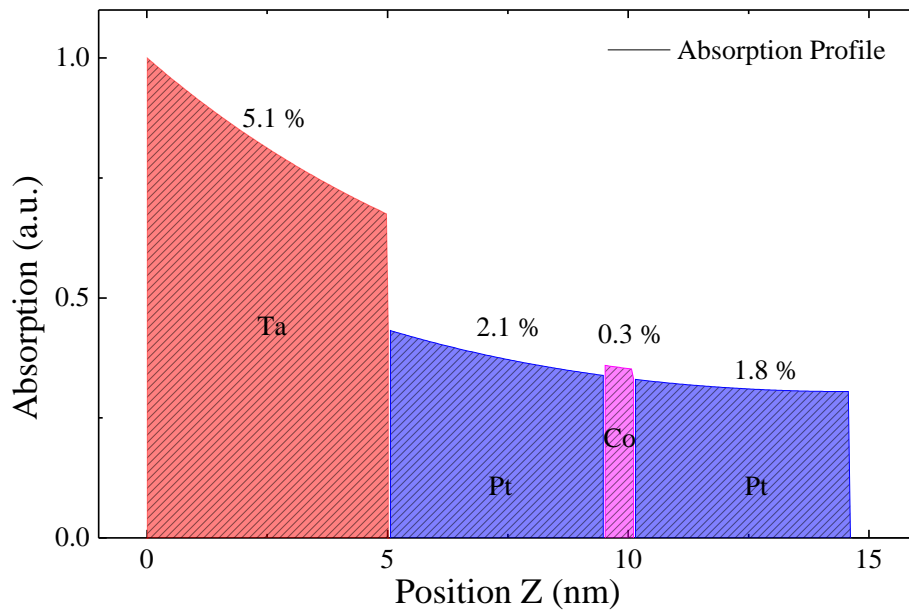


FIGURE III.28: Absorption profile in Ta/Pt/Co/Pt multilayer at 800nm.

conclusions about the relation between the sign of the MCD and the reversal direction in AOS should be the same for (Co/Tb) and (Co/Pt) films.

Outline of the experiment

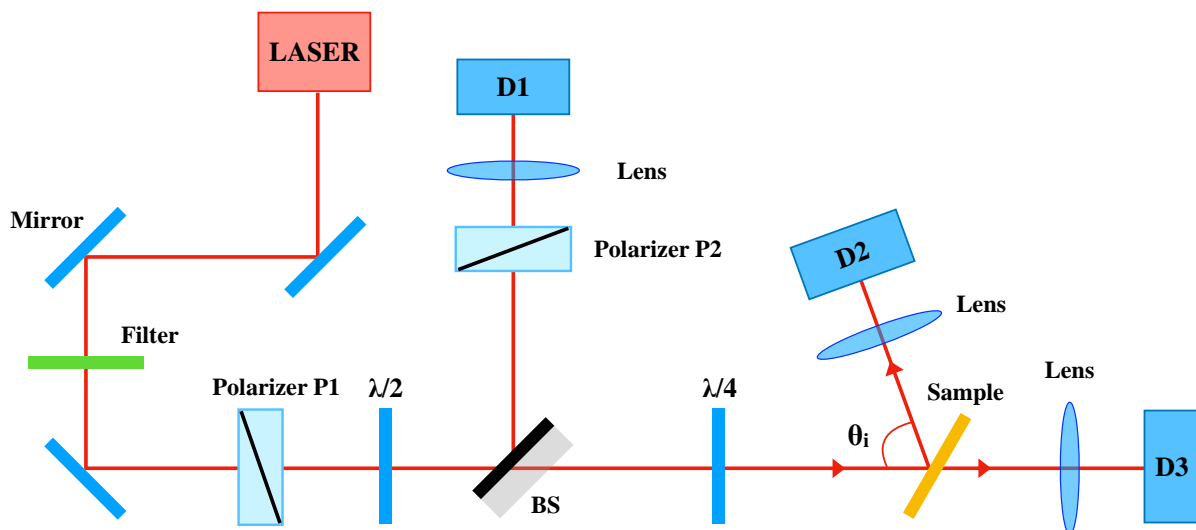


FIGURE III.29: Schematic representation of the experimental setup to measure the transmission and the reflection of the sample.

In order to access the magnetic circular dichroism, the absorption of circular polarization in the two magnetic states must be measured. Consequently, we need to know the transmission *and* the reflection of the CoTb alloy as a function of the helicity and the saturation magnetization direction. For this purpose, we performed a modulated balanced photodetection method with a lock-in amplifier and Si amplified photodiodes. The experimental setup is represented in Fig. III.29. The pulsed laser beam is first linearly polarized with the polarizer *P1*. The half-wave plate ($\lambda/2$) combined with a density filter allowed us to attenuate and precisely monitor the

incident laser power. Then, the laser beam is divided in two with a beam-splitter and sent in a first photodetector $D1$, that is the reference signal P_{ref} . The other part of the beam is circularly polarized with a quarter wave-plate ($\lambda/4$). Note that the quarter wave-plate is located after the beam-splitter to avoid any alteration of the helicity. The sample is placed at an angle θ_i with respect to the optical axis. The reflected signal P_R is collected in another photodiode $D2$, while the transmitted laser beam P_T in the photodiode $D3$. We mention that the reflection and the transmission were not measured at the same time, and the second photodetector was successively placed at the position $D2$ and $D3$. However, in both reflection or transmission configuration, the same incident power was used in order to allow us to deduce the absorption.

Usually absorption measurements are done with a continuous source of light, here the use of a pulsed laser implies certain issues. First, the magnetization of the CoTb may be reversed upon fs laser pulse excitation. That is why we used an incident laser power below the switching threshold to make sure which of the magnetization state is probed. Second, the output power of our fs laser source experiences fluctuations of $\lesssim 1\%$ per pulse. Since we expect a dichroism of the same order of magnitude, direct measurement of the MCD will not be possible. For this reason, we did the modulation on the difference between the reference signal and the reflection (resp. transmission), i.e., we measured $P_R - P_{\text{ref,R}}$ (resp. $P_T - P_{\text{ref,T}}$). The sample was saturated in one direction and illuminated with σ^+ laser pulses. Then, with the second polarizer $P2$, the difference signal was brought to almost 0 and measured. The photodiodes are thus in a balanced configuration. Further, the material was saturated in the opposite direction and we measured the difference signal without changing $P2$. This procedure was repeated several times, and for σ^- polarization and in transmission. Moreover, the phase in the lock-in amplifier was kept constant throughout the experiment, i.e., in reflection and transmission configuration.

Experimental results

The results are displayed in Fig. III.30. The measurements were performed at an incident angle $\theta_i = 19^\circ$. Fig III.30(a,b) shows the transmitted ($P_T - P_{\text{ref,T}}$) and reflected ($P_R - P_{\text{ref,R}}$) signals, respectively, for a σ^+ polarized laser beam. The red arrows indicate in which direction the sample was saturated. One can see that the transmission of a σ^+ laser beam is higher when the magnetization is pointing up. Conversely, the reflection is lower for a magnetization pointing up. The opposite is observed for the transmission and reflection of the σ^- beam as seen in Fig. III.30(c,d). The average values are summed up for σ^+ and σ^- polarizations in Table III.2 & III.3, respectively.

σ^+	$P_T - P_{\text{ref,T}} (\mu V)$	$P_R - P_{\text{ref,R}} (\mu V)$
↑	145.6 ± 1.9	-792.8 ± 5.3
↓	-41.3 ± 1.4	120.6 ± 5.1

TABLE III.2: Transmission and reflection average values for σ^+ polarized laser beam.

σ^-	$P_T - P_{\text{ref,T}} (\mu V)$	$P_R - P_{\text{ref,R}} (\mu V)$
↑	-68.7 ± 1.8	-32.3 ± 4.3
↓	-3.7 ± 1.7	-887.9 ± 3.3

TABLE III.3: Transmission and reflection average values for σ^- polarized laser beam.

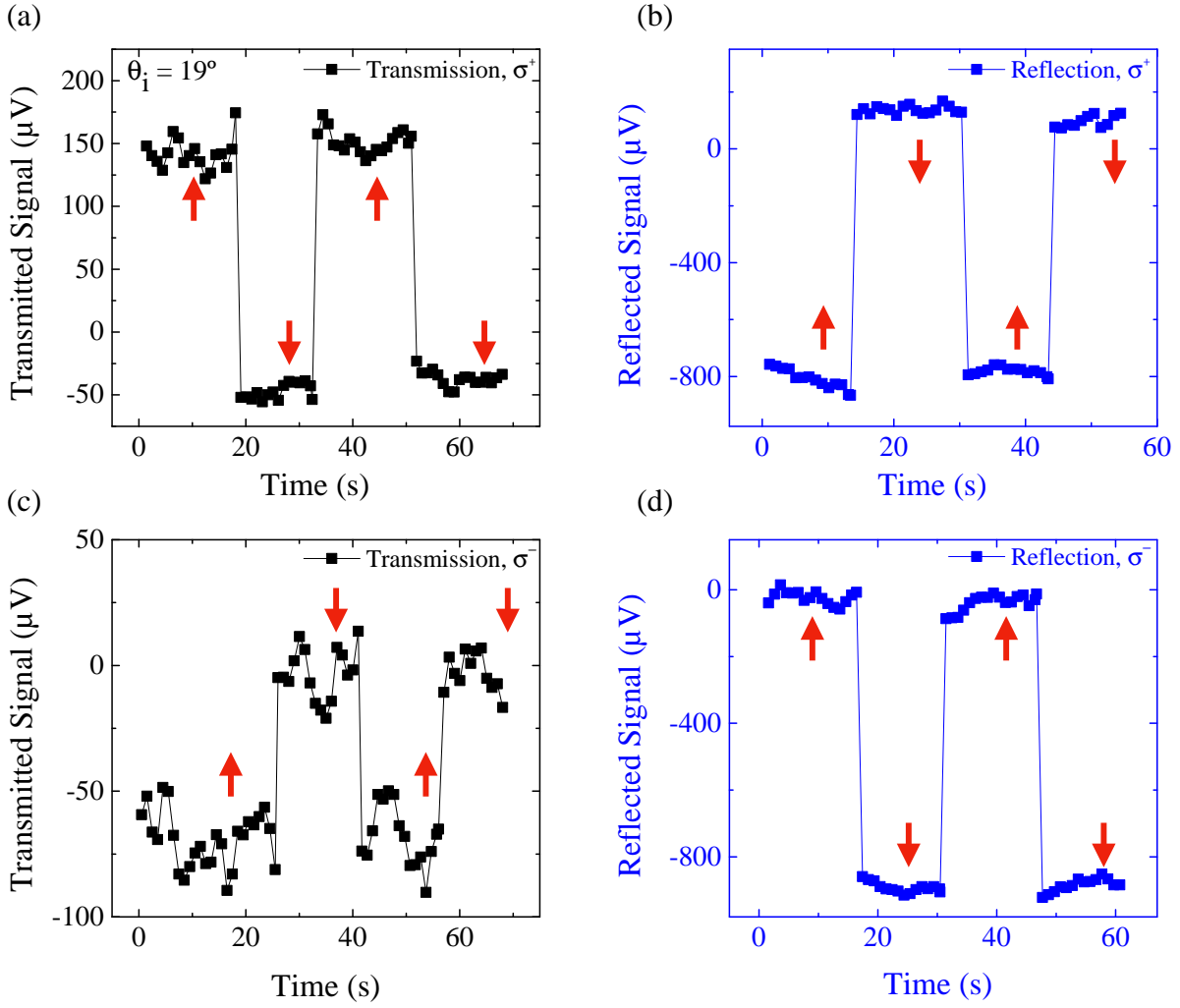


FIGURE III.30: Transmission and reflection measurements for (a,b) a σ^+ and (c,d) σ^- polarized incident beam as a function of the direction of saturation magnetization. An upward (resp. downward) red arrow indicates a magnetization pointing 'up' (resp. 'down'). The transmitted (resp. reflected) signal is defined as the difference between the transmission (resp. the reflection) and the reference, $P_T - P_{ref,T}$ (resp. $P_R - P_{ref,R}$).

Knowing the voltage of the reference signals ($P_{ref,T} = 5.45$ mV, $P_{ref,R} = 24.0$ mV), it is possible to deduce the change of transmission (resp. reflection) as a function of the magnetization. For instance, for σ^+ , $\frac{\Delta T}{T} = 3.3\%$ and $\frac{\Delta R}{R} = -3.9\%$. Moreover, one can calculate the absorbance with an incident signal of $P_i = 45.3$ mV. It is found that the $\text{Co}_{70}\text{Tb}_{30}$ alloy absorbs $\sim 35\%$ of the incident light, with the absorption A defined as:

$$\begin{aligned}
 A(\uparrow) &= P_i - (P_{T,m}^\uparrow + P_{ref,T} + P_{R,m}^\uparrow + P_{ref,R}) \\
 A(\downarrow) &= P_i - (P_{T,m}^\downarrow + P_{ref,T} + P_{R,m}^\downarrow + P_{ref,R}) \\
 A(\uparrow) - A(\downarrow) &= (P_{T,m}^\downarrow + P_{R,m}^\downarrow) - (P_{T,m}^\uparrow + P_{R,m}^\uparrow)
 \end{aligned} \tag{5.7}$$

where $P_{T,m}$ and $P_{R,m}$ are the measured difference signals in transmission and reflection, respectively. Finally, we can now obtain the sign of the MCD, which is proportional to the difference

of absorption between the magnetization -up and -down state for a circularly polarized beam $A(\uparrow) - A(\downarrow)$ as given by Eq. 5.7. Notably, the reference and incident signals do not affect the calculation of the difference of absorption $A(\uparrow) - A(\downarrow)$. The results are the following:

- $A(\uparrow, \sigma^+) - A(\downarrow, \sigma^+) = 726.5 \pm 3.9 \mu V \implies A(\uparrow, \sigma^+) > A(\downarrow, \sigma^+)$
- $A(\uparrow, \sigma^-) - A(\downarrow, \sigma^-) = -790.5 \pm 3 \mu V \implies A(\uparrow, \sigma^-) < A(\downarrow, \sigma^-)$

The difference in absorption for σ^+ and σ^- polarization should be the same in absolute, the small difference we observed might be due to the laser power fluctuations. Nonetheless, it comes that σ^+ (resp. σ^-) polarization absorbs more in a M^+ (resp. M^-). To confirm the latter we reproduced the measurements with a different incident angle $\theta_i = 30^\circ$ and we found the same sign for the MCD. Furthermore, in the same setup, we performed AOS and DW motion experiments. The AOS results for the $\text{Co}_{70}\text{Tb}_{30}$ alloy are depicted in Fig. III.31(a). σ^+ (resp. σ^-) reverses the magnetization -down (resp. -up). Interestingly, this means that circularly polarized light brings the material into the *most* absorbent state. In other terms, for a σ^+ (resp. σ^-) polarized laser beam, locally the temperature will be higher in the M^+ (resp. M^-) domain. Moreover, we prove that the CoTb alloy also exhibits HD-AODW motion as shown in Fig. III.31(b). As we demonstrated with linear polarization, in a presence of a temperature gradient a DW moves towards hotter regions. Therefore, assuming a thermal mechanism based on the MCD, a σ^+ (resp. σ^-) beam would induce a displacement towards the hotter domain, i.e. the M^+ (resp. M^-) domain, which is in contradiction with what we observed [see. Fig. III.15 & III.31(b)]. Hence, it appears that we may exclude a light-induced DW motion via a pure thermal process as we discussed in section 5.3, for the thermal gradient is in the opposite direction to the reported DW displacement. Nonetheless, care must be taken and one should verify the sign of the MCD via another technique such as ellipsometry measurements that yield the dielectric tensor.

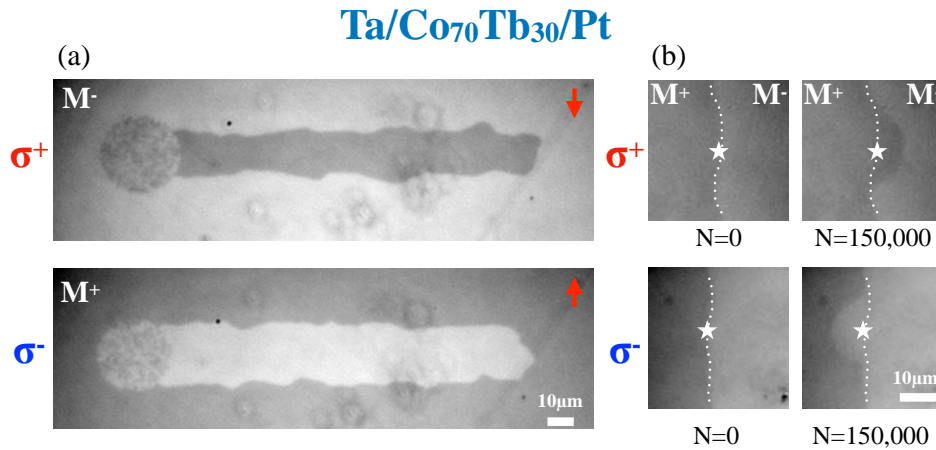


FIGURE III.31: Magneto-optical Faraday images in $\text{Co}_{70}\text{Tb}_{30}$ alloy showing (a) HD-AOS and (b) HD-AODW motion induced by 40-fs circularly polarized laser pulses. (a) The laser fluence is set to 18.5 mJ cm^{-2} and the 40 fs laser beam is swept over the sample surface at $40 \mu\text{m s}^{-1}$. (b) The laser fluence is set just below the switching threshold, which is of 16.8 mJ cm^{-2} . On the left is shown the DW configuration before laser excitation and on the right after $N = 150,000$ pulses for a laser beam initially centered on the DW.

5.5 Thermal spin transfer torque via spin-Seebeck effect

In section 3.4 we saw that a DW could be efficiently moved with a thermal gradient via the spin-Seebeck effect (SSE) [42, 47–49]. A legitimate question is whether we can explain the

helicity-dependent laser-induced DW motion we observed with the SSE. Indeed, due to the MCD that we evidenced in the previous section a temperature gradient undoubtedly appears across the DW and gives rise to a spin current via the SSE [75]. A temperature gradient may act on the DW as an entropic field that drags the DW towards hotter regions (minimization of the free energy) [48, 49] as theoretically discussed with the 2TM in section 5.3. However, if the sign of the MCD we measured is confirmed, the effect of the entropic field may be ruled out as we reported a DW motion in the opposite direction. The other possibility to induce DW motion in a temperature gradient is with the magnonic SSE. Magnons carry angular momentum that can be transferred to the local magnetization and lead to a displacement of the DW via STT [42, 47]. Thermally excited magnons always diffuse towards colder regions. However, conflicting conjectures have been reported in the literature about the direction of DW motion under a magnon flow. Some studies pointed out that the DW displacement is in the direction of the magnon flow [76–78] or towards the hotter regions [42, 47]. Finally, Wang *et al.* demonstrated with micromagnetic simulations that the direction of magnons-induced DW motion depends upon the spin-wave frequency [79]. In the high frequency limit, magnons are transmitted through the wall and the DW moves in the opposite direction. While for low frequencies, the spin-wave is reflected and the DW moves in the same direction as the magnon flow. Thus, in order to explain with the SSE helicity-dependent all-optical domain wall motion, the only possibility will be that low frequency magnons are generated by the laser and are reflected on the DW.

6 Summary and perspectives

In this chapter, we investigated the underlying mechanism of helicity-dependent all-optical switching in (Co/Pt) multilayers by examining the optical response of a domain wall at a laser fluence below the switching threshold. We gave evidence of helicity-dependent all-optical domain wall motion in ferromagnetic (Co/Pt) thin films. Thus, regarding the multistep two-step all-optical switching process, we confirm the likelihood of a helicity-dependent magnetization recovery taking place through helicity-dependent domain wall motion in ferromagnets. Indeed, starting from a demagnetized and multi-domain state, circularly polarized laser pulses will induce the growth or shrinkage of domains depending on the light helicity. The regime of the helicity-dependent remagnetization was reported in the literature to be in the ms timescale. This slow recovery or full reversal of the magnetization, unlike the ultrafast toggle switching observed in GdFeCo, is consistent with the slow domain wall dynamics we revealed. Moreover, we demonstrated that helicity-dependent all-optical domain wall motion can also be exhibited in ferrimagnetic CoTb alloys, hence suggesting a similar all-optical switching mechanism than the one in ferromagnetic (Co/Pt) multilayers. This corroborates what was already suggested by El Hadri *et al.* [1, 4]. However, we anticipate a different mechanism in FePt granular media, as the domain walls are strongly pinned by grain boundaries. In addition, by studying the influence of the linear polarization, we proved that a domain wall can indeed be moved in presence of a temperature gradient. The latter may explain the magnetization reversal induced by a single linearly polarized laser pulse observed by Vomir *et al.* [5].

We also evidenced that all-optical domain wall motion results from the balance of three contributions, namely: a helicity effect, a temperature gradient due to the laser heating and the pinning effects. The helicity effect on the domain wall can in fact be explained by the inverse Faraday effect. Yet, a precise estimation of the effective magnetic field and the parameters ruling domain wall motion in ultrathin Pt/Co/Pt films would be required to confirm an inverse Faraday effect-based mechanism. On the other hand, magnetic circular dichroism measurements seem to indicate that a purely thermal process of all-optical domain wall motion is quite unlikely. Indeed, the only possibility would be via a magnonic spin current arising from the

spin-Seebeck effect and that produces a spin-wave of low frequency. Though, further investigations of the magnetic circular dichroism in ferromagnetic (Co/Pt) multilayers are needed.

Lastly, we expect that a wider range of magnetic materials would show helicity-dependent all-optical switching, given that the magnetic properties and the local defects are tuned in order to allow a high laser-induced domain wall mobility. Finally, we also observed deterministic laser-induced domain wall motion in ferromagnetic micro-stripes with PMA which is interesting in terms of technological applications. Indeed, this could open a new path for racetrack memories and magnetic recording technologies considering a laser beam focalized in the sub-micron scale to manipulate domain walls in nanostripes. In addition, energies in the sub-nJ range are sufficient to displace a domain wall with light. And finally, there is no heat accumulation that could damage the structure, while Joule heating is a major issue when applying current pulses.

References

1. El Hadri, M. S. *et al.* Two types of all-optical magnetization switching mechanisms using femtosecond laser pulses. *Physical Review B* **94**, 064412 (Aug. 2016).
2. Takahashi, Y. K. *et al.* Accumulative Magnetic Switching of Ultrahigh-Density Recording Media by Circularly Polarized Light. *Physical Review Applied* **6**, 054004 (Nov. 2016).
3. Medapalli, R. *et al.* Multiscale dynamics of helicity-dependent all-optical magnetization reversal in ferromagnetic Co/Pt multilayers. *Physical Review B* **96**, 224421 (Dec. 2017).
4. El Hadri, M. S. *et al.* Domain size criterion for the observation of all-optical helicity-dependent switching in magnetic thin films. *Physical Review B* **94**, 064419 (Aug. 2016).
5. Vomir, M., Albrecht, M. & Bigot, J. Y. Single shot all optical switching of intrinsic micron size magnetic domains of a Pt/Co/Pt ferromagnetic stack. *Applied Physics Letters* **111**, 242404 (2017).
6. Néel, L. Anisotropie magnétique superficielle et surstructures d'orientation. *J. Phys. Radium* **15**, 225–239 (1954).
7. Carcia, P. F., Meinhardt, A. D. & Suna, A. Perpendicular magnetic anisotropy in Pd/Co thin film layered structures. *Applied Physics Letters* **47**, 178–180 (1985).
8. Carcia, P. F. Perpendicular magnetic anisotropy in Pd/Co and Pt/Co thin-film layered structures. *Journal of Applied Physics* **63**, 5066–5073 (1988).
9. Daalderop, G. H. O., Kelly, P. J. & den Broeder, F. J. A. Prediction and confirmation of perpendicular magnetic anisotropy in Co/Ni multilayers. *Physical Review Letters* **68**, 682–685 (Feb. 1992).
10. Cullity, B. D. & Graham, C. D. *Introduction to Magnetic Materials* (Wiley-IEEE press, 2008).
11. Kirilyuk, A., Ferre, J. & Renard, D. *Temperature Effects On Domain Wall Dynamics In Ultrathin Ferromagnetic Films in Digests of International Magnetism Conference* (1993).
12. Parkin, S. S. P., Hayashi, M. & Thomas, L. Magnetic Domain-Wall Racetrack Memory. *Science* **320**, 190 (Apr. 2008).
13. Allwood, D. A. *et al.* Magnetic Domain-Wall Logic. *Science* **309**, 1688 (Sept. 2005).
14. Hayashi, M., Thomas, L., Moriya, R., Rettner, C. & Parkin, S. S. P. Current-Controlled Magnetic Domain-Wall Nanowire Shift Register. *Science* **320**, 209 (Apr. 2008).
15. Jamet, J. P. *et al.* Giant enhancement of the domain wall velocity in irradiated ultrathin magnetic nanowires. *IEEE Transactions on Magnetics* **37**, 2120–2122 (2001).
16. Atkinson, D. *et al.* Magnetic domain-wall dynamics in a submicrometre ferromagnetic structure. *Nature Materials* **2**, 85–87 (Jan. 2003).
17. Metaxas, P. J. *et al.* Creep and Flow Regimes of Magnetic Domain-Wall Motion in Ultrathin Pt/Co/Pt Films with Perpendicular Anisotropy. *Physical Review Letters* **99**, 217208 (Nov. 2007).
18. Gorchon, J. *et al.* Pinning-Dependent Field-Driven Domain Wall Dynamics and Thermal Scaling in an Ultrathin Pt/Co/Pt Magnetic Film. *Physical Review Letters* **113**, 027205 (July 2014).
19. Kirilyuk, A., Ferré, J., Grolier, V., Jamet, J. P. & Renard, D. Magnetization reversal in ultrathin ferromagnetic films with perpendicular anisotropy. *Journal of Magnetism and Magnetic Materials* **171**, 45–63 (1997).
20. Quach, D. T. *et al.* Analysis of Magnetic Relaxation With Pre-Existing Nucleation Sites Based on the Fatuzzo-Labruno Model. *IEEE Transactions on Magnetics* **51**, 1–4 (2015).
21. Fatuzzo, E. Theoretical Considerations on the Switching Transient in Ferroelectrics. *Physical Review* **127**, 1999–2005 (Sept. 1962).
22. Labruno, M., Andrieu, S., Rio, F. & Bernstein, P. Time dependence of the magnetization process of RE-TM alloys. *Journal of Magnetism and Magnetic Materials* **80**, 211–218 (1989).

23. Lahtinen, T. H. E., Franke, K. J. A. & van Dijken, S. Electric-field control of magnetic domain wall motion and local magnetization reversal. *Scientific Reports* **2**, 258 (Feb. 2012).
24. Van de Wiele, B., Laurson, L., Franke, K. J. A. & van Dijken, S. Electric field driven magnetic domain wall motion in ferromagnetic-ferroelectric heterostructures. *Applied Physics Letters* **104**, 012401 (2014).
25. Franke, K. J. A. *et al.* Reversible Electric-Field-Driven Magnetic Domain-Wall Motion. *Physical Review X* **5**, 011010 (Feb. 2015).
26. Schellekens, A. J., van den Brink, A., Franken, J. H., Swagten, H. J. M. & Koopmans, B. Electric-field control of domain wall motion in perpendicularly magnetized materials. *Nature Communications* **3**, 847 (May 2012).
27. Chiba, D. *et al.* Electric-field control of magnetic domain-wall velocity in ultrathin cobalt with perpendicular magnetization. *Nature Communications* **3**, 888 (June 2012).
28. Bauer, U., Emori, S. & Beach, G. S. D. Voltage-gated modulation of domain wall creep dynamics in an ultrathin metallic ferromagnet. *Applied Physics Letters* **101**, 172403 (2012).
29. Berger, L. Low-field magnetoresistance and domain drag in ferromagnets. *Journal of Applied Physics* **49**, 2156–2161 (1978).
30. Vernier, N., Allwood, D. A., Atkinson, D., Cooke, M. D. & Cowburn, R. P. Domain wall propagation in magnetic nanowires by spin-polarized current injection. *EPL (Europhysics Letters)* **65**, 526 (2004).
31. Yamaguchi, A. *et al.* Real-Space Observation of Current-Driven Domain Wall Motion in Submicron Magnetic Wires. *Physical Review Letters* **92**, 077205 (Feb. 2004).
32. Hayashi, M. *et al.* Current Driven Domain Wall Velocities Exceeding the Spin Angular Momentum Transfer Rate in Permalloy Nanowires. *Physical Review Letters* **98**, 037204 (Jan. 2007).
33. Hayashi, M. *et al.* Dependence of Current and Field Driven Depinning of Domain Walls on Their Structure and Chirality in Permalloy Nanowires. *Physical Review Letters* **97**, 207205 (Nov. 2006).
34. Meier, G. *et al.* Direct Imaging of Stochastic Domain-Wall Motion Driven by Nanosecond Current Pulses. *Physical Review Letters* **98**, 187202 (May 2007).
35. Heyne, L. *et al.* Direct observation of high velocity current induced domain wall motion. *Applied Physics Letters* **96**, 032504 (2010).
36. Kläui, M. *et al.* Controlled and Reproducible Domain Wall Displacement by Current Pulses Injected into Ferromagnetic Ring Structures. *Physical Review Letters* **94**, 106601 (Mar. 2005).
37. Miron, I. M. *et al.* Fast current-induced domain-wall motion controlled by the Rashba effect. *Nature Materials* **10**, 419 (May 2011).
38. Ravelosona, D., Mangin, S., Katine, J. A., Fullerton, E. E. & Terris, B. D. Threshold currents to move domain walls in films with perpendicular anisotropy. *Applied Physics Letters* **90**, 072508 (2007).
39. Ravelosona, D., Lacour, D., Katine, J. A., Terris, B. D. & Chappert, C. Nanometer Scale Observation of High Efficiency Thermally Assisted Current-Driven Domain Wall Depinning. *Physical Review Letters* **95**, 117203 (Sept. 2005).
40. Moore, T. A. *et al.* High domain wall velocities induced by current in ultrathin Pt/Co/AlO_x wires with perpendicular magnetic anisotropy. *Applied Physics Letters* **93**, 262504 (2008).
41. Malinowski, G., Boulle, O & Kläui, M. Current-induced domain wall motion in nanoscale ferromagnetic elements. *Journal of Physics D: Applied Physics* **44**, 384005 (2011).
42. Yan, P., Wang, X. S. & Wang, X. R. All-Magnonic Spin-Transfer Torque and Domain Wall Propagation. *Physical Review Letters* **107**, 177207 (Oct. 2011).
43. Jia, X., Xia, K. & Bauer, G. E. W. Thermal Spin Transfer in Fe-MgO-Fe Tunnel Junctions. *Physical Review Letters* **107**, 176603 (Oct. 2011).
44. Yu, H., Granville, S., Yu, D. P. & Ansermet, J. P. Evidence for Thermal Spin-Transfer Torque. *Physical Review Letters* **104**, 146601 (Apr. 2010).

45. Kovalev, A. A. & Tserkovnyak, Y. Thermoelectric spin transfer in textured magnets. *Physical Review B* **80**, 100408 (Sept. 2009).
46. Yuan, Z., Wang, S. & Xia, K. Thermal spin-transfer torques on magnetic domain walls. *Solid State Communications* **150**, 548–551 (2010).
47. Hinzke, D. & Nowak, U. Domain Wall Motion by the Magnonic Spin Seebeck Effect. *Physical Review Letters* **107**, 027205 (July 2011).
48. Schlickeiser, F., Ritzmann, U., Hinzke, D. & Nowak, U. Role of Entropy in Domain Wall Motion in Thermal Gradients. *Physical Review Letters* **113**, 097201 (Aug. 2014).
49. Moretti, S., Raposo, V., Martinez, E. & Lopez-Diaz, L. Domain wall motion by localized temperature gradients. *Physical Review B* **95**, 064419 (Feb. 2017).
50. Torrejon, J. *et al.* Unidirectional Thermal Effects in Current-Induced Domain Wall Motion. *Physical Review Letters* **109**, 106601 (Sept. 2012).
51. Tetienne, J. P. *et al.* Nanoscale imaging and control of domain-wall hopping with a nitrogen-vacancy center microscope. *Science* **344**, 1366 (June 2014).
52. Lambert, C.-H. *et al.* All-optical control of ferromagnetic thin films and nanostructures. *Science* **345**, 1337 (Sept. 2014).
53. El Hadri, M. S. *et al.* Electrical characterization of all-optical helicity-dependent switching in ferromagnetic Hall crosses. *Applied Physics Letters* **108**, 092405 (2016).
54. Cornelissen, T. D., Córdoba, R. & Koopmans, B. Microscopic model for all optical switching in ferromagnets. *Applied Physics Letters* **108**, 142405 (2016).
55. Sandig, O. *et al.* Movement of magnetic domain walls induced by single femtosecond laser pulses. *Physical Review B* **94**, 054414 (Aug. 2016).
56. Janda, T. *et al.* Inertial displacement of a domain wall excited by ultra-short circularly polarized laser pulses. *Nature Communications* **8**, 15226 (May 2017).
57. John, R. *et al.* Magnetisation switching of FePt nanoparticle recording medium by femtosecond laser pulses. *Scientific Reports* **7**, 4114 (2017).
58. Gorchon, J., Yang, Y. & Bokor, J. Model for multishot all-thermal all-optical switching in ferromagnets. *Physical Review B* **94**, 020409 (July 2016).
59. Kimel, A. V. *et al.* Ultrafast non-thermal control of magnetization by instantaneous photomagnetic pulses. *Nature* **435**, 655–657 (May 2005).
60. Ellis, M. O. A., Fullerton, E. E. & Chantrell, R. W. All-optical switching in granular ferromagnets caused by magnetic circular dichroism. *Scientific Reports* **6**, 30522 (July 2016).
61. Mendil, J. *et al.* Resolving the role of femtosecond heated electrons in ultrafast spin dynamics. *Scientific Reports* **4**, 3980 (Feb. 2014).
62. Kim, C. H. *et al.* Coherent phonon control via electron-lattice interaction in ferromagnetic Co/Pt multilayers. *Scientific Reports* **6**, 22054 (Mar. 2016).
63. Khorsand, A. R. *et al.* Role of Magnetic Circular Dichroism in All-Optical Magnetic Recording. *Physical Review Letters* **108**, 127205 (Mar. 2012).
64. Tsema, Y. *et al.* Helicity and field dependent magnetization dynamics of ferromagnetic Co/Pt multilayers. *Applied Physics Letters* **109**, 072405 (2016).
65. Beaurepaire, E., Merle, J. C., Daunois, A. & Bigot, J. Y. Ultrafast Spin Dynamics in Ferromagnetic Nickel. *Physical Review Letters* **76**, 4250–4253 (May 1996).
66. Kuiper, K. C. *et al.* Spin-orbit enhanced demagnetization rate in Co/Pt-multilayers. *Applied Physics Letters* **105**, 202402 (2014).
67. Atxitia, U. & Chubykalo-Fesenko, O. Ultrafast magnetization dynamics rates within the Landau-Lifshitz-Bloch model. *Physical Review B* **84**, 144414 (Oct. 2011).
68. Van Kesteren, H. W. & Zeper, W. B. Controlling the Curie temperature of Co/Pt multilayer magneto-optical recording media. *Journal of Magnetism and Magnetic Materials* **120**, 271–273 (1993).

69. Charilaou, M. *et al.* Magnetic properties of ultrathin discontinuous Co/Pt multilayers: Comparison with short-range ordered and isotropic CoPt_3 films. *Physical Review B* **93**, 224408 (June 2016).
70. Uba, S. *et al.* Optical and magneto-optical properties of Co/Pt multilayers. *Physical Review B* **53**, 6526–6535 (Mar. 1996).
71. Lee, Y. P., Kim, K. W., Gontarz, R. & Kudryavtsev, Y. V. Optical and magneto-optical properties of Co/Pt multilayered films. *Current Applied Physics* **1**, 451–454 (2001).
72. Hashimoto, S., Ochiai, Y. & Aso, K. Film thickness dependence of magneto-optical and magnetic properties in Co/Pt and Co/Pd multilayers. *Journal of Applied Physics* **67**, 4429–4431 (1990).
73. Atkinson, R. *et al.* Fundamental optical and magneto-optical constants of Co/Pt and CoNi/Pt multilayered films. *Journal of Magnetism and Magnetic Materials* **162**, 131–138 (1996).
74. Werner, W. S. M., Glantschnig, K. & Ambrosch-Draxl, C. Optical Constants and Inelastic Electron-Scattering Data for 17 Elemental Metals. *Journal of Physical and Chemical Reference Data* **38**, 1013–1092 (2009).
75. Uchida, K. *et al.* Observation of the spin Seebeck effect. *Nature* **455**, 778–781 (Oct. 2008).
76. Han, D.-S. *et al.* Magnetic domain-wall motion by propagating spin waves. *Applied Physics Letters* **94**, 112502 (2009).
77. Yan, P., Cao, Y. & Sinova, J. Thermodynamic magnon recoil for domain wall motion. *Physical Review B* **92**, 100408 (Sept. 2015).
78. Wang, W. *et al.* Magnon-Driven Domain-Wall Motion with the Dzyaloshinskii-Moriya Interaction. *Physical Review Letters* **114**, 087203 (Feb. 2015).
79. Wang, X.-g., Guo, G.-h., Nie, Y.-z., Zhang, G.-f. & Li, Z.-x. Domain wall motion induced by the magnonic spin current. *Physical Review B* **86**, 054445 (Aug. 2012).

Chapter IV

Size effects of all-optical switching in patterned ferromagnetic thin films

1 Introduction

In the fourth chapter of this thesis, our aim was to investigate the size effects of all-optical switching in ferromagnetic thin films when scaling down the dimensions for a potential integration of AOS in magnetic memory & data storage devices. The study of size effects is intrinsically related to the role of the dipolar field in AOS. It was demonstrated that by suppressing the dipolar energy gain for domain formation in the ultrathin-film limit HD-AOS could be exhibited [1]. On the other hand, evidence were given that demagnetizing field was instead a key feature to observe AOS, specifically intervening in the nucleation process in the cumulative reversal mechanism of AOS [2, 3]. Moreover, so far deterministic all-optical switching of micro- and nano-scale patterns was reported only in ferrimagnetic GdFeCo alloys [4, 5]. Here, we present the first attempts of studying the size effects of HD-AOS in ferromagnetic (Co/Pt) multilayers patterned into microstructures. We employ two different approaches to probe the laser-induced magnetization reversal in the micro-patterns: first, static magneto-optical Faraday imaging and second, by combining optical excitation with transport measurements in Hall cross devices via the anomalous Hall effect. In section 2, we detail these two approaches and characterize the studied patterned devices. In section 3, we report helicity-dependent all-optical switching of (Co/Pt) microdots of a diameter as small as $3 \mu\text{m}$ when sweeping the laser beam. Quantification of magnetization reversal is provided by electrical characterization of AOS. In a sweeping configuration, we show that the microdots behave in a similar way than the full film. However, in section 4, in a static beam configuration, we give evidence that a larger number of laser pulses is required to reverse the magnetization in microdots compared to the full film. This is an indication that indeed the dipolar field actually eases the reversal in AOS. These results should provide new insights for the integration of AOS in magnetic data storage devices.

2 Principle of the experiments and sample characterization

Ultrafast magnetization switching in the picosecond timescale using ultrashort laser pulses has been demonstrated in multiple cases in ferrimagnetic GdFeCo alloys [6, 7] but also in exchange-coupled (Co/Pt)/GdFeCo [8]. In addition, AOS is an energy-efficient process in the fJ range [9], unlike current-induced magnetization switching that often requires energies in the pJ range [10, 11]. Therefore, to achieve ultrafast energy-efficient ultrahigh density magnetic data storage

with AOS, the next step is to study the size effects when implementing AOS in micro- or nano-structures as in bit-patterned magnetic recording [12, 13]. Furthermore, patterned films can be considered as a discrete medium, hence removing the influence of the dipolar fields from the surrounding areas as in contrast in continuous films. Thus, this allowed us to investigate at the same time the effect of dipolar fields in all-optical switching.

2.1 Outline of the experiments

We present here two methods to probe the magnetization reversal in patterned (Co/Pt) ultra-thin films in a sweeping or static laser beam configuration.

Static Faraday imaging

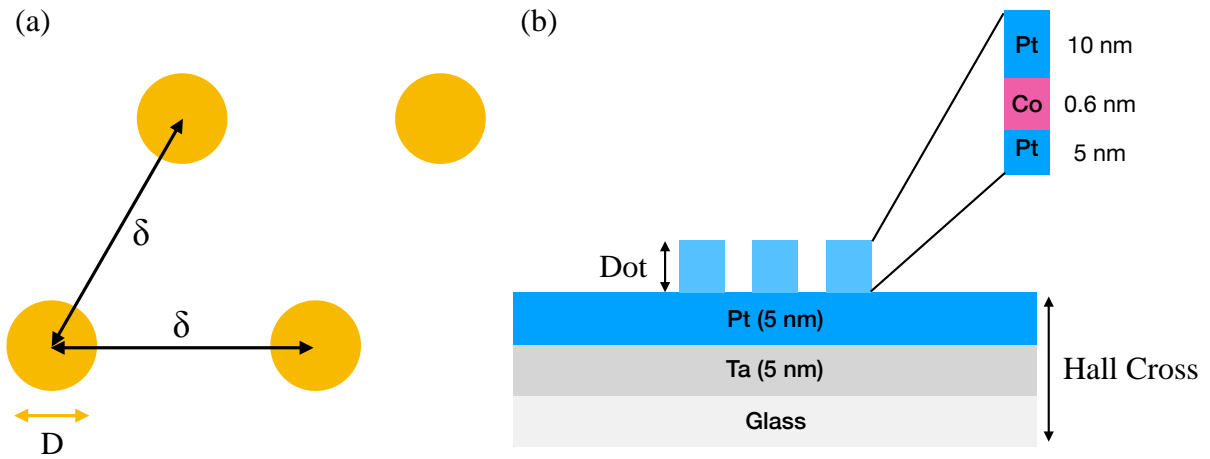


FIGURE IV.1: Schematic representations of (Co/Pt) multilayers films patterned into (a) arrays of microdots and (b) Hall cross devices with on top microdots.

The first method relies on static magneto-optical Faraday imaging. The investigated ferromagnetic films are a (Co/Pt) single layer or bilayer structure: Glass/Ta(5 nm)/Pt(4.5 nm)/[Co(0.6 nm)/Pt(0.7 nm)]_N/Pt(3.8 nm) with $N = 1$ or 2 grown by DC magnetron sputtering. The (Co/Pt) films were patterned into arrays of microdots by UV lithography via an etching process as represented in Fig. IV.1(a). The diameter of the microdots D ranges from 2 to 10 μm . The microdots are arranged in a hexagonal array with a spacing distance (from center to center) $\delta = 3D$. Hence, the dipolar fields from neighboring dots can be neglected as it scales in $1/r^3$. The (Co/Pt) single layer or bilayer continuous films both exhibit HD-AOS with 40 fs circularly polarized laser pulses [14, 15]. These materials once patterned have a weak magneto-optical contrast when imaged in our microscope setup. Consequently, in order to probe the magnetization we proceeded as follows. An image was taken before laser excitation when the sample is saturated, and another image after laser irradiation. A Gaussian filter was applied to both magneto-optical images. Then, the subtraction of these two images allowed us to observe magnetic contrast. Further, M^+ and M^- domains were digitally recolored. In the rest of this chapter, static images we will show correspond to digitally recolored differential Faraday images as described above.

Electrical characterization

However, precise probing of the laser-induced switching in small structures is difficult to achieve with magneto-optical images. Hence, we implemented a more quantitative approach based on magneto-transport measurements. El Hadri *et al.* successfully probed HD-AOS in ferromagnetic (Co/Pt) Hall crosses via the anomalous Hall effect [14, 16]. In 1881, Hall discovered that the "pressing electricity" effect (Hall effect) was ten times larger in ferromagnetic materials than in non-magnetic conductors [17]. This is known as the anomalous Hall effect (AHE). Indeed, in non-magnetic conductors, the Hall resistivity ρ_{xy} linearly increases with the applied magnetic field as expected from the Lorentz force. On the other hand, in magnetic materials, ρ_{xy} initially steeply increases with the field, and at larger field values it saturates. The AHE contribution was found to be proportional to the magnetization M_z . The Hall resistivity relation in magnetic conductors was then empirically established and expressed as: $\rho_{xy} = R_N H_z + R_{AHE} M_z$, where R_N and R_{AHE} are the normal and anomalous Hall effect coefficient, respectively [18] (and refs. therein). The anomalous Hall coefficient has an intrinsic contribution, the Berry-phase curvature effects, and extrinsic contributions due to skew scattering and the side-jump mechanism [19, 20]. In materials with a large spin-orbit coupling, spin-dependent scattering of conduction electrons is enhanced which leads to an AHE larger than the normal Hall effect [21].

The large AHE in ferromagnets can be used to probe the magnetic state of the microdots after laser irradiation. Hence, we patterned a (Co/Pt) single layer structure into microdots on top of a Hall cross by UV lithography as schematically displayed in Fig. IV.1(b). For this purpose, we increased the Pt buffer layer thickness and to conserve the sample symmetry the Pt top layer thickness was also increased. Consequently, we grew by DC magnetron sputtering the following stack: Glass/Ta(5 nm)/Pt(10 nm)/Co(0.6 nm)/Pt(10 nm). This allowed us to successively pattern the Hall cross and then the microdots with the same deposited film. At the end of the lithography - etching process, it results a Hall cross device in Glass/Ta(5 nm)/Pt(5 nm) and on top Pt(5 nm)/Co(0.6 nm)/Pt(10 nm) microdots. To perform the electrical characterization, a DC current of $I = 0.5$ mA is injected in the device. The Hall voltage is measured at zero applied field with a nanovoltmeter, and is thus proportional to the magnetization. Depending on the Hall cross width, the current density j_x ranges from 3 to 50×10^5 A m⁻², which is at least 5 orders of magnitude smaller than the current density used in current-induced magnetization switching via STT or SOT. In addition, the symmetry of the sample was preserved, thus a magnetization switching by STT is unlikely.

Laser beam configurations

In order to investigate the size effects in patterned (Co/Pt) MLs, we carried out two types of experiments based on the laser beam configuration. HD-AOS was probed with the two methods aforescribed. The first approach is called "sweeping beam experiment". As seen in Fig. IV.2(a), the fs laser beam is swept over the array of microdots over a distance of ~ 200 μ m at a constant speed of 40 μ m s⁻¹. The top picture in Fig. IV.2(a) shows the laser beam profile on the microdots. Considering the laser FWHM of about 50 μ m, several microdots are exposed at the same time to the laser. Therefore, the microdots in the outer parts of the laser beam will experience a smaller laser power than the microdots in the inner part of the beam spot. Laser-induced magnetization reversal in the microdots arrays was probed according to the static image processing technique. Similarly, as seen in Fig. IV.2(b), the laser beam is swept over the length of the magnetic wire along the x -axis, and parallel to the current injection direction. In this case, HD-AOS is probed via the AHE. Only the microdots located in the center of the

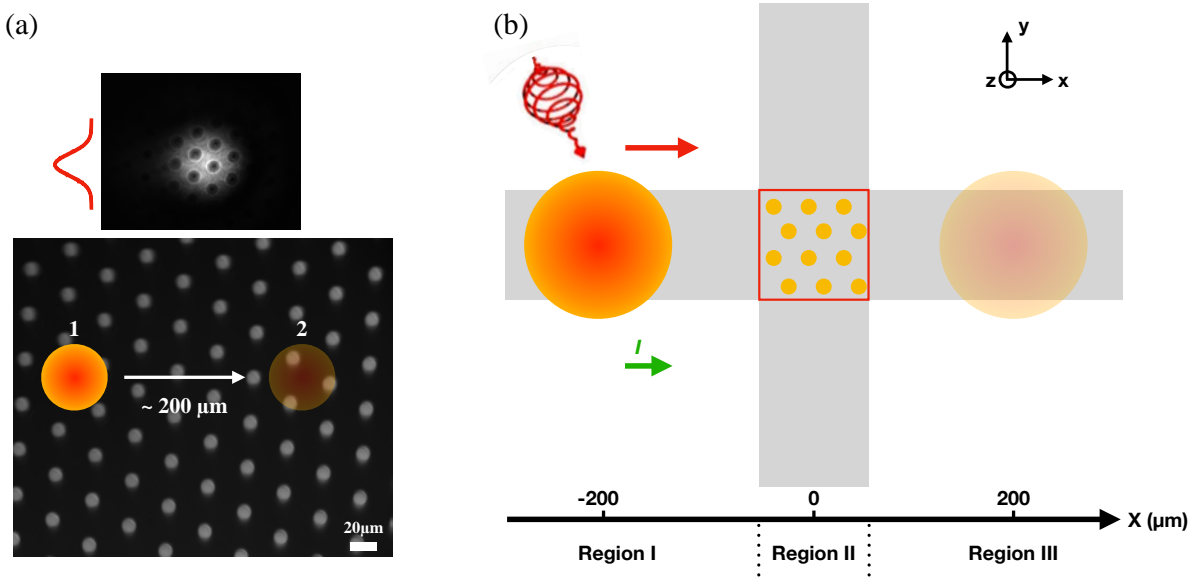


FIGURE IV.2: Description of the "sweeping beam experiments" (a) in arrays of microdots and (b) in a Hall cross with microdots on top of it. (a) the top picture represents the laser beam profile on the patterned film. The laser beam is swept over the sample surface from position 1 to 2 over $\sim 200 \mu\text{m}$. (b) The laser beam is swept along the x -axis parallel to the current density \vec{j}_x . The laser beam is turned off $200 \mu\text{m}$ away from the center of the Hall bar.

Hall cross will contribute to the Hall voltage measured along the y -axis. Thus, the Hall voltage measurement gives information about the average magnetic state of the microdots. Notably, the laser beam spot size is larger than the Hall-bar width. After each laser exposure, the Hall voltage of the two corresponding saturated state is measured. The second approach is called "static beam experiment". The laser beam spot is kept at a fixed position either on a single microdot in the array or centered on the Hall cross. In the latter case, a Hall cross with a single dot in its center was specifically patterned to probe HD-AOS in a static beam configuration. In this configuration, we used the pulse picker to send a finite number of laser pulses N . This allows us to investigate the multishot and cumulative nature of AOS in (Co/Pt) microdots compared to in the full film as studied by El Hadri *et al.* [14].

2.2 Magnetic characterization of the samples

Prior to laser irradiation, the patterned samples were first magnetically characterized. The (Co/Pt) single and bilayer structures have a coercivity of $\sim 50 \text{ mT}$ as measured by VSM (see Fig. II.2). To study the magnetization reversal of the microdots arrays, we performed MOKE image recording with a commercial MOKE microscope while applying an out-of-plane field. Magnetic field-induced reversal was systematically analyzed with a tracking software from APREX solutions that enables us to detect intensity changes of small structures in the recorded MOKE videos. The software uses an adaptative thresholding method. We were able to run the program for arrays of dots with a diameter ranging from 10 to $4 \mu\text{m}$. The results are shown in Fig. IV.3. The black curves indicate the detected changes of magneto-optical Kerr intensity, i.e. the number of reversed dots, as a function of the applied field. A high number of dots were assessed, more than 80 for the largest structures and from 500 to 1200 for the smallest. The red curves are the corresponding derivatives. One can see that magnetization reversal is not uniform but instead a clear distribution of the switching field can be observed. Moreover,

magnetization reversal starts at field values much higher than for the full film. In addition, it is found that as the dots diameter goes down the switching field distribution is shifted towards higher values. This can be understood in the sense that local defects are not uniformly distributed over the surface of a sputtered film. Thus, after the lithography process, the dots do not have the same probability of having nucleation sites. As smaller dots require higher fields to switch, a legitimate question is whether we should expect an increase of the laser switching power threshold when reducing the diameter as compared to the full film. Nonetheless, it can be seen that the central coercive field for the 4- μm dots is smaller than the one for the array of 6- μm . This is related to statistics as a different number of dots were assessed. Besides, the arrays were patterned in different locations on the continuous film. Finally, noticeably in the MOKE videos, the magnetization of neighboring dots may switch almost simultaneously. This confirms that the dots are decoupled. Indeed, if a dot is reversed, then the dipolar field would induce an alternating magnetization configuration of the neighboring dots.

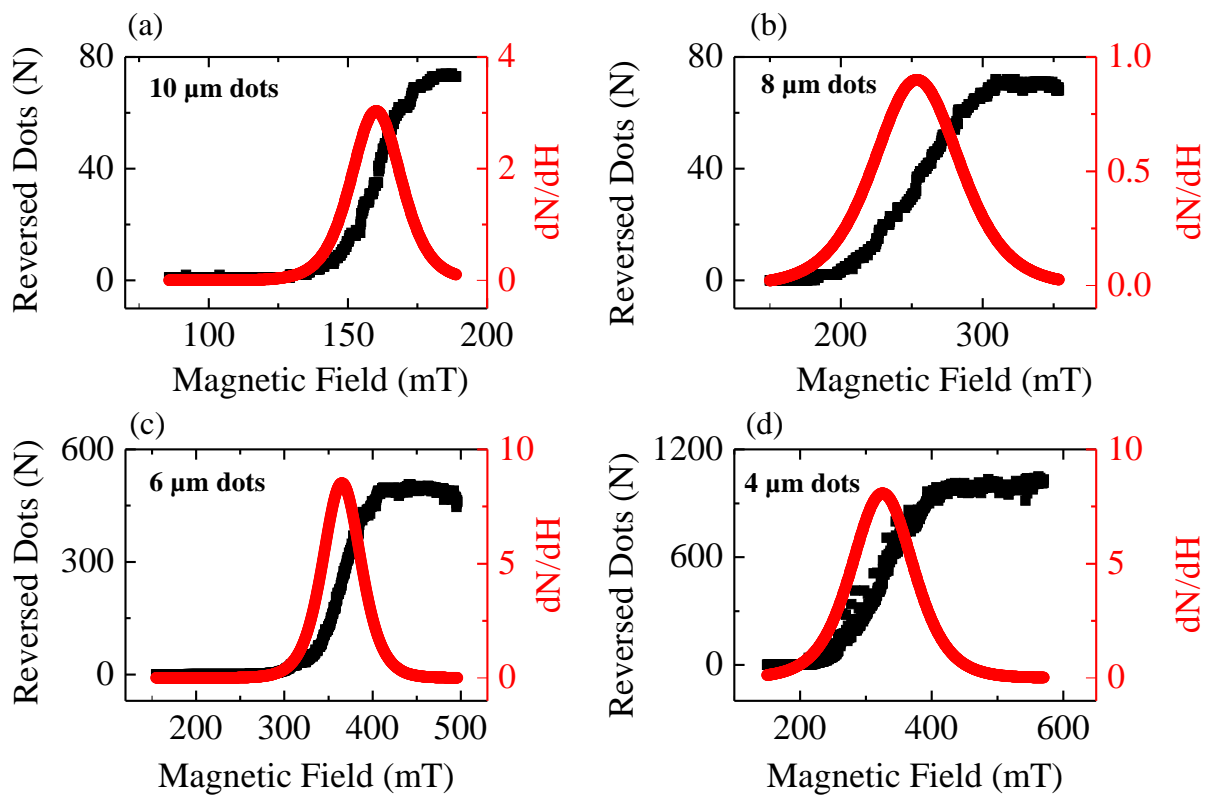


FIGURE IV.3: Evolution of the detected reversed microdots against the applied field and as a function of the dots diameter $D = 10$ (a), 8 (b), 6 (c) and 4 μm (d).

Before performing the electrical probing of HD-AOS of the microdots in the sweeping or static beam configuration, the Hall crosses with the dots are characterized in a magneto-transport measurement station. Fig. IV.4(a) shows an example of the results for a 40- μm wide Hall cross with on top 3- μm dots that we studied in the sweeping beam experiments. The field is applied perpendicular to the sample. First, it is verified that after the lithography process, the PMA of the (Co/Pt) structure is preserved. Second, as observed in the MOKE videos, switching gradually takes place for a field between 75 and 125 mT. Most interestingly, ΔV_H , the change in the Hall voltage when going from one saturation direction to the other, is equal to 4 μV . This will allow us to deduce the magnetic state of the dots after laser excitation. As seen in the magneto-optical Faraday image in Fig. IV.4(b), 20 dots are located in the center of the Hall cross. Thus, the measured Hall voltage indicates the average magnetic state of these 20 dots. Although one could see what it may seem to be microdots outside of the Hall bar, these are

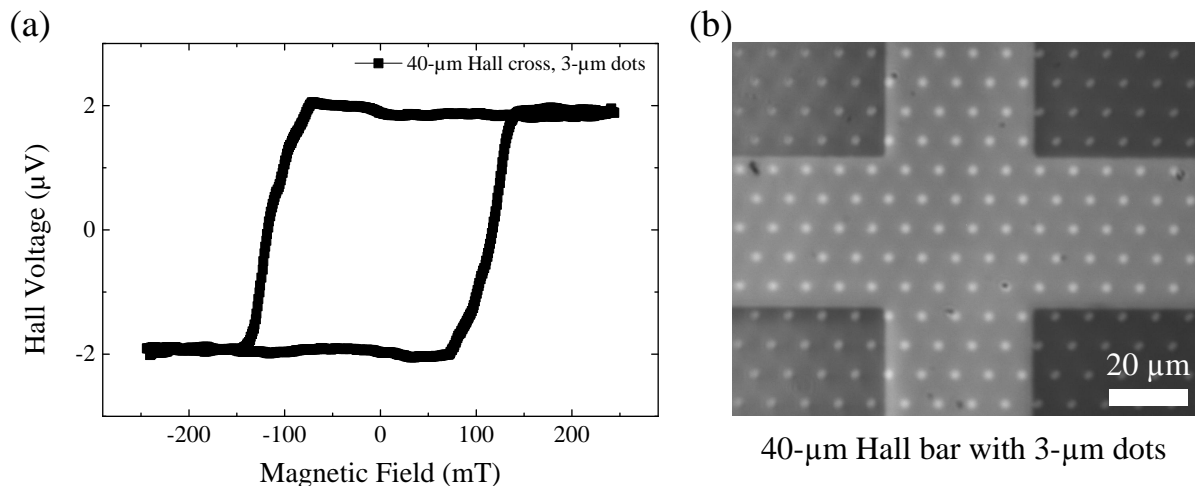


FIGURE IV.4: (a) Magneto-transport characterization and (b) magneto-optical imaging of a 40- μm wide Hall cross with on top 3- μm dots.

only the marks left on the glass substrate by the photoresist after removal at the end of the lithography process.

3 Sweeping beam experiments on (Co/Pt) microdots

3.1 Static imaging of the microdots arrays

We first investigated the size effects of HD-AOS by studying the microdots arrays in the sweeping beam approach. The laser beam is swept over the sample surface at a constant speed of $40 \mu\text{m s}^{-1}$. The four possible combinations of circular polarization and initial saturation direction were examined, namely: (σ^+, \uparrow) , (σ^-, \uparrow) , (σ^+, \downarrow) and (σ^-, \downarrow) . The arrow indicates the direction in which the sample was initially saturated. The results are shown in Fig. IV.5 for $(\text{Co/Pt})_{x2}$ microdots exposed to 40-fs laser pulses. In Fig. IV.5, on the left is presented the initial saturated "raw" image and, on the right, digitally recolored and processed differential magneto-optical images after sweeping the laser. Indeed, the patterned (Co/Pt) films have a weak magneto-optical contrast, and thus differential imaging was necessary to observe magnetic domains. A blue (resp. red) contrast represents a magnetization-up (resp. -down) domain. After subtraction of the initial saturated image, the dots that did not switch appear as "white". A highlighting of the dots contour is added as a guide for the eye. HD-AOS is observed in the $(\text{Co/Pt})_{x2}$ continuous film above a laser fluence threshold of 4 mJ cm^{-2} . In the sweeping beam experiments, reproducible reversal of the dots could be reported for a laser fluence of 9 mJ cm^{-2} . No reversed domains were observed for (σ^+, \uparrow) and (σ^-, \downarrow) . In contrast, as seen in Fig. IV.5(a) for 10- μm dots, σ^+ (resp. σ^-) polarized laser pulses are able to reverse dots initially saturated -down (resp. -up). This is the clear signature of HD-AOS. Yet, one can see that only a few dots are completely switched, while others are in a multidomain state. Nonetheless, most of the dots in the multidomain state seem to exhibit a majority of magnetization-up (resp. -down) domains when exposed to a σ^+ (resp. σ^-) polarized beam. Full reversal of microdots of a diameter as small as $4 \mu\text{m}$ could also be observed as seen in Fig. IV.5. However, below this size, we could not unambiguously determine the magnetic state, as the magnetic domains can hardly be optically resolved. Similar results were obtained with the (Co/Pt) single layer structure.

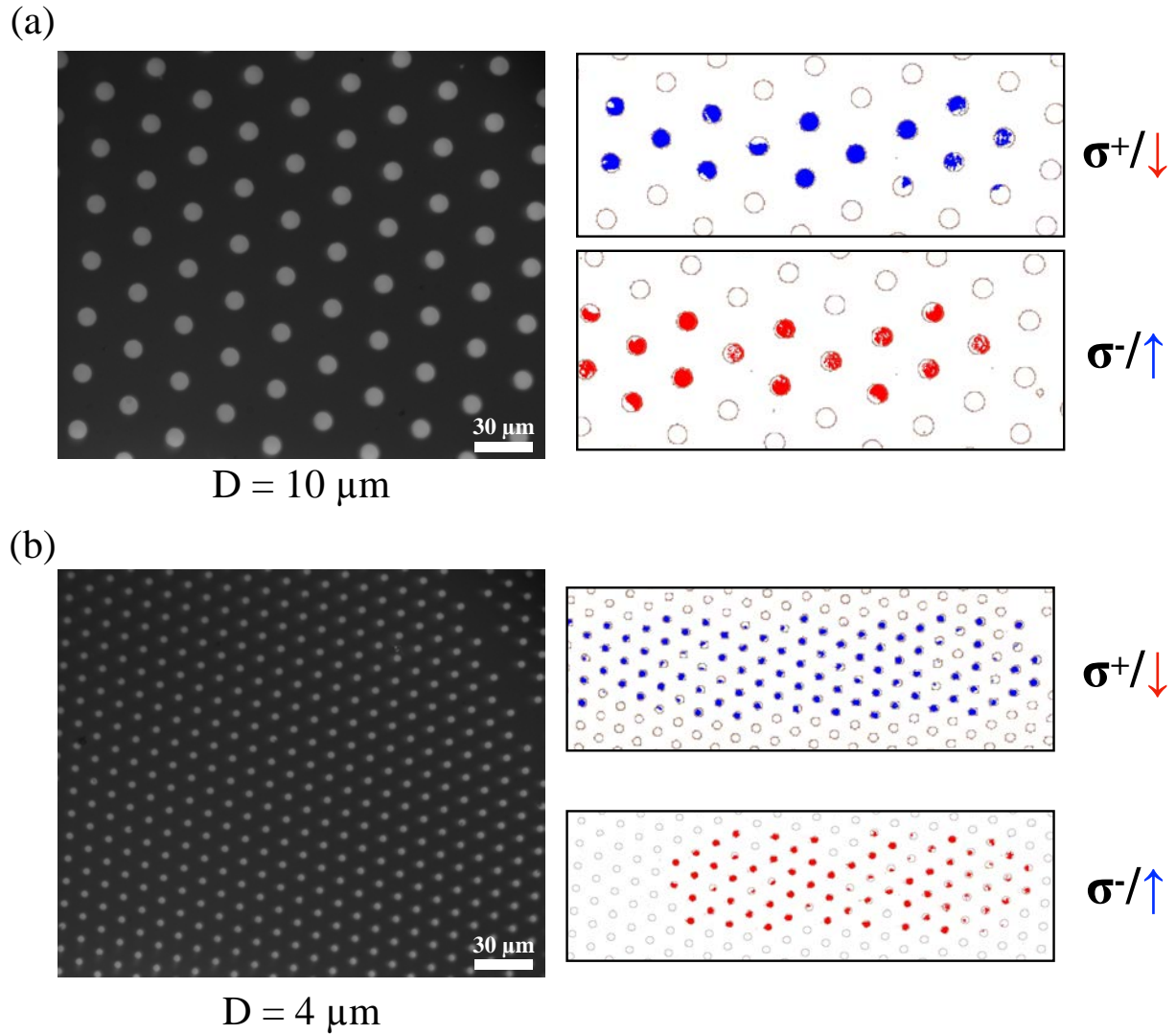


FIGURE IV.5: Helicity-dependent all-optical switching of $(\text{Co/Pt})_{x2}$ microdots with a diameter of (a) $10 \mu\text{m}$ and (b) $4 \mu\text{m}$. On the left, the raw magneto-optical Faraday image when the sample is initially saturated. On the right, digitally recolored differential processed magneto-optical images after sweeping a 40-fs circularly polarized laser beam.

Notably, a laser fluence higher than in the full film was required to reverse the microdots. As a result, we thereafter investigated the laser fluence dependence upon irradiation of (Co/Pt) microstructures. Moreover, we noticed that in the $(\text{Co/Pt})_{x2}$ full film, sweeping the 40-fs laser beam could lead to helicity-independent domain wall dragging. This behavior gradually faded away when increasing the laser pulse width. For a 600-fs laser beam, a clean HD-AOS was observed. Therefore, in the rest of this chapter, the pulse width was set to 600 fs (and measured with the autocorrelator). Furthermore, HD-AOS in (Co/Pt) MLs was proved to be a cumulative and slow process that occurs in the millisecond timescale with 35-fs [14] and 4-ps [22] laser pulses.

The switching threshold in the $(\text{Co/Pt})_{x2}$ continuous film exposed to 600-fs laser pulses was found to be 6.7 mJ cm^{-2} . In the patterned $(\text{Co/Pt})_{x2}$ film, the laser fluence was varied from 7.1 to 11.8 mJ cm^{-2} . Below 7 mJ cm^{-2} , no reversal could be reported. The results are depicted in Fig. IV.6(a) for an array of $6\text{-}\mu\text{m}$ dots irradiated with a σ^- laser beam. The dots were initially

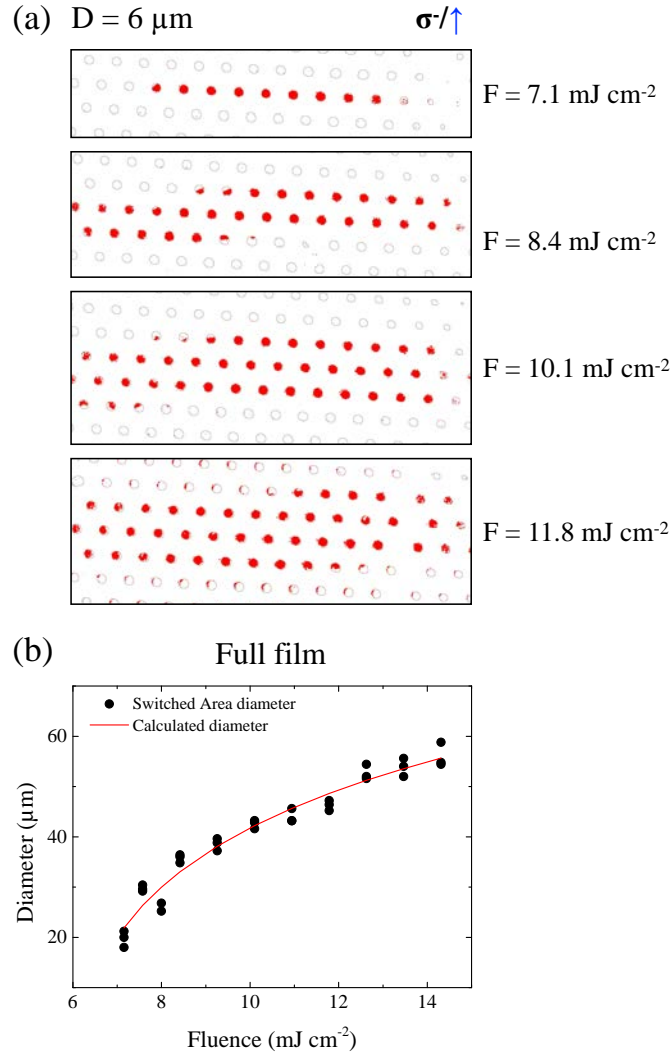


FIGURE IV.6: (a) Laser fluence dependence of all-optical switching in a (Co/Pt) bi-layer structure patterned into a $6\text{-}\mu\text{m}$ dots array and exposed to 600-fs σ^- polarized laser pulses. The sample is initially saturated in the up-direction. (b) Evolution of the size of the switched area when sweeping the laser beam in the $(\text{Co/Pt})_{x2}$ continuous film.

saturated up. Unlike in the previous case, most of the dots are fully switched, which clearly indicates a "cleaner" HD-AOS. As the laser fluence increases, more rows of reversed dots can be seen. Each row is separated by a distance d_{space} of approximately $12.7 \mu\text{m}$ compared to the laser beam spot FWHM which is about $55 \mu\text{m}$. The observed laser fluence dependence can be correlated with the size of the reversed region when sweeping the laser beam on the continuous film. Indeed, we measured the diameter of the switched area in the $(\text{Co/Pt})_{x2}$ full film for a laser fluence ranging from 7.1 to 14.2 mJ cm^{-2} . The results are shown in Fig. IV.6(b). Due to the Gaussian shape of the laser beam spot, the switched area diameter D_{switch} scales as $\frac{\text{FWHM}}{2 \ln 2} \sqrt{-2 \ln (F/F_{\text{th}})}$, where F_{th} is the threshold fluence. Let's take the example of $F = 10.1 \text{ mJ cm}^{-2}$, in the patterned film we observed 3 rows of reversed dots. The latter is consistent with the switched area diameter of $40 \mu\text{m}$ measured in the full film, as the number n of rows of dots the laser can reverse is given by $D_{\text{switch}}/d_{\text{space}}$, e.g. for $F = 10.1 \text{ mJ cm}^{-2}$ $n \simeq 3.2$. We reproduced the same experiments in arrays of dots with a diameter ranging from 10 to $4 \mu\text{m}$. Independently of the dot size, HD-AOS when sweeping the laser beam emerged for a fluence above 7 mJ cm^{-2} . On the other hand, only the number of switched dots varied as previously explained. Thus,

no particular difference in the laser fluence dependence between the continuous film and the patterned arrays could be observed when sweeping the laser beam.

Though, accurate quantification with the static image processing technique is difficult, and in addition information may be lost during the processing. Therefore, we tried to perform magnetic force microscopy (MFM) after laser exposure on the patterned films. However, we could not obtain a magnetic contrast on the microdots. The reason is that these structures are too large to be imaged by MFM. Indeed, the MFM tip is sensitive to the gradient of the dipolar field coming out of the dot along the z -axis, which decreases when the dot size goes up. A more accurate probing of HD-AOS in microdots is achieved via AHE measurement in the (Co/Pt) Hall crosses with on top microdots, which will be discussed in the next section.

3.2 Electrical characterization of (Co/Pt) microdots on top of a Hall cross

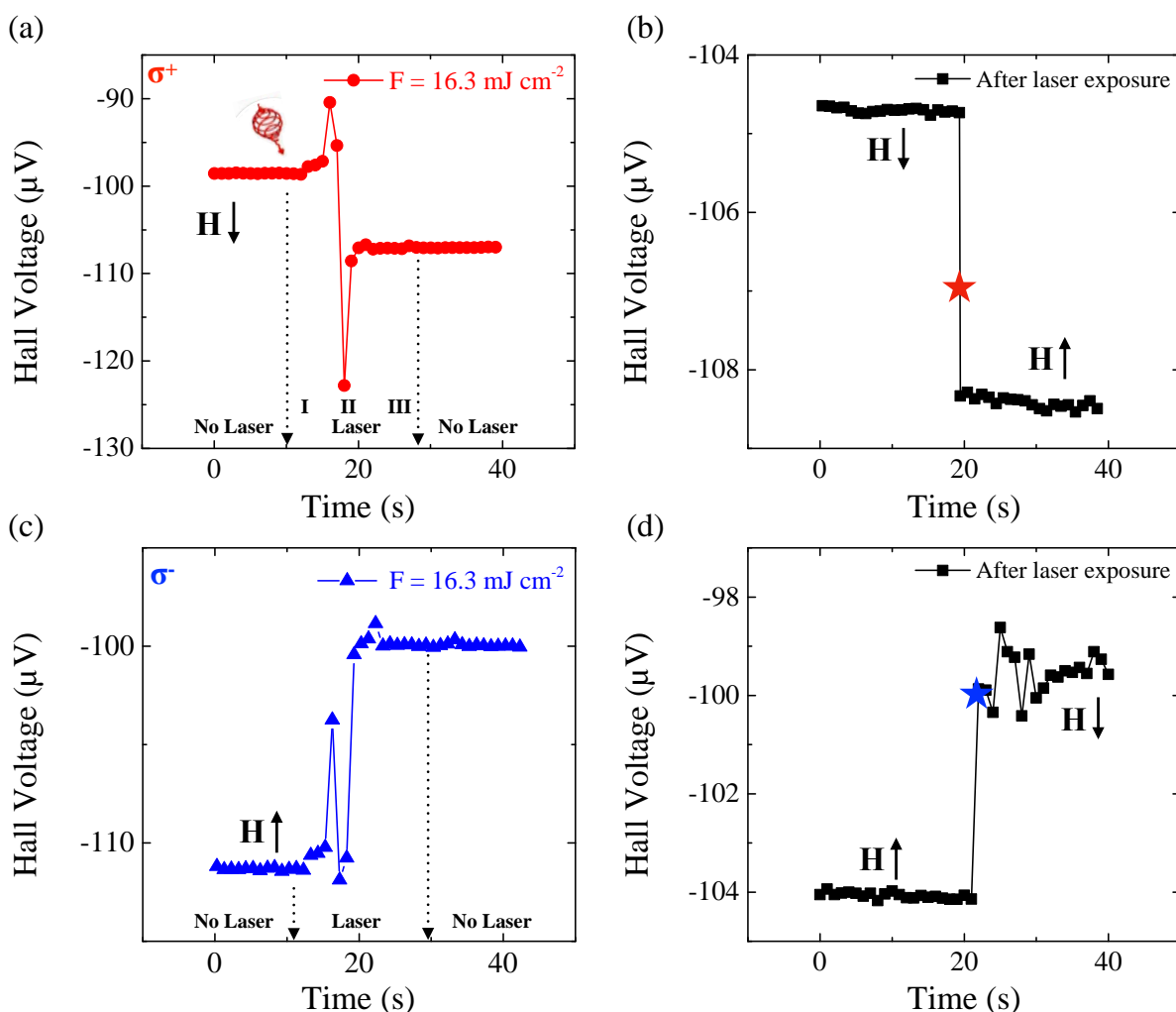


FIGURE IV.7: Time evolution of the Hall voltage in a $40\text{-}\mu\text{m}$ wide Hall cross with on top $3\text{-}\mu\text{m}$ dots when sweeping a 600-fs laser beam with (a) σ^+ and (c) σ^- polarization. (b) and (d) Hall voltage measured for the two magnetization saturation directions after the laser exposure. The laser fluence is set to 16.3 mJ cm^{-2} .

In the sweeping beam approach, as explained in Fig. IV.5, the laser beam is swept along the magnetic wire in the Hall bar. Three regions can be defined. First, region I. when the laser is initially far away from the center of the Hall cross ($\sim 200 \mu\text{m}$). Second region II. the laser

gets closer to the center of the Hall cross and finally region III. when the laser beam moves away from the Hall cross. The sample is first saturated. Then, the Hall voltage measurement is launched, with an acquisition point every 500 ms. After 10 s, the laser is turned on and swept over the Hall cross. When the laser beam reaches 200 μm past the center of the Hall cross, it is turned off and the Hall voltage measurement continues for a couple of seconds in order to evaluate the average Hall voltage after laser exposure. Thereafter, we measured again the Hall voltage for the two saturation directions in order to determine the magnetic state of the dots after laser irradiation. Indeed, we noticed that after each laser exposure, the Hall resistivity irreversibly changed. Yet, ΔV_H remained the same. Fig. IV.7(a) shows the result for the 40- μm Hall cross, 3- μm dots when sweeping a σ^+ polarized beam at a fluence of 16.3 mJ cm^{-2} for the microdots initially saturated down. A large jump of the Hall voltage is observed when the beam reaches the center of the Hall cross. This jump and the irreversible change in the Hall resistivity are likely to be due to the high laser heating effects. In fact, the jump ($\sim 20 \mu\text{V}$) is much larger than the change of the Hall voltage when reversing the dots $\Delta V_H = 4 \mu\text{V}$ as seen in Fig. IV.4. The Hall voltage further stabilizes when the beam moves away and is finally turned off. After laser irradiation $V_H = -107 \mu\text{V}$. Following the laser excitation, the sample is saturated in both direction and the Hall voltage is measured as seen in Fig. IV.7(b). ΔV_H is unchanged and the final Hall voltage after the laser exposure is represented by the red star. It is found a switching ratio of 65 %. We performed the same experiment with σ^- polarization and a sample initially saturated up. Almost a complete switching of $\sim 92 \%$ was observed as seen in Fig. IV.7(c,d). In contrast, no magnetization reversal occurred with σ^- (resp. σ^+) polarization when the sample is saturated -down (resp -up). Thus, this is a clear demonstration of helicity-dependent all-optical switching of an array of 3- μm (Co/Pt) dots when sweeping a fs laser beam. The difference in the switching ratio between the two opposite helicities is likely to be related to the stochastic nature of the amount of laser-induced magnetization switching, while the reversal direction is deterministic.

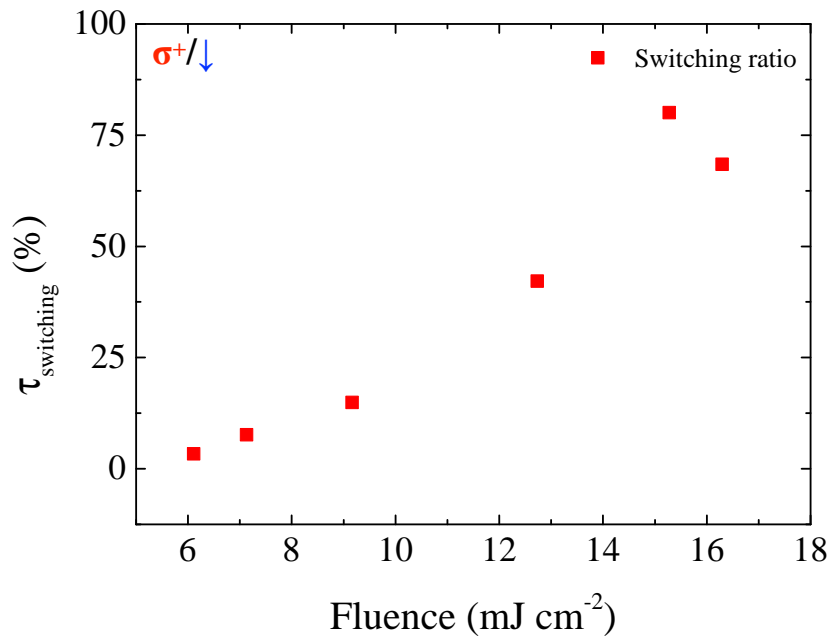


FIGURE IV.8: Switching ratio as a function of the laser fluence when sweeping a 600-fs σ^+ laser beam in a 40- μm Hall cross with 3- μm dots on top. The sample is initially saturated down.

Furthermore, we investigated the laser fluence dependence of the reversal of the microdots

upon laser irradiation. The laser fluence ranged from 6 mJ cm^{-2} (the full film switching threshold) to 16.3 mJ cm^{-2} (below the damage threshold of the thin Ta(5 nm)/Pt(5 nm) Hall cross). σ^+ polarization was used to induce magnetization reversal of the microdots. The switching ratio was measured for each laser fluence as previously discussed. The results are depicted in Fig. IV.8. As the laser fluence is increased, the switching ratio goes up. A maximum switching of $\sim 85\%$ is reached for $F = 15.2 \text{ mJ cm}^{-2}$. A further increase led to a drop of the switching ratio and finally to the damage of the Hall cross. Due to the high laser heating and considering the thin thickness of the Hall cross, the device was rapidly non functional which prevented us from determining the stochastic component of the laser-induced switching. The evolution of the switching ratio can be understood in terms of the switched area diameter when sweeping the laser beam in the full film as discussed in section 3.1. The $40\text{-}\mu\text{m}$ wide Hall cross contains 20 $3\text{-}\mu\text{m}$ dots in its center (5 rows). At low fluences, only the dots in the central rows can be switched. As the fluence increases, the switched area diameter goes up and more rows of dots are reversed. Yet, to completely switch all the dots in the Hall cross, a large switched area diameter of at least $40 \mu\text{m}$ is required, hence a large laser fluence. As a result, the dots in the outer parts of the Hall cross can be reversed, however the dots in the central part experience laser overheating and are demagnetized. Consequently, the switching ratio drops. Thence, we confirm that there is no significant difference between the continuous and patterned film with respect to the laser fluence dependence of AOS.

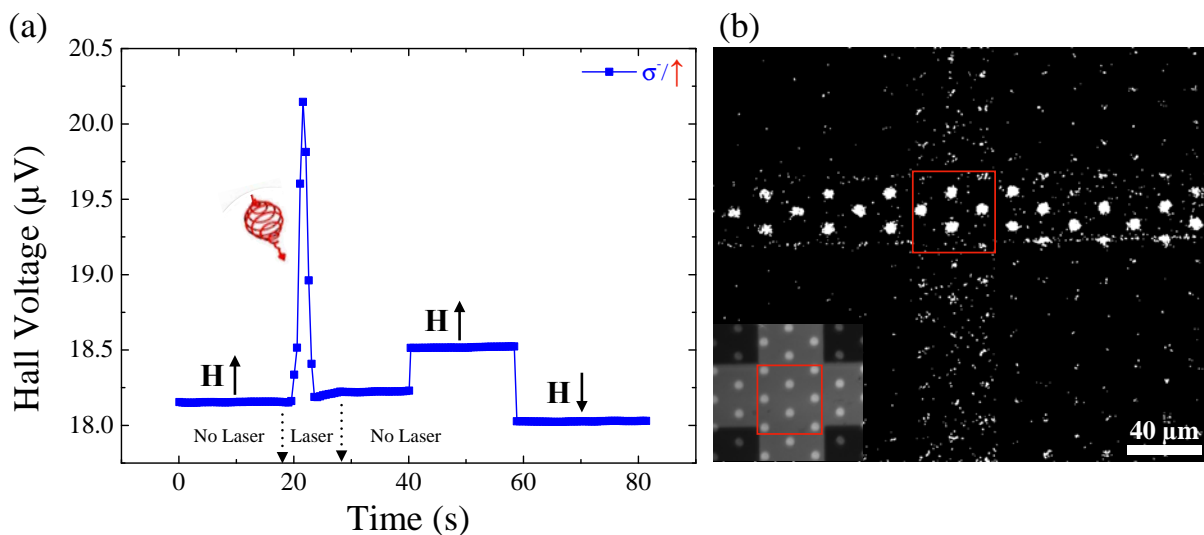


FIGURE IV.9: (a) Electrical characterization when sweeping the fs laser beam on a $40\text{-}\mu\text{m}$ wide Hall cross with $6\text{-}\mu\text{m}$ dots on top. A switching of about 50 % is achieved. (b) Processed differential magneto-optical image before and after laser exposure showing that 4 dots out of 8 switched in the center of the Hall cross.

Additionally, the measured Hall voltage in our experiments is the average Hall voltage of an assembly of dots. Therefore, questions can be raised regarding the magnetic state of each dot and how it contributes to the average Hall voltage. In fact, several magnetic configurations of the dots could yield the same switching ratio. To remove this ambiguity, the sweeping beam experiment was reproduced in a $40\text{-}\mu\text{m}$ wide Hall cross with on top $6\text{-}\mu\text{m}$ dots, for which the magnetic state can be clearly determined with the Faraday microscope. Fig. IV.9(a) shows the electrical characterization when sweeping the fs σ^- polarized beam for a sample initially saturated down. By the same method previously introduced, we found a switching ratio of about 50 % for $F = 11 \text{ mJ cm}^{-2}$. The ambiguity of this result is that all the dots could be demagnetized or instead half of the dots contained in the Hall cross switched. To resolve this issue, we took a magneto-optical image before and after the laser exposure and electrical characterization. The

processed differential image is shown in Fig. IV.9(b). 8 microdots are located in the center of the Hall cross as seen in the raw magneto-optical image (see inset). On the other hand, the differential image clearly indicates that the magnetization of only 4 dots was reversed (the ones that did not switch appear as dark in the differential image). Thus, this confirms that indeed only half of the $6\text{-}\mu\text{m}$ dots switched.

3.3 Summary

In this section, we presented a first attempt to investigate the size effects of HD-AOS in patterned ferromagnetic thin films when sweeping a circularly polarized laser beam. We evidenced HD-AOS of (Co/Pt) microdots with a diameter as small as $3\text{ }\mu\text{m}$. We were able to more accurately probe the reversal of the microstructures by measuring the anomalous Hall voltage in a Ta/Pt Hall cross with Pt/Co/Pt microdots on top. This novel approach should allow a statistical quantification of the switching ratio, provided the stack and Hall cross structure is adequately modified to increase the device lifetime when exposed to laser pulses. We demonstrated that although a slightly higher fluence is first needed to start switching the (Co/Pt) microdots, no particular laser fluence dependence was observed when sweeping the laser beam. It seems that in a sweeping beam configuration, the microdots behave in a similar manner than the continuous film. However, as the arrays of microdots are discrete media, HD-AOS when sweeping the laser cannot be explained by domain wall dragging, but instead a nucleation/propagation process is likely to happen within each dot as reported in the Pt/Co/Pt films.

4 Static beam experiments on (Co/Pt) microdots: influence of the number of laser pulses

In this section, we will focus on studying the microscopic reversal mechanism of patterned (Co/Pt) films compared to the continuous film. It is clear that HD-AOS in ferromagnets is a multishot and cumulative process [14, 22–24]. Yet, the question is how this cumulative switching changes when the material dimensions are scaled down to form a micropattern. For this purpose, we studied the magneto-optical response of a *single* dot when exposed to a train of laser pulses. In this case, the laser beam is kept at a fixed position and centered on the microdot. HD-AOS is probed via either static magneto-optical Faraday imaging or electrical characterization as previously introduced. With a pulse picker, we will control the number of laser pulses sent to excite the material.

4.1 Static imaging of the microdots arrays

In the section, the investigated material is the Pt(4.5 nm)/Co(0.6 nm)/Pt(4.5 nm) single layer structure that exhibits HD-AOS and HD-AODW motion. We first studied the continuous film upon irradiation by a train of laser pulses with a static beam. The laser pulse width was set to 600 fs and the laser fluence to 7 mJ cm^{-2} , which is slightly above the threshold. The sample is initially saturated up and σ^- polarization is used to induce magnetization reversal. With a pulse picker, we sent $N = 10, 20, 50$ and 100 laser pulses. A magneto-optical image was taken after each laser exposure and the magnetic state was subsequently re-initialized prior the next train of laser pulses. This was repeated three times for each number of laser pulses. The results are shown in the differential magneto-optical images in Fig. IV.10. After each train of laser pulses,

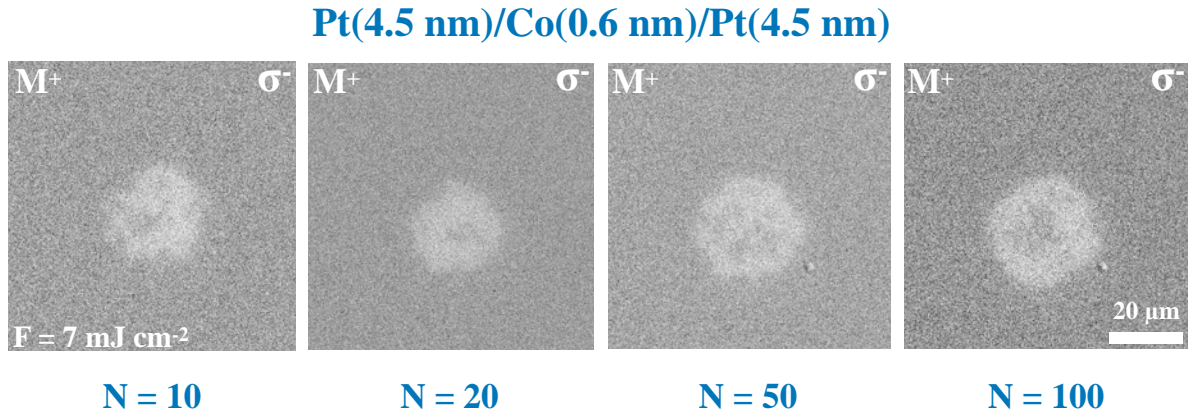


FIGURE IV.10: Differential magneto-optical images of a Pt/Co/Pt continuous film after laser exposure and as a function of the number of laser pulses (N). The sample is initially saturated up (M^+) and exposed to σ^+ polarization. The laser fluence is set to 7 mJ cm^{-2} . The number of laser pulses to excite the material was controlled with a pulse picker.

a multidomain state is reached. Yet, qualitatively a majority of magnetization-down domains seems to emerge. To verify the latter, we tried to quantify the switching ratio. In the raw magneto-optical images, the mean intensity I_{laser} of the pumped area was measured. This will give information about the average magnetic state after laser exposure. The mean intensities for a film uniformly saturated in either direction, I_{M^+} and I_{M^-} , were also measured. Thus, we define the switching ratio for a σ^+ polarized beam as: $\tau = \frac{I_{M^+} - I_{\text{laser}}}{I_{M^+} - I_{M^-}}$ (%). Fig. IV.11(a) features the switching ratio as a function of the number of laser pulses in the Pt/Co/Pt continuous film. It is found that for $N \geq 10$, more than 50 % of the pumped area was reversed.

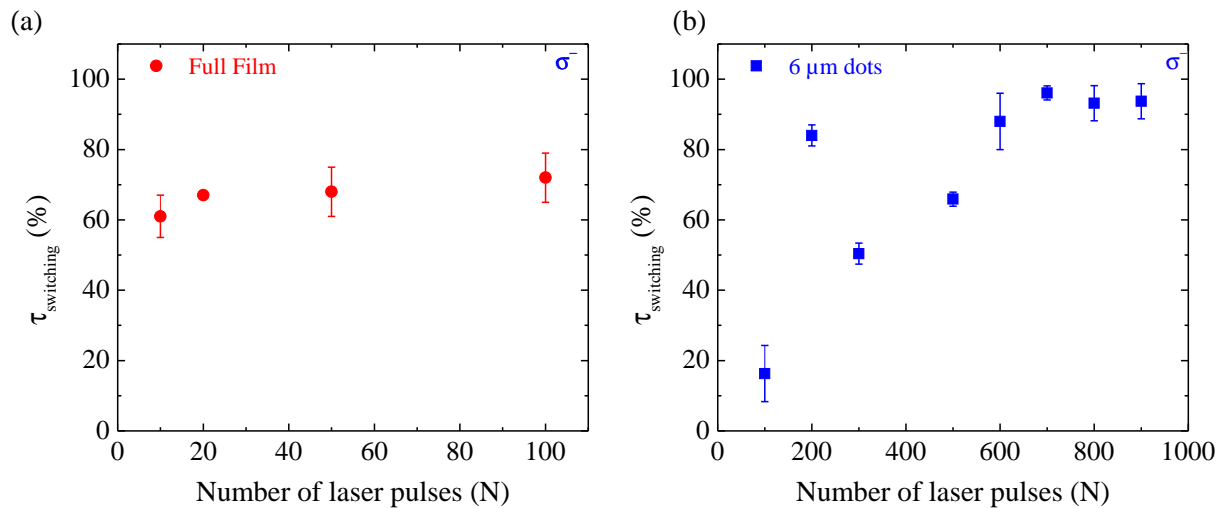


FIGURE IV.11: Switching ratio as a function of the number of laser pulses for a static beam configuration in the Pt/Co/Pt (a) full film and (b) patterned into a $6\text{-}\mu\text{m}$ dot.

Furthermore, we reproduced the experiment under the same conditions on a $6\text{-}\mu\text{m}$ dot initially saturated up and excited with σ^- polarization. The mean intensity of the microdot is measured after each train of laser pulses. Fig. IV.11(b) shows the switching ratio for $100 \leq N \leq 900$. A reliable switching of more than 50 % is achieved only for $N \geq 200$. For $N = 100$, in average the laser pulses induced only 16 % of reversal of the microdot magnetization. In contrast, with 100 laser pulses, 72 % of the pumped area in the full film was switched. Thus, interestingly

it seems that a higher number of laser pulses, at least 10 times higher, is required to switch the magnetization of a $6\text{-}\mu\text{m}$ dot compared to the continuous film. However, in the Pt/Co/Pt single layer structure, the magneto-optical contrast was weak compared to the background noise, especially for the microdot. Hence, quantification is difficult and a more accurate method is required, specifically for smaller microdots. Therefore, we performed a similar experiment where the laser-induced magnetization switching is probed by electrical characterization in a Hall cross via the AHE as presented in the previous section.

4.2 Electrical characterization of a single (Co/Pt) microdot on top of a Hall cross

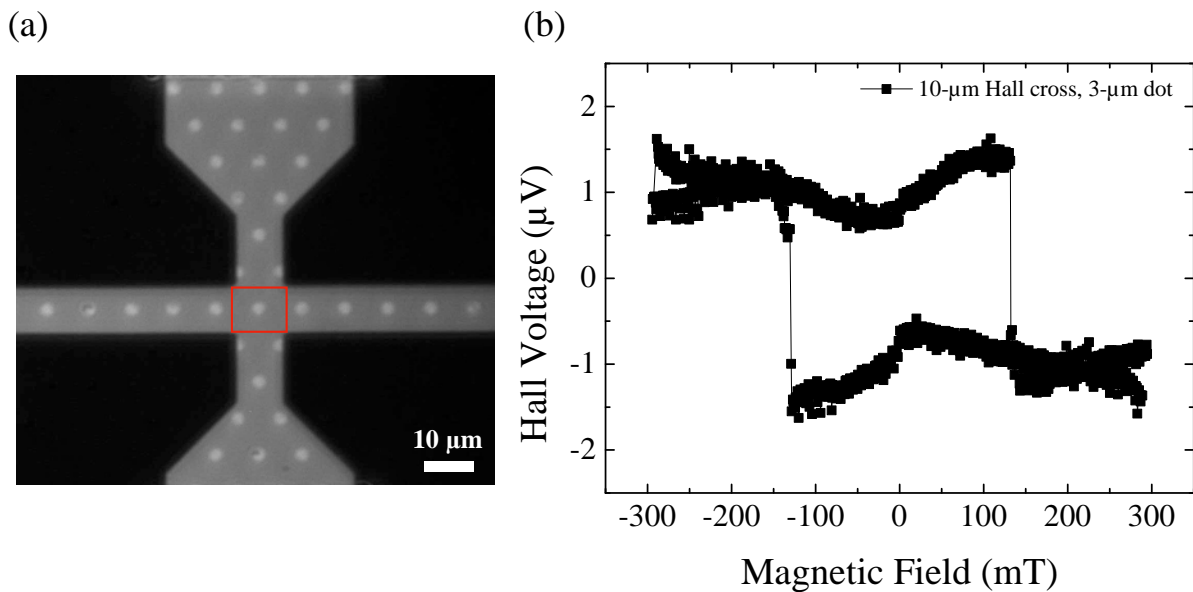


FIGURE IV.12: (a) Magneto-optical image of a Ta(5 nm)/Pt(5 nm) Hall cross with on top a single $3\text{-}\mu\text{m}$ Pt(5 nm)/Co(0.6 nm)/Pt(10 nm) dot in its center. (b) Magnetization characterization by magneto-transport measurement via the anomalous Hall effect.

Unlike in section 3.2, for which the Hall cross contained an assembly of microdots in its center, here we patterned a Ta(5 nm)/Pt(5 nm) Hall cross with a *single* $3\text{-}\mu\text{m}$ Pt(5 nm)/Co(0.6 nm)/Pt(10 nm) dot in its center as seen in Fig. IV.12(a). However, the anomalous Hall voltage of a single $3\text{-}\mu\text{m}$ dot is expected to be much lower than for the assembly of 20 microdots. As result, we patterned a narrower $10\text{-}\mu\text{m}$ wide Hall bar to increase the current density to $5 \times 10^6 \text{ A m}^{-2}$ for an input dc current of 0.5 mA. Consequently, we were able to electrically characterize the magnetic state of the single $3\text{-}\mu\text{m}$ dot via the anomalous Hall effect. The magneto-transport measurement as a function of the applied out-of-plane field is depicted in Fig. IV.12(b). Magnetization reversal of the microdot is accompanied by a change of the Hall voltage of $\Delta V_H \simeq 2.5 \text{ }\mu\text{V}$ for a coercive field of 150 mT.

In this experiment, the laser beam was kept at a fixed position and centered on the Hall cross. The sample was initially saturated up and further exposed to σ^- polarization. The laser fluence was set to 10 mJ cm^{-2} . After each train of laser pulses, the Hall voltage corresponding to both magnetization saturation directions was measured. The number of laser pulses ranged from 1000 to 3000. For each number of laser pulses, the measurement was repeated three times. Below $N = 1000$, no laser-induced change of the magnetization of the $3\text{-}\mu\text{m}$ dot could be observed. An example for $N = 2000$ is shown in Fig. IV.13(a). For $t < 10 \text{ s}$, the sample is saturated up and not exposed to the laser beam. A large jump of the Hall voltage occurs when the train of

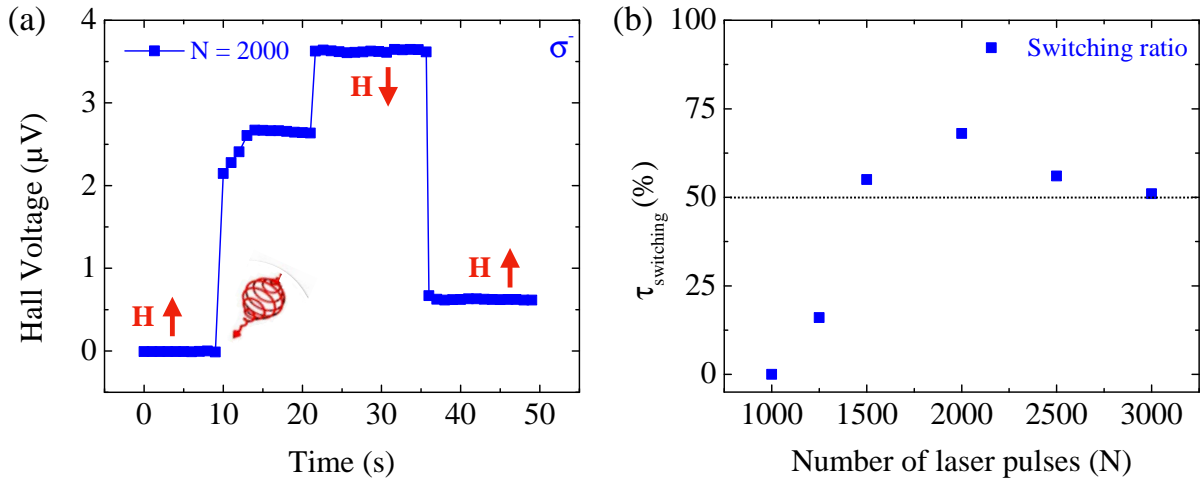


FIGURE IV.13: (a) Electrical characterization of all-optical switching in a Ta/Pt Hall cross with on top a single $3\text{-}\mu\text{m}$ Pt/Co/Pt dot exposed to $N = 2000$ σ^- polarized laser pulses. (b) Average switching ratio as a function of the number of laser pulses as defined in the text.

laser pulses is sent to excite the material. Further, the material is saturated down then up. An offset of about $0.5 \mu\text{V}$ can be observed, which corresponds to the irreversible change of the Hall resistivity of the sample. The latter can be attributed to the ultra high laser heating of the thin Ta(5 nm)/Pt(5 nm) Hall bar. Yet, the change of the Hall voltage upon reversal of the direction of the applied out-of-plane field remains the same as prior to the first laser exposure. This indicates that the magnetic medium was not damaged by the train of laser pulses. By comparing the Hall voltage after laser irradiation to ΔV_H , for $N = 2000$ a switching ratio of 67 % is found.

Fig. IV.13(b) shows the average switching ratio for $1000 \leq N \leq 3000$. A switching of more than 50 % is obtained for $N \geq 1500$. The maximum laser-induced magnetization reversal is accomplished with $N = 2000$. A higher number of laser pulses seems to bring the microdot into a demagnetized state, which may hint that the laser fluence was too high. Notably, a higher fluence was necessary in the Hall cross measurement as the Pt buffer and top layer thickness was increased for the lithography process. As a comparison, at a lower fluence, 10 laser pulses were sufficient to reverse the magnetization of the pumped area in the Pt/Co/Pt continuous film. Hence, it is clear that a larger number of laser pulses is required to reverse the magnetization of the $3\text{-}\mu\text{m}$ than for the continuous film. Moreover, the results for the 6- and $3\text{-}\mu\text{m}$ dots suggest that as the diameter of the microdot goes down, the required number of laser pulses to induce magnetization switching increases. Yet, the latter would need to be confirmed by performing the electrical characterization of HD-AOS in Hall crosses as a function of the microdot diameter. In addition, as previously discussed we were limited by the lifetime of the device to carry out a more statistical approach to determine the switching ratio.

4.3 Summary and discussion

In this section, we investigated the influence of the number of laser pulses in the helicity-dependent all-optical magnetization switching of a single Pt/Co/Pt microdot for a static laser beam. It was found that a higher number of laser pulses is required to achieve AOS in a microdot than in the continuous film. As the size of the microdot goes down, the necessary number of laser pulses seem to increase. These results highlight the major role of the dipolar field

in the magnetization reversal mechanism of AOS. Indeed, a magnetic dot senses only its self-demagnetizing field. On the other hand, in a continuous film, the region pumped by the laser is subject to the dipolar field from the surrounding area. In the latter, AOS appears to necessitate a lesser number of laser pulses than in the former. Thus, it demonstrates that actually the dipolar field eases the magnetization switching in AOS. This may be counter-intuitive as Lambert *et al.* proved that ferromagnetic (Co/Pt) multilayers exhibited HD-AOS when reducing the thickness in order to suppress the dipolar energy gain for domain formation in the ultrathin-film limit [1]. Yet, it was proved that in ferromagnets magnetization reversal takes place through a cumulative process that involves nucleation and helicity-dependent domain wall propagation as evidenced in the previous chapter III [16, 22, 23]. Thence, in the continuous film, the dipolar field from the surrounding areas may help the nucleation step making the AOS more energy-efficient.

5 Summary and perspectives

In the fourth chapter of this thesis, we presented a first attempt to investigate the size effects of AOS in patterned (Co/Pt) ultrathin films. Two experimental approaches were employed. Indeed, the fs circularly polarized laser beam was either swept over the sample surface or kept at a fixed position allowing thus a precise monitoring of the number of laser pulses to excite the material. Moreover, the laser-induced magnetization switching of the microdots was probed by static magneto-optical imaging or by electrical characterization via the anomalous Hall effect measurement in a Hall cross patterned with microdots on top. The second method appeared to be a better and more accurate technique to probe HD-AOS in small structures while magnetic domains cannot be easily optically resolved in microdots with a diameter below $3 \mu\text{m}$.

We demonstrated that HD-AOS could also be exhibited in microdots with a diameter as small as $3 \mu\text{m}$. Yet, when sweeping the laser beam, no particular difference in the laser fluence dependence of the reversal with respect to the continuous film was found. We successfully probed HD-AOS of a single $3\text{-}\mu\text{m}$ dot with a Hall cross via the anomalous Hall effect. It allowed us to gain insight into the switching mechanism. Indeed, it appeared that magnetization reversal in a (Co/Pt) microdot requires a much higher number of laser pulses than in the continuous film. This suggests that in fact the dipolar field eases the laser-induced magnetization switching making all-optical switching more energy-efficient in the continuous film. Thus, it comes out that ferromagnetic (Co/Pt) multilayers are not the ideal candidate for integrating all-optical switching in ultrahigh density magnetic data storage or memory devices. To confirm the latter, the size effects of all-optical switching should be extended to nano-patterns probed by electrical characterization. For a further investigation, the Hall cross structure needs to be reconsidered in order to enhance the device lifetime and for a better statistical approach. A solution would be to improve the heat diffusion in the Hall cross to prevent laser overheating. On the other hand, at the nanometer scale, MFM imaging will become a relevant technique to probe the magnetic state after laser exposure.

Finally, this novel approach to probe all-optical switching in microstructures patterned on top of a Hall cross paves the way to an interesting new field that combines optics and spintronics. Indeed, one could imagine to associate current-induced magnetization reversal via spin-transfer or spin-orbit torque to helicity-dependent all-optical switching to manipulate the magnetization of nano-patterns. Magnetic field and laser heating were combined for heat-assisted magnetic recording. Similarly, current pulses coupled to circularly polarized laser pulses could be then used to achieve ultrahigh density and ultrafast magnetic recording.

References

1. Lambert, C.-H. *et al.* All-optical control of ferromagnetic thin films and nanostructures. *Science* **345**, 1337 (Sept. 2014).
2. Hoveyda, F, Hohenstein, E, Judge, R & Smadici, S. Demagnetizing fields in all-optical switching. *Journal of Physics: Condensed Matter* **30**, 035801 (2018).
3. Ogasawara, T., Iwata, N., Murakami, Y., Okamoto, H. & Tokura, Y. Submicron-scale spatial feature of ultrafast photoinduced magnetization reversal in TbFeCo thin film. *Applied Physics Letters* **94**, 162507 (2009).
4. Le Guyader, L. *et al.* Demonstration of laser induced magnetization reversal in GdFeCo nanostructures. *Applied Physics Letters* **101**, 022410 (2012).
5. Le Guyader, L. *et al.* Nanoscale sub-100 picosecond all-optical magnetization switching in GdFeCo microstructures. *Nature Communications* **6**, 5839 (Jan. 2015).
6. Radu, I. *et al.* Transient ferromagnetic-like state mediating ultrafast reversal of antiferromagnetically coupled spins. *Nature* **472**, 205–208 (Mar. 2011).
7. Yong, X. *et al.* Ultrafast Magnetization Manipulation Using Single Femtosecond Light and Hot-Electron Pulses. *Advanced Materials* **29**, 1703474 (2017).
8. Gorchon, J. *et al.* Single shot ultrafast all optical magnetization switching of ferromagnetic Co/Pt multilayers. *Applied Physics Letters* **111**, 042401 (2017).
9. Savoini, M. *et al.* Highly efficient all-optical switching of magnetization in GdFeCo microstructures by interference-enhanced absorption of light. *Physical Review B* **86**, 140404 (Oct. 2012).
10. Bedau, D. *et al.* Ultrafast spin-transfer switching in spin valve nanopillars with perpendicular anisotropy. *Applied Physics Letters* **96**, 022514 (2010).
11. Liu, H. *et al.* Ultrafast switching in magnetic tunnel junction based orthogonal spin transfer devices. *Applied Physics Letters* **97**, 242510 (2010).
12. Albrecht, T. R. *et al.* Bit Patterned Media at 1 Tdot/in² and Beyond. *IEEE Transactions on Magnetics* **49**, 773–778. ISSN: 0018-9464 (2013).
13. Richter, H. J. *et al.* Recording potential of bit-patterned media. *Applied Physics Letters* **88**, 222512 (2006).
14. El Hadri, M. S. *et al.* Two types of all-optical magnetization switching mechanisms using femtosecond laser pulses. *Physical Review B* **94**, 064412 (Aug. 2016).
15. El Hadri, M. S. *et al.* Domain size criterion for the observation of all-optical helicity-dependent switching in magnetic thin films. *Physical Review B* **94**, 064419 (Aug. 2016).
16. El Hadri, M. S. *et al.* Electrical characterization of all-optical helicity-dependent switching in ferromagnetic Hall crosses. *Applied Physics Letters* **108**, 092405 (2016).
17. Hall, E. H. XVIII. On the “Rotational Coefficient” in nickel and cobalt. *The London, Edinburgh, and Dublin Philosophical Magazine and Journal of Science* **12**, 157–172 (Sept. 1881).
18. Nagaosa, N., Sinova, J., Onoda, S., MacDonald, A. H. & Ong, N. P. Anomalous Hall effect. *Reviews of Modern Physics* **82**, 1539–1592 (May 2010).
19. Luttinger, J. M. Theory of the Hall Effect in Ferromagnetic Substances. *Physical Review* **112**, 739–751 (Nov. 1958).
20. Berger, L. Side-Jump Mechanism for the Hall Effect of Ferromagnets. *Physical Review B* **2**, 4559–4566 (Dec. 1970).
21. Moritz, J, Rodmacq, B, Auffret, S & Dieny, B. Extraordinary Hall effect in thin magnetic films and its potential for sensors, memories and magnetic logic applications. *Journal of Physics D: Applied Physics* **41**, 135001 (2008).
22. Medapalli, R. *et al.* Multiscale dynamics of helicity-dependent all-optical magnetization reversal in ferromagnetic Co/Pt multilayers. *Physical Review B* **96**, 224421 (Dec. 2017).

23. Takahashi, Y. K. *et al.* Accumulative Magnetic Switching of Ultrahigh-Density Recording Media by Circularly Polarized Light. *Physical Review Applied* **6**, 054004 (Nov. 2016).
24. Gorchon, J., Yang, Y. & Bokor, J. Model for multishot all-thermal all-optical switching in ferromagnets. *Physical Review B* **94**, 020409 (July 2016).

Chapter V

Conclusions and future challenges in all-optical switching

In this thesis, we investigated the magneto-optical response of ferromagnetic (Co/Pt) multilayer ultrathin films upon femtosecond laser irradiation. The field of magnetization manipulation by ultrashort laser pulses emerged over the past decade as a topic of great interest in ultrafast nanomagnetism. First, we aimed at gaining insight into the underlying mechanism of the laser-induced magnetization reversal in ferromagnetic materials. Second, we were interested in exploring the size effects of all-optical switching when structuring the ferromagnetic ultrathin films into micropatterns to study the feasibility of integrating all-optical switching in ultrahigh density magnetic data storage devices. We present here a summary of the results obtained in this thesis.

Recently, several advances were made regarding the all-optical switching mechanism in ferromagnetic materials. It was demonstrated that in ferromagnets, all-optical switching is a cumulative and multishot process in two steps: a helicity-independent demagnetization corresponding to a multidomain state followed by a helicity-dependent magnetization recovery. The cumulative nature of all-optical switching was evidenced in (Co/Pt) multilayers, FePt granular media but also in ferrimagnetic CoTb alloys. It appeared that materials could be classified in two categories with respect to the mechanism: on one hand a single pulse toggle switching in GdFeCo alloys and on the other hand a multi-pulse slow helicity-dependent magnetization switching. The cumulative nature of all-optical switching has been well established by several studies. Yet, the helicity-dependent magnetization recovery mechanism had not been examined yet. We thus tried to elucidate it.

Growing evidence suggested the importance of domain wall mobility and magnetic domains in the helicity-dependent magnetization recovery of all-optical switching. Therefore, we investigated the response of domain wall in Pt/Co/Pt thin films upon laser irradiation. We indeed demonstrated helicity-dependent all-optical domain wall motion in (Co/Pt) multilayers with femto- or pico-second laser pulses and with no applied magnetic field [published in *Phys. Rev. B.* **97**, 054419 (2018)]. This highlights a new possibility to deterministically manipulate domain walls using only light. From a technological point of view, a new type of racetrack memories and logic devices could emerge. Indeed, one could imagine to use plasmonic nanoantennas to obtain a nanofocused laser beam spot to control the domain wall in nanowires. In addition, we also evidenced helicity-dependent domain wall motion in CoTb alloys, which may be another hint that the all-optical switching mechanism in ferrimagnetic CoTb alloys is similar to the one in ferromagnetic materials.

We studied multiple parameters that can affect the laser-induced domain wall motion such as the laser power and the laser beam position with respect to the domain wall. We inspected the influence of linear polarization and the degree of light ellipticity. This allowed us to propose a

mechanism for the all-optical domain wall motion. It came out that the laser-induced domain wall displacement result from the balance of three contribution: the temperature gradient due to the laser heating, the helicity effect and the pinning effects.

Further, we studied the mechanism that could be responsible for the helicity effect in the domain wall displacement that we observed. Helicity-dependent all-optical switching in GdFeCo alloys was explained by a thermal mechanism based on magnetic circular dichroism. Similarly, single pulse helicity-independent toggle switching in the same material was proved to be a result of ultrafast laser heating effects affecting the dynamics of the two sublattices. Conversely, conflicting studies can be found in the literature regarding the effect of helicity in all-optical switching in ferromagnetic materials. A theoretical work suggested an athermal mechanism relying on the inverse-Faraday effect and a single pulse switching. Yet, up-to-date no ultrafast single pulse helicity-dependent switching has been reported in (Co/Pt) films. On the contrary, several studies explored the possibility of a thermal multishot process. In this context, we wanted to see if we could discriminate these two mechanisms based on the helicity-dependent all-optical domain wall motion we reported.

Thusly, we demonstrated that by modeling a fs laser pulse by a small effective field of 10 mT with the same duration as the laser pulse width, combined with a temporal and spatial temperature distribution calculated with the phenomenological two-temperature model, we were able to reproduce the deterministic laser-induced domain wall motion. Yet, the simulated domain wall displacement per pulse highly depends on the domain wall inertia and the pinning barrier. A precise measurement of the parameters ruling domain wall propagation in the Pt/Co/Pt thin films we studied would lead to more accurate simulations. Moreover, we have also explored a pure thermal mechanism based on magnetic circular dichroism. We found that indeed a small percentage ($\gtrsim 1\%$) of difference of light absorption between left- and right- circular polarization leads to a temperature difference great enough to unpin a domain wall. A question was raised regarding the direction of the temperature gradient across the domain wall, hence of the effective thermal field, compared to the observed domain wall displacement direction for a given light helicity. Consequently, we measured the light absorption as a function of the magnetization saturation direction and helicity of the incident light. We found a sign of the magnetic circular dichroism that does not match the direction of the reported domain wall displacement. As a result, we ruled out a pure thermal mechanism based on magnetic circular dichroism to explain the helicity-dependent all-optical domain wall motion [to be submitted]. Yet, further experimental investigations of the sign of the magnetic circular dichroism are required to confirm the latter.

Finally, the main attraction of all-optical switching is the possibility to pave the way for innovative ultrahigh density and ultrafast magnetic data storage devices. To study the feasibility of implementing all-optical switching in data storage or memory devices, it is important to understand the size effects in all-optical switching when structuring the material into micro- and nano-patterns. So far, such work was carried out only in GdFeCo micro- or nano-structures. We investigated the size effects in all-optical switching in patterned (Co/Pt) thin films. It was decided to first analyze the laser-induced magnetization reversal in micropatterns. We employed two different approaches to probe HD-AOS in the (Co/Pt) microdots. The first method consisted in static magneto-optical imaging. In the second approach, the laser-induced change in magnetization is probed by electrical characterization of a Hall cross via the anomalous Hall effect. We patterned a Ta/Pt Hall cross with (Co/Pt) microdots on top to deduce the magnetic state of the microstructures after laser exposure by magneto-transport measurement. This method allows a better quantification of the switching ratio. We performed the experiments with either sweeping the laser beam over the sample surface or for a static beam configuration. We demonstrated the helicity-dependent all-optical magnetization switching of (Co/Pt)

microdots with a diameter as small as $3\ \mu\text{m}$. It was also discovered that no particular difference between the continuous film and the micro-patterns could be exhibited in the sweeping beam configuration.

Later, we investigated the influence of the number of laser pulses. Surprisingly, we gave evidence that a higher number of laser pulses is required to induce magnetization reversal in a microdot compared to the full film when exposed to 600-fs laser pulses. It seemed that the smaller the diameter, the higher the number of laser pulses to observe laser-induced switching. These results provided interesting insight into the all-optical switching mechanism [to be submitted]. Indeed, it suggests that the dipolar field eases the magnetization switching in the continuous film upon laser irradiation, hence making all-optical switching more energy-efficient in the continuous film. Thus, it appears that (Co/Pt) is not an ideal candidate to integrate all-optical switching into ultrahigh density magnetic data storage devices. One would need to extend this study to nano-patterns to confirm the latter. Moreover, in our experiments, the probing of HD-AOS was difficult with the static imaging as the small magnetic domains could not be optically resolved. Regarding the magneto-transport measurement, our devices suffered from a critical short lifetime that prevented us from carrying out a more statistical approach. The adequate structure and thickness of the Hall cross should be reconsidered to allow accurate and reproducible quantification of the switching ratio after laser exposure. Yet, the electrical characterization via the AHE was a powerful tool to probe HD-AOS. With the devices we patterned by UV lithography, one could even think of a new research field that combines magnetization switching induced by current pulses via STT or SOT with HD-AOS.

It is believed that the research carried out in this thesis enhances our current understanding of the underlying physics and mechanism of all-optical switching in ferromagnetic materials. It is clear now that all-optical switching in ferromagnets takes place through a nucleation and helicity-dependent domain wall propagation. Nonetheless, the origin of the helicity effect remains obscure. Further investigation would be required to elucidate the microscopic origin of the helicity effect in all-optical switching. We have also provided a new insight into the possible integration of all-optical switching in magnetic data storage or memory devices. One aspect that has not been addressed in this thesis is the dynamics of the phenomena we studied within a shorter timescale following the laser pulse excitation. One would likely gain valuable information for instance in the domain wall depinning process. We understand that the rich physics of all-optical switching remains highly debated and an open question. We hope that our results open the way to new research directions in all-optical switching.

Conclusions et perspectives futurs dans le retournement tout-optique

Dans cette thèse, nous avons étudié la réponse magneto-optique de couches minces de Co/Pt à la suite d'impulsions laser femtoseconde. Le domaine de la manipulation de l'aimantation par impulsions lasers ultracourtes a émergé au cours de la dernière décennie et a présenté un grand intérêt pour la communauté scientifique travaillant sur le contrôle ultra-rapide de l'aimantation. Tout d'abord, notre but était de mieux comprendre le mécanisme à l'origine du renversement de l'aimantation induit par impulsions laser. Par ailleurs, nous étions intéressés par l'étude des effets de taille du retournement tout-optique lorsque les films ferromagnétiques sont structurés en motifs à l'échelle du micromètre, et cela dans le but d'explorer la faisabilité de l'intégration du retournement tout-optique dans des technologies de sauvegarde l'information à très haute densité. Nous présentons ici un résumé des résultats obtenus au cours de ce travail de recherche en thèse.

Récemment de nombreuses avancées majeures ont été faites dans la compréhension du retournement tout-optique de l'aimantation des matériaux ferromagnétiques. Il a été démontré que dans les ferro-aimants le renversement tout-optique était un phénomène cumulatif et un processus à multiples pulses se déroulant en deux étapes : une désaimantation indépendante de l'hélicité et correspondant à un état multi-domaines, suivie par une ré-aimantation dépendant de l'hélicité. L'aspect cumulatif du retournement tout-optique a été mis en évidence dans de nombreux matériaux notamment dans les multicouches de Co/Pt, les FePt granulaires ainsi que dans les alliages ferrimagnétiques de CoTb. Il est alors apparu que les matériaux pouvaient être classés en deux catégories selon le mécanisme de renversement : d'un côté le retournement en une seule impulsion indépendamment de la polarisation de la lumière comme dans les alliages de GdFeCo, et d'un autre côté le renversement lent et multi-pulse qui dépend de l'hélicité. Bien que l'aspect cumulatif du retournement tout-optique eût été bien établi par plusieurs études, le mécanisme à l'origine de la ré-aimantation dépendant de l'hélicité n'avait pas été éclairci. Nous avons donc essayé de l'élucider.

De plus en plus de résultats expérimentaux tendaient à pointer vers une importance de la mobilité des parois de domaines et du rôle des domaines magnétiques dans le renversement tout-optique dépendant de l'hélicité. En conséquence, nous avons étudié la réponse des parois de domaines dans les couches minces de Pt/Co/Pt à la suite d'impulsions lasers. En effet, nous avons démontré qu'il était possible de manipuler les parois de domaines de manière déterministe dans les multicouches de (Co/Pt) avec des impulsions laser femto- ou pico-seconde et polarisées circulairement, et ce sans appliquer de champ magnétique externe [publication dans *Phys. Rev. B.* **97**, 054419 (2018)]. Ce résultat original met en avant une nouvelle façon de contrôler le déplacement de parois de domaines uniquement avec de la lumière. D'un point de vue technologique, cela pourrait servir à l'implémentation de nouveaux appareils logiques et de mémoires à pistes. Effectivement, à l'aide de nano-antennes il est possible de focaliser un faisceau laser à l'échelle du nanomètre et ainsi de pouvoir manipuler les parois de domaines dans des nano-fils. De plus, nous avons observé le déplacement tout-optique et dépendant de

l'hélicité également dans les alliages ferrimagnétiques de CoTb, ce qui serait une autre indication que ce type de matériaux partagent un mécanisme de renversement de l'aimantation similaire à celui des couches ferromagnétiques.

Nous avons mené l'étude du déplacement de parois induit par impulsions laser en fonction de plusieurs paramètres tels que la puissance du faisceau laser et la position du centre du faisceau par rapport à la position initiale de la paroi de domaine. Nous nous sommes également intéressé à l'influence de la polarisation linéaire et du degré d'éllipticité de la lumière. Cela nous a permis de proposer un mécanisme microscopique de ce déplacement de parois tout-optique. Il est apparu que le déplacement de parois induit par impulsions laser résulte de la compétition entre le gradient de température dû au chauffage du laser et de l'effet de l'hélicité de la lumière. Par ailleurs, il est nécessaire de considérer les effets de piégeages et le paysage énergétique à la surface du matériau.

De plus, nous nous sommes penché sur la possible origine de l'effet de l'hélicité de la lumière sur le déplacement de paroi que nous avons observé. Le retournement tout-optique dépendant de l'hélicité dans les alliages de GdFeCo avait été expliqué par un mécanisme purement thermique basé sur le dichroïsme circulaire magnétique. Le renversement induit par une seule impulsion laser avait également été démontré comme résultant d'effets ultra-rapides de chauffage laser affectant la dynamique de l'aimantation des deux sous-réseaux. A l'inverse, de nombreuses conclusions contradictoires peuvent être trouvées dans la littérature concernant l'effet de l'hélicité dans le retournement tout-optique des couches ferromagnétiques. Des travaux théoriques ont suggéré un mécanisme athermique basé sur l'effet Faraday inverse et un renversement en une seule impulsion. Pour autant, jusqu'à aujourd'hui aucun retournement ultra-rapide en une seule impulsion et dépendant de l'hélicité n'a été observé dans les couches ferromagnétiques de Co/Pt. A contrario, plusieurs études ont exploré la possibilité d'un mécanisme thermique et multi-pulse. C'est dans ce contexte que nous avons voulu voir si nous pouvions discriminer ces deux types de mécanismes, l'un purement thermique et l'autre se fondant sur des effets opto-magnétiques athermiques, par le biais de la compréhension du déplacement de parois tout-optique et dépendant de l'hélicité que nous avons observé.

Ainsi, nous avons démontré que par modélisant une impulsion laser fs par un faible champ magnétique effectif de l'ordre de 10 mT et avec la même durée que l'impulsion laser, et en combinaison avec un profil de température spatial et temporel calculé par le modèle phénoménologique à deux températures, nous étions en mesure de reproduire le déplacement déterministe de parois de domaines induit par laser. Cependant cette modélisation du déplacement tout-optique de parois de domaines dépend énormément des paramètres utilisés ainsi que de l'inertie de la paroi et de la barrière de piégeage qui ne sont pas clairement connus dans nos systèmes. De fait, une mesure précise des paramètres régissant le déplacement de parois dans les multicouches (Co/Pt) que nous avons étudié serait nécessaire au préalable pour une modélisation plus adéquate. Nous avons aussi envisagé un mécanisme purement thermique qui se fonde sur le dichroïsme circulaire magnétique. Nous avons trouvé qu'un faible dichroïsme d'à peine 1 % pour la différence d'absorption de lumière entre la polarisation circulaire-gauche et circulaire-droit serait suffisant pour créer un gradient de température pouvant dépiéger une paroi de domaine. Néanmoins une question demeure concernant le sens de ce gradient de température aux bords de la paroi en comparaison au sens du déplacement que nous avons observé dans nos expériences pour une hélicité donnée. Par conséquent, afin de répondre à cette question nous avons mesuré l'absorption de la lumière en fonction de l'orientation de l'aimantation à saturation et de l'hélicité de la polarisation circulaire. Nous avons trouvé que le signe du dichroïsme circulaire magnétique était en désaccord avec le sens du déplacement de parois que nous avons observé. De fait, nous avons pu exclure un mécanisme purement

thermique fondé sur le dichroïsme circulaire magnétique et son interprétation en champ magnétique effectif pour expliquer le déplacement tout-optique de parois de domaines [publication à venir]. Cependant, d'autres mesures expérimentales seront nécessaires afin de confirmer ce résultat surprenant et notamment par d'autres méthodes de mesures telle que l'ellipsométrie Kerr.

Finalement l'attractivité du retournement de l'aimantation tout-optique repose sur la possibilité de mettre en place des dispositifs innovants de stockage de l'information non seulement à très haute densité mais surtout à des échelles de temps ultra-courtes. Pour étudier la faisabilité de l'intégration du renversement tout-optique dans de tels dispositifs et mémoires magnétiques, il est important de comprendre les effets de taille lorsque le matériau est structuré en motifs à de très petites échelles. Jusqu'à présent de telles études n'ont été menées que dans les alliages ferrimagnétiques de GdFeCo structurés en micro- ou nano-disques. Dans cette thèse, nous avons présenté les premières tentatives de l'étude des effets de taille du retournement tout-optique dans des couches minces ferromagnétiques de Co/Pt. En premier lieu, il est apparu convenable de d'abord explorer le renversement de l'aimantation de micro-structures à l'aide d'impulsions laser. Nous avons mis en place deux méthodes pour sonder l'état magnétiques des micro-structures après excitation laser. La première méthode consiste en de l'imagerie magnéto-optique en statique et différentiel. Dans la deuxième approche, le changement de l'aimantation induit par le laser est sondé par caractérisation électrique via l'effet Hall anormal. Pour ce faire nous avons fabriqué une croix de Hall en Ta/Pt avec des micro-plots de Pt/Co/Pt par-dessus qui nous a permis de déduire l'état magnétique après impulsions laser par mesure de magnéto-transport. Cette méthode a l'avantage d'être plus quantitative quant à la mesure du taux de renversement induit par le laser en comparaison aux méthodes d'imagerie statique. Nous avons mis en place deux types d'expériences pour lesquelles la configuration du laser a été changée : dans un cas, le faisceau laser est balayé à la surface de l'échantillon (réseaux de plots ou croix de Hall), dans l'autre cas le faisceau laser est maintenu fixe et centré sur un plot. Nous avons montré que nous pouvions reproduire le retournement de l'aimantation tout-optique dépendant de l'hélicité de micro-plots de (Co/Pt) avec un diamètre aussi petit que 3 microns. Par ailleurs, nous avons mis en évidence qu'il n'existait pas de différence particulière entre le film continu et les micro-motifs dans le cas du balayage du faisceau laser.

Par la suite, nous nous sommes penchés sur l'influence du nombre de impulsions nécessaires au renversement étant donné l'origine cumulative du retournement tout-optique. De manière inattendue, nous avons observé qu'un plus grand nombre d'impulsions laser était requis pour induire un renversement de l'aimantation dans un micro-plot en comparaison aux couches continues après exposition à des impulsions d'une durée de 600 fs. Par ailleurs, il semblerait que plus le diamètre du plot est petit, plus le nombre d'impulsions nécessaires pour observer le retournement tout-optique augmente. Ces résultats surprenant permettent d'améliorer notre compréhension du mécanisme du renversement de l'aimantation tout-optique [publication à venir]. En effet, ces résultats suggèrent que le champ dipolaire aide le renversement de l'aimantation dans les couches continues par impulsions laser, qui de fait rend le retournement tout-optique plus efficace énergétiquement dans les couches continues. Ainsi, il semblerait que les systèmes de (Co/Pt) ne sont pas des candidats idéaux pour l'intégration du retournement tout-optique dans des dispositifs de stockage de l'information à très haute densité et ultra-rapide. Cependant il serait nécessaire d'étendre cette étude à des plots de plus petite taille, à l'échelle du nanomètre par exemple pour confirmer ces conclusions. Il est notamment attendu qu'à partir d'une certaine taille le plot ne puisse prendre que deux états magnétiques bien définis selon l'orientation de l'aimantation, et qui pourraient potentiellement rendre le renversement induit par laser plus facile. Néanmoins, il faut noter qu'à l'échelle du nanomètre la stabilité thermique du plot deviendra un problème à considérer.

De plus, dans nos expériences nous avons dû faire face à un certain nombre de complications. Tout d'abord, l'imagerie statique et différentielle ne permet pas de sonder de manière précise l'état magnétique après excitation laser de plots de petites tailles comme il devient difficile de résoudre optiquement les domaines magnétiques. C'est pourquoi nous nous sommes orientés vers des mesures de transport qui ont eux aussi révélés quelques soucis. Les dispositifs de croix de Hall souffraient d'une durée de vie très courte due aux effets de chauffage extrême par le laser ce qui nous a empêché de mettre en place une méthode systématique et statistique de mesure du taux de renversement de l'aimantation par impulsions laser dans les micro-plots. Il serait donc nécessaire de revoir la structure adéquate et l'épaisseur de la croix de Hall pour permettre des mesures précises et reproductibles du taux de renversement de l'aimantation. Cependant, il est à noter que la caractérisation électrique par l'effet Hall anormal est un outil puissant pour sonder le retournement tout-optique. Enfin, avec les dispositifs que nous avons fabriqué par photo-lithographie, de nouvelles expériences pourraient être envisagées pour la combinaison du renversement de l'aimantation par impulsions laser et par spin-transfer torque ou spin-orbit torque, ce qui constituerait un nouveau domaine de recherche.

Pour finir, nous pensons que les travaux de recherches menés durant cette thèse améliorent l'état actuel de notre connaissance sur la compréhension des mécanismes physiques à l'origine du renversement de l'aimantation tout-optique dans les matériaux ferromagnétiques. En effet, il est admis désormais que le renversement tout-optique dans les ferro-aimants se met en place par une première étape de nucléation suivie d'une propagation des parois de domaines selon l'hélicité. Pour autant, l'origine microscopique de l'effet de l'hélicité sur une paroi de domaine ferromagnétique reste très peu connue et requiert davantage d'investigations. Nous avons également fourni de nouvelles indications pour la possible intégration du retournement tout-optique de l'aimantation dans des dispositifs de stockage de l'information à très haute densité et ultra-rapide. L'un des aspects qui n'a pas été abordé dans cette thèse est notamment l'étude de la dynamique des phénomènes que nous avons étudié et ce sur une échelle de temps assez courte suivant l'impulsion laser. Par l'étude de la dynamique de la propagation de parois induit par impulsions laser, de nombreuses informations pourraient en être extraites telle que l'inertie de la paroi et la barrière de piégeage. Il est évident que la physique derrière le retournement tout-optique de l'aimantation est très riche et que de nombreuses questions demeurent en suspens. Nous pensons que ce travail de thèse permettra d'envisager de nouvelles directions de recherche dans le retournement tout-optique de l'aimantation de matériaux ferromagnétiques.